

# Configurable Organic Electrochemical Transistors with Printed Functional Materials for Multiplexed Sweat Analysis

Présentée le 24 juin 2022

Faculté des sciences et techniques de l'ingénieur  
Laboratoire des Microsystèmes Souples  
Programme doctoral en microsystèmes et microélectronique

pour l'obtention du grade de Docteur ès Sciences

par

**Silvia DEMURU**

Acceptée sur proposition du jury

Prof. S. Carrara, président du jury  
Dr. D. Briand, directeur de thèse  
Prof. G. Malliaras, rapporteur  
Prof. A. Bonfiglio, rapporteuse  
Prof. Ph. Renaud, rapporteur

Don't let anyone rob you of your imagination, your creativity, or your curiosity. It's your place in the world; it's your life. Go on and do all you can with it, and make it the life you want to live. -Mae Carol Jemison

# Acknowledgments

First of all, I want to thank my supervisor Danick Briand for guiding me during this exciting Ph.D. journey. I cannot thank you enough for all the time you spent sharing your knowledge and advice with me and for your help in staying focused and enthusiastic about this research every day. Thanks to you, I am now a better scientist (and a more precise and organized person!).

I would like to express my deepest gratitude to the jury members of the private defense: Prof. Philippe Renaud from EPFL, Prof. Sandro Carrara from EPFL, Prof. Annalisa Bonfiglio from Università di Cagliari, and Prof. George Malliaras from Cambridge University. I am honored to have you on the jury to review my scientific work and the thesis manuscript with your highly valuable advice and knowledge in the field.

A warm thank you goes to Peter Van der Wal, the person that every scientific environment needs. You are a truly kind and knowledgeable person, and several generations of Ph.D. students in Microcity would have been lost without you many times (including me!); thanks for all the time passing by my office if I had a scientific question or just for chatting.

Special thanks go to all the collaborators of the WeCare project for the great discussions about sweat and wearables these four years: Céline Lafaye, Mathieu Saubade, and Vincent Gremeaux-Bader from the CHUV team, Shih-Chii Liu, Ilya Kiselev, and Shu Wang from the Zurich team, and Cecilia Jimenez, Cesar Fernandez, Paco Serra, Josep Maria Margarit Taulé, and Meritxell Rovira from the Barcelona team; it was great to know you and to spend time with you around Lausanne, Neuchatel, Zurich, and Barcelona, and of course lately during all the online meetings.

Thanks to the collaborators from Paris Diderot University: Giorgio Mattana, Vincent Noel, Benoît Piro, and Khalil Chennit, I truly appreciate the warm welcome you gave me to your laboratory in Paris, and I had a fantastic time with you discussing about electrochemistry and organic transistors these years.

Special thanks go to Herbert Shea for his support and the nice discussions during the group meetings and to the amazing LMTS group full of talented and interesting people, making the laboratory environment a great place to be every day. Thanks to Myriam Poliero for her kind help and the fun conversations all time. Thanks to my old and new office mates Alessione Mancinelli, Ryan van Dommelen, Nicolas Fumeaux, and James Bourelly for a great time these years (and for not complaining too much about my loud voice!). I am particularly grateful to Jaemin Kim, Brince Kunnel, Alexis Marette, and Rubaiyet Haque; your contributions and knowledge helped me so much during the thesis. Thanks also

to Morgan Monroe and Fatemeh Farsijani for the great times; we should keep on organizing the lab-ladies dinners. To the people that are (or were) in Microcity these years, it was great to interact with each one of you: Giulio Grasso, Valentin Py, Samuel Schlatter, Edouard Leroy, Bekir Aksoy, Ulas Adiyen, Vito Cacucciolo, Mehdi Benbedda, Alexandre Poulin, Ulas Adiyen, Merlin Monroe, Claudio Almeida, Florian Hartmann, Jean-Baptiste Chossat, Krishna Digumarti, Robert Hennig, Shai Shmulevich, Ronan Hinchet, Djen Kühnel, Michael Smith, Fabio Albuquerque, Min Gao, Sylvain Schaller, Juan Zarate, Christine de Saint-Aubin, Xiaobin Ji, Joanna Bitterli, and Pieter Vlugter.

Thanks to the people that helped me in different projects along the way and that I had the pleasure to co-supervise: Marc O. Joho, Angélique Bionaz, Jérémy Jayet, Le Hoang Giau, Cheng-Hua Huang, Jeanneret-Grosjean Guillaume Joël, and El Chazli Marwan.

Grazie to the “Lausanne team” of friends for all the fun these years, with a special mention to Soumya Yandrapalli, Gianfranco Piredda, Adele Fanelli, and Sammy Cerida. Ringrazio le mie migliori amiche sarde, perché ogni volta che torno a Ozieri è come se non me ne fossi mai andata: Marta Mellino, Rosaria Testoni, Giulia Spanu, Cinzia Contini, Serena Contini, Miriam Murgia, Miriam Dessì, Elettra Putzu, e Federica Borghi.

Il grazie più grande va a mia madre Itria Duras, mio padre Gianni Demuru, e mia sorella Alessia Demuru; grazie per il vostro infinito supporto e incoraggiamento tutti questi anni che ho passato in giro per il mondo!

Last but not least, thanks to Luca Nela for all the support, the fun, and the laughs; these four years passed so fast with you. Thanks for all the hiking around Switzerland, I would probably be in a terrible physical (and mental!) shape without you. I am looking forward to the next adventures here with you!

# Abstract

Monitoring human sweat with wearable biochemical sensors could give insights into the hydration, fatigue, and health status, tracking the variations of biomarkers non-invasively and in real-time. To this end, organic electrochemical transistors (OECTs) are gaining significant importance thanks to their high signal amplification, simple architecture, and mechanical flexibility of the organic layer. Despite these properties, their use to analyze complex biological fluids, such as sweat, is still limited due to the lack of cross-sensitivity, stability, and sensing mechanism studies. In addition, further integration of several OECTs sensors into wearable solutions would unveil the potential of this platform for real-time health monitoring.

This thesis investigates OECT sensors with different gate materials and bio-recognition layers at the electrode interfaces to achieve multiplexed sensing. We demonstrate that devices with different architectures can be combined into multi-OECT platforms to detect a large number of analytes such as ions, pH, metabolites, and antigens. By using additive manufacturing techniques, the integration of the sensors array into microfluidics is facilitated, leading to digitally-configurable wearable platforms. In addition, the sensing mechanisms of the presented devices are investigated by combining electrical modeling with electrochemical impedance spectroscopy (EIS), revealing important insights into their operation and potentially enabling significant improvements in their performance.

The first study explores OECTs for real-time multi-ion sensing. The OECT array is made by inkjet printing poly(3,4-ethylene dioxythiophene):polystyrene sulfonate (PEDOT:PSS) channels and silver nanoparticles gates and contacts. To improve their specificity, different ion-selective membranes for  $K^+$ ,  $Na^+$ , and  $H^+$  sensing are cast onto the PEDOT:PSS channels. The OECTs integrated into a flexible fluidic channel show successful discrimination of different ions in real-time at the sweat concentration ranges.

In the second study, hybrid PEDOT:PSS and polyaniline (PANI) active channels were developed and investigated to optimize the pH sensing performances compared to OECTs with  $H^+$ -selective membranes. With the active layer made of a combination of the inkjet-printed PEDOT:PSS and the electro-polymerized PANI, high pH sensitivity and linearity are achieved in the 4 to 10 pH range. EIS analysis relates the sensor response to a substantial increase of capacitance on the PANI/PEDOT:PSS interface at acidic pH.

In the third study, inkjet-printed OECT devices for enzymatic sensing of glucose and lactate, exploiting a full-graphene gate electrode, are investigated. The OECT sensors with graphene gates, in the presence of ferrocene, show higher sensitivity, linearity, and repeatability than OECTs made of standard inkjet-

printed silver nanoparticle-based gate electrodes and previously reported printed devices. EIS reveals a decrease in charge-transfer resistance at the graphene gate interface during the enzymatic detection.

The fourth study shows OECTs with antibodies immobilized on gold gates to detect low cortisol concentrations. High signal amplification of the binding events at the gate interface was achieved by optimizing the PEDOT:PSS channel design, measuring cortisol in the nM-range in PBS and real sweat samples. Experimentally, the sensor response was attributed to an increase in capacitance of the gate interface with the binding, which analytical electrical models confirmed.

The outcome of these studies enables the development of novel wearable and configurable organic electrochemical transistor arrays for multiplexed sensing. The proof-of-concept of an integrated and miniaturized multi-OECT platform is finally demonstrated to analyze ions in sweat.

The results presented here pave the way towards the realization of a fully integrated, wearable, OECT-based, multi-sensing platform enabling real-time monitoring of dehydration, fatigue, and stress levels.

**Keywords:** Organic electrochemical transistor, biosensor, sweat analysis, chemical sensor array, wearable, polymeric foil, inkjet printing, ion selective membrane, enzyme, antibody

# Sommario

Il monitoraggio del sudore umano con sensori biochimici indossabili potrebbe fornire informazioni sull'idratazione, l'affaticamento e lo stato di salute delle persone, monitorando le variazioni di diversi biomarcatori in modo non invasivo e in tempo reale. Per questa applicazione, i transistori elettrochimici organici (OECT) stanno acquisendo un'importanza significativa grazie alla loro elevata amplificazione del segnale, all'architettura semplice e alla flessibilità meccanica del materiale organico. Nonostante queste proprietà, il loro uso per analizzare fluidi biologici complessi, come il sudore, è ancora limitato a causa della mancanza di studi sulla sensibilità incrociata, sulla stabilità e sul meccanismo di rilevamento del segnale. Inoltre, l'integrazione di diversi sensori OECTs in dispositivi indossabili aiuterebbe a dimostrare il potenziale di questa piattaforma per il monitoraggio della salute in tempo reale.

Questa tesi studia i sensori OECT con diversi materiali di gate e molecole per il bio-riconoscimento alle interfacce degli elettrodi per ottenere un rilevamento multiplex. Dimostriamo che i dispositivi con diverse architetture possono essere combinati in piattaforme multi-OECT per rilevare un gran numero di analiti come ioni, pH, metaboliti e antigeni. Utilizzando tecniche di produzione additiva, l'integrazione dell'array di sensori in un sistema microfluidico è facilitato, portando a piattaforme indossabili digitalmente configurabili. Inoltre, i meccanismi di rilevamento dei dispositivi presentati sono studiati combinando la modellazione elettrica con la spettroscopia d'impedenza elettrochimica (EIS), rivelando importanti informazioni nel loro funzionamento e potenzialmente consentendo miglioramenti significativi della loro performance.

Il primo studio esplora gli OECT per il rilevamento di diversi ioni in tempo reale. L'array OECT è costituito dalla stampa "inkjet" di canali di poli(3,4-etilene diossitiofene): polistirene sulfonato (PEDOT:PSS) ed elettrodi di gate e contatti di nanoparticelle d'argento. Per migliorare la loro specificità, diverse membrane ione-selettive per il rilevamento di  $K^+$ ,  $Na^+$  e  $H^+$  vengono depositate sui canali PEDOT:PSS. Gli OECT integrati in sistema fluidico flessibile riescono a discriminare diversi ioni in tempo reale nelle concentrazioni rilevate nel sudore umano.

Nel secondo studio, sono stati sviluppati e studiati i canali attivi ibridi PEDOT:PSS e polianilina (PANI) per ottimizzare le prestazioni di rilevamento del pH rispetto agli OECT con membrane  $H^+$ -selettive. Con lo strato attivo costituito da una combinazione di PEDOT:PSS stampato "inkjet" e PANI elettropolimerizzato, si ottengono un'elevata sensibilità e linearità del pH nell'intervallo da 4 a 10 pH. L'analisi EIS mette in relazione la risposta del sensore con un aumento sostanziale della capacità sull'interfaccia PANI/PEDOT:PSS a pH acido.

Nel terzo studio, vengono studiati dispositivi OECT stampati per il rilevamento enzimatico di glucosio e lattato, sfruttando un elettrodo gate completamente in grafene. I sensori OECT con gate di grafene, in presenza di ferrocene, mostrano una maggiore sensibilità, linearità e ripetibilità rispetto agli OECT realizzati con elettrodi gate standard a base di nanoparticelle d'argento stampato e dispositivi stampati precedentemente riportati. EIS rivela una diminuzione della resistenza al trasferimento di carica all'interfaccia del gate del grafene durante il rilevamento enzimatico.

Il quarto studio mostra OECT con anticorpi immobilizzati su elettrodi di gate d'oro per rilevare basse concentrazioni di cortisolo. L'elevata amplificazione del segnale degli eventi di legame all'interfaccia del gate è stata ottenuta ottimizzando il design del canale PEDOT:PSS, misurando il cortisolo nell'intervallo nM in PBS e campioni di sudore reale. Sperimentalmente, la risposta del sensore è stata attribuita a un aumento della capacità dell'interfaccia del gate con il legame del cortisolo, che i modelli elettrici analitici hanno confermato.

Il risultato di questi studi permette lo sviluppo di nuovi array di transistori elettrochimici organici indossabili e configurabili per il rilevamento multiplex. Il prototipo di una piattaforma integrata e miniaturizzata multi-OECT è finalmente dimostrato per analizzare gli ioni nel sudore.

I risultati qui presentati aprono la strada verso la realizzazione di una piattaforma multisensore completamente integrata, indossabile, basata su dispositivi OECT, che consente il monitoraggio in tempo reale della disidratazione, fatica e livelli di stress.

Parole chiave: transistore elettrochimico organico, biosensore, analisi del sudore, sensori chimici integrati, dispositivo indossabile, substrato polimerico, elettrodo stampato, membrana iono-selettiva, enzima, anticorpo



# Résumé

La mesure de la sueur humaine à l'aide de capteurs biochimiques portables pourrait donner des indications sur l'hydratation, la fatigue et l'état de santé, en suivant les variations des biomarqueurs de manière non invasive et en temps réel. À cette fin, les transistors électrochimiques organiques (OECT) gagnent en importance grâce à leur forte amplification du signal, leur architecture simple et la flexibilité mécanique de la couche organique. Malgré ces propriétés, leur utilisation pour analyser des fluides biologiques complexes, tels que la sueur, est encore limitée en raison du manque d'études sur la sensibilité croisée, la stabilité et le mécanisme de détection. En outre, l'intégration de plusieurs capteurs OECTs dans des solutions portables révélerait le potentiel de cette plateforme pour l'évaluation de la santé en temps réel.

Cette thèse étudie les capteurs OECT avec différents matériaux de grille et des couches de bio-reconnaissance aux interfaces des électrodes pour réaliser une détection multiplexée. Nous démontrons que des dispositifs avec différentes architectures peuvent être combinés en plateformes multi-OECT pour détecter un grand nombre d'analytes tels que les ions, le pH, les métabolites et les antigènes. En utilisant des techniques de fabrication additive, l'intégration du réseau de capteurs dans la microfluidique est facilitée, conduisant à des plateformes portables numériquement configurables. En outre, les mécanismes de détection des dispositifs présentés sont étudiés en combinant la modélisation électrique et la spectroscopie d'impédance électrochimique (SIE), révélant des informations importantes sur leur fonctionnement et permettant potentiellement des améliorations significatives de leur performance.

La première étude explore les OECT pour la détection multi-ionique en temps réel. La matrice OECT est fabriquée en imprimant par jet d'encre des canaux en poly(3,4-éthylène dioxythiophène):polystyrène sulfonate (PEDOT:PSS) et des grilles et contacts en nanoparticules d'argent. Pour améliorer leur spécificité, différentes membranes sélectives d'ions pour la détection de  $K^+$ ,  $Na^+$  et  $H^+$  sont déposées sur les canaux PEDOT:PSS. Les OECTs intégrés dans un canal fluide flexible montrent avec succès une différenciation de plusieurs ions en temps réel dans les gammes de concentration de sueur.

Dans la deuxième étude, des canaux actifs hybrides en PEDOT:PSS et polyaniline (PANI) ont été développés et étudiés pour optimiser les performances de détection du pH par rapport aux OECTs avec des membranes sélectives de  $H^+$ . Avec la couche active constituée d'une combinaison de PEDOT:PSS imprimé jet d'encre et de PANI électropolymérisé, une sensibilité et une linéarité élevées du pH sont obtenues dans la gamme de 4 à 10 pH. L'analyse SIE relie la réponse du capteur à une augmentation substantielle de la capacité sur l'interface PANI/PEDOT:PSS à un pH acide.

Dans la troisième étude, des dispositifs OECT imprimés par jet d'encre pour la détection enzymatique du glucose et du lactate, exploitant une électrode de grille entièrement en graphène, sont étudiés. Les capteurs OECT avec des grilles en graphène, en présence de ferrocène, démontrent une sensibilité, une linéarité et une répétabilité plus élevées que les OECT fabriqués avec des électrodes de grille standard à base de nanoparticules d'argent imprimées par jet d'encre et les dispositifs imprimés précédemment rapportés. L'analyse SIE révèle une diminution de la résistance au transfert de charge à l'interface de la grille en graphène pendant la détection enzymatique.

La quatrième étude montre des OECT avec des anticorps immobilisés sur des grilles en or pour détecter de faibles concentrations de cortisol. Une amplification élevée du signal des événements de liaison à l'interface de la grille a été obtenue en optimisant la conception du canal PEDOT:PSS, mesurant le cortisol dans la gamme des nM dans du PBS et des échantillons de sueur réels. Expérimentalement, la réponse du capteur a été attribuée à une augmentation de la capacité de l'interface de la grille avec la liaison, ce que les modèles électriques analytiques ont confirmé.

Le résultat de ces études permet le développement de nouveaux réseaux de transistors électrochimiques organiques configurables et portables pour la détection multiplexée. La preuve de concept d'une plateforme multi-OECT intégrée et miniaturisée est finalement démontrée pour analyser les ions dans la sueur.

Les résultats présentés ici ouvrent la voie à la réalisation d'une plateforme multi-détection entièrement intégrée, portable et basée sur l'OECT, permettant d'évaluer en temps réel la déshydratation, la fatigue et les niveaux de stress.

Mots-clés : Transistor électrochimique organique, biocapteur, analyse de la sueur, réseau de capteurs chimiques, appareil portable, feuille polymère, impression à jet d'encre, membrane sélective d'ions, enzyme, anticorps

# Table of Contents

Acknowledgments .....	1
Abstract .....	3
Sommario .....	5
Résumé .....	7
Table of Contents .....	9
List of Journal articles .....	13
List of Figures .....	14
List of Tables.....	26
Chapter 1     Introduction .....	27
1.1     Biosensors.....	27
1.1.1     Wearable biochemical sensors for sweat analysis .....	29
1.2     Organic transistor-based biochemical sensors.....	31
1.2.1     PEDOT:PSS-based organic electrochemical transistors.....	33
1.3     Challenges and motivations.....	35
1.3.1     Challenges in sweat science and biosensing.....	35
1.3.2     Challenges in the field of OECT biosensors.....	35
1.3.3     Motivations.....	36
1.4     Thesis structure.....	37
Chapter 2     State-of-the-art.....	42
2.1     OECTs for biochemical sensing .....	42
2.1.1     OECTs for ion sensing.....	44
2.1.2     OECTs for enzymatic-based sensing.....	45
2.1.3     OECTs for antibody- or aptamer-based sensing.....	46
2.2     Analysis of the sensing mechanisms and design .....	48
2.3     Technology and integration .....	50

2.3.1	OECTs for sweat sensing.....	51
2.4	Summary and contributions.....	52
Chapter 3	Real-time multi-ion sensing using organic electrochemical transistors (Paper I) .....	55
3.1	Introduction .....	56
3.2	Results and Discussion .....	57
3.2.1	Characterization of the inkjet-printed layers .....	57
3.2.2	Electrical analysis without the ion-selective membranes .....	59
3.2.3	Electrical analysis with the ion-selective membranes .....	60
3.2.4	Array integration into the microfluidic system and sensing .....	63
3.3	Conclusions .....	65
3.4	Experimental Section.....	66
3.4.1	Fabrication and layers characterization .....	66
3.4.2	Membranes preparation .....	67
3.4.3	Microfluidics fabrication .....	67
3.5	Supporting Information of Chapter 3.....	69
Chapter 4	OECTs with PANI/PEDOT:PSS active layers for pH sensing (Paper II) .....	74
4.1	Introduction .....	75
4.2	Materials and methods.....	77
4.2.1	Inks, chemicals and solutions preparation .....	77
4.2.2	Inkjet printing of the organic electrochemical transistors.....	77
4.2.3	Electropolymerization of the PANI layer on the PEDOT:PSS channel .....	78
4.2.4	Imaging .....	78
4.2.5	Testing .....	78
4.3	Results and discussion .....	80
4.3.1	Electropolymerization and morphology of the hybrid PEDOT:PSS-PANI layer.....	80
4.3.2	Electrical characterization of the PEDOT:PSS-PANI transistors.....	82
4.3.3	Detection of pH variations.....	83

4.3.4	Analysis of the sensing mechanism .....	86
4.4	Conclusions .....	87
4.5	Supporting Information of Chapter 4.....	89
Chapter 5	Inkjet-printed graphene-gated OECT for enzymatic-based sensing (Paper III) .....	92
5.1	Introduction .....	93
5.2	Experimental section .....	95
5.2.1	Functional inks .....	95
5.2.2	Inkjet printing of the organic electrochemical transistors.....	95
5.2.3	Enzymatic solutions.....	97
5.2.4	Membrane preparation.....	97
5.2.5	Sensing protocol .....	97
5.2.6	Characterization and testing .....	98
5.3	Results and discussion .....	99
5.3.1	Electrical characterization of the OECTs .....	99
5.3.2	Real-time sensing with the OECTs.....	100
5.3.3	The sensing mechanism.....	103
5.4	Conclusions .....	106
5.5	Supporting Information of Chapter 5.....	108
Chapter 6	OECTs with antibody-coated gates for cortisol sensing in human sweat (Paper IV) .	116
6.1	Introduction .....	117
6.2	Results .....	119
6.2.1	Devices and electrical measurements .....	119
6.2.2	Cortisol biosensing .....	122
6.2.3	Sensing mechanism .....	125
6.2.4	Sweat analysis.....	127
6.3	Discussion.....	130
6.4	Methods .....	131

6.4.1	Biofunctionalization .....	131
6.4.2	Device fabrication.....	131
6.4.3	Electrochemical testing.....	132
6.4.4	Sweat collection.....	133
6.4.5	Liquid chromatography-tandem mass spectrometry.....	133
6.5	Supporting Information of Chapter 6.....	135
Chapter 7	Integrated multi-OECT platform for multiplexed sweat analysis (Paper V) .....	141
7.1	Introduction .....	142
7.2	Results and Discussion .....	143
7.2.1	OECT platforms .....	143
7.2.2	Characterization of ion-sensitive and ion-selective OECTs .....	145
7.2.3	Multi-analyte detection using the integrated OECT array .....	147
7.2.4	Calibration and sweat analysis with the multi-ion OECTs.....	148
7.3	Conclusions .....	150
7.4	Experimental Section.....	150
7.4.1	Sensors platform materials and processing.....	150
7.4.2	Ion-selective membranes preparation .....	151
7.4.3	Electronics readout .....	151
7.4.4	Sensors characterization and analyte measurements .....	152
7.4.5	Sweat samples.....	152
7.5	Supporting Information of Chapter 7.....	154
Chapter 8	Conclusions and outlook.....	157
8.1	Conclusions .....	157
8.2	Outlook .....	159
References	.....	162
<i>Curriculum Vitae</i>	.....	183

# List of Journal articles

The structure of this thesis is organized based on the following journal articles:

**Paper I.** Demuru, S., Kunnel, B. P., and Briand, D. Real-Time Multi-Ion Detection in the Sweat Concentration Range Enabled by Flexible, Printed, and Microfluidics-Integrated Organic Transistor Arrays. *Adv. Mater. Technol.* 2000328, 5, 1–9 (2020). <https://doi.org/10.1002/admt.202000328>

**Paper II.** Demuru, S., Kunnel, B. P., and Briand, D. Thin film organic electrochemical transistors based on hybrid PANI / PEDOT: PSS active layers for enhanced pH sensing. *Biosens. Bioelectron.* X 7, 1–9 (2021). <https://doi.org/10.1016/j.biosx.2021.100065>

**Paper III.** Demuru, S., Huang, C., Parvez, C., Worsley, R., Mattana, G., Piro, B., Vincent, N., Casiraghi, C., and Briand, D. All-Inkjet-Printed Graphene-Gated Organic Electrochemical Transistors on Polymeric Foil as Highly-Sensitive Enzymatic Biosensors. *ACS Applied Nano Materials* 5, 1, 1664–1673 (2022). <https://doi.org/10.1021/acsanm.1c04434>

**Paper IV.** Demuru, S., Kim, J., El Chazli, M., Lafaye, C., Bruce, S., Dupertuis, M., Binz, P.-A., Saubade, M., and Briand, D. Antibody-coated wearable organic electrochemical transistors for cortisol monitoring in human sweat. *Manuscript submitted for publication* (2022).

**Paper V.** Demuru, S., Kim, J., Kiselev, I., Jeanneret-Grosjean, G. J., Saubade, M., Lafaye, C., Liu, S.-C., and Briand, D. Integrated fully-printed organic electrochemical transistors platform for multiplexed sweat analysis. *Manuscript in preparation* (2022).

# List of Figures

Figure 1-1: General schematic of a biosensor.[2].....	27
Figure 1-2: Examples of multiple biosensors for wearable healthcare applications.[5].....	28
Figure 1-3: Clinical application of wearable biosensors. (a) Difference of ions measured through sweat stimulation (iontophoresis) in normal subjects and patients with cystic fibrosis (CF). (b) Correlation on glucose in interstitial fluid and plasma for diabetes management. [27] The figure is modified from the original publication.....	30
Figure 1-4: Cross-section of the OECTs and OFETs devices. The red circles indicate the different interfaces where the biosensing reaction can take place.[4] ECP stands for Electrically Conductive Polymer and OSC for Organic Semiconductor. The figure is modified from the original publication....	32
Figure 1-5: Schematic of an OECT channel highlighting the electrical and ionic charges interaction (a), the structure of an OECT device (b), and electrical characteristics in an electrolyte solution (c).[52] The figure is modified from the original publication.....	34
Figure 2-1: Ion sensitive properties depending on the gate material in OECTs. Comparison of gold (Au), platinum (Pt), and silver/silver chloride (Ag/AgCl) gates at a fixed ionic concentration in (a) and variable ionic concentrations in (b-d).[47] The figure is modified from the original publication. ....	44
Figure 2-2: Comparison of the sensing performances of gold-gated OECTs functionalized with antibodies or aptamers. (a) OECT with anti-rabbit IgG antibody on the gate during IgG sensing. (b) OECT with the anti-IL-6 antibody on the gate during IL-6 sensing. (c) OECT with aptamers on the gate during epinephrine sensing. (d) OECT with nanobody on the gate during COVID-19 antigen detection. Modified from [67], [125], [102], [69].....	48
Figure 3-1: Graphical abstract. Organic electrochemical transistor arrays with multiple ion-selective membranes for real-time ion sensing.....	55



Figure 3-2: a) Schematic of the integrated organic transistors into the microfluidic system and zoom with the cross-section in (b). c,d) Images of the transistors, without and with microfluidics in (c) and (d), respectively.....	58
Figure 3-3: a-c) The electrical characteristics of the DMSO treated OEET in PBS 1X (0.155 M NaCl, pH 7). d) Transfer curves at different ionic concentrations of KCl including DI water as a baseline. e) Time measurements with different ionic solutions and concentrations. f) Leakage current with different ionic solutions and concentrations.....	60
Figure 3-4: a-c) Sketches of OEETs with different ion-selective membranes. d-f) Simplified interactions between an electrolyte solution, the ion-selective membranes, and the PEDOT:PSS active layer considering (d) the potassium ionophore-based membrane, (e) the sodium ionophore X-based membrane and (f) the hydrogen ionophore I-based membrane. The chemical name of the respective ionophore is reported in the image. The sulfonate groups and the polarons (holes) of the organic layers are also represented, with the respective permeated ions de-doping the PEDOT by removing the polarons.....	61
Figure 3-5: Organic transistors electrical responses in PBS (0.155 m NaCl + 0.155 m KCl, pH 7) with (a-c) lower (~2 $\mu$ L) and (d-f) higher (~5 $\mu$ L) volume of the three different ion-selective membranes. The results are compared to a bare device (no membrane). The analysis includes transfer characteristics in (a,d), transconductance in (b,e) and time response in (c,f).....	62
Figure 3-6: Ion sensing with the integrated microfluidic system for OEETs without a membrane in (a,e), with the K <sup>+</sup> selective membrane in (b,f), the Na <sup>+</sup> selective membrane in (c,g), and the H <sup>+</sup> selective membrane in (d,h). The sensitivity tests are shown in (a-c) and the selectivity tests in (e-h). The solutions (except the pH buffers) were made with KCl or NaCl dissolved in DI water. V <sub>ds</sub> = -0.4 V, while V <sub>gs</sub> was fixed close to the transconductance peak (0.1-0.4 V) for each device. ....	64
Figure S3-7: Cross-sections of the OEET devices. a) Multi-layer materials including the reservoir used for the electrolyte confinement. b) Final integrated microfluidics system. ....	69
Figure S3-8: Analysis with different printed PEDOT:PSS layers. a) Sheet resistance before and after DMSO post-treatment and a different number of layers (dry state); the points are averaged with n=4	

samples. b) Transconductance peak of the post-treated layers and a different number of layers. c) Transconductance values versus the thickness of the layers, tested with PBS 1X (0.155 M NaCl) and in the PMMA reservoir ( $V_{ds} = -0.4$  V); the  $g_m$  values are averaged with  $n=4$  samples for 4 printed layers and  $n=2$  for 1 to 3 printed layers, while the thickness measurements are averaged with  $n=3$  samples for 4 printed layers and  $n=2$  for 1 to 3 printed layers..... 69

Figure S3-9: Resistance analysis for four printed layers of PEDOT:PSS. Change of resistance in time for untreated and treated PEDOT:PSS channels (dry); the values are averaged with  $n=4$  samples of the same batch and monitored in time. .... 70

Figure S3-10: Mechanical flexibility analysis for the integrated OECT array into microfluidics. The electrical resistance of four PEDOT:PSS channels was measured before (unbent) , during the three bending conditions at the radius of 20 mm (a), 15 mm (b), and 10 mm (c), and after the removal from the plastic support (unbent). The values are reported in (d), normalized with the resistance measured before starting the bending tests ( $n=4$ ). The array of OECTs was attached to the rounded plastic supports through double-side tape..... 70

Figure S3-11: Calibration curves for the OECTs into the microfluidics system. a,e) Calibration without a membrane using KCl solutions. b,f) Calibration with  $K^+$  membrane using KCl solutions. c,g) Calibration with  $Na^+$  membrane using NaCl solutions. d,h) Calibration with  $H^+$  membrane using pH buffer solutions. Sensing values including deionized (DI) water in (e-h), in (h) including the influence of pH without  $H^+$  membrane.  $V_{ds} = -0.4$  V, and  $V_{gs}$  was fixed close to the transconductance peak depending on the device. The sensing analysis was performed on the same printed batch with a PEDOT:PSS thickness of  $115 \pm 28$  nm ( $n=3$ ). .... 71

Figure S3-12: Reproducibility analysis. Comparison of OECTs normalized sensing responses for two devices from two printed batches: a) without membrane in KCl solution, b) with the  $K^+$  membrane in KCl solutions, c) with the  $Na^+$  membrane in NaCl solutions, and d) with the  $H^+$  membrane in pH buffers. The testing was performed with the devices integrated into the microfluidics system. The results were normalized with the respective signal in DI water for the devices in (a), (b), and (c), and in neutral pH

buffer for the devices in (d). $V_{ds} = -0.4$ V, and $V_{gs}$ was fixed close to the transconductance peak depending on the device.....	72
Figure 4-1: Graphical abstract. Organic electrochemical transistors with hybrid PANI/PEDOT:PSS active layers for pH sensing. ....	74
Figure 4-2: Fabrication from digital manufacturing to electropolymerization. (a,b) Optical images of the inkjet-printed organic transistors on the flexible polyimide substrate, (c) schematics of the printing fabrication steps, (d) schematics of the 3-electrode setup used for the aniline electro-deposition, and (e) representation of the pH sensing transistor.....	79
Figure 4-3: Electropolymerization on the PEDOT:PSS layers. (a) Voltammogram of the electrochemical oxidative polymerization of aniline from 2 to 10 cycles, (b) optical images of the PEDOT:PSS-DMSO layers with different polymerized cycles (3, 6, 10), SEM images at different scales without electrodeposited polyaniline in (c) and with polyaniline in (d). The samples in (d) were obtained by 6-cycles electropolymerization. ....	81
Figure 4-4: Electrical characteristics in PBS 1X with the different electropolymerization cycles. (a) Transfer characteristics and (b) extracted transconductances without PANI and with different PANI-content. $V_{drain-source} = -0.4$ V in all the transfer curves.....	82
Figure 4-5: pH sensing in the OECTs configuration. Transfer characteristics of the organic transistors: (a) without the PANI layer on the PEDOT:PSS channel, (b) with 3 cycles-PANI, (c) with 6 cycles-PANI, and (d) with 10 cycles-PANI. Tests from pH 10 to pH 4, $V_{drain-source} = -0.4$ V in all the cases. ....	84
Figure 4-6: Calibration curves of the hybrid OECTs. Calibration curves with 6 cycles of PANI (a,c) and 10 cycles of PANI (b,d). The curves represent the voltage shifts in (a,b) and the current shifts in (c,d). Tests performed going from pH 10 to pH 4, $V_{drain-source} = -0.4$ V in all the cases. ....	85
Figure 4-7: Analysis of the sensing mechanism through EIS. EIS analysis including (a) the reactance versus the angular frequency for a PEDOT:PSS-only layer, (b) the reactance versus the angular frequency for a 6-cycles PANI-PEDOT:PSS layer, and (c) a sketch with the simplified electrical circuit and possible sensing mechanism in terms of voltage drops at the two electric double layer (EDL) interfaces. ....	87

Figure S4-8: Electropolymerization. (a) Optical image with the PEDOT:PSS layer after 10 cycles of polymerization without DMSO treatment, and (b) voltammogram of the polymerization of aniline from 2 to 10 cycles using the PEDOT:PSS channel without DMSO treatment. ....	89
Figure S4-9: Morphological analysis with FIB and confocal microscopes. (a,b) FIB cross-section of a PANI-PEDOT:PSS layer, and (c,d) zoom of the cross-section. (e,f) Analysis of different morphology parameters obtained with the confocal microscope. The measured values in (e,f) include the thickness of the PEDOT:PSS layers. ....	89
Figure S4-10: Morphological analysis with SEM and AFM. SEM images without PANI in (a) and with PANI in (b), and AFM images without PANI in (c) and with PANI in (d).....	90
Figure S4-11: Electrical characteristics with high-PANI content. Transfer curve (a) and output curve (b) with 10-cycles of PANI on the PEDOT:PSS channel. $V_{\text{drain-source}} = -0.4 \text{ V}$ in (a).....	90
Figure S4-12. Reversibility study. Transfer curves of the hybrid OECTs with 10 cycles of PANI (a,b) and 6 cycles of PANI (c,d). The testing was performed from high to low pH in (a,c) and back from low to high pH in (b,d). $V_{\text{drain-source}} = -0.4 \text{ V}$ in all the cases. ....	91
Figure 5-1: Graphical abstract. Organic electrochemical transistors with printed graphene gates for enzymatic-based sensing. ....	92
Figure 5-2: Design, working principle, and fabrication of the devices. (a) Optical image of the OECTs with graphene gates, (b) top-view schematics of a graphene-gated OECT and a silver-gated OECT showing the materials and the simplified enzymatic reaction, and the bias applied during testing, and (c) cross-section with the fabrication steps. ....	96
Figure 5-3: Electrical characteristics. Output (a) and (b) transfer characteristics of a silver-gated OECT, and output (c) and transfer (d) of a graphene-gated OECT. Tests in PBS 1X, pH 7.....	100
Figure 5-4: Glucose sensing, using only the enzyme for the detection on a silver-gated OECT (a) and on a graphene-gated OECT (b), and corresponding calibration curves (c). Sensing using both the enzyme and ferrocene (29:1 ratio) for a silver-gated OECT (d) and a graphene-gated OECT (e), and corresponding calibration curves (f). The enzyme is dissolved in PBS 1X. ....	102

Figure 5-5: Enzymatic immobilization test. (a) Optical image of the OECT with a membrane based on the GOx enzyme immobilized around the graphene-gate, (b) glucose sensing with the device, and (c) calibration curve with standard deviation for 4 devices. ....	103
Figure 5-6: Electrochemical impedance spectroscopy analysis. Nyquist plots of the silver-gate electrode (a) and the graphene-gate electrode (b) versus an Ag/AgCl reference, with only the enzyme in PBS, the enzyme and ferrocene (29:1 ratio), and adding 700 $\mu$ M of glucose. (c) Enzymatic reaction with the detection at the graphene electrode interface, (d) cross-section showing the potential transduction principle of OECTs and the electrochemical reactions, (e) schematics of the extracted model with the graphene-gate electrode, and (f) the detection mechanism in terms of voltage change. ....	106
Figure S5-7: Repeatability study. Calibration curves using only the enzyme for the detection with a silver-gated OECT (a) and with a graphene-gated OECT (b). Calibration curves using both the enzyme and ferrocene (29:1 ratio) with a silver-gated OECT (c) and with a graphene-gated OECT (d). Each calibration shows the results for three different devices. The GOx enzyme is dissolved in PBS 1X. ....	108
Figure S5-8: Leakage current in the OECTs during sensing. (a) OECT with a silver gate using only the GOx enzyme for the glucose detection and (b) using the enzyme and ferrocene. (c) OECT with a graphene gate using only the enzyme for the detection and (d) using the enzyme and ferrocene. ....	109
Figure S5-9: Sensing comparison. Glucose sensing with a graphene-gated device, with a fixed gate voltage of 0.1 V (far from the transconductance peak) in (a), relative calibration curve in (b), and relative leakage current in (c). ....	110
Figure S5-10: Limit of detection for glucose sensing. Typical sensing characteristics with the graphene-gated OECTs for glucose detection at low concentrations in (a) and calibration curves (b).....	111
Figure S5-11: Lactate sensing. (a) Sensing lactate in the sweat concentration range using both the LOx enzyme and ferrocene (29:1 ratio) and (b) corresponding calibration curves. (c) Sensing characteristics for lactate detection at low concentration using both the enzyme and ferrocene (29:1 ratio) and (d) calibration curves for three devices. ....	111

Figure S5-12: Leakage current with the membrane. Typical leakage current of the graphene-gated devices during glucose sensing with the GOx membrane immobilized around the gate electrode.....	112
Figure S5-13: Test with hydrogen peroxide. Sensing in time at different hydrogen peroxide concentrations with the silver-gated OECT in (a), with the corresponding calibration curve in (b), and the leakage current in (c). Sensing in time with the graphene-gated OECT in (d), with the corresponding calibration curve in (e), and the leakage current in (f). The hydrogen peroxide is diluted in PBS 1X.....	112
Figure S5-14: Cyclic voltammetry measurement. CV measurement for the graphene-gate electrode versus an Ag/AgCl reference, with only the GOx enzyme in PBS, the enzyme and ferrocene (29:1 ratio), and adding 700 $\mu\text{M}$ of glucose in (a), and with only PBS and adding 700 $\mu\text{M}$ of hydrogen peroxide ( $\text{H}_2\text{O}_2$ ) in (b). Scan rate 10 mV/s. ....	113
Figure S5-15: Raman spectroscopy. Raman spectra of the graphene layers before sintering, after sintering (250°C for 1 hour), and after the testing with hydrogen peroxide. The measurements are performed at 10 mW (a) and 100 mW (b) laser power. ....	113
Figure S5-16: Amplification mechanism. (a) Schematic of an OECT, and (b) schematic of the 2-electrode configuration. Glucose sensing tests with a graphene-gated OECT compared to the sensing tests in the 2-electrode mode (c), and zoom on the latter (d). Tests with the GOx enzyme and ferrocene in solution (29:1 ratio). The results for three different devices are reported for each configuration. In the OECT mode: $V_{\text{gs}} = 1 \text{ V}$ , $V_{\text{ds}} = -0.4 \text{ V}$ . In the amperometric mode: Voltage = 1 V. ....	114
Figure 6-1: Graphical abstract. Flexible OECTs with antibody-coated gates for cortisol detection. ....	116
Figure 6-2: Organic transistor structure and sticker application. (a) Schematic of the biosensing principle involved and structure of the OECT devices, including antibody-coated gate electrodes and the organic PEDOT:PSS channel for current amplification; the latter shows three OECT devices with different PEDOT:PSS channels of an increased width per length ratio. (b) Application of cortisol sensing sticker on the human skin for sweat collection during sports activities; the microfluidic part with the multiple inlets is placed in contact with the skin. ....	120

Figure 6-3: Organic transistor electrical characteristics. (a) Output characteristics with a  $V_{gs}$  voltage sweep from -1 to 1 V with a step of 0.25 V for devices having the anti-cortisol antibody on the gate electrode and a PEDOT:PSS W/L=1.2. (b) Comparison of transfer characteristics without and with antibodies, for a fixed PEDOT:PSS W/L=1.2 and a fixed drain voltage  $V_{ds}=-0.4$  V. (c) Multiple transfer characteristics for devices with all the different W/L and antibody on the gate, and (d) respective transconductance  $g_m$ . The tests are in PBS 1X (0.15 M), pH 7..... 122

Figure 6-4: Real-time cortisol sensing. (a) Cortisol measurement with PEDOT:PSS W/L=12.5 and thiol/EDC/antibody gate chemistry. (b) Cortisol measurement with PEDOT:PSS W/L=12.5 and thiol/EDC/NHS/antibody gate chemistry. (c) Control measurement with multiple PBS injections with PEDOT:PSS W/L=12.5 and thiol/EDC/antibody gate chemistry. (d) Cortisol measurement with PEDOT:PSS W/L=1.5 and thiol/EDC/antibody gate chemistry. (e) Cortisol measurement with PEDOT:PSS W/L=0.25 and thiol/EDC/antibody gate chemistry. (f) Control measurement with multiple PBS injections with PEDOT:PSS W/L=0.25 and bare gold gates. (g) Calibration curves at the multiple sensing conditions, and (h) multiple control measurements. The error bars represent the standard deviation from the average obtained from multiple devices. The tests are at  $V_{ds}=-0.4$  V and  $V_{ds}=0.6$  V..... 124

Figure 6-5: Sensing mechanism analysis. (a) Nyquist plots of the gate electrode tested at the different cortisol concentrations versus an Ag/AgCl wire ( $V_{dc}=0.6$  V,  $V_{ac}=10$  mV, frequency= $10^5$ -0.1 Hz). (b) Extracted variations of the real part of the impedance from the Nyquist plots at 0.1 Hz (n=3). (c) Extracted variations of double-layer capacitances from the equivalent circuit. (d) Simulated current variations per decade of cortisol concentrations extracted from the simplified OECT capacitance model. The error bars represent the standard deviation from the average obtained from three devices. The impedance spectroscopy was performed in PBS 1X (0.15 M) following 5 minutes of incubation at the desired cortisol concentration. The gate electrodes had thiols/EDC/NHS/antibody on their surfaces. .... 126

Figure 6-6: Real sweat testing. (a) Schematic of the protocol followed to test real sweat samples collected during indoor cycling and validated with liquid chromatography-tandem mass spectrometry. (b) Time response of the device at low cortisol concentration. (c) Time response of the device at high cortisol

concentration. (d) Extracted variations drain current through the baseline shift before and after the sweat sample. (e) Comparison with the values measured by LC-MS/MS and the OECTs current variations measured after 250 s of stabilization. The OECT tests are at a fixed drain voltage  $V_{ds}=-0.4$  V and gate voltage  $V_{gs}=0.6$  V..... 129

Figure S6-7: OECT sensors fabrication and assembly. (a) Wafer-like polyimide substrate with the fabricated devices. (b) Assembly of the gate electrode on the substrate through acrylic adhesive. (c) Assembly of the microfluidics to form the wearable sticker and assembly of the reservoir. (d) Cross-section with the multiple plastic layers and adhesives for the microfluidics, and (e) for the reservoirs. (f) Image and output characteristics of the integrated devices into the microfluidics without the electrolyte and (g) with the electrolyte (PBS 1X, W/L=12.5)..... 135

Figure S6-8: X-ray photoelectron spectra on gold gates. (a) S2p and (b) N1s peaks of bare gold electrodes, gold electrodes with thiol monolayers, and gold electrodes with capture antibody after thiol activation. The thiol activation was done using EDC chemistry..... 136

Figure S6-9: Thiol functionalization and characteristics. (a) Transfer characteristics of the transistors with bare gold gate electrodes. (b) Transfer characteristics of the transistors with gate electrodes and thiol monolayer (without antibody and thiol activation). The devices have a W/L=12.5 (very short channel), and a drain voltage  $V_{ds}= -0.4$  V. The tests are performed in PBS 1X (0.15 M), pH 7. .... 136

Figure S6-10: Different thiol activation. Transfer characteristics of the transistors with the antibody on the gold gates and two different thiol activations before the antibody are immobilized. The device for which NHS is specified in the label had an EDC/NHS chemistry. The devices have a W/L=12.5 (very short channel), and a drain voltage  $V_{ds}= -0.4$  V. The tests are performed in PBS 1X (0.15 M), pH 7..... 137

Figure S6-11: Leakage current. Simultaneous  $I_{ds}$  and  $I_{gs}$  current variation during the real-time sensing measurement with multiple subsequent cortisol injections (1, 10, 100, and 1000 nM). The devices have a W/L=12.5 (very short channel), an EDC/NHS chemistry for the thiol activation and antibody immobilization. They are biased by applying a drain voltage  $V_{ds}= -0.4$  V and a gate voltage  $V_{gs}= 0.6$  V. The tests are performed in PBS 1X (0.15 M), pH 7. .... 137



Figure S6-12: Impedance spectroscopy. (a) Control experiments showing the Nyquist plots of two control gates, having the antibody on the gates and incubated with only PBS (no cortisol) for 5 minutes. (b) Example of the Bode plot for different cortisol concentrations. The measurements are performed at  $V_{dc}=0.6$  V,  $V_{ac}=10$  mV, frequency= $10^5$ -0.1 Hz with a two-electrode setup versus an Ag/AgCl wire. .. 138

Figure S6-13: Impedance spectroscopy on the gate electrode. (a) Equivalent circuit used to fit the impedance spectra, including a constant phase element (CPE). (b) The extracted double layer capacitance from the model for three devices. All the CPE elements had a constant phase equal to 0.9 or higher. . 138

Figure S6-14: PEDOT:PSS impedance. Extraction of the double-layer capacitance and the relative volumetric capacitance ( $C_v$ ) of three different PEDOT:PSS electrodes from the imaginary impedance versus the inverse of the angular frequency. The measurements are performed at  $V_{dc}=0.1$  V,  $V_{ac}=10$  mV, frequency= $10^5$ -0.1 Hz with a two-electrode setup versus an Ag/AgCl wire. .... 139

Figure S6-15: OECT electrical model for cortisol sensing and experimental results. (a) Extracted  $\Delta I_{ds}$  per cortisol concentration from the OECT electrical model and corresponding experimental values for OECTs with very-short channels ( $W/L=12.5$ ), and (b) with short-channels ( $W/L=1.5$ ) and long-channels ( $W/L=0.25$ ). The graphs include the linear fitting of the sensing results for each condition. .... 139

Figure S6-16: Comparison with the values measured by liquid chromatography-tandem mass spectrometry and the OECTs, considering the current variations measured from the OECT devices (at 250 s), and the calibration curve with a standard deviation for  $n=4$  OECTs. The calibration includes a correction due to noise variations of the sensors during the injections, shifting upwards the calibration of 6  $\mu$ A/dec. The linear fitting is performed excluding the calibration point at 100 pM. The OECT tests are at a fixed drain voltage  $V_{ds}=-0.4$  V and gate voltage  $V_{gs}=0.6$  V. .... 140

Figure 7-1: Graphical abstract. Integrated multi-ion OECT platform for multiplexed sweat analysis. . 141

Figure 7-2: OECT array for multi-ion sensing. (a) Picture showing the integrated patch with four organic electrochemical transistors and the wearable read-out electronics. (b) Cross section with the inkjet printing

and sintering fabrication steps. (c) Application for ion-selective sensing by coating some OECTs with ion-selective membranes and optical image of the respective membrane. ....	144
Figure 7-3: Pseudo-reference OECT gate electrode. SEM images before (a) and after (b) chloridation of the gate electrodes, and respective EDS measurements (c,d).....	145
Figure 7-4: Electrical characterization of the organic electrochemical transistors with and without different ion-selective membranes. (a) Output characteristics without any membrane, (b) output characteristics with the $K^+$ membrane, (c) output characteristics with the $Na^+$ membrane, and (d) transfer characteristics with and without membranes. The measurements are performed with the portable electronics in a solution containing 120 mM NaCl and 20 mM KCl. ....	146
Figure 7-5: Multi-analyte detection with the OECT arrays. (a) Variations of the multiple OECT sensors to $Na^+$ concentrations, (b) to $K^+$ concentrations, and (c) to mixed $Na^+$ and $K^+$ concentrations. $V_{ds} = -0.4$ V, $V_{gs} = 0.1$ V in all the cases.....	147
Figure 7-6: Sweat analysis with the OECT arrays. (a) Table with the $Na^+$ and $K^+$ concentrations of the sweat samples measured by commercial sensors and tested with the OECTs. (b) Testing of real sweat samples after the calibration of the OECT devices. (c) Comparison of the extracted concentrations from the $K^+$ -selective OECT sensors versus the the standard commercial sensors for $K^+$ sensing. (d) Comparison of extracted concentrations from the $Na^+$ -selective OECT sensors versus the standard commercial sensors for $Na^+$ sensing, or the OECT sensor without any membrane versus the results for both $Na^+$ and $K^+$ sensing with commercial sensors. $V_{ds} = -0.4$ V, $V_{gs} = 0.1$ V in all the cases. ....	149
Figure S7-7: The transconductance of the OECTs. (a) Transconductance of the OECTs measured with the portable electronics. (b) Optical image of the $K^+$ membrane, and (c) the respective thickness profile. (d) Optical image of the $Na^+$ membrane, and (e) the respective thickness profile.....	154
Figure S7-8: Sensitivity and selectivity. (a) Sensitivity with the K-selective membrane versus KCl. (b) Sensitivity with the Na-selective membrane versus NaCl. (c) Sensitivity without membrane versus NaCl. (d) Selectivity with the K-selective membrane versus NaCl. (e) Selectivity with the Na-selective membrane versus KCl. (f) Sensitivity without membrane versus KCl.....	154

Figure S7-9: Ion sensing with the semiconductor parameter analyzer. (a) Time characteristics of an OECT without any membranes, and relative calibration curves in (b). (c) Time characteristics with a $K^+$ -selective membrane, and (d) relative calibration curve. ....	155
Figure S7-10: Calibration for sweat analysis. (a,c) Calibration of two integrated patches before sweat analysis with low and high concentrations, and (b,d) calibration curves of the $K^+$ and $Na^+$ sensors and the sensor without the membrane. ....	155
Figure S7-11: Design and connections. Optical microscopy image with relevant dimensions for the interconnection part of the patches. ....	156

# List of Tables

Table 1: OECT with active channel made of PEDOT:PSS, EGOFET with active channel of other polymers (such as pentacene and PH3T), EGFET/ISFET with other active layers. Note: ISM=Ion-Selective Membrane, smc=semiconductor, and CNTs= Carbon Nanotubes. ....	43
Table 2. Literature comparison for ion-sensitive and ion-selective organic transistors. The table compares the sensitivity, the integration level (gate, membrane, and microfluidics if present), the substrate material (flexible or rigid), and the fabrication method (lithography or printing) for different ion-sensitive and ion-selective transistors reported in the literature, including the applied drain voltage and chosen design parameters. EGOFET stands for Electrolyte-Gated Organic Field-Effect Transistor. ....	73
Table 3: Literature comparison for pH-sensitive organic electrochemical transistors (OECTs) on flexible substrates. The table compares the fabrication method, the gate and channel materials, the sensitivity in terms of current and voltage, and the pH-range tested for different pH-sensitive transistors reported in the literature. ISM stands for Ion-Selective Membrane.....	91
Table 4: Literature comparison. Glucose sensing performances compared with the literature for organic electrochemical transistors. ....	115
Table 5: EIS fitting for the graphene electrodes. The charge transfer resistance ( $R_{ct}$ ) and double-layer capacitance ( $C_{dl}$ ) with the relative constant-phase element number ( $n$ ). The values are reported for two devices for each testing conditions. The glucose concentration is fixed at 700 $\mu$ M. ....	115

# Chapter 1 Introduction

*This chapter presents an introduction to the research in this thesis. It includes a background in the biosensors and wearable biosensors field with the main achievements, including sweat analysis applications and the development of organic transistor-based biosensors as the organic electrochemical transistors (OECTs). This chapter concludes with the challenges and motivation of this research and a description of the thesis structure.*

## 1.1 Biosensors

The International Union of Pure and Applied Chemistry (IUPAC) defines a biosensor as a device that uses specific biochemical reactions mediated by isolated enzymes, immunosystems, tissues, organelles, or whole cells to detect chemical compounds by electrical, thermal, or optical signals.[1] Hence, a biosensor is composed of two units: a biorecognition unit (such as enzymes, antibodies) and a transducer unit (such as electrochemical, thermal, optical), which convert a biochemical recognition event into a measurable signal (Figure 1.1).[2] The first example of a biosensor was introduced by Clark and Lyons in 1962,[3] demonstrating the monitoring of glucose concentrations in blood samples with electrochemical sensors and using the enzyme glucose oxidase. Since then, especially since the end of the 1990s, the biosensors field has widely expanded and allowed the development of portable devices for several medical applications.[4]

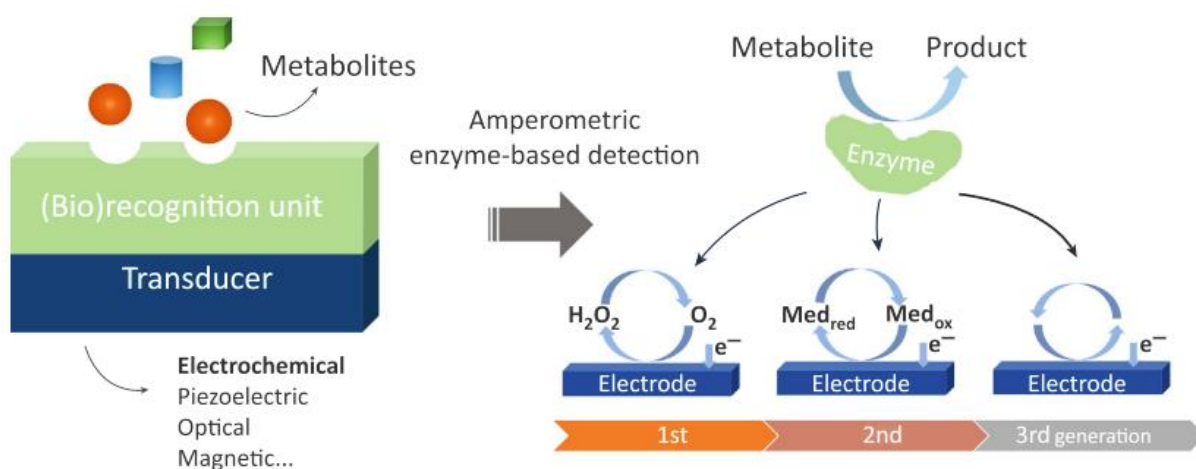


Figure 1-1: General schematic of a biosensor.[2]

Some essential inventions in the biosensors field include the glucose test strips for blood measurements in 1987, devices for subcutaneous glucose monitoring in 1991, DNA biosensors in 1998, devices for continuous glucose monitoring in 2000, and nano-bio sensors in the 2000s. [5] These discoveries paved the way for the novel research on biosensors for healthcare monitoring. The latest research in the biosensor field targets the monitoring of biofluids that can be non-invasively accessed, such as sweat, tears, saliva, and interstitial fluid (Figure 1-2).[5] The focus is on achieving the real-time monitoring of multiple analytes such as ions, hormones, and metabolites for personalized and preventive healthcare applications. The biosensors are integrated into flexible, wearable platforms on the skin,[6]–[8] on contact lenses and eyeglasses,[9] on the teeth and mouthguard,[10] or on textiles.[11] These applications generally use standard amperometric and potentiometric electrochemical sensors.

For amperometric (or voltammetric) detection, three-electrode systems with the working electrode, reference electrode, and counter electrode are used. The reference electrode controls the potential at the working electrode, while the counter electrode passes the current with its potential adjusted to balance the reaction occurring at the working electrode. This system is used commonly used for enzymatic-based detection, coating the working electrode with an enzymatic membrane.[10], [12], [13] A two-electrode

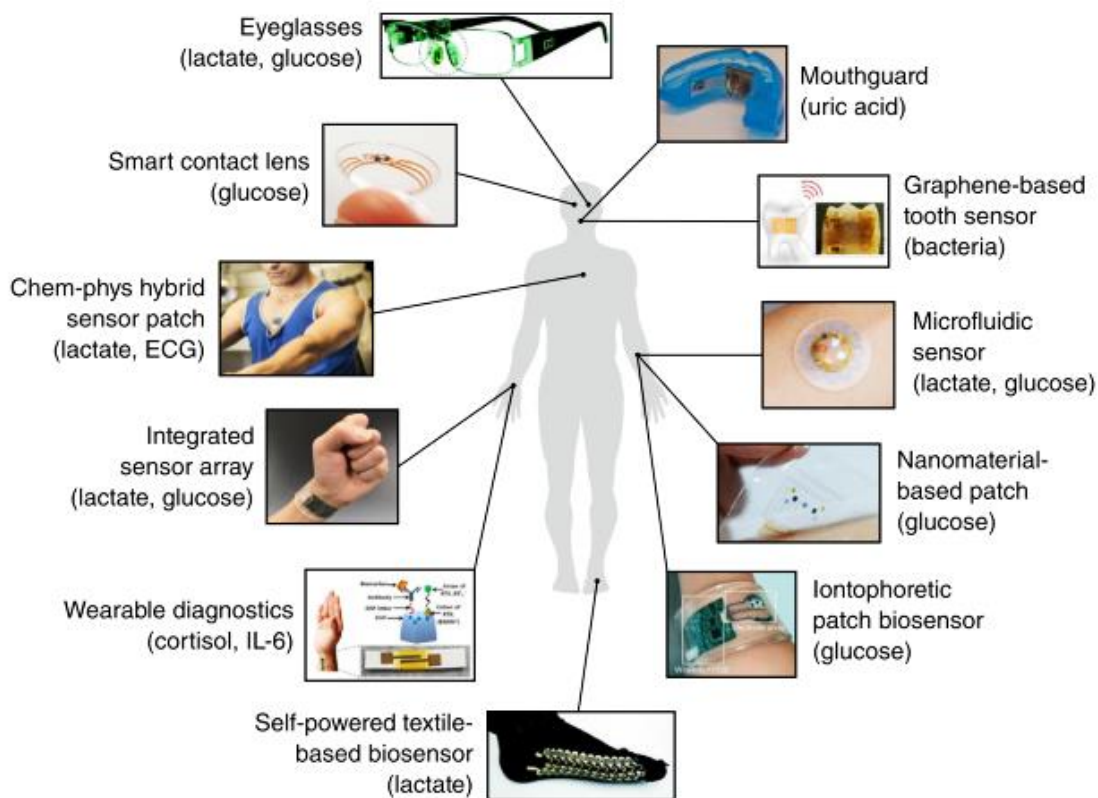


Figure 1-2: Examples of multiple biosensors for wearable healthcare applications.[5]

amperometric system composed of a working electrode and an Ag/AgCl electrode as both reference and counter electrode was also used for wearable enzymatic-based sensing.[6] Then, a two-electrode system with an indicator electrode and a reference electrode is commonly used for potentiometric measurements of ions. The indicator electrode measures the voltage changes in the presence of the ion of interest versus the reference electrode. It generally has an ion-sensitive and selective coating.[6], [12], [14]

### *1.1.1 Wearable biochemical sensors for sweat analysis*

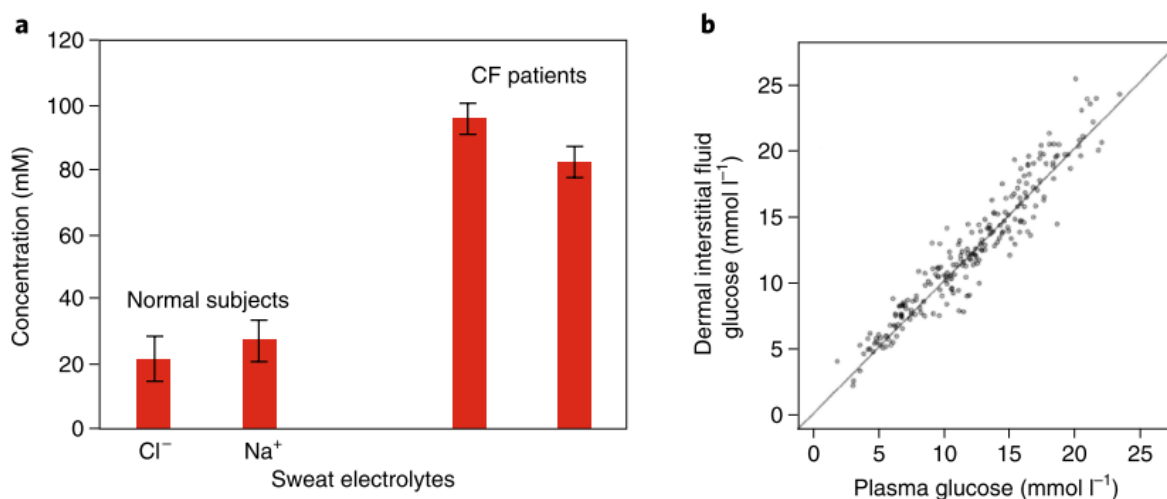
Sweat is one of the most promising biofluids for non-invasive analysis since it is one of the easiest to access non-invasively with a wearable patch.[6] Electrochemical sensors integrated into a wearable microfluidic system could allow continuous *in situ* and real-time monitoring of sweat composition. Nowadays, the research based on sweat analysis focuses on the detection of ions and sweat lost for dehydration studies,[15]–[18] cortisol for stress monitoring,[19]–[21] cytokines for inflammatory response analysis,[22] therapeutic drugs monitoring,[23] and metabolites such as glucose for diabetes,[24] and lactate for exercise intensity and fatigue.[25] However, the studies on the correlation of these sweat analytes with blood levels are still relatively unexplored.[26] One of the main difficulties is represented by the sweat evaporation, which can modify the concentrations of analytes, preventing a reliable analysis of the sweat composition. This issue can be potentially resolved by wearable technologies.[27] Also, due to the variable sweat rate and sweat composition among different body regions and individuals, there are several challenges in realizing wearable devices with clinical relevance for health monitoring.[28]

Among sweat analytes, sodium ( $\text{Na}^+$ ) and chloride ( $\text{Cl}^-$ ) ions have the highest concentration in sweat (10-100 mM),[27] and present an active reabsorption process in the body.[29] This means that the sweat rate can affect their concentration measured in sweat (the higher the sweat rate, the higher their concentration). Hence, these ions are correlated poorly with blood levels.[29] The clinical relevance of measuring  $\text{Na}^+$  and  $\text{Cl}^-$  is limited without proper sweat rate measurements and correlation with environmental factors.[18], [28] A patch with integrated microfluidics and colorimetric sensors (dye-based sensing) called the Gx Sweat Patch, commercialized by The Gatorade Company and a startup called Epicore Biosystems, monitors changes in  $\text{Na}^+$  and local sweat loss.[30] The startup was founded as a spinout from Northwestern University's Querrey Simpson Institute for Bioelectronics and John Rogers Laboratory in 2017. However, the clinical relevance of this device is not proven. Other startups also work on ion and dehydration sensors, such as Xsensio from EPFL, using transistor-based technology.[31] So far, the use of these sweat ion measurements for diagnosis is demonstrated only for cystic fibrotic patients (CF) through sweat stimulation (Figure 1-3a). CF patients have a malfunction of a regulator channel

involved in the ion reabsorption, causing an increased ion concentration in sweat,[29] and a wearable commercial device for the stimulation and collection of sweat for cystic fibrosis diagnosis called Macroduct was approved in 1997.[32] Such sweat stimulation is achieved with iontophoresis technology.[33] On the other hand, sweat potassium ( $K^+$ ) ion has a passive transport, and recent studies show that it is better correlated with blood levels, particularly with sweat stimulation.[34]

For glucose in sweat, a good correlation between sweat and blood has not been demonstrated yet using wearable biosensors. Instead, there is a good correlation between glucose in the interstitial fluid and blood (Figure 1-3b),[27] and a commercial wearable glucose sensor based on electrochemical detection for interstitial fluid analysis and diabetes management called Freestyle Libre, is available since 2017.[5], [35] Several challenges still exist for reliable glucose measurements in sweat, also due to the low concentration in sweat in the range of  $\sim 10$ -100s  $\mu M$  (about 100 times smaller than in blood),[27], [36] and due to the wide sweat pH variations, which can interfere with the commonly-used electrochemical enzymatic-based detection.[8] In 2021, Joseph Wang demonstrated that a correlation between blood and sweat glucose could be achieved using a correction factor extracted from personalized equations after several sweat tests and blood tests, using a “touch-based” sensor measuring the small sweat amounts on the fingertips.[24]

There are also several challenges for measuring highly-diluted molecules such as cortisol. This hormone has a passive sweat transport, and a good correlation with blood levels was demonstrated without



*Figure 1-3: Clinical application of wearable biosensors. (a) Difference of ions measured through sweat stimulation (iontophoresis) in normal subjects and patients with cystic fibrosis (CF). (b) Correlation on glucose in interstitial fluid and plasma for diabetes management. [27] The figure is modified from the original publication.*

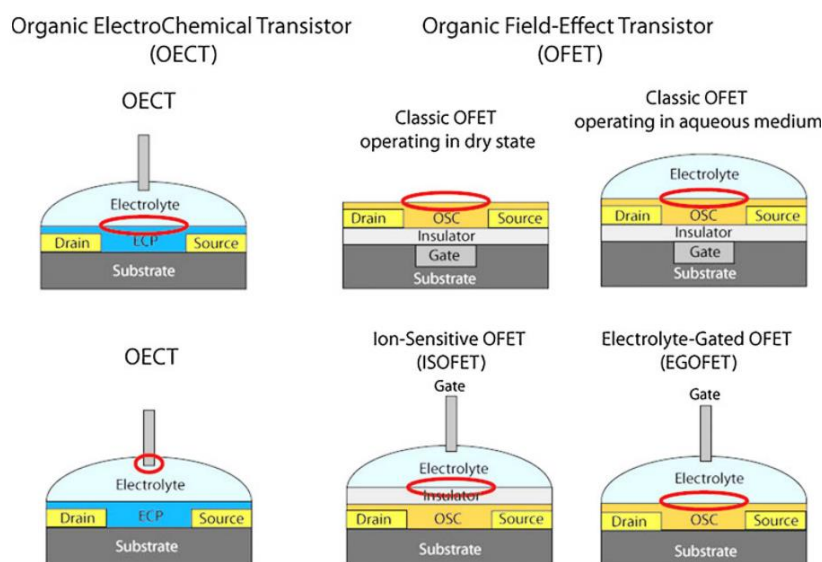


sweat stimulation (i.e., in natural sweat).[19] The main challenge relies on the low concentration of this hormone, which is 1000 times smaller than glucose levels in sweat, being in the tens of nM range.[27] Recent technological advances with transistor-based biosensors are allowing the detection of these highly diluted molecules with high sensitivities.[20], [37], [38] In fact, transistors can play an essential role in wearable applications since they can potentially exhibit high sensitivity, and they are simple to be miniaturized and integrated into portable electronic devices. [4], [20], [39], [40]

## 1.2 Organic transistor-based biochemical sensors

Transistors are three-terminal devices where the electrical conductivity of the semiconducting channel between two electrodes, called the source and the drain, is modulated by a third electrode called the gate. The implementation of silicon-based transistors as chemical sensors was demonstrated with the introduction of the Ion-Sensitive Field-Effect Transistor (ISFET) by Bergveld in 1970.[41] They are based on standard metal-oxide-semiconductor field-effect transistors (MOSFETs), achieving sensitivity to ions in solution by exposing both the reference electrode and the insulator layer to the electrolyte, replacing the standard gate with a reference Ag/AgCl electrode.[4] The bare insulator, made notably of silicon or metallic thin oxide films, is generally sensitive to pH variations, and ion-selective polyvinyl chloride (PVC)-based membranes can be added on top to achieve selectivity to ions. The interest of ISFET over conventional potentiometric ion-selective electrodes are the small size, mass fabrication, short response time, and low output impedance.[41] Also, in 1970, a variant called Chem-FET for detecting various biochemicals depending on the biofunctionalization layers was proposed by the pioneering work of Bergveld and Janata.[42] Functional layers such as antibodies or aptamers were added directly to the dielectric layer in contact with the electrolyte. The binding of the analyte of interest caused a change in the interfacial potential of the dielectric/electrolyte interface. The main drawback was that the chemistry for attaching bio-layers to dielectrics is less controlled and stable than the ones available for electrodes such as gold.[42] Another architecture proposed to overcome these limitations was the Extended-Gate (EG) FETs, in which the standard MOSFET has a second external gate (floating gate), extended away from the semiconductor, that can be functionalized easily for bio-detection. This floating gate is capacitively coupled to the gate electrode in contact with the dielectric of the FET.[37], [42] However, the main drawbacks of these silicon-based technologies are the relatively high cost if produced in low quantities, particularly for large-area EG-FETs,[42], [43] and the problematic packaging and integration onto flexible substrates (contact pads, wire bonding, encapsulation) and into a microfluidic system for wearable applications.[44], [45]

A class of transistors called Organic Field-Effect Transistors (OFETs) or Organic Thin-Film Transistors (OTFT) started to gain interest thanks to their simple fabrication process, biocompatibility, mechanical flexibility, and compatibility with printing techniques enabling the low-cost fabrication of disposable biosensors.[46], [47] While their performance and stability are lower than inorganic devices for applications such as logic circuits, they offer several advantages for biosensors and other applications such as optoelectronics and photovoltaics.[48] Among the OTFTs, there are two types of transistors called Organic Electrochemical Transistors (OECTs) and Electrolyte-Gated Organic Field-Effect Transistors (EGOFETs),[4] where the electrolyte is directly in contact with the organic layer without any insulator layer. This structure enables the direct interaction between ionic and electronic charges in the organic channel.[49] The main difference between the two types of organic transistors is that while EGOFETs form an electrical double-layer between the organic channel and the electrolyte as standard FETs, in OECTs, the ions permeate into the organic material.[42] This phenomenon in OECTs causes a volumetric change of the doping state of the organic material, with significant modulations of drain current at very low gate voltages.[50] A summary of these classes of sensors is presented in Figure 1-4. The devices can be used as biosensors adding a biorecognition layer either at the gate/electrolyte or at the electrolyte/channel interfaces (red circle in Figure 1-4).[4], [46] Besides the simple fabrication into flexible substrates at a low cost, OECTs also offer improved sensing performances thanks to their mixed ionic-electronic properties.



*Figure 1-4: Cross-section of the OECTs and OFETs devices. The red circles indicate the different interfaces where the biosensing reaction can take place.[4] ECP stands for Electrically Conductive Polymer and OSC for Organic Semiconductor. The figure is modified from the original publication.*

### 1.2.1 PEDOT:PSS-based organic electrochemical transistors

The first OECT was reported by Wrighton in 1984,[51] starting a new direction in the OTFTs field. Several different conducting polymers, including poly(3-methylthiophene), polypyrrole, polycarbazole, polyaniline, and poly(3,4-ethylenedioxythiophene), were investigated for the channels of OECTs.[47] Nowadays, the most used organic material for OECTs is the conducting polymer poly(3,4-ethylenedioxythiophene) doped with poly(styrene sulfonate) (PEDOT:PSS). PEDOT:PSS has two phases, the one with electronic charge carriers in the form of polarons (holes) is the PEDOT phase, and the one with the ionic charge carriers is the PSS phase (Figure 1-5a).[52] The PEDOT material is in an oxidized state (p-type doped using the terms for electronic devices), with mobile holes that can move from one chain to another through a process called hopping.[50] The contact electrodes called the source and drain define the PEDOT:PSS channel through which holes flow once a voltage ( $V_{ds}$  or  $V_D$ ) is applied, resulting in an electrical current ( $I_{ds}$  or  $I_D$ ). Once a positive voltage is applied with the third electrode called gate ( $V_{gs}$  or  $V_G$ ), the  $I_{ds}$  current decreases (Figure 1-5c). This decreased current is commonly explained as a dedoping phenomenon due to the injection of cations ( $V_{gs} > 0$ ) into the PEDOT:PSS channel, causing a compensation of the  $PSS^-$  anions (Figure 1-5b).[50] Once the gate voltage is removed, cations should migrate back into the electrolyte medium, and the original conductivity of the PEDOT:PSS channel can be restored.[53] The modulation of the channel conductivity can be described with the following equation:



Cations (represented as  $Na^+$ ) electrically compensate the PSS acceptors, and the holes (represented as  $h^+$ ) are removed from the PEDOT. This volumetric dedoping allows having very high transconductance ( $g_m$ ), hence a very high variation of drain-source current ( $\Delta I_{ds}$ ) for the variation of the gate voltage ( $\Delta V_{gs}$ ). They can be viewed as an amplifier, in which the input signal ( $V_{gs}$ ) is amplified going to the output ( $I_{ds}$ ).[55] The  $g_m$ , which can be defined as the derivative of channel current with respect to gate voltage, reaches peak values  $>1$  mS and normalized values  $g_m/W$  ( $g_m$ /channel width) of a few hundreds of S/m. These values are the highest ever reported for transistor-based biosensors, lower only compared to solid-state III–V semiconductor devices.[56] OECTs exhibit the highest normalized  $g_m/V_{ds}$  values (a few thousand mS/V), thanks to their very-low voltage operation. The high OECT transconductance is related to the fact that it is directly proportional to the ratio  $\frac{Wd}{L}$  ( $W$ =channel width,  $d$ =channel thickness,  $L$ =channel length).[57] This scaling with the thickness, and not only  $W/L$ , is one of the main differences between OECTs versus standard FETs.

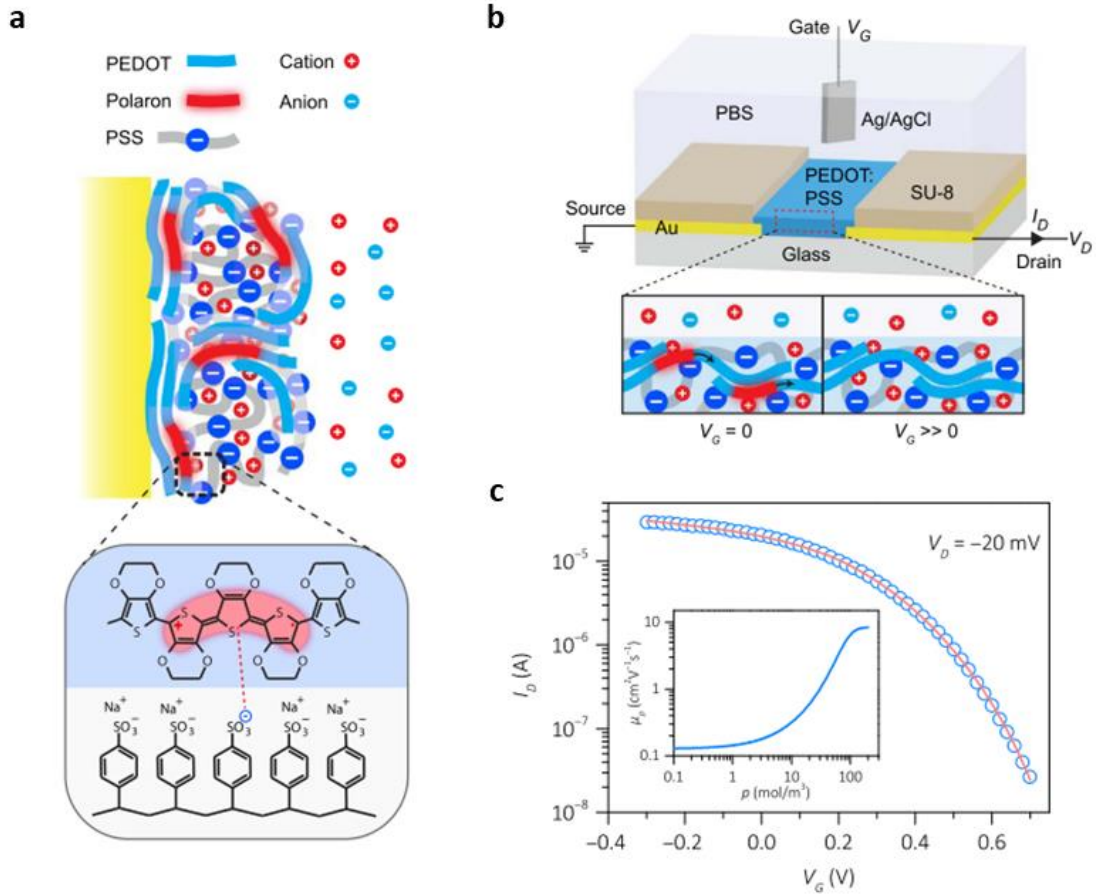


Figure 1-5: Schematic of an OECT channel highlighting the electrical and ionic charges interaction (a), the structure of an OECT device (b), and electrical characteristics in an electrolyte solution (c).[52] The figure is modified from the original publication.

Their performances are also independent of the gate-channel distance, allowing more flexibility in their design than standard transistors.[58] The gate of these devices can be either placed on top of the channel (top-gated) or on the side of the channel (side-gated) on the same substrate.[49] The side-gated configuration is convenient for wearable biosensing.[20]

The unique ionic and electronic charges interaction in OECTs sets them apart from conventional transistor technology, necessitating novel device models for describing their behaviour.[59] The pioneering OECT model was introduced in 2007 by Bernardis & Malliaras.[60] The device was modeled as composed of an electronic and an ionic circuit, the first circuit described with standard transistor equations and the latter circuit modeled as a resistor and a capacitor in series. Hence, the main novelty is the introduction of an ionic coupling between the gate and channel. In 2015, Friedlein *et al.* introduced

non-uniform mobility into the Bernards–Malliaras model.[54] Other models were then proposed to describe other OECT phenomena (at negative  $V_{gs}$  and low charge-carrier concentrations),[58] using drift-diffusion equations in the Prigodin and the Tybrandt models.[61] A model by Lüssem in 2020 takes into account the ionic lateral current in OECTs.[62]

While a basic knowledge of the OECT operating principle allowed the implementation of the devices in different biosensing applications (see Chapter 2 State-of-the-art), a thorough understanding of the device physics and the influence of the material properties is still limited.[54] Moreover, the detection mechanisms of OECTs having recognition elements at the different interfaces (gate or channel) for different molecules are still largely unknown due to the complex nature of both the PEDOT:PSS channels and the bio-layer interfaces.[46], [49] These factors strongly limit the development of OECT platforms for healthcare applications, including sweat sensing. The relevance of OECTs for biosensing in complex biofluids such as sweat still requires further investigation.

## 1.3 Challenges and motivations

### 1.3.1 *Challenges in sweat science and biosensing*

- Sweat evaporation and skin contamination can modify the concentrations of analytes in sweat.[27] Also, some analytes on the skin are sweat-rate dependent; hence a change of concentration may not be linked to a change in health status (i.e., dehydration for a change in sodium concentration) but just to a change in sweat rate.[29]
- Sweat pH can have high variations, influencing the signal of enzymatic sensors.[8] Furthermore, the biorecognition layers are not fully selective, and sweat contains several analytes.[63]
- Sweat contains hormones, proteins, and peptides present at low and very low concentrations (nM and pM ranges), which are difficult to be detected.[27] The possibility to analyze these highly diluted molecules could give novel insights into the health status of individuals.

### 1.3.2 *Challenges in the field of OECT biosensors*

- OECTs for the real-time and simultaneous monitoring of multiple analytes with different bio-functionalized interfaces still need to be demonstrated. Depending on the analyte of interest and its concentration, it is necessary to adapt and optimize the OECT architecture, notably the device geometry, bio-functionalized interface, and gate material.[64] Studies are required to understand

further the role of the different integrated gates and functional materials on the performances of the devices.[47], [65], [66]

- The detection mechanisms involved in OECTs with different functionalization layers (ion-selective membranes, enzymes, antibodies) at the gate or channel interfaces still need to be well-understood.[46], [49], [67] The sensing mechanism mainly remains unclear and complicated to be categorized (based on capacitive, resistive, or a combination of changes at the interfaces).
- The implementation of the devices is mainly limited to a single-analyte detection and a single-shot measurement in a non-integrated configuration.[67]–[72] Development of optimized technologies and integration processes enabling fully-integrated platforms for the continuous multi-sensing of analytes are needed. These should include the simple fabrication of planar integrated gate electrodes, the implementation of appropriate materials depending on the functionalization process, and the sensors integration into a microfluidic system for continuous analysis. The use of additive manufacturing techniques such as inkjet printing to fully fabricate the OECTs on flexible substrates is gaining attention but still demands some specific investigations.[42], [73], [74]
- There is still the need to demonstrate the applicability of OECTs for wearable biosensing applications.[20], [75] Moreover, the stability and repeatability of the sensing devices require some investigations for the monitoring of real-biofluids,[76] particularly for the detection of low concentrated sweat analytes (such as cortisol, which is in the nM-range).

### *1.3.3 Motivations*

This thesis work aims to overcome the aforementioned challenges, studying the sensing mechanisms and performances of OECTs implementing different bio-functionalization layers and gate materials applied to sweat analysis. These studies focus on OECT sensors for the detection of multiple ions ( $K^+$  and  $Na^+$ ), pH, metabolites (glucose and lactate), and cortisol, aiming at fully-integrated OECTs platforms for the real-time and continuous monitoring of biofluids. This research also tackles the improvement of the hardware technology by developing microfluidics-integrated multi-sensing OECT platforms based on digital manufacturing (i.e., inkjet-printing). This approach brings the advantages of being easily configurable, allowing the choice of the gate material and functionalization depending on the analyte of interest and its concentration. The main motivations are the following:

- **OECT sensors.** Analyze the applicability of OECTs for sensing multiple analytes (including ions, metabolites, and hormones) reliably in real-time and at different concentration ranges (mM down to sub-nM) in more complex biofluids such as sweat. OECTs have the potential to amplify the

signal generated by the interaction with low-concentrated molecules for very high-sensitivity applications (hormones, proteins, and peptides), which are particularly difficult to be detected with standard electrochemical methods. However, scientific progresses have to be made to better understand the sensing mechanisms involved in OECT sensors, particularly for the antibody-antigen detection of highly-diluted molecules. Such studies are necessary to enable multi-sensing and multiplex sensing in biofluids with OECTs.

- **Integrated technology for wearables.** Advance OECTs integration into potentially wearable systems by applying thin-film printing technologies on flexible substrates. Within this scope, we are investigating the performances of OECTs with integrated gate electrodes made of different printed nanomaterials tuned to target the detection of different analytes. The integration of wearable sensors into microfluidics can overcome the issue of the biofluid evaporation and contamination. Notably considering sweat, being collected by the microfluidic channels, it is then stored and separated from the skin surface. Thanks to their miniaturization, multiple OECT sensors could be integrated into the same microfluidic reservoir and wearable platform.
- **Multi-sensing and sweat analysis.** Develop OECT biosensors arrays with different bio-recognition layers, hence through multiplexed sensing, that could contribute to overcome several issues related to the analysis of real biofluids. By acquiring multiple sensor signals in real-time, the responses of various semi-selective sensors can be considered collectively to generate some patterns indicative of an analyte and its concentration, even if the individual sensor cannot transduce that information precisely. Also, sensing multiple analytes such as glucose/lactate and pH could resolve the issue of enzymatic activity variation due to pH, compensating the metabolite sensor signal according to the pH level detected. Finally, measuring some analytes that are sweat rate-independent as potassium in parallel could help to determine if a change in the sensor signal comes indeed from variations in the analyte concentration, the sweat rate, or other factors (i.e., electrical and environmental factors).

## 1.4 Thesis structure

Following this introduction in Chapter 1, this thesis is organized in the following way.

**Chapter 2:** This chapter aims to cover the detailed state-of-the-art of OECTs for biosensing and sweat sensing. This chapter clarifies significant discoveries and highlights some limitations of the current research in the field. It concludes by describing the main achievements reported in this thesis.

**Chapter 3:** This chapter is dedicated to investigating the use of flexible and printed OECTs for multi-ion sensing and the direct integration of membranes of the organic channels. The design and fabrication of the organic electrochemical transistors based on PEDOT:PSS and silver nanoparticle inks deposited by inkjet-printing on flexible polyimide substrates were performed. Then, the functionalization process of the PEDOT:PSS active layers with three different ion-selective membranes (ISMs) was studied. The ISMs contain potassium, sodium, and hydrogen ionophores into polyvinyl chloride (PVC) matrices. Studying the effects of the membrane composition and volume on the electrical performances of the transistors, state-of-the-art sensing performances (10  $\mu\text{A}/\text{dec}$  for each sensor) and proof of selectivity versus interfering ions in the sweat concentration ranges were obtained. This result was achieved using 2  $\mu\text{L}$  volumes of the membranes directly drop-cast on the active layers. The sensitivity and selectivity of the devices were demonstrated by real-time measurements at the relevant sweat concentration ranges while integrated into a laser-patterned flexible fluidic channel.

This chapter is based on the following article, reprinted (adapted) with permission from *Adv. Mater. Technol.* 5, 2000328, 1–9 (2020), copyright 2020 John Wiley and Sons.

**Paper I.** Demuru, S., Kunnel, B. P. & Briand, D. Real-Time Multi-Ion Detection in the Sweat Concentration Range Enabled by Flexible, Printed, and Microfluidics-Integrated Organic Transistor Arrays. *Adv. Mater. Technol.* 5, 2000328, 1–9 (2020).

**My contribution:** Main author, I contributed to all the aspects of the work. This includes: the original idea (use of ISMs on the PEDOT:PSS), conceiving and designing the experiments, designing and fabricating the devices, performing all the electrochemical testing, analyzing the experimental data, and writing the manuscript.

**Chapter 4:** This chapter proposes using OECTs with hybrid PEDOT:PSS/polyaniline channel for optimizing their pH sensing performances. For multiplexed analysis, such a pH sensor could be implemented for correcting the pH dependence of multi-ion and enzymatic sensing OECTs for a more accurate analysis. The devices have a printed silver pseudo-reference gate electrode. PEDOT:PSS-based OECTs can detect different ions in solution, but the variations of their electrical characteristics against pH are lower in sensitivity compared to other sensing methods. With a hybrid active layer based on an inkjet-printed PEDOT:PSS and an electro-polymerized PANI, high pH sensitivity and linearity can be achieved following six aniline electro-polymerization cycles. The AFM and SEM imaging analyses showed the formation of a porous PANI microstructured layer on the PEDOT:PSS film. The analysis of the detection mechanism by performing electrochemical impedance spectroscopy measurements demonstrated a 9X higher interfacial capacitance when decreasing the pH (increasing the  $\text{H}^+$  concentration) with the hybrid



layer compared to a bare PEDOT:PSS layer. This phenomenon happens because, going to higher levels of  $H^+$  concentration, particularly with PANI on the channel, there is a rise of interfacial charge from the  $H^+$  doping that increases the capacitance. Also, the porosity of the PANI layer can contribute to the accumulation of ions at the interface, enhancing the capacitive effect.

The present chapter is based on the postprint version of the following publication, open access under CC BY 4.0.

**Paper II.** Demuru, S., Kunnel, B. P. & Briand, D. Thin film organic electrochemical transistors based on hybrid PANI / PEDOT: PSS active layers for enhanced pH sensing. *Biosens. Bioelectron. X* 7, 1–9 (2021).

**My contribution:** Main author, I contributed to all the aspects of the work. This includes: conceiving the original idea (PANI on the PEDOT:PSS) and the experiments, designing and fabricating the devices, performing all the electrochemical testing, analyzing the experimental data, and writing the manuscript.

**Chapter 5:** This chapter presents a novel implementation of the previously characterized devices in Chapter 3 applied to the enzymatic-based detection of glucose and lactate in the sweat ranges. The role of the graphene gate electrode material compared to the silver pseudo-reference gate electrode previously optimized for ion-sensing was investigated. These studies focus on graphene for the gates since it is available as inkjet-printable solutions to develop integrated 2D material-based devices for enzymatic sensing. The electrical characteristics, sensing effects, and impedance of silver-gated OECT versus graphene-gated OECTs for the enzymatic detection of glucose were compared. The graphene-gated devices showed a 4X higher sensitivity towards glucose for the same concentration range (suitable for glucose detection in sweat and the blood, from tens of  $\mu M$  to a few mM), higher linearity, and reproducibility compared to the devices with the silver-pseudo reference. Compared to the state-of-the-art, we report one of the highest sensitivity values for printed OECT devices with a normalized signal change of about 20%/dec and up to 70% for 5 mM glucose. Similar sensing results were obtained for enzymatic lactate detection. The electrochemical impedance spectroscopy analysis showed a 7X decrease of polarization resistance upon adding glucose in solution at a fixed concentration with the graphene-gate electrode. On the other hand, the silver electrodes showed a slight change of impedance once adding glucose. The sensing performances with and without the mediator ferrocene were also analyzed, finding improved linearity and reproducibility with ferrocene. Cyclic voltammetry analyses suggest that the improved performances with ferrocene are due to a potential buffer effect and the improved sensitivity is due to the oxidation of hydrogen peroxide at high voltages with the graphene gates.

This chapter is based on the following article, reprinted (adapted) with permission from *ACS Applied Nano Materials* 5, 1, 1664–1673 (2022), copyright 2022 American Chemical Society.

**Paper III.** Demuru, S., Huang, C.-H., Parvez, C., Worsley, R., Mattana, G., Piro, B., Vincent, N., Casiraghi, C., and Briand, D. All-Inkjet-Printed Graphene-Gated Organic Electrochemical Transistors on Polymeric Foil as Highly-Sensitive Enzymatic Biosensors. *ACS Applied Nano Materials* 5, 1, 1664–1673 (2022).

**My contribution:** Main author, I contributed to all the aspects of the work. This includes the original idea (graphene gate for enzymatic sensing), the functionalization steps, designing part of the electrochemical experiments and performing all the tests, fabricating the devices, and writing the manuscript.

**Chapter 6:** This chapter proposes to implement anti-cortisol antibody-coated gold gates to detect cortisol in sweat. Gold-gated devices have a high transconductance at a lower voltage than the previously-used graphene gates, being suitable for sensing low concentrated molecules. Further, a standardized functionalization process based on thiol monolayers was applied to the gold electrodes for the immobilization of the antibody. By modifying the PEDOT:PSS width versus length ratio, the sensitivity of the devices was enhanced thanks to an amplification of the antibody-antigen binding events at the gate electrode when measuring the variations of drain current. The use of a short channel (width/length ratio equal to 12.5), coupled with an antibody-coated gate area of 3 mm<sup>2</sup>, allowed the detection of the highly diluted cortisol molecules in the nM range, with a limit of detection of 100 pM, in high ionic strength solutions. High sensing performances of ~50  $\mu$ A/dec of cortisol are measured in real-time after 5 minutes of stabilization per concentration. The sensing mechanisms, investigated through impedance spectroscopy, showed an increase of double-capacitance in the presence of cortisol, and these experimental variations were correlated to modification of the drain current of the device using analytical electrical models. The effective measurement of cortisol variations is demonstrated in real human sweat samples.

The present chapter is based on the preprint version of the following publication.

**Paper IV.** Demuru, S., Kim, J., El Chazli, M., Lafaye, C., Bruce, S., Dupertuis, M., Binz, P.-A., Saubade, M., and Briand, D. Antibody-coated wearable organic electrochemical transistors for cortisol monitoring in human sweat. *Manuscript submitted for publication* (2022).

**My contribution:** Main author, I contributed to all the aspects of the work. This includes the original idea (antibody-antigen detection on the gate), the functionalization steps, designing all the electrochemical experiments and performing all the tests, the printing, and writing the manuscript.

**Chapter 7:** This chapter shows a proof-of-concept implementation of some of the previously developed biochemical sensing OECT devices into an integrated platform for the analysis of ions in sweat.

The devices are fully inkjet-printed for simple digital integration onto flexible substrates and into a flexible microfluidic system through simple lamination. The ion-selective membranes and the insulator for the silver connections are printed through a simple casting process. Multiple integrated OECT devices, including devices with sodium and potassium membranes and devices without any membrane, are measured simultaneously in PBS solutions and real sweat samples, thanks to the use of a wireless, custom-made read-out electronics. The implementation of the OECTs array in combination with the read-out electronics allows recording the multiple OECTs signals in real-time and the multiplexed discrimination of different cations in the same solution.

The present chapter is based on the preprint version of the following publication.

**Paper V.** Demuru, S., Kim, J., Kiselev, I., Jeanneret-Grosjean, G. J, Saubade, M., Lafaye, C., Liu, S.-C., and Briand, D. Integrated fully-printed organic electrochemical transistors platform for multiplexed sweat analysis. *Manuscript in preparation* (2022).

**My contribution:** Co-author with J. Kim, I contributed to several aspects of the work. This includes: conceiving and designing the experiments, designing the devices and developing the technologies implemented, performing part of the electrochemical testing and the functionalization steps, and writing the manuscript.

## Chapter 2 State-of-the-art

*This chapter covers the state-of-the-art of OECTs for multi-biosensing and sweat sensing. It includes the analysis of multiple biochemical sensing applications depending on the gate materials, type of functionalization, and functionalized interfaces and a comparison with other transistor-based sensors. This chapter concludes with a general summary and the main contributions of this thesis.*




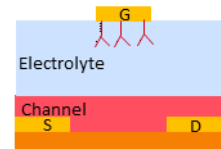










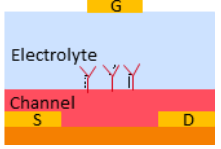







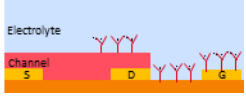


### 2.1 OECTs for biochemical sensing

OECTs with multiple bio-functionalization layers at different interfaces are reported for various sensing applications. The influence of gate material, type of functionalization, and the functionalized interface on the sensing performances is often unclear. The design, actuation voltages, the PEDOT:PSS conductivity, and the bio-layer after the functionalization of the transistors can be largely different, making comparisons difficult.[49] Moreover, the stability of the PEDOT:PSS layers plays an important role when performing measurements with multiple solutions to avoid false detections,[76] particularly at low concentrations of the analyte. Table 1 summarizes some of the main biochemical sensing applications demonstrated for OECTs and other types of transistors. Multiple research publications are included, divided by transistor type, functionalized interface, and type of functionalization.

In OECTs for ion sensing applications, the channel is generally functionalized using ion-selective membranes (ISMs), especially for the selective sensing of sodium, potassium, and calcium.[72], [75], [77], [78] For enzymatic-based sensing, the gate-electrode is often functionalized with different enzymes for multiple metabolites detection, including glucose,[79]–[82] lactate,[82]–[87], cholesterol,[83] uric acid,[81] glutamate, and acetylcholine.[88] Often, both the gate and the channel are covered with enzymes.[86], [87], [89]–[91] For antibody-based sensing, several antibodies can be immobilized on the gate electrodes for the detection of various antigens (cytokines,[92] immunoglobulins,[67] and COVID-19 [69], [93]). The channel interface is rarely functionalized for antibody-based sensing applications, because of possible damage or decrease in the transduction performances of the PEDOT:PSS channel following the functionalization steps. For other types of transistors, the carbon-based and oxide-based channels of EGFET are frequently functionalized for antibody-antigen detection,[38], [94]–[97] possibly because these layers are better withstanding the multiple functionalization steps and long incubations required than the PEDOT:PSS layers. Finally, EGOFET is reported mostly for antibody-antigen detection applications with a functionalized gate.[98]–[101] From these examples, it is evident that a single OECT

device can be used to detect a large variety of analytes using various configurations, making this device the most versatile and employed organic transistor for biosensing applications.[46] The simplicity of the fabrication of the PEDOT:PSS-based devices compared to other transistors is one of the main advantages of its comprehensive employment in the biochemical sensing field.

*Table 1: OECT with active channel made of PEDOT:PSS, EGOFET with active channel of other polymers (such as pentacene and PH3T), EGFET/ISFET with other active layers. Note: ISM=Ion-Selective Membrane, smc=semiconductor, and CNTs= Carbon Nanotubes.*

 ISM  Enzyme  Antibody (or aptamers)	OECT (PEDOT:PSS)	EGOFET (Organic smc)	EGFET/ISFET (Inorganic smc, graphene, CNTs)
<b>Functionalized gate</b> 	 Glucose [79], [80], uric acid and glucose [81], glucose and lactate and cholesterol [83], glucose and lactate [82],[84] lactate [85], glutamate and acetylcholine [88]  IL-6 [92], IgG [67], COVID-19 (nanobody) [69], epinephrine (aptamers)[102], COVID-19 IgG [93]   Cancer marker (labeled antibody) [103]  pH [104]	 IL-4 [98], TNF $\alpha$ (cytokine) [99], [100], IgG [101]  Acetylcholine [105]	 K <sup>+</sup> and Na <sup>+</sup> and pH [31]  Glucose [106]  Cortisol (aptamers) [37]
<b>Functionalized channel</b> 	 K <sup>+</sup> [77],[72], K <sup>+</sup> and Ca <sup>2+</sup> , K <sup>+</sup> and Na <sup>+</sup> and Ca <sup>2+</sup> [78], cortisol (molecularly imprinted membrane) [20], Ca <sup>2+</sup> and NH <sub>4</sub> <sup>+</sup> [75], K <sup>+</sup> and Na <sup>+</sup> [107]  Prostate antigen [108], ovalbumin epitopes [109], bacteria [110]	 Na <sup>+</sup> [111]  Sepsis marker [112]	 Alpha-synuclein (protein)[97], troponin I [113], hormone TSH [94], cortisol [95], cortisol (aptamer) [96],[38]  Acetylcholine [114], glucose [115], urea [116], creatinine [117]  pH and K <sup>+</sup> and Na <sup>+</sup> [118]
<b>Functionalized gate + channel</b> 	 Lactate [86], glucose [89], [90], [73], glucose and lactate [87], ethanol [91]		 Glucose and lactate [119]

### 2.1.1 OECTs for ion sensing

In OECTs for ion sensing, different integration levels are proposed, showing consistent sensing performances among the literature in terms of  $\mu\text{A}/\text{dec}$ . OECTs without any ISMs, hence with bare PEDOT:PSS channels, have average ion-sensitive properties of about 10s of  $\mu\text{A}/\text{dec}$  and Nernstian responses using a standard Ag/AgCl external reference electrode as a gate electrode.[47] The gate material strongly influences the transfer characteristics and thus the ion sensing properties of the devices, which is generally attributed to the different gate/electrolyte interfaces properties. Non-polarizable electrodes, such as Ag/AgCl, have significant current modulations in OECTs at low voltages (Figure 2-1a,b), while polarizable electrodes such as gold and particularly platinum show low current modulations at higher voltages (Figure 2-1a,c-d).

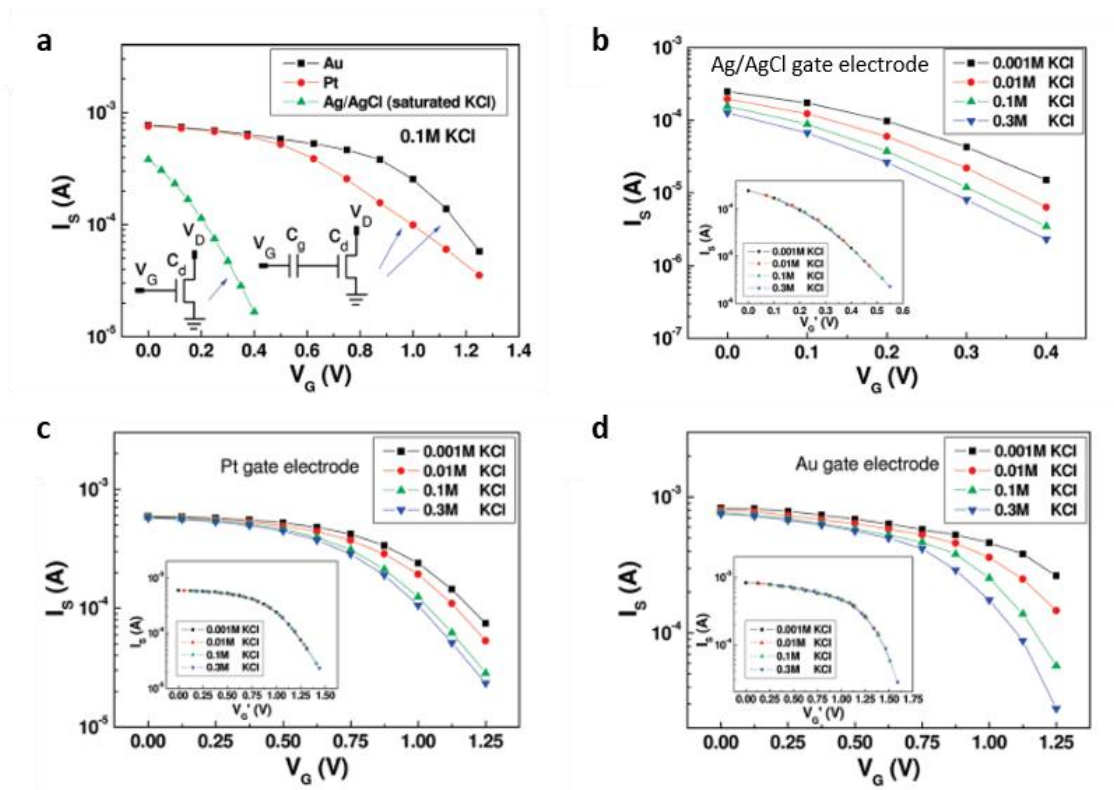


Figure 2-1: Ion sensitive properties depending on the gate material in OECTs. Comparison of gold (Au), platinum (Pt), and silver/silver chloride (Ag/AgCl) gates at a fixed ionic concentration in (a) and variable ionic concentrations in (b-d).[47] The figure is modified from the original publication.

In non-polarizable electrodes, the charge can be transferred across the gate/electrolyte interface, and the gate capacitance does not play a role at low frequencies. On the other hand, the gate capacitance should be taken into account with polarizable electrodes.[59] During ion sensing, the drain current decreases with the increase of ions concentration.

An ISM can be added on the PEDOT:PSS channel to achieve ion-selective properties. ISMs contain an ionophore, a cation exchanger, and a polymeric matrix such as polyvinyl chloride (PVC).[120] The careful proportions between these elements allow high ion selectivity, linearity, and sensitivity. Ion-selective OECTs can integrate an ISM on the PEDOT:PSS channel in different configurations. The most-reported architecture consists of an external Ag/AgCl gate electrode, an inner liquid electrolyte on the PEDOT:PSS channel, and an ISM on top of the latter [72], [77]. The best sensing performance reported in  $I_{ds}$  current variation is about 50  $\mu\text{A}/\text{dec}$  with the inner electrolyte and about 100s  $\mu\text{A}/\text{dec}$  with a thin polyelectrolyte film containing mobile sodium ions.[107] EGOFETs with ISMs on the channel and with an inner electrolyte showed lower sensing performances in terms of current equal to about 0.5  $\mu\text{A}/\text{dec}$ , and they are rarely employed for this application.[111] All the publications for ion sensing with ISMs use pseudo-reference silver-based or reference gates.[20], [72], [75], [77], [78]

A limitation of using these devices for wearable ion sensing is that they are generally fabricated on rigid substrates with a limited integration level, particularly of the gate electrode, which is floating on the electrolyte solution. Furthermore, the use of inner electrolytes in bulky reservoirs between the channel and ISM can further limit their use for wearable applications. These points are further discussed and extended in Chapters 3, Chapter 4, and Chapter 7.

### *2.1.2 OECTs for enzymatic-based sensing*

OECTs are the most studied transistor type for enzymatic-based detection. Hence, while EGOFETs are used only as potentiometric devices, OECTs are presented both as potentiometric and amperometric sensors.[46] They show relatively consistent results among the different publications in the literature, particularly in terms of normalized variation of signal from the baseline (without the metabolite present).[121] The most employed enzymes are the oxidase enzymes (such as glucose oxidase for glucose detection), with [90] or without [122] mediators such as ferrocene. These are mostly dissolved in solution [90], [122] or fixed in a membrane on the gate electrode.[83] Dynamic ranges of about 1-1000  $\mu\text{M}$  depending on the gate material used (mostly platinum-based and PEDOT:PSS-based gates) are generally reported.[81]–[83], [90] The sensitivities are  $\sim 10\%/ \text{dec}$  of metabolite concentration. The lowest limit of detection (LOD) achieved was 30 nM with a relatively complex gate electrode made of platinum-Nafion-

graphene flakes-polyaniline with the enzyme grafted through graphene oxide,[81] and generally is about 0.1-1  $\mu\text{M}$  in the previously mentioned publications. Hence, the highest sensing performances are achieved by carefully choosing and modifying the gate material since it directly contributes to the sensing mechanism (see *Analysis of the sensing mechanisms and design*). When the metabolite of interest increases in concentration, there is a decrease of drain-source current in the channel.

It is essential to mention that in enzymatic-based OECT measurements, where the gate electrode is used for the bio-detection, the potential in the solution is not precisely controlled.[46] This limits the applications for real biofluid sensing to precisely quantify the concentration of metabolites if the ionic concentrations can also vary. Also, it was shown that an OECT sensitivity is not higher than an amperometric sensor in terms of normalized signal variation,[46] thus making the advantage of OECTs compared to standard amperometric sensors still unclear. Cross-sensitivity and multiplexed studies with enzymatic-based and ion-selective sensors are not yet reported, which would enable overcoming possible OECT signal variations due to simultaneous ionic and pH changes in the biofluid of interest. Finally, the use of multilayer gate materials and complex fabrication process[81] poses another limitation to implement reproducible enzymatic-based OECTs. Some of these challenges are addressed in Chapter 5.

### 2.1.3 OECTs for antibody- or aptamer-based sensing

While electrochemical biosensing with antibodies is very attractive for many applications, it is limited due to the charge screening of the target antigen by the ions present in biofluids.[123] Considering OECT devices, two works reported the detection of target molecules with antibodies on the gate electrode in the aM-pM ranges[67] and in the 10 pM – 100 nM ranges[93] in high ionic strength PBS solutions. These initial results suggest that OECT could be potentially used as a highly-sensitive tool for antibody-antigen detection in biofluids containing several ions, such as sweat, overcoming the limitations of standard electrochemical sensors.

Both antibody- and aptamer-based approaches present advantages and drawbacks. The main advantage of antibodies is that they are commercially available for a wide range of sensing applications, while producing aptamers for several targets is still challenging. On the other hand, aptamers often offer better sensitivities in biological fluids, and they are more stable at high temperatures than antibodies.[124]

The reported concentration ranges where OECTs operate can largely vary for antibody- and aptamer-based detection applications, even if employing the same device architecture. A limited dynamic range around 100 nM for the detection of IL-6 (LOD=95 nM) was shown in Ref. [92], an aM-pM dynamic range



for IgG detection with a much lower LOD (LOD=6 aM) in Ref. [67], and a dynamic range in the pM-nM range for COVID-19 IgG detection (LOD=10 nM) in Ref. [93]. In all cases, a similar sensing configuration based on OECTs with PEDOT:PSS channels and gold gates functionalized with antibodies (tested in buffer solution) is employed. For the IgG detection, the devices show a decrease of  $I_{ds}$  current increasing the IgG concentration (Figure 2-2a), while for the IL-6 detection, it is reported that the normalized  $I_{ds}$  current ( $\Delta I/I$ ), in absolute values, increases with the increase in concentration (Figure 2-2b). It is important to notice that for IgG detection, the devices were biased at negative  $V_{gs}$  without giving explanations, while they are normally actuated at positive  $V_{gs}$ . Using aptamers with the same OECT configuration and materials, dynamic ranges of pM-nM (LOD=90 pM) for epinephrine detection were demonstrated (Figure 2-2c).[102] While these works had the antibody- or aptamer-based bilayer on the gate, some works also showed the use of bio-layers on the channel interface.

An interesting example is the detection of *E. Coli* bacteria on the channel, where they compared the use of Ag/AgCl or Pt gates.[110] Better sensitivities in terms of mV/dec and a LOD for bacteria concentrations were achieved using the polarizable Pt gates compared to the non-polarizable Ag/AgCl gates. In 2021, a PEDOT:PSS-based OECT functionalized with an optimized nanobody–SpyTag on the gold gate was demonstrated, achieving a LOD of 0.28 fM and a dynamic range of fM-nM for spike proteins of COVID-19 in human saliva (Figure 2-2d)[69] and representing the best performance achieved so far with these devices. The devices show an increase in normalized current due to the decrease of drain-source current during the  $I_{ds}$ - $V_{gs}$  measurements. They demonstrated measurements in human saliva, nasopharyngeal swabs, and serum, showing the potential of organic transistors for real biosensing analysis. On the other hand, this was achieved with in-house developed nanobodies rather than commercial antibodies, limiting, for the moment, further applications by other groups. The use of antibodies in OECT devices for analyses in real biofluids will be further discussed in Chapter 6.

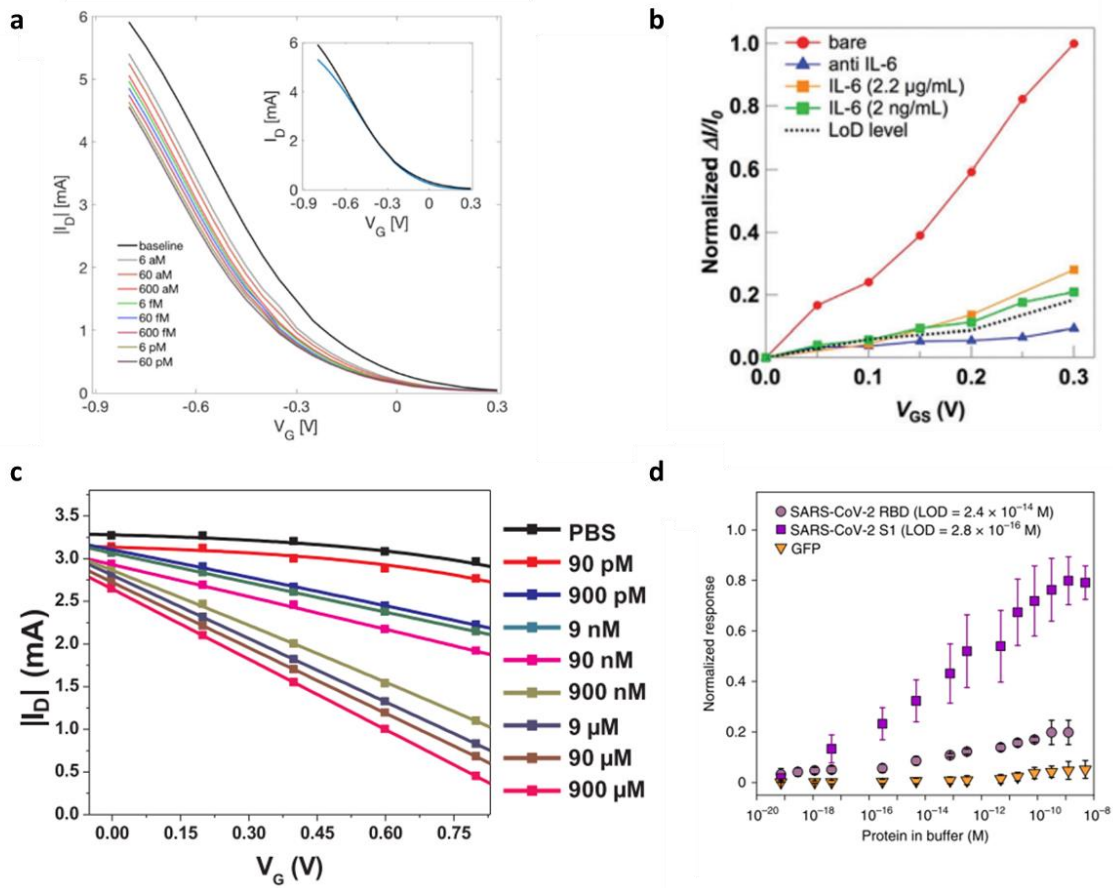


Figure 2-2: Comparison of the sensing performances of gold-gated OEETs functionalized with antibodies or aptamers. (a) OEET with anti-rabbit IgG antibody on the gate during IgG sensing. (b) OEET with the anti-IL-6 antibody on the gate during IL-6 sensing. (c) OEET with aptamers on the gate during epinephrine sensing. (d) OEET with nanobody on the gate during COVID-19 antigen detection. Modified from [67], [125], [102], [69].

## 2.2 Analysis of the sensing mechanisms and design

The sensing mechanisms involved in the presence of different bio-functionalization layers are often challenging to determine due to the complex nature of the interactions involved and possible process variability (biolayer properties, ion-organic material interactions, gate material properties, and device architecture).[49] However, there are a few examples in the literature where the sensing and biosensing mechanisms of OEETs are investigated. Thanks to these analyses, the optimal design to achieve high sensing performances can be discussed.

For OECTs without ISMs, the sensing mechanism at different ionic concentrations was modeled and experimentally proven to be similar to the Donnan equilibrium for semipermeable membranes.[126] By combining this model with the previously developed model by Friedlein *et al.*, [54] they could predict the potential at the electrolyte/channel interface by comparing the ion concentration in the solution and the number of fixed charges in the PEDOT:PSS channel. It is important to note that they used OECTs with a non-polarizable Ag/AgCl pseudo-reference gate electrode, and the potential at the channel/electrolyte interface was modeled and proven experimentally to follow the Nernst slope of 59 mV/dec up to large ionic concentrations (0.5 M). It was also proven that optimal ion-sensing performances are primarily dependent on the type of gate material used, with the best performances using Ag-based gates.[127] With ion-selective membranes, the OECT responses are generally analyzed in terms of the selectivity of the membranes, as it is commonly done for ion-selective electrodes.[78] The detection happens because only the desired ions with the ISM (with a specific selectivity) will contribute to the dedoping of the PEDOT:PSS channel.[75]

For enzymatic sensing, a model was proposed by Bernards and Malliaras in 2008,[128] which is now commonly used for explaining most of the enzymatic-based OECT sensors research. The model was applied experimentally to OECTs having platinum polarizable gate electrodes. It is based on the “effective gate voltage” concept, which considers the Faradaic contribution to the gate potential during the enzymatic reaction. When the metabolite of interest (such as glucose) is added to a solution containing the relative enzyme (such as glucose oxidase), the  $H_2O_2$  produced is oxidized at the gate electrode, and the electrons transferred at the gate cause a decrease of potential at the gate/electrolyte interface. Thus, there is an increase of potential felt by the electrolyte and the channel, causing a reduction of drain-source current (change of current modulation). This phenomenon can be described as an increased effective gate voltage in the presence of glucose. It was well-validated with experiments, reproducing the  $I_{ds}$  current variation with increased glucose concentrations in terms of effective gate voltage variations.

Macchia *et al.* in 2018 used the OECT model by Bernards and Malliaras to explain their results for antibody-antigen detection of IgG using antibodies on the gate electrode.[67] By fitting the sensing curves for IgG detection with the model, they described the sensing in terms of a decrease of capacitance at the gate electrode with the increase of IgG, causing a reduction of drain-source current. They attributed this effect to the binding mechanism decreasing the dielectric constant of the bio-layer at the gate interface. Also, they reported through theoretical calculations that the sensitivity of the devices can be optimized by designing the gate electrode to have a gate capacitance that is five times larger than the channel capacitance. However, this was not confirmed with experimental work, such as electrochemical impedance spectroscopy at the gate electrode or other techniques.

## 2.3 Technology and integration

With the increasing demand for mass-production and low-cost sensors, printed biochemical sensors are of high interest for point-of-care and wearable applications.[129] Among all the printing techniques, inkjet printing, a non-contact “drop-on-demand” technique, allows the controlled digital deposition of small quantities of ink for either rapid prototyping or large-scale/large-area production.[74] The PEDOT:PSS ink often includes different chemicals to improve its conductivity and stability. The conductivity of the untreated polymer is generally equal to a few S/cm, and treatments or mixing with the solvent dimethyl sulfoxide (DMSO) or ethylene glycol (EG) can improve the conductivity up to 1000 times.[130]–[132] The PEDOT:PSS electrical conductivity is enhanced thanks to an improved crystallinity,[133] leading to enhanced electrical characteristics and stability in the transistor configuration.[130] Also, a post-treatment based on concentrated sulfuric acid demonstrated a strongly enhanced crystallization and stability in contact with electrolytes.[132] A study published in 2022 reported on the importance of adding fresh (3-glycidyloxypropyl)trimethoxysilane (GOPS) to cross-link the PEDOT:PSS material to maximize the stability in solutions.[76]

Considering all the reported OECT biosensors in Table 1, only two were fully made by inkjet-printing technologies.[91], [109] Both devices were made entirely of inkjet-printed PEDOT:PSS (channel, gate, and contacts) on flexible substrates. One work had antibodies immobilized on the gate, but the device was not tested for biosensing, showing only electrical characteristics without the analyte present. The other work showed the enzymatic-based detection of alcohol. Only another research reported a fully-printed, functionalized, and tested OECT device for biosensing,[73] using hybrid printing technologies including carbon-black gate, source, and drain contacts by doctor blade, and PEDOT:PSS channel by inkjet printing, on biodegradable Clarifoil substrates. The device was tested for the enzymatic-based detection of glucose using a reservoir for confining the electrolyte. Some other devices have only the PEDOT:PSS channel printed, either using screen-printing,[104] or inkjet.[67]

The design considerations are dependent on the biochemical sensing application targeted. For ion sensing, change in the silver-based pseudo-reference gate electrode area (and relative gate/channel ratio) does not influence the sensing performances since there is no potential drop at the gate interface.[134] For enzymatic-based sensing, the gate electrode takes part in the detection mechanism (often platinum- or carbon-based materials). Small areas of the gate electrodes (small gate area per channel area ratios) are reported to give better-normalized sensitivities.[64] Since the modulation of the channel current is worse than with large gates, the shift in modulation with the addition of the analyte is proportionally more significant with small gates than with large gates. For antibody-based sensing, the influence of design

geometries on the sensing characteristics was not experimentally proven. Since the detection mechanism is not well-understood, there is a lack of clear design guidelines for the gate and channel interfaces. The PEDOT:PSS geometry can be modified, and the increase of the channel width (W) times the thickness (d) versus length (L) ratio  $\frac{Wd}{L}$  leads to a linear increase in the current amplification.[57] This increase was shown to ultimately saturate for small channel designs due to parasitic contact resistances.[135]

Generally, most devices are fabricated on glass, with lithography-patterned PEDOT:PSS channels and contacts and external gate electrodes immersed in the common electrolyte solution (not integrated into the substrate).[68], [69], [72], [79], [107], [108], [110] Some works had the devices lithography-patterned on silicon or glass substrates with the gate integrated into the latter (planar configuration), and a reservoir to contain the electrolyte (covering both gate and channel).[80], [86], [88], [90], [102] Few others had the same fabrication and testing conditions but were fabricated on flexible substrates.[81], [85] Considering devices with antibody-coated gate electrodes, several works reported an incubation with the analyte of interest only at the gate electrode (device not integrated) and then a successive assembly into an OECT configuration for testing.[67], [69], [93], [136]

So far, the highest integration level in the OECT systems was reached with the following few implementations. Three works proposed the integration of multiple OECTs with different enzymes (in all cases for glucose and lactate, plus cholesterol in one) into a microfluidic system.[82], [83], [87] The devices were lithography patterned, and the gate was integrated into the rigid glass substrate. In two cases, the devices were tested for single-shot point-of-care saliva analysis. Then, another work proposed OECTs made by screen printing (Ag/AgCl gates, planar integration) and lithography, on a flexible substrate, with multiple ISMs (without inner electrolyte) for  $K^+$ ,  $Na^+$ , and  $Ca^{2+}$  sensing.[78] By integrating various ion-OECTs with standard thin-film transistors, the voltage at the output of a multiplexer circuit was measured at increased ion concentrations. However, this work mainly focused on the technological integration and did not address the real-time sensing dynamics.

Finally, to the best of our knowledge, only two works have reported the use of integrated OECTs for sweat sensing, as discussed in the next paragraph.

### *2.3.1 OECTs for sweat sensing*

Researchers at Stanford University demonstrated using OECTs devices for sweat sensing for cortisol and ion sensing in 2018 and 2019, respectively.[20], [75] Both the cortisol sensing and the ion sensing OECT devices were tested for real sweat analysis on the skin, with a good correlation with standard

measurement techniques. They performed single-shot time measurements on the skin for a few seconds. The ion sensing devices are tested for calcium and ammonium ions directly integrating ISMs on the PEDOT:PSS channel.[75] In the latter, for the *ex-situ* analysis, it is used an Ag/AgCl pellet as a gate electrode. In both cases, a brush-printed integrated Ag/AgCl gate was used for the on-body measurements with a similar design. The cortisol sensors have a molecularly imprinted membrane selective to cortisol on the PEDOT:PSS channel and show a sensitivity of 2.68  $\mu\text{A}/\text{dec}$  in the range of 0.01 to 10.0  $\mu\text{M}$  cortisol.[20] In both cases, the possible cross-sensitivity interferences in sweat were minimized using selective membranes on the PEDOT:PSS channel. These results are promising for applying OECTs in the sweat science field. However, several open challenges exist to using OECTs for continuous monitoring, particularly with bio-layers made of antibodies and enzymes.

## 2.4 Summary and contributions

This chapter reviewed the OECT state-of-the-art identifying the main limitations in applying OECTs for biosensing, mainly focusing on: ions, metabolites, and antigens sensing using as biofunctionalization ISMs, oxidase enzymes, and antibodies, respectively.

The primary limitations are summarized in the following points:

- The effective use of OECT sensors for biosensing in real biofluids such as sweat still needs to be demonstrated. Ion-selective OECTs are rarely tested in biofluids, and they were never tested for continuous measurements on the human skin. The same applies to continuous measurements in biofluids using enzymatic-based OECTs. This is due to missing multiplexed and cross-sensitivity studies testing ion-selective OECTs and enzymatic-based OECTs measuring the same biofluid (for instance, the variations in ion concentration can influence the signal with enzymatic-based OECTs). The limited number of studies is possibly due to the complex fabrication processes required for the realization the different biosensors mentioned above, which prevents their integration in arrays. Overall, the advantages of using OECTs compared to standard amperometric sensors are not clearly established.
- OECT sensors applied for antibody-antigen detection show variable results and limited characterization in biofluids. The variability is possibly due to the complex interaction of the gate-biolayer interfaces and the different device architectures tested. The sensing mechanism with antibodies at the gate interface is not well-understood and experimentally proven.

Antibody-coated OECTs were never tested in real sweat samples, and design rules on how to optimize their design to improve the sensing performances are missing.

- Significant developments in fabrication and integration methods for OECT devices is required for wearable applications since, at the moment, they are mostly fabricated on rigid, bulky configurations with external gate electrodes. Concerning ion-selective OECTs, the ISM is generally suspended over inner electrolytes on the PEDOT:PSS channel, making it challenging to integrate the devices into wearables. The enzymatic-based detection with OECTs is focused on using multi-layer gate materials requiring a complex fabrication process. For antibody-based detection, the gate electrode is generally incubated separately from the channel with the antigen of interest, demanding to assemble the different parts into an OECT configuration afterward.

To address the aforementioned challenges, this thesis presents innovative contributions on multiple topics as follows:

**OECT sensors.** This thesis includes scientific contributions to the study and development of ion-selective ( $K^+$  and  $Na^+$ ), pH-sensitive, enzymatic-based, and antibody-based OECT devices. Beside ions, the research covers the sensing of glucose, lactate, and cortisol. Different nanomaterials for the gate electrodes, including silver nanoparticles and graphene nanosheets inks, are investigated depending on the functionalization strategies adopted for the various analytes.

*Ions:* Silver nanoparticle-based pseudo-reference gates are demonstrated to be effective for ion-selective sensing and pH sensing configurations. The real-time sensing of  $Na^+$ ,  $K^+$ , and  $H^+$  using the respective ISMs directly placed in contact with the PEDOT:PSS channels is demonstrated. Electroplated polyaniline on the PEDOT:PSS channels improved the sensing response towards pH variations compared to pristine PEDOT:PSS devices and devices with  $H^+$  ISM membranes. Electrochemical impedance spectroscopy measurements demonstrated a higher interfacial capacitance when decreasing the pH with the hybrid film than a bare PEDOT:PSS layer.

*Glucose and lactate:* Printed silver and graphene-gated devices are compared for enzymatic-based sensing of metabolites such as glucose and lactate. Improved sensitivity, linearity, and reproducibility are demonstrated using graphene-gated devices compared to silver-gated ones. This work shows the importance of the mediator ferrocene for controlling the solution potential in the OECT configurations for reliable measurements. It also shows the amplification effect of OECTs compared to standard amperometric measurements, with a 1000X higher current variation with the OECTs devices for glucose

detection. The analysis with electrochemical impedance spectroscopy showed that the sensing mechanism is related to a decrease of charge-transfer resistance at the gate interface in the presence of glucose, increasing the current modulation of the devices, in agreement with the theory on enzymatic-based sensing.

*Cortisol:* For antibody-based sensing, the development of OECTs with antibody-coated gates to detect low cortisol concentrations is demonstrated. An optimized architecture and device configuration involving functionalized gold gates and enhanced sensitivity tuning the PEDOT:PSS channel design is presented. The sensing mechanism is related to an increase of capacitance of the gate interface with the binding events through impedance spectroscopy measurements. These experimental findings are confirmed with OECT electrical models. These results can be used to optimize OECTs applied to antibody-antigen detection.

**Integrated technology for wearables.** This thesis shows the development of inkjet-printed multi-sensing OECTs with integrated gate electrodes on flexible polymeric foils. The proposed digital fabrication process, functional materials, and design configuration allow the simple integration of multiple OECTs and microfluidics into a configurable and potentially wearable fashion. The respective ISMs directly cover the PEDOT:PSS channels for the ion-selective sensors, and their printed pseudo-reference silver-based gates are integrated onto the same substrate in a planar configuration. The silver gate is substituted with a functional graphene printed gate to achieve higher sensing performances for enzymatic detection. For the antibody-antigen-based OECT sensors, an antibody-coated gold gate with a standard thiol functionalization process is used. The developed devices can be integrated into a flexible, wearable microfluidic system for allowing direct sweat collection. Finally, multiple miniaturized OECT ion sensors are tested simultaneously using custom-made portable electronics.

**Multi-sensing and sweat analysis.** The sensing of the multiple aforementioned analytes is optimized to achieve high biochemical sensing performances in the sweat concentration ranges. The sensitivity for ions, glucose, and lactate are shown based on real-time drain current measurements in all the cases. Also, through the antibody-coating of OECT gates, the detection of nM concentrations of cortisol was demonstrated. The analysis was performed by measuring the drain current in time following successive incubations of 5 minutes each with an increased cortisol concentration. The devices with ISMs ( $K^+$  and  $Na^+$ ) and antibodies were tested with real sweat samples extracted during sports activities, confirming that the flexible sensors can effectively distinguish ions and cortisol variations.



## Chapter 3 Real-time multi-ion sensing using organic electrochemical transistors (Paper I)

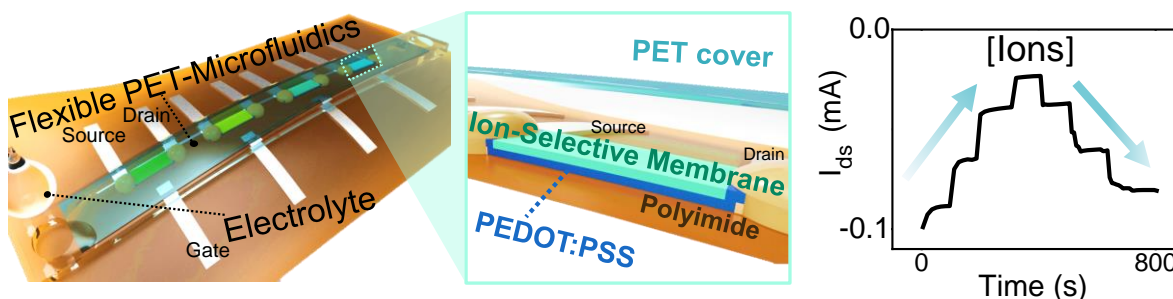


Figure 3-1: Graphical abstract. Organic electrochemical transistor arrays with multiple ion-selective membranes for real-time ion sensing.

Organic electrochemical transistors (OECTs) show remarkable promise as biosensors, thanks to their high signal amplification, simple architecture, and the intrinsic flexibility of the organic material. Despite these properties, their use for real-time sensing in complex biological fluids, such as human sweat, is strongly limited due to the lack of cross-sensitivity and selectivity studies and the use of rigid and bulky device configurations. Here, the development of a novel flexible microfluidics-integrated platform with an array of printed ion-selective OECTs enables multi-ion detection in a wearable fashion. This is achieved by coating the poly(3,4-ethylene dioxythiophene):polystyrene sulfonate (PEDOT:PSS) channels of the transistors with three different ion-selective membranes (ISMs). Systematic electrical and sensing analysis of the OECTs with ISMs show a minimal impact of the membranes on the electrical and time responses of the transistors while providing high ion selectivity. This work combines for the first time real-time and selective multi-ion detection with an array of inkjet-printed and flexible organic transistors coated with different ISMs, demonstrating state-of-the-art sensing capabilities of  $\sim 10 \mu A \text{ dec}^{-1}$  for potassium, sodium, and pH. This flexible OECTs sensing platform paves the way to the next generation devices for continuous electrolytes monitoring in body fluids.

### 3.1 Introduction

There is a growing interest in wearable non-invasive or minimally invasive devices that can continuously analyze biofluids such as interstitial fluid, tears, saliva or sweat.[5], [6], [27], [34], [68], [137]–[139] Electrolytes such as sodium and potassium ions ( $\text{Na}^+$  and  $\text{K}^+$ ) are of fundamental importance for biological processes, including control of the hydration status, nerve and muscle impulse transmission, osmotic pressure balance and pH regulation.[72], [140], [141] The monitoring of electrolyte imbalance in everyday life with a wearable device would help notably to understand, predict and prevent pathologies related to moderate and strong dehydration caused, for instance, by excessive heat, intensive exercise, and harmful working conditions.[142]–[145] More precisely, in human sweat, the concentration of  $\text{Na}^+$  changes between 10–100 mM, it is sweat rate-dependent and associated with dehydration.[27], [29], [144]  $\text{K}^+$  concentration level ranges between 1–18.5 mM with a sweat rate-independent partitioning.[27], [29] Also, pH can strongly vary between 3–8 units,[27] with changes associated with dehydration and muscle fatigue.[144], [145]

For the next generation of wearable ion sensors, key requirements include mechanical flexibility, simple array patterning for multi-parametric analysis, and microfluidics integration for continuous sampling.[40], [78], [81], [146]–[149] Conventionally, selective ion measurements are performed using potentiometric two-electrode systems, in which the potential drop between an Ion Selective Membrane (ISM) and a reference electrode is measured.[147], [150], [151] However, standard potentiometric sensors are difficult to integrate into an array configuration in a microfluidic platform, due to their high output impedance,[78] and the difficult miniaturization of a stable reference electrode.[152]–[154] Organic electrochemical transistors (OECTs) are an interesting alternative to conventional potentiometric sensors, overcoming some of these limitations.[55]

The OECTs are three-terminal devices (drain, source, and gate), with the source and the drain electrodes connected by a conducting polymeric channel. The organic channel is based on conjugated polymer-polyelectrolyte blends, such as the mainly used poly(3,4-ethylene dioxythiophene):polystyrene sulfonate (PEDOT:PSS).[88], [148], [155], [156] This active material enables mixed ionic and electronic charges interaction, with ionic conduction provided by the PSS polyelectrolyte chains and electronic conduction by nanometric-sized PEDOT crystallites.[57], [126], [157] In the presence of an electrolyte and once a positive gate voltage is applied, the dissolved cations are injected into the PEDOT:PSS channel. The cations compensate electrostatically the sulfonate anions of the PSS phase, subsequently lowering the drain current (hole de-doping) in the bulk of the layer.[55], [68] This technology, without the need for a reference electrode, allows a facile miniaturization.[104], [154] Moreover, the mechanical flexibility of the PEDOT:PSS channel,[148], [158] the compatibility with digital manufacturing such as inkjet

printing,[109], [159]–[161] and the very low output impedance,[78] make OECTs promising candidates for the development of configurable and wearable sensor arrays. Besides, the device physics results in novel electrical characteristics that were never observed in other types of transistors, both organic and inorganic-based, such as a very high transconductance at very low voltages,[57], [162]–[164] enabling high signal amplification and sensitivity.[72], [81], [165]

OECTs (PEDOT:PSS-based) on flexible substrates are reported for different bio-sensing applications, including chemical and biochemical sensors on plastic,[78], [81], [166] elastomeric,[167] and paper substrates.[91] However, several challenges in the development of OECTs for wearable bio-sensing applications still remain, with the main problem being the selectivity to the target analyte.[77] Despite the importance of measurements in complex biological fluids such as human sweat, in which multiple ions and other analytes are present, this issue is still rarely taken into account.

With the use of an ion-selective membrane, only the desired cations will contribute, with a certain selectivity, to the de-doping of the PEDOT:PSS layer.[72], [78], [168], [169] However, the behavior of organic transistors for selective ion sensing has been almost exclusively reported for single devices on rigid substrates,[68], [72] with the ISM suspended on an inner electrolyte (liquid or hydrogel). In 2019, OECTs made by a combination of screen printing and lithography on a flexible substrate with multiple ISMs (without inner electrolyte) have been presented,[78] however, while focusing on the technological integration, the transfer characteristics and responses in time in presence of the analytes were not studied.

In this work, we demonstrate an array of inkjet-printed flexible OECTs that perform real-time, sensitive and selective detection of potassium ( $K^+$ ), sodium ( $Na^+$ ), and hydrogen ( $H^+$ ) ions at physiologically relevant concentrations. Their PEDOT:PSS channels were coated with three different ionophore-based ion-selective membranes, which were developed to have a minimal impact on the electrical and time responses of the transistors while maintaining high ion selectivity. The proposed array of thin-film transistors was integrated into a flexible microfluidic system, enabling continuous measurements of electrolytes in body fluids.

## 3.2 Results and Discussion

### 3.2.1 Characterization of the inkjet-printed layers

In this work, organic electrochemical transistors were inkjet-printed on a flexible 125  $\mu m$ -thick polyimide foil (PI) substrate, using conductive-grade PEDOT:PSS (1 S/cm, 1.3 wt % dispersion in  $H_2O$ ) for the active layer, and silver nanoparticles ink for the gate, source, and drain electrodes (Figure 3-2). The active organic channel area is 1 x 3  $mm^2$ , with an overlap of  $\sim 1 mm^2$  to the source and drain contacts. The active gate has a planar on foil configuration with an area of 1 x 1  $mm^2$  and a  $\sim 1 mm$  gap from the

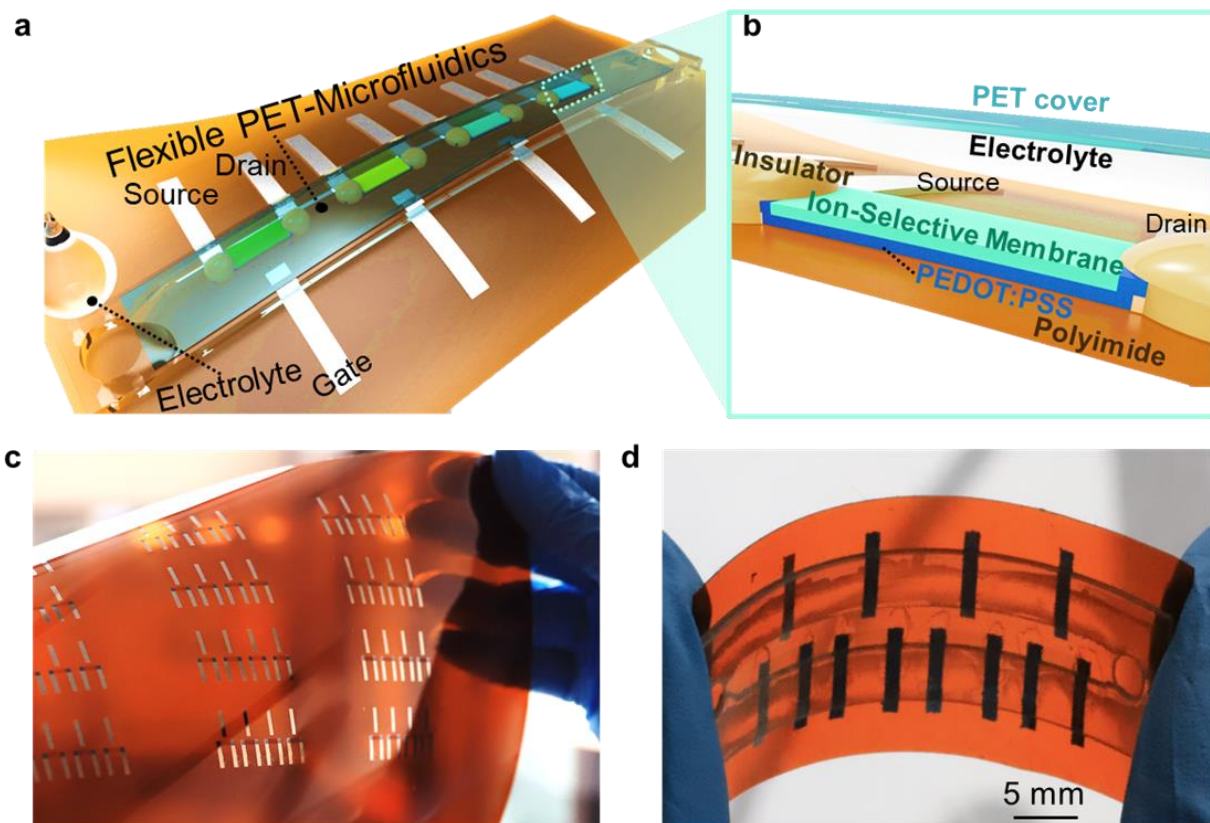


Figure 3-2: a) Schematic of the integrated organic transistors into the microfluidic system and zoom with the cross-section in (b). c,d) Images of the transistors, without and with microfluidics in (c) and (d), respectively.

channel. Instead of using floating wires or pellets as external gate electrodes,[72], [126], [162] the proposed design enables straightforward integration of multiple sensing transistors into microfluidics (Figure 3-2a,d). The schematics of the cross-sections of the integrated OECTs array are illustrated in Figure S3-7.

Four layers were printed to obtain a continuous PEDOT:PSS film (Figure S3-8). The organic layers were post-treated by drop-coating dimethyl sulfoxide (DMSO).[170] DMSO post-treatment strongly improves the PEDOT:PSS electrical conductivity and crystallinity,[133] leading to enhanced electrical characteristics in a transistor configuration.[130] A film thickness of  $115 \pm 28$  nm ( $n=3$ ) and sheet resistance of  $0.96 \pm 0.06$  k $\Omega$ /sq ( $n=4$ ) (Figure S3-8) is achieved with the post-treatment and four printed layers. In a printed batch of a total of 52 transistors, 2 had a significantly higher resistance ( $> 40$  %) than

the others, possibly due to some defects in the printing layer, leading to a fabrication yield of 96 %. Moreover, we observed after ~20 days that the resistance of the treated PEDOT:PSS layers increased by just ~10 % (Figure S3-9), while for the untreated layers increased of ~200 % likely due to higher water and oxygen absorption from the air.[171] The silver electrodes exhibit a conductivity of ~15 kS/cm for two printed layers with a thickness of ~200 nm. The mechanical flexibility of the system, hence its wearability, was assessed by attaching the integrated device on curved surfaces of different radii equal to 20, 15, and 10 mm (Figure S3-10), and by measuring the changes in resistance of the PEDOT:PSS channels. A change of less than 0.1 %, defined as the absolute value of  $\frac{R-R_{unbended}}{R_{unbended}} \times 100$ , is reported, showing that the bending of the platform does not significantly change the channel conductivity and therefore the electrical characteristics.

### 3.2.2 Electrical analysis without the ion-selective membranes

The configuration employed for testing the DMSO-treated OEETs is shown in the inset of Figure 3-3a and in Figure S3-7a, with a poly(methyl methacrylate) (PMMA) reservoir integrated to the PI foil to confine the Phosphate-Buffered Saline (PBS) solution. The electrical testing includes drain current-gate voltage ( $I_{ds}$ - $V_{gs}$ ) measurements in Figure 3-3a,c and drain current-drain voltage ( $I_{ds}$ - $V_{ds}$ ) measurements in Figure 3-3b, with hysteresis and leakage current. The OEETs exhibit a transconductance,  $g_m$  ( $\Delta I_{ds}/\Delta V_{gs}$ ), of  $247 \pm 24 \mu S$  for the same printed batch (n=3) and  $238 \pm 129 \mu S$  for multiple printed batches (4 batches, n=8), with a peak close to 0 V (Figure 3-3a). Such variability is common for inkjet-printed polymers, due to some variations in thickness and uniformity of the printed organic layers, affecting the electrical resistance of the channel and the related transconductance. Considering the design parameters, with a width to length ratio equal to 0.3 and a thickness of ~100 nm, the reported transconductance values are comparable with lithographically-patterned OEETs.[57], [162] The ON-OFF ratio of the devices is ~60 (n=3). As expected, we observe an increase of the leakage current with the gate voltage applied (Figure 3-3c), likely due to the silver gate oxidation in the presence of chloride ions.[172]

To further investigate the influence of ions at the organic channel and the gate electrode interfaces, electrical measurements at different ionic concentrations in the range of 1–50 mM (Figure 3-3d-f) are performed. When the concentration of potassium chloride (KCl) increases, a shift of the curve towards a lower drain current is observed, while the response in DI water ( $<10^{-6}$  M) is quasi-flat (Figure 3-3d). Figure 3-3e and Figure 3-3f show, respectively, the  $I_{ds}$  and  $I_{gs}$  variations in time upon the addition of multiple concentrations of NaCl and KCl, with the gate and the drain voltages fixed. The leakage current  $I_{gs}$ , probably due to the variations of potential on the gate electrode at different chloride concentrations,[56] is

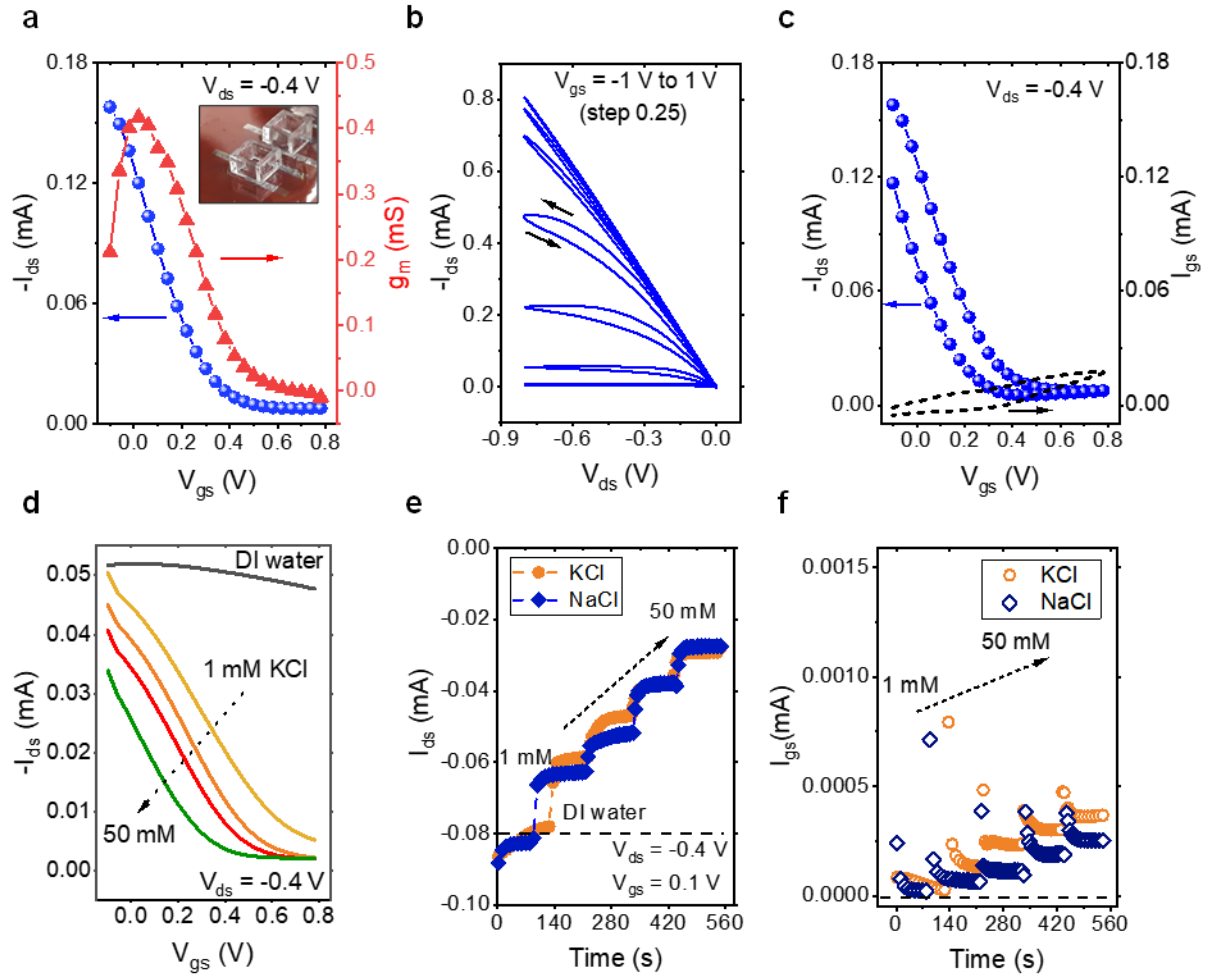


Figure 3-3: a-c) The electrical characteristics of the DMSO treated OEET in PBS 1X (0.155 M NaCl, pH 7). d) Transfer curves at different ionic concentrations of KCl including DI water as a baseline. e) Time measurements with different ionic solutions and concentrations. f) Leakage current with different ionic solutions and concentrations.

much smaller ( $>100\times$  less) compared to the  $I_{ds}$  values in Figure 3-3e. Hence, according to the device physics,[55] since the  $I_{ds}$  current depends on the cations injection, we can conclude that there is a negligible effect of chloride on the sensing response.

### 3.2.3 Electrical analysis with the ion-selective membranes

As previously shown in Figure 3-3e, monovalent ions such as sodium and potassium have the same effect in the de-doping of the organic polymer, thus requiring the use of a specific ion-selective membrane

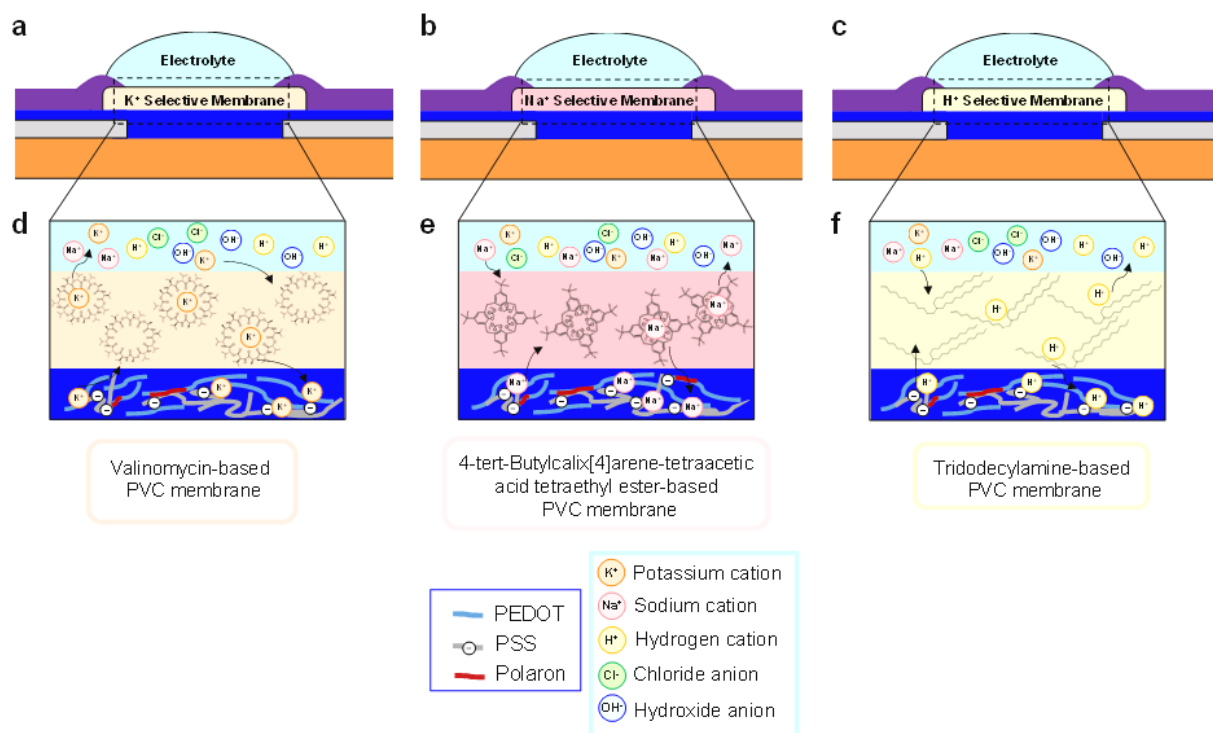


Figure 3-4: a-c) Sketches of OEETs with different ion-selective membranes. d-f) Simplified interactions between an electrolyte solution, the ion-selective membranes, and the PEDOT:PSS active layer considering (d) the potassium ionophore-based membrane, (e) the sodium ionophore X-based membrane and (f) the hydrogen ionophore I-based membrane. The chemical name of the respective ionophore is reported in the image. The sulfonate groups and the polarons (holes) of the organic layers are also represented, with the respective permeated ions de-doping the PEDOT by removing the polarons.

for being differentiated. In this study, we prepared ISMs based on valinomycin, sodium ionophore X, and hydrogen ionophore I in polyvinyl chloride (PVC) matrices, to achieve selectivity for K<sup>+</sup>, Na<sup>+</sup>, and H<sup>+</sup> ions, respectively. These three cases of interest are depicted in Figure 3-4: With the use of an optimized ISM, the number of ions present in the electrolyte that can dynamically interact with the underlying PEDOT:PSS layer, and electrostatically compensate the PSS negative charges, should be considerably less. Hence, the polarons (holes) de-doping is dependent on the selective membrane (Figure 3-4d-f).

However, the thickness of the drop-casted ISM on standard ion-selective electrodes can reach hundreds of micrometers, depending on the electrode area and solution volume.[173] Such thick membranes can significantly hinder the transistor response, which is typically within few milliseconds thanks to the extremely thin active layer.[174] To investigate this effect, the three different ISMs are cast on the organic layers of the transistors with two thicknesses and tested in a PBS solution with a fixed concentration of



sodium and potassium at pH 7. The volume of the membranes was  $\sim 2 \mu\text{L}$  and  $\sim 5 \mu\text{L}$  for each ISM, fully covering the PEDOT:PSS layer, resulting in an average thickness of deposited material equal to  $33 \pm 7 \mu\text{m}$  ( $n=9$ ) or  $54 \pm 15 \mu\text{m}$  ( $n=7$ ), respectively. The electrical characteristics of devices with thinner membranes are shown in Figure 3-5a-c while those for thicker membranes are presented in Figure 3-5d-f. The thin membrane led to a better transistor modulation (Figure 3-5a) compared to the thicker one (Figure 3-5d), with a transconductance shift of 0.1–0.4 V with respect to 0.4 V–0.7 V. The larger  $g_m$  shift for the thick membranes can be explained by the lower membrane permeability, leading to fewer ions

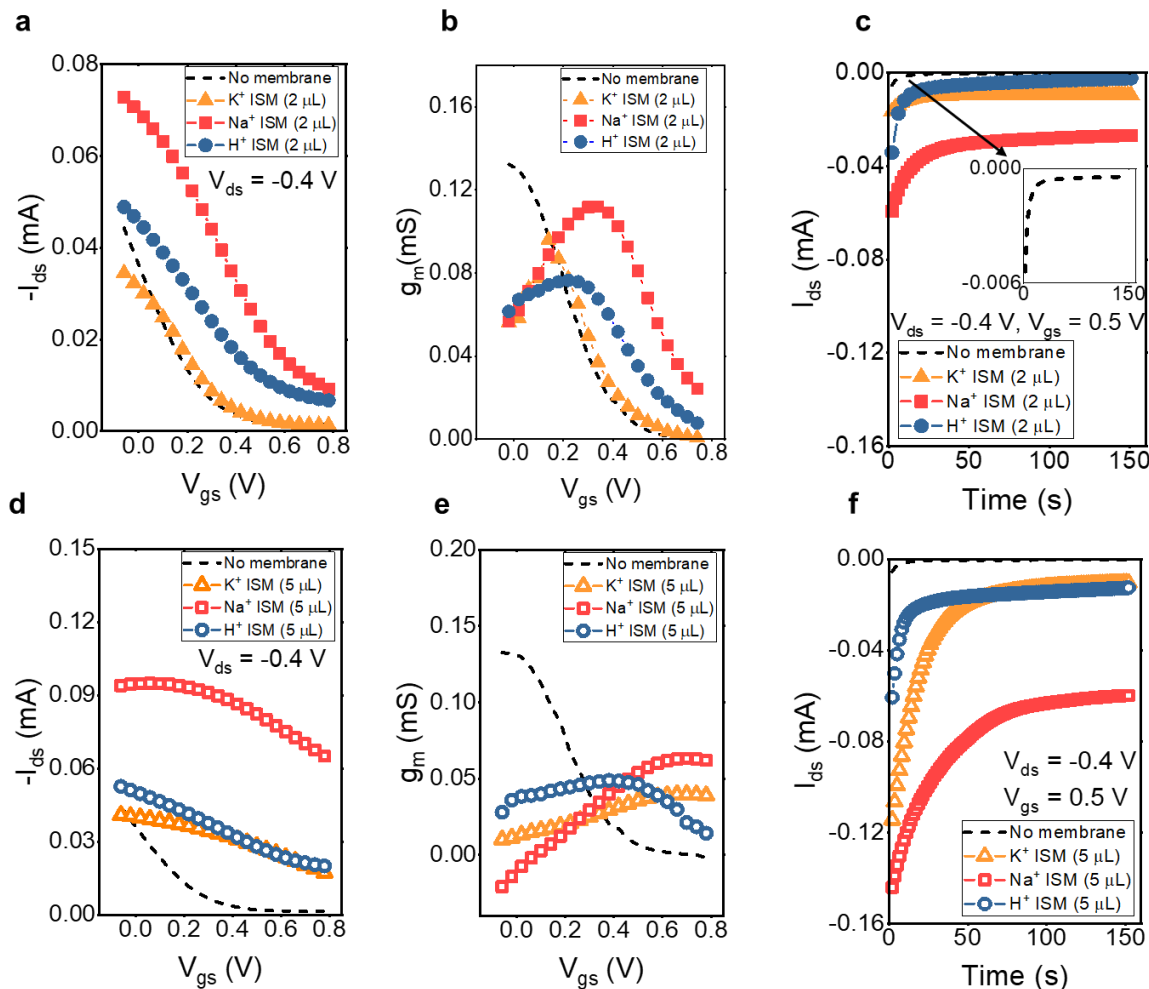


Figure 3-5: Organic transistors electrical responses in PBS (0.155 m NaCl + 0.155 m KCl, pH 7) with (a-c) lower ( $\sim 2 \mu\text{L}$ ) and (d-f) higher ( $\sim 5 \mu\text{L}$ ) volume of the three different ion-selective membranes. The results are compared to a bare device (no membrane). The analysis includes transfer characteristics in (a,d), transconductance in (b,e) and time response in (c,f).



reaching the PEDOT:PSS layers. Such an effect can be compensated by a higher gate voltage, resulting in stronger ions injection. Besides, this results in similar transconductance values for no-membrane and thin-membranes (Figure 3-5b) devices, while a three-fold  $g_m$  decrease is observed for thick-membrane devices (Figure 3-5e). The time response ( $\tau$ ) of the devices was extracted by fitting their response curves in Figure 3-5c,f with an exponential decay function. The values are equal to  $5.75 \pm 0.25$  s ( $n=2$ ) for devices without any membrane, increasing with the sodium and potassium membranes to  $12 \pm 4$  s ( $n=2$ ) for the thin membranes (2.11X increase), and  $25 \pm 7$  s ( $n=2$ ) for the thick membranes (4.35X increase). The  $H^+$  sensor shows a relatively faster response, which is less influenced by the membrane thickness, with values equal to 6.5 s for the thin membrane and 7.5 s for the thick membrane (Figure 3-5f), due possibly to higher penetration of the ions. The measured current changes can be due to the previously mentioned variability related to the printing process, and further comparisons will be done in the next section particularly considering the normalized sensitivity.

### 3.2.4 Array integration into the microfluidic system and sensing

The OECTs with the thinner ion-selective membranes are integrated into a PET microfluidics system as shown in Figure 3-2a,b. This integrated flexible platform, with four transistors included, is used for measuring in time ionic solutions at different physiologically relevant concentrations, performing sensitivity (Figure 3-6a-d) and selectivity (Figure 3-6e-h) tests. Ionic solutions of 1–100 mM are made with KCl or NaCl dissolved in DI water, while pH buffer solutions in the range of 4–7 are employed for the pH measurements.

For the sensitivity analysis (Figure 3-6a-d), the ions are injected in the microfluidics inlet from a low to a high and subsequently high to low concentration. DI water is used as a baseline solution when starting and finishing all the tests. A measurement without any selective membrane is presented in Figure 3-6a. All the sensors exhibit very good stability in time with low drift for the time of the measurements. The sensitivity, proportional to the logarithmic of the concentrations (Figure S3-11), is extracted from the steady-state response after each injection. The value is equal to  $18 \pm 2$   $\mu A \text{ dec}^{-1}$  for devices without any membrane,  $7.5 \pm 1.5$   $\mu A \text{ dec}^{-1}$  with the  $K^+$  membrane,  $6.5 \pm 0.5$   $\mu A \text{ dec}^{-1}$  with the  $Na^+$  membrane (to KCl or NaCl concentrations, respectively), and  $11 \pm 1$   $\mu A \text{ pH}^{-1}$  with the  $H^+$  membrane. The sensitivity values are averaged from two devices coming from the same printed batch. The sodium and potassium sensors show reversibility from low to high and high to low concentrations. With the  $H^+$  membrane, the devices present instability when starting and finishing the measurements in DI water, likely due to the non-negligible ionic strength of the solution (Figure 3-6d,h).

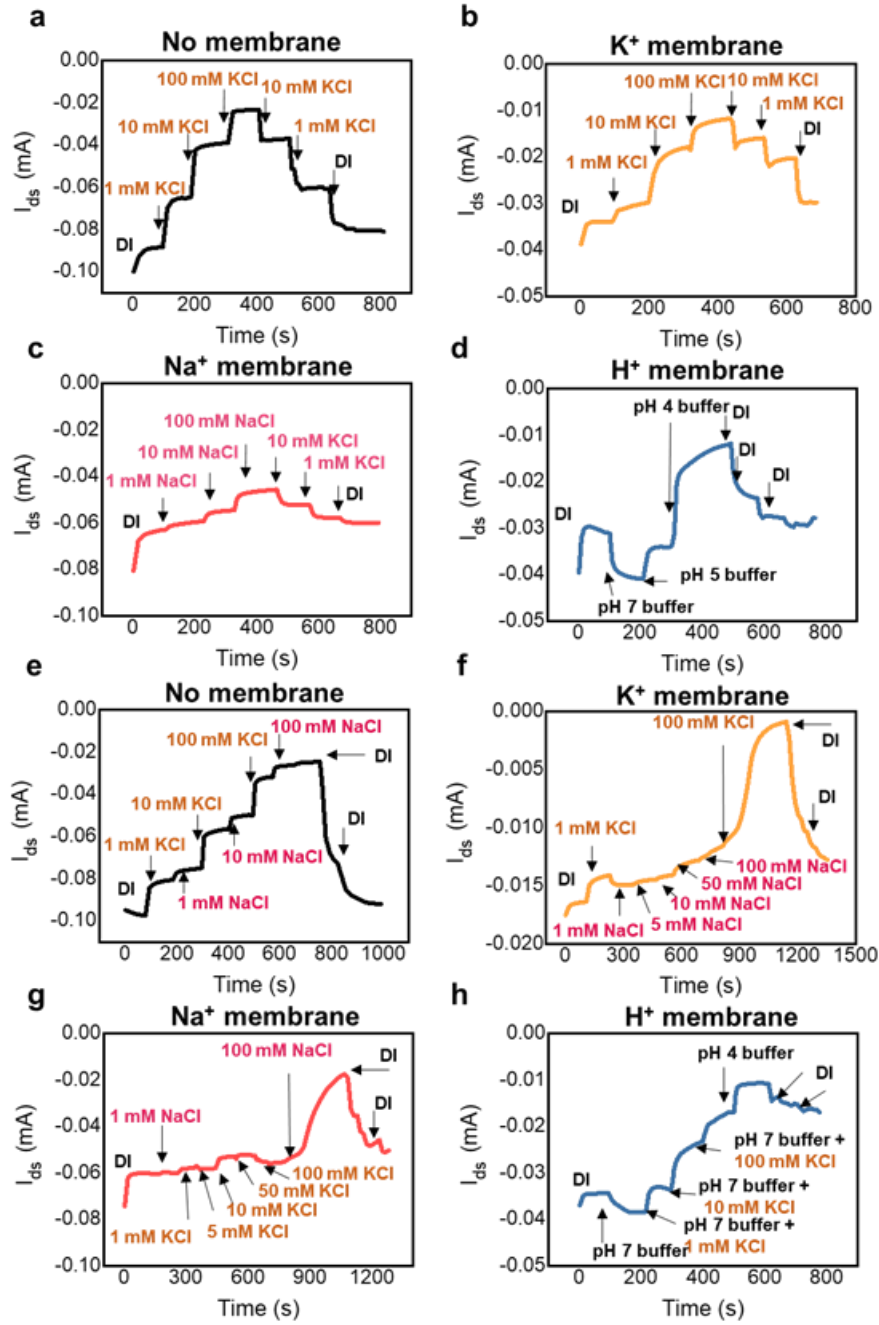


Figure 3-6: Ion sensing with the integrated microfluidic system for OECTs without a membrane in (a,e), with the  $K^+$  selective membrane in (b,f), the  $Na^+$  selective membrane in (c,g), and the  $H^+$  selective membrane in (d,h). The sensitivity tests are shown in (a-c) and the selectivity tests in (e-h). The solutions (except the pH buffers) were made with  $KCl$  or  $NaCl$  dissolved in DI water.  $V_{ds} = -0.4$  V, while  $V_{gs}$  was fixed close to the transconductance peak (0.1-0.4 V) for each device.

Most importantly, the selectivity of the OECTs with ISMs is clearly shown from the ionic measurements in time (Figure 3-6e-h). The OECTs without any membrane have almost the same responses towards KCl and NaCl changes in concentration (Figure 3-6e), while the transistors with the ISMs show a much smaller response towards the respective tested interfering ion (Figure 3-6f,g). At a high concentration of salt equal to 100 mM, from the division of the signal obtained for the non-interfering ions by the signal for the interfering ions, a 12X higher signal towards K<sup>+</sup> to Na<sup>+</sup> with K<sup>+</sup>-ISM and a 3X higher signal towards Na<sup>+</sup> to K<sup>+</sup> with Na<sup>+</sup>-ISM were extracted. Considering the pH measurements, the selectivity test is performed adding a background of different salt concentrations at a fixed pH buffer solution (Figure 3-6h). The signal measured for a pH 4 buffer resulted to be 2X higher than the signal from the highly concentrated background (100 mM) in the pH 7 buffer, calculated starting from the same buffer solution without ions being added.

To analyze the reproducibility among the printed devices, a normalized sensitivity was extracted for four devices of each type and coming from two different fabrication batches (Figure S3-12). The normalized sensitivity, calculated as the absolute value of  $\frac{I_{response} - I_{baseline}}{I_{baseline}} \times 100$ , was of  $23 \pm 0.7 \text{ \%} \cdot \text{dec}^{-1}$  without the membrane,  $29 \pm 3 \text{ \%} \cdot \text{dec}^{-1}$  with the K<sup>+</sup> membrane,  $13 \pm 3 \text{ \%} \cdot \text{dec}^{-1}$  with the Na<sup>+</sup> membrane, and  $28 \pm 4 \text{ \%} \cdot \text{dec}^{-1}$  with H<sup>+</sup> membrane, extracted using DI water as a baseline for Na<sup>+</sup>, K<sup>+</sup>, and neutral pH buffer for H<sup>+</sup>. It can be concluded that all types of sensing devices exhibit a small variation of their sensitivity, confirming the reproducibility of the fabrication approach. It can be noticed that for the Na<sup>+</sup> sensor the normalized sensitivity is smaller than the others, possibly due to a lower ion permeability of the membrane.

### 3.3 Conclusions

In summary, we have demonstrated a flexible platform of inkjet-printed sensing transistors with the PEDOT:PSS active layers coated with three different ion-selective membranes. In comparison to literature, in which the ISM were suspended above inner filling solutions,[111] or gels,[68] in bulky reservoirs, here the ISMs are directly cast on the organic channel. By adding a small volume of the membrane and having enhanced membrane permeability, a minimum impact on the device performances in terms of transfer characteristics and time response is achieved while providing high ion selectivity. The multiple ion-selective electrochemical transistors are also integrated into a flexible microfluidics system. This novel platform allows real-time, multi-ion sensing with low cross-sensitivity. The OECTs selectivity is proven in real-time, extracting a 12X higher signal towards potassium to sodium with the K<sup>+</sup>-ISM, a 3X higher signal towards sodium to potassium with the Na<sup>+</sup>-ISM, and a 2X higher signal towards H<sup>+</sup> to a

high salt background with the  $H^+$ -ISM. All the ion-selective sensors exhibit a sensitivity of  $\sim 10 \mu A \text{ dec}^{-1}$  with good stability for the time of the measurements. However, the  $H^+$  sensor linearity and selectivity should be further improved, potentially by implementing an active-gate material such as polyaniline.[104] Proof of reproducibility is demonstrated in terms of normalized sensitivity among two different printed batches.

A summary table comparing our OECTs with the literature is reported in the Supplementary (Table 2). The ion-selective devices in this work have a 20X higher sensitivity than reported lithographically-patterned ion-selective EGOFETs (Electrolyte-Gated Organic Field-Effect Transistors).[111] They also show sensitivities comparable to lithographically patterned OECTs on glass substrates without,[47] and with a suspended ISM,[68] all within the order of tens of  $\mu A \text{ dec}^{-1}$ . Their sensitivity could be further improved by modifying the proposed design of the OECTs, such as by increasing the W/L ratio, which would result in an increase of their transconductance. Finally, for the first time, these sensing capabilities are combined with a high level of integration and a simple fabrication with digitally manufacturing technologies, to have a low cost, wearable, and multi-sensing platform. Our OECTs could be further scaled down, integrating more sensors into a smaller microfluidic system, with minimal sample volume required, hence enabling real-time multi-electrolytes monitoring in everyday life.

## 3.4 Experimental Section

### 3.4.1 Fabrication and layers characterization

The fabrication was performed with a Dimatix DMP printer (Fujifilm) using the 10 pL cartridges. The PEDOT:PSS (1 S/cm, 1.3 wt % dispersion in  $H_2O$ , Sigma Aldrich) and the silver nanoparticle (PV Nano Cell) inks were sonicated for 5 minutes and subsequently filtered with a  $0.2 \mu m$  pore-size filter when filling the respective cartridges. The polyimide substrate ( $125 \mu m$ -thick) was treated with oxygen plasma before printing. The Dimatix substrate holder was kept at  $40^\circ C$ . The process started with the printing of 2 layers of the silver gate, source and drain electrodes and subsequent sintering at  $150^\circ C$  for 1 hour. Then, the PEDOT:PSS layers were printed (1 to 4 layers), post-treated by dispersing dimethyl sulfoxide (DMSO) solvent fully covering the PEDOT:PSS film and subsequently cured at  $120^\circ C$  for 20 minutes. The OECTs were designed to be simple to integrate as an array into the microfluidics while limiting as well the ON-current for future portable implementations at low power. All the electrical resistance measurements were performed using a multimeter connected between the drain and source contacts of the PEDOT:PSS. The thicknesses measurements were performed using a laser scanning microscope (Keyence VK-X1000 Series), with 50X and 10X magnification for the PEDOT:PSS layers and the membranes, respectively.

The thickness measurements were confirmed with the Wyko NT1100 (Veeco) and the profilometer Alphastep IQ (Tencor).

### 3.4.2 Membranes preparation

All the chemicals have been purchased from Sigma Aldrich unless otherwise stated. The  $H^+$  ion-selective membrane was prepared by dissolving hydrogen I ionophore (1.92 mM), potassium tetrakis(4-chlorophenyl)borate (1.01 mM), bis(2-ethylhexyl)sebacate (153.51 mM), and polyvinyl chloride (3.3 wt/vol%) in tetrahydrofuran. The solution was thoroughly mixed for 1 hour to get a homogenous membrane. For the  $Na^+$  membrane, sodium ionophore X (1.5 mM), sodium tetrakis[3,5-bis(trifluoromethyl)phenyl]borate (0.940 mM), bis(2-ethylhexyl) sebacate (232.420 mM), and polyvinyl chloride (5 wt/vol%) were dissolved in tetrahydrofuran by thoroughly mixing until getting a transparent solution. Finally, the  $K^+$  membrane was prepared by dissolving potassium ionophore valinomycin (5.142 mM), sodium tetraphenyl boron (4.174 mM), bis(2-ethylhexyl) sebacate (433.25 mM), and polyvinyl chloride (9.371 wt/vol %) in cyclohexanone. The prepared  $K^+$  solution was thoroughly mixed for 1 hour to get a homogenous mixture. All the prepared solutions were stored at 4 °C. The membranes were drop-cast on the organic layer before the insulation of the drain-source contacts, to avoid the confinement of the membrane. After casting, a drop of 100 mM KCl or NaCl solution in DI water was left on the  $K^+$  or  $Na^+$  membrane respectively, and a drop of pH 4 buffer on the  $H^+$  membrane, to stabilize the membrane for one hour. The sensors were washed with DI water before the sensing experiments.

*Ionic solutions:* For the pH sensing tests, buffer concentrate solutions (Titrisol) were employed. For potassium and sodium sensing tests, NaCl (Sigma Aldrich) and KCl (Merck) were used and dissolved in DI water. The basic PBS 1X solution was made using monopotassium phosphate ( $KH_2PO_4$  from Merck, 1 mM), NaCl (155 mM), and disodium phosphate ( $Na_2HPO_4$  from Merck, 2.966 mM). For the experiments related to the effect of the membrane thickness on the OECTs electrical characteristics, KCl (155 mM) was added to the previous mixture.

### 3.4.3 Microfluidics fabrication

A PET foil (125  $\mu m$ -thick) was used for the flexible fluidics system. The foil was patterned by  $CO_2$  laser etching (Trotec Speedy300 laser cutter) to define the shape of the micro-fluidic channel, the reservoir, the inlet and the outlet. The PET fluidics system was made by lamination of the patterned PET layer with a PET top cover, bonded using a double-side silicone adhesive (ARclear 8932EE). The adhesive was used also to fix the fluidics system to the organic transistor arrays on polyimide.

*Characterization and data analysis:* The OECTs were tested by either injection of the electrolyte solutions in the microfluidics system or confining the solution in PMMA reservoirs, fixed using the double-sided ARclear adhesive. The PMMA reservoirs were laser cut using the  $CO_2$  laser with the

adhesive laminated before the cutting. The OECTs source and drain contacts, close to the PEDOT:PSS layer, were insulated using a transparent dielectric to avoid the electrolyte to be in contact with the silver electrodes. The measurements at different ionic concentrations with the PMMA reservoirs were performed starting from 10  $\mu$ L DI water and subsequently adding 10  $\mu$ L solutions at different concentrations (1–50 mM). Before performing sensing measurements with the microfluidics system,  $I_{ds}$ - $V_{gs}$  characteristics in PBS 1X were acquired for each sensor and repeated five times, to extract the voltage at the peak of transconductance and stabilize the signal. The sensors were then washed three times by injections of 1 ml DI water. The sensing in microfluidics was performed with injections using a syringe (~0.4 ml solution for injection). The testing was performed with the different ISMs on the same array, measuring one device of the fully functionalized OECTs array at the time and switching between devices. All the OECTs electrical measurements were acquired using a semiconductor parameter analyzer (Agilent 4155A), with an integration time of 20 ms (medium) or 320 ms (long). The data were analyzed with the software Origin 2019b.

### 3.5 Supporting Information of Chapter 3

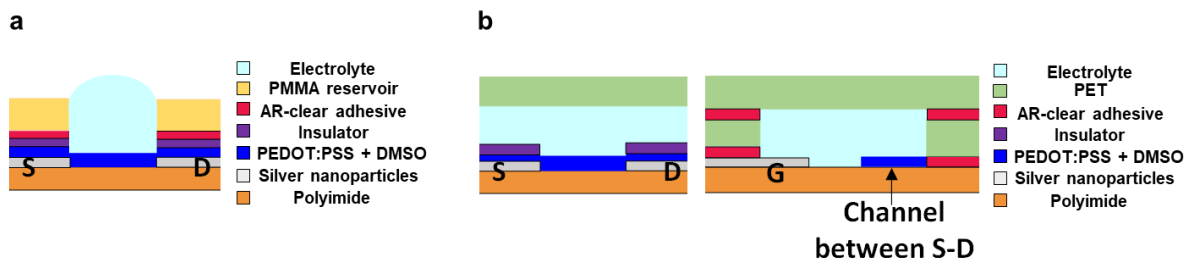


Figure S3-7: Cross-sections of the OECT devices. a) Multi-layer materials including the reservoir used for the electrolyte confinement. b) Final integrated microfluidics system.

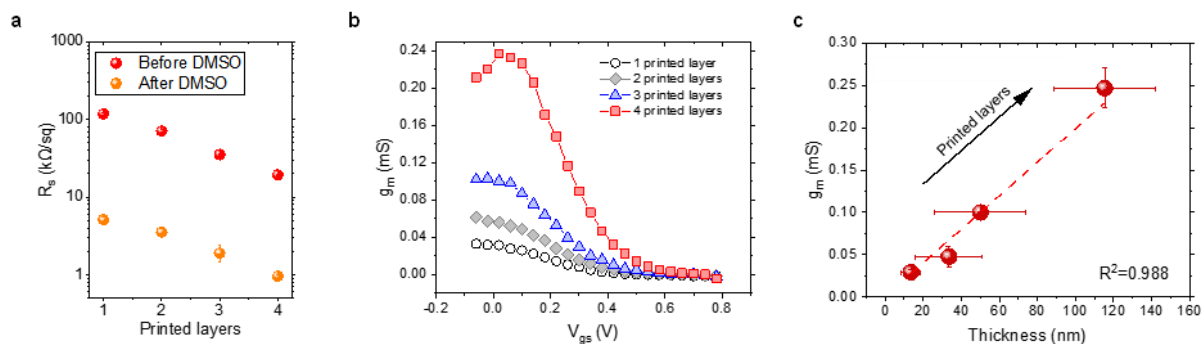


Figure S3-8: Analysis with different printed PEDOT:PSS layers. a) Sheet resistance before and after DMSO post-treatment and a different number of layers (dry state); the points are averaged with  $n=4$  samples. b) Transconductance peak of the post-treated layers and a different number of layers. c) Transconductance values versus the thickness of the layers, tested with PBS 1X (0.155 M NaCl) and in the PMMA reservoir ( $V_{ds} = -0.4$  V); the  $g_m$  values are averaged with  $n=4$  samples for 4 printed layers and  $n=2$  for 1 to 3 printed layers, while the thickness measurements are averaged with  $n=3$  samples for 4 printed layers and  $n=2$  for 1 to 3 printed layers.

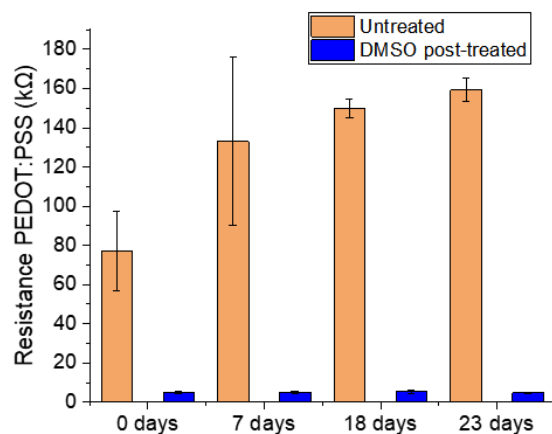


Figure S3-9: Resistance analysis for four printed layers of PEDOT:PSS. Change of resistance in time for untreated and treated PEDOT:PSS channels (dry); the values are averaged with  $n=4$  samples of the same batch and monitored in time.

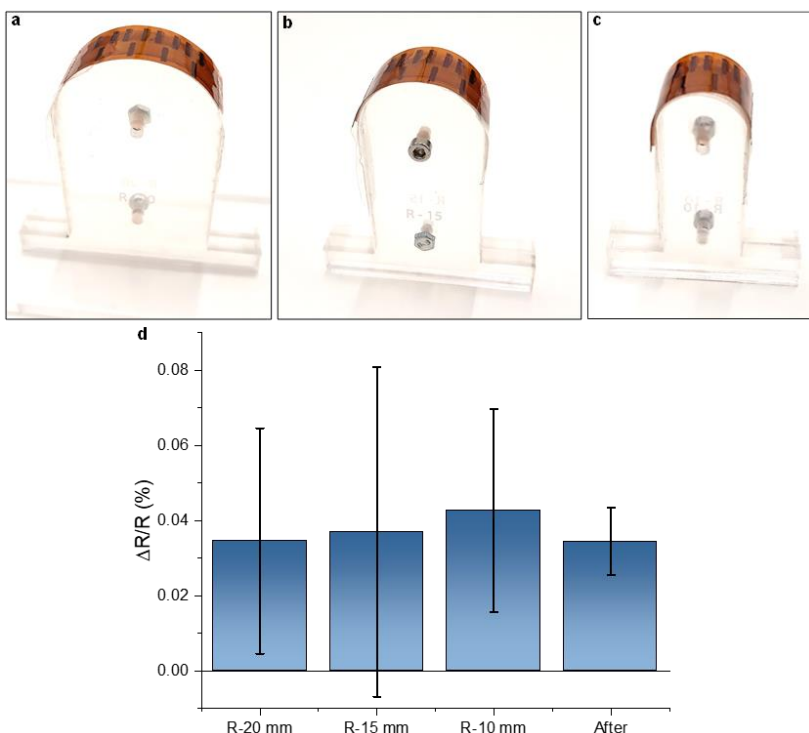


Figure S3-10: Mechanical flexibility analysis for the integrated OEET array into microfluidics. The electrical resistance of four PEDOT:PSS channels was measured before (unbent), during the three bending conditions at the radius of 20 mm (a), 15 mm (b), and 10 mm (c), and after the removal from the plastic support (unbent). The values are reported in (d), normalized with the resistance measured before starting the bending tests ( $n=4$ ). The array of OEETs was attached to the rounded plastic supports through double-side tape.



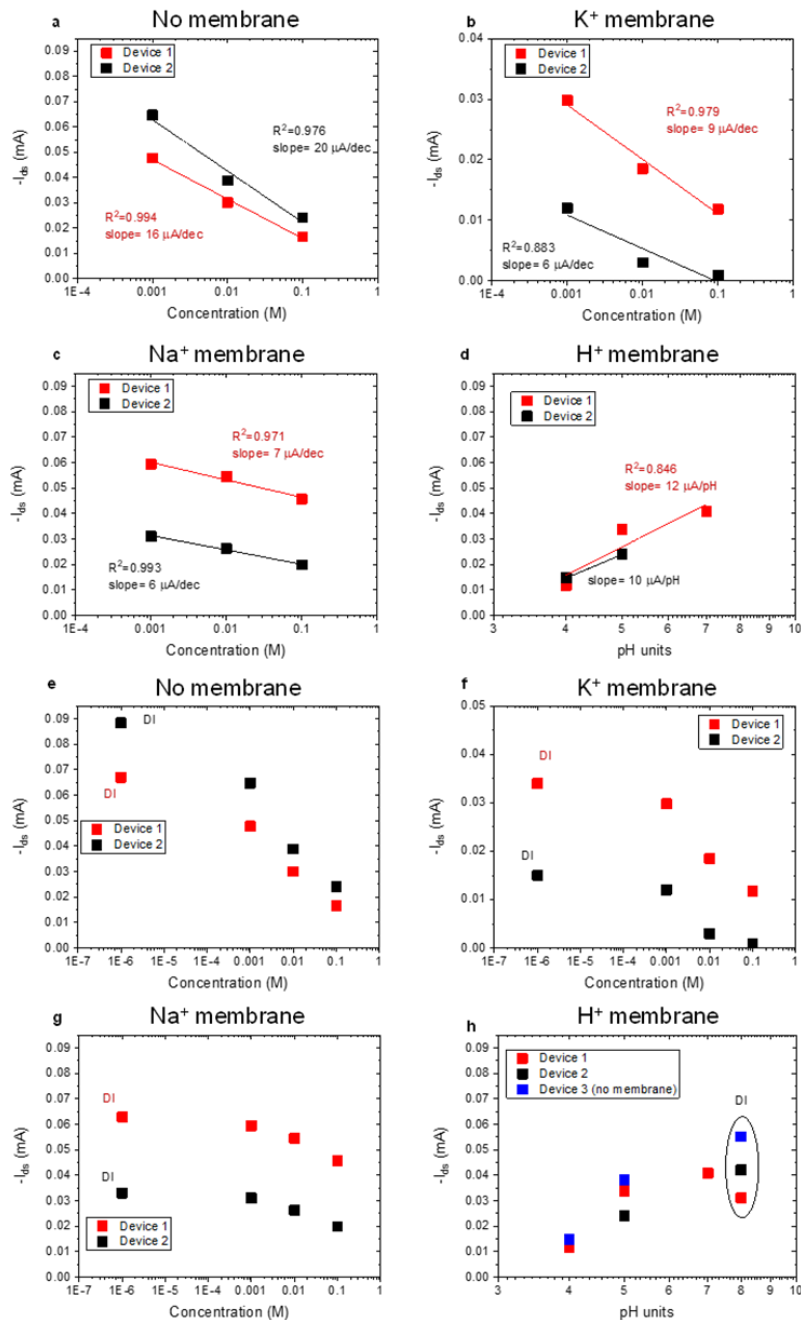


Figure S3-11: Calibration curves for the OECTs into the microfluidics system. a,e) Calibration without a membrane using KCl solutions. b,f) Calibration with  $\text{K}^+$  membrane using KCl solutions. c,g) Calibration with  $\text{Na}^+$  membrane using NaCl solutions. d,h) Calibration with  $\text{H}^+$  membrane using pH buffer solutions. Sensing values including deionized (DI) water in (e-h), in (h) including the influence of pH without  $\text{H}^+$  membrane.  $V_{ds} = -0.4 \text{ V}$ , and  $V_{gs}$  was fixed close to the transconductance peak depending on the device. The sensing analysis was performed on the same printed batch with a PEDOT:PSS thickness of  $115 \pm 28 \text{ nm}$  ( $n=3$ ).

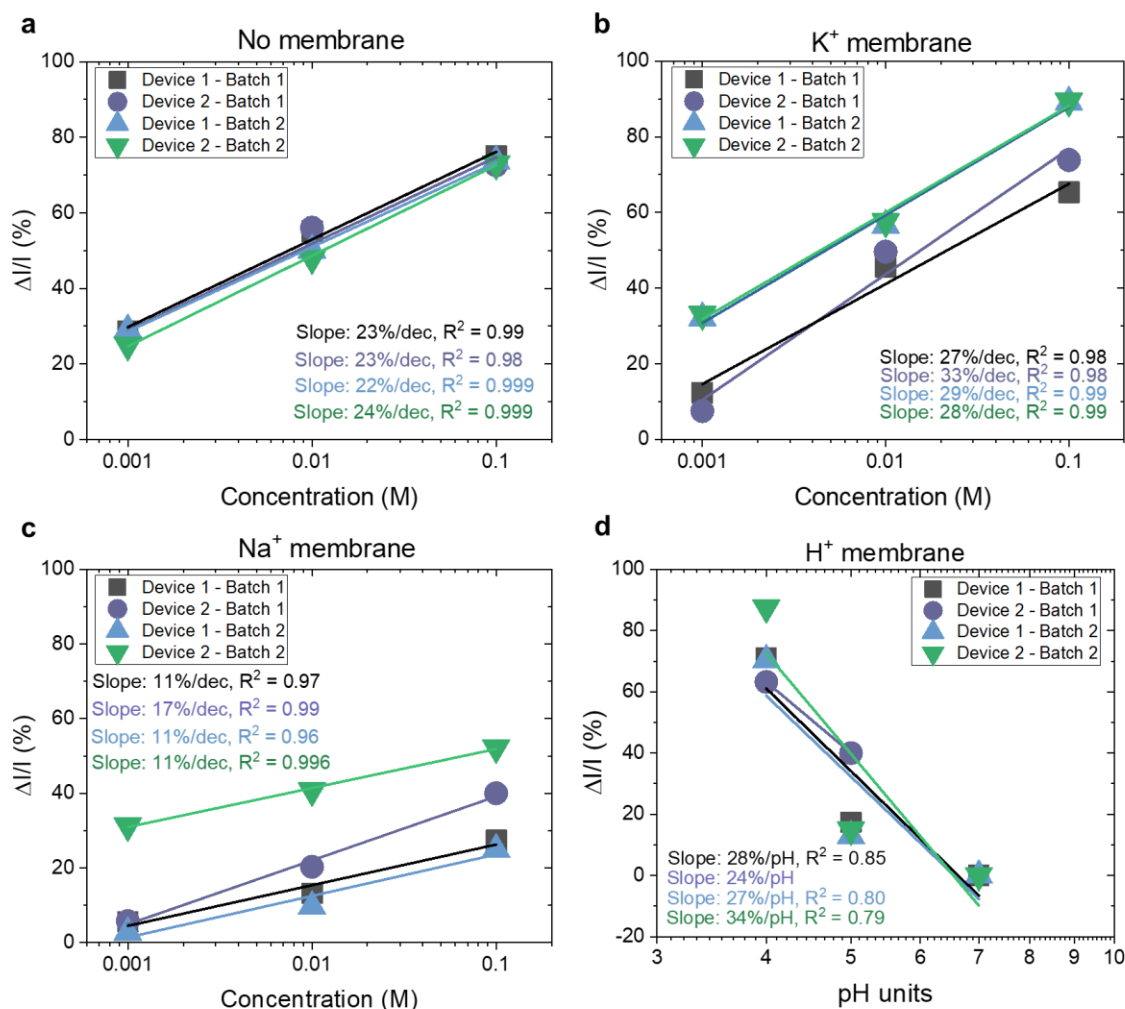


Figure S3-12: Reproducibility analysis. Comparison of OECTs normalized sensing responses for two devices from two printed batches: a) without membrane in KCl solution, b) with the  $K^+$  membrane in KCl solutions, c) with the  $Na^+$  membrane in NaCl solutions, and d) with the  $H^+$  membrane in pH buffers. The testing was performed with the devices integrated into the microfluidics system. The results were normalized with the respective signal in DI water for the devices in (a), (b), and (c), and in neutral pH buffer for the devices in (d).  $V_{ds} = -0.4$  V, and  $V_{gs}$  was fixed close to the transconductance peak depending on the device.

Table 2. Literature comparison for ion-sensitive and ion-selective organic transistors. The table compares the sensitivity, the integration level (gate, membrane, and microfluidics if present), the substrate material (flexible or rigid), and the fabrication method (lithography or printing) for different ion-sensitive and ion-selective transistors reported in the literature, including the applied drain voltage and chosen design parameters. EGOFET stands for Electrolyte-Gated Organic Field-Effect Transistor.

Devices	Ion	Sensitivity ( $\mu\text{A}\cdot\text{dec}^{-1}$ )	$V_{\text{ds}}$ (V)	W/L	Thickness (nm)	Integration	Material / Process	Ref.
<b>Ion-selective EGOFET</b>	$\text{Na}^+$	$\sim 0.5$	-0.1	0.0004	Not reported	External gate, suspended ISM	Flexible, lithography	[111]
<b>Ion-selective OECT</b>	$\text{K}^+$	$\sim 50$	-0.7	1	Not reported	External gate, suspended ISM	Rigid, lithography	[68]
<b>OECT</b>	All (no ISM)	$\sim 20$	-0.1	30	$\sim 80$	External gate (Ag/AgCl)	Rigid, lithography	[47]
<b>Multi-ion selective OECTs</b>	$\text{K}^+, \text{Na}^+, \text{pH}$ No ISM	$\sim 10$ for each $\sim 20$	-0.4 -0.4	0.3	$\sim 100$	On-foil gate, ISM on channel, PET- microfluidics	Flexible, printed	This work

# Chapter 4    OECTs    with    PANI/PEDOT:PSS

## active layers for pH sensing (Paper II)

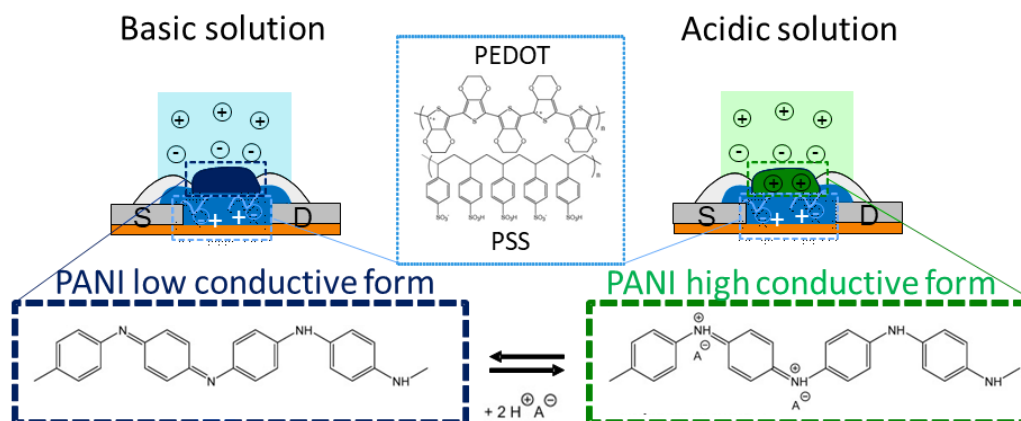


Figure 4-1: Graphical abstract. Organic electrochemical transistors with hybrid PANI/PEDOT:PSS active layers for pH sensing.

We report on organic electrochemical transistors (OECTs) with active channels made of hybrid inkjet-printed poly(3,4-ethylenedioxythiophene):polystyrene sulfonate (PEDOT:PSS) and electropolymerized polyaniline (PANI) layers, exhibiting simultaneously improved electrical and pH sensing characteristics. The aniline electropolymerization with an optimum 6-cycles of cyclic voltammetry forms a porous PANI microstructured layer on the PEDOT:PSS film, resulting in high signal linearity and sensitivity of about 100 mV/pH and 20  $\mu$ A/pH. The electrochemical impedance spectroscopy analysis demonstrates a 9X higher-change of interfacial capacitance when decreasing the pH with the hybrid PANI-PEDOT:PSS layer, in comparison to a bare PEDOT:PSS layer. The simple fabrication process and the high signal amplification pave the way for flexible and higher-performance pH-sensitive OECTs. These scalable devices, combined with ion-selective OECTs, would lead to a novel tool for multi-parametric analysis in different biofluids.

## 4.1 Introduction

There is a growing interest to measure multiple analytes in biofluids such as blood, saliva, sweat, and tears, developing portable tools for multi-parametric analysis [5], [6]. These analytes include notably ions such as sodium, potassium, chloride, metabolites as lactate and glucose, and low-concentrated biomarkers such as proteins and cytokines [27]. A parameter of high importance is the monitoring of pH, as a valuable health-information itself or for the calibration of electrochemical sensors measuring other analytes. Notably, pH variations in the blood correlate to the cortisol levels [145], making it overall a promising indicator of the health status of individual. The pH in blood stays in the 7.35-7.45 range, with mild changes being dangerous for health, and generally cannot be outside the 6.8-7.8 values [175]. In the case of saliva, the pH can vary from 5 to 7.6 depending on the food and beverage consumption [176]. Considering sweat, the pH regulation is related to lactic acid production [141]. Its pH can significantly vary from 3 to 8 [27], and values in the literature between 4 and 7 being mainly reported [177]. It was also shown that the measurement of pH can be applied to the calibration of enzymatic-based measurements, such as for accurate glucose monitoring in sweat [8].

Different types of bio-chemical sensors are being studied to develop such novel low-cost, wearable devices for personalized medicine and health analysis [46]. Among these, organic electrochemical transistors (OECTs), thanks to their mixed ionic-electronic charge transport and their intrinsic flexibility, allow a high signal amplification and improved interfaces with soft biological systems [40], [50], [62], [178]–[180]. The OECT, a three-terminal device, with the source and drain electrodes connected by an organic conductor (channel) and the gate electrode coupled to the conducting channel by an electrolyte, is of particular interest because of the very high sensitivities that can be achieved for multiple biochemical sensing applications [46], [58], [181], [182].

Poly(3,4-ethylenedioxythiophene):polystyrene sulfonate (PEDOT:PSS) is a conjugated polymer-polyelectrolyte and the mainly used active material in OECTs [62]. The PEDOT:PSS channel is doped and dedoped by cations in ionic solutions once a positive gate voltage is applied, exhibiting a mixed ionic-electronic transport and a very high signal amplification [72], [183]. Thanks to PEDOT:PSS, being a low-cost material that can be simply printed onto flexible substrates, the cost-effective manufacturing of OECTs sensors can be envisioned [184]–[186]. PANI was also implemented as the active channel in OECTs, in the form of single-PANI nanowires [187] or recently PANI-microchannels on interdigitated electrodes demonstrating complementary circuits [188]. However, in general, only few works report on PANI-channel OECTs compared to PEDOT:PSS, possibly due to their lower signal transduction.

PEDOT:PSS-based OECTs are reported for different sensing applications, such as ion-sensing of sodium and potassium, enzymatic-based sensing of glucose and lactate [72], [127], [189], or aptamer and antibody-based detection of different low-concentrated biomarkers [67], [102]. An OECT with an  $H^+$ -selective membrane covering the PEDOT:PSS channel was recently reported [186], but the devices had low signal linearity and limited dynamic range (4 to 7 pH). OECTs (PEDOT:PSS-based) for pH sensing are reported only with the integration of different pH-sensitive materials on the gate electrodes, such as a pH-sensitive dye [166] or by using polyaniline (PANI) as gate electrode material [104], the latter exhibiting however a sub-Nernstian response to pH variations.

Among the most commonly studied conductive polymers [2], PANI is being considered for pH sensing since it has the unique property of the pH-dependent tuning of its doping and dedoping state [190]. Indeed, in an acid solution, PANI is doped by the  $H^+$  ions, passing from the emeraldine base to the emeraldine salt form, which exhibits high electrical conductivity. Instead, when the organic material is exposed to basic solutions, the captured  $H^+$  ions are neutralized by  $OH^-$ , resulting in the opposite effect. Thanks to this mechanism, PANI is mostly used for pH-sensitive indicator electrodes in standard two-electrode potentiometric sensors [191] and, in the same configuration only, has been combined with PEDOT:PSS for improved electrochemical pH-sensing characteristics in terms of sensitivity and stability [192].

Herein, PANI-PEDOT:PSS-based OECTs are proposed to simultaneously reach a high electrochemical transduction performance and a high and linear pH-sensing response. Therefore, we report for the first time on OECTs with a hybrid active channel made of inkjet-printed PEDOT:PSS thin film covered by an electro-polymerized PANI layer applied to pH sensing. The electrical characteristics of the transistors are analyzed in electrolyte solutions at different pH levels relevant for biofluids analysis. The PANI-PEDOT:PSS devices with 6-cycles aniline polymerization exhibit much higher pH sensitivity and linearity compared to the use of a bare PEDOT:PSS channel and to the devices with thicker and thinner PANI layers. The micro/nanostructure of the electropolymerized PANI-layers is studied using different techniques, such as SEM, AFM, and confocal microscopy. The working mechanism of the novel hybrid organic electrochemical transistors is analyzed through electrochemical impedance spectroscopy.

## 4.2 Materials and methods

### 4.2.1 Inks, chemicals and solutions preparation

The PEDOT:PSS solution (1 S/cm, 1.3 wt % dispersion in H<sub>2</sub>O) was purchased from Sigma Aldrich. The silver nanoparticle ink was purchased from PV Nano Cell (Sicrys I50T-13). The Phosphate Buffer Saline (PBS) 1X solution was made using 1 mM monopotassium phosphate (KH<sub>2</sub>PO<sub>4</sub> from Merck), 155 mM NaCl (from Sigma Aldrich), and 2.966 mM disodium phosphate (Na<sub>2</sub>HPO<sub>4</sub> from Merck). For the pH sensing tests, buffer concentrate solutions (Titrisol) were employed. The aqueous solution for the electropolymerization process was made of aniline (0.1 M, from Sigma Aldrich) and HNO<sub>3</sub> (1 M, from Merck). Dimethyl sulfoxide (DMSO) was purchased from Sigma Aldrich.

### 4.2.2 Inkjet printing of the organic electrochemical transistors

Thin-film organic electrochemical transistors were inkjet printed with a Dimatix DMP printer (Fujifilm, 10-pL cartridges) on flexible polyimide substrates (125 µm-thick). The silver nanoparticle-ink was used for the source, drain, and gate electrodes, and the PEDOT:PSS ink for the active layer (Figure 4-2a,b). The channel area is about 0.5 mm x 0.8 mm, and the gate-channel gap is about 0.5 mm. The electrical contact of 2 mm x 2 mm (Figure 4-2b) is designed for a simple connection during the successive electropolymerization step.

For the fabrication of these devices, the PEDOT:PSS solution and the silver nanoparticle inks were sonicated for 5 minutes and subsequently filtered with a 0.2 µm pore-size filter when filling the respective cartridges. The polyimide substrate is treated with oxygen plasma before printing. The Dimatix plate is kept at 40 °C during the printing. First, two layers of the silver ink were printed for the gate, source, and drain electrodes, and subsequently sintered at 180 °C for 1 hour. Then, the four layers of PEDOT:PSS were printed and subsequently post-treated with DMSO fully-covering the PEDOT:PSS film, and finally cured at 120 °C for 20 minutes. Such a DMSO post-treatment method is one of the most effective in the literature for achieving PEDOT:PSS films of high electrical conductivity and crystallinity [130]. The fabrication process is summarized in the schematic of Figure 4-2c.

### *4.2.3 Electropolymerization of the PANI layer on the PEDOT:PSS channel*

The electropolymerization of aniline on the PEDOT:PSS channel is carried out with a 3-electrode setup, as represented in Figure 4-2d. The working electrode is the inkjet-printed PEDOT:PSS layer and an insulator is used to cover the silver and the silver-PEDOT:PSS contacts, leaving an open window of around 0.3-0.4 mm<sup>2</sup>. An Ag/AgCl wire is employed as the reference electrode and a platinum wire as the counter electrode. Cyclic voltammetry is performed for the electropolymerization, with the potential applied from 0 to 0.95 V, then down to -0.01 V and back to 0, with a scan rate of 100 mV/s, similar to previously reported work [192]. The electrochemical transistors with different electropolymerization cycles equal to 3, 6, and 10, hence with varying thicknesses of deposited PANI, are tested for pH sensing, as shown in Figure 4-2e. The electropolymerization was performed with a potentiostat (Multi Autolab M204, Metrohm).

### *4.2.4 Imaging*

Thickness measurements and optical images were obtained with a laser scanning microscope (Keyence VK-X1000 Series). For the thickness measurements, the maximum magnification (50X) was used. Top-view images by SEM (instrument JEOL JSM-7500TFE) and AFM (instrument Dimension Edge ScanAsyst) measurements were performed on PEDOT films without and with the PANI layer. A cross-section in the PANI-PEDOT:PSS was defined and the subsequent SEM images were acquired with a dual-beam FIB/SEM instrument (FEI Scios) with the addition of gold and platinum layers.

### *4.2.5 Testing*

The OECTs electrical characteristics were acquired using a semiconductor parameter analyzer (Agilent 4155A). The  $I_{ds}$ - $V_{gs}$  characteristics were repeated three to five times for stabilization of the signal, and each  $I_{ds}$ - $V_{gs}$  measurement took around 2 minutes. For confining the testing solutions, PMMA reservoirs were laser cut using a CO<sub>2</sub> laser and attached to the sensors thanks to a silicone adhesive. The sensors were washed three times with DI water when changing the test solution. Electrochemical Impedance Spectroscopy (EIS) measurements were acquired using the potentiostat and employing a 3-electrode setup, using the PEDOT:PSS or the PEDOT:PSS-PANI layers as the working electrode, an Ag/AgCl wire as the reference electrode, and a platinum wire as the counter electrode. The frequency was changed from 10<sup>5</sup> to 0.1 Hz, applying an AC voltage equal to 10 mV and a DC voltage equal to 0.1 V.



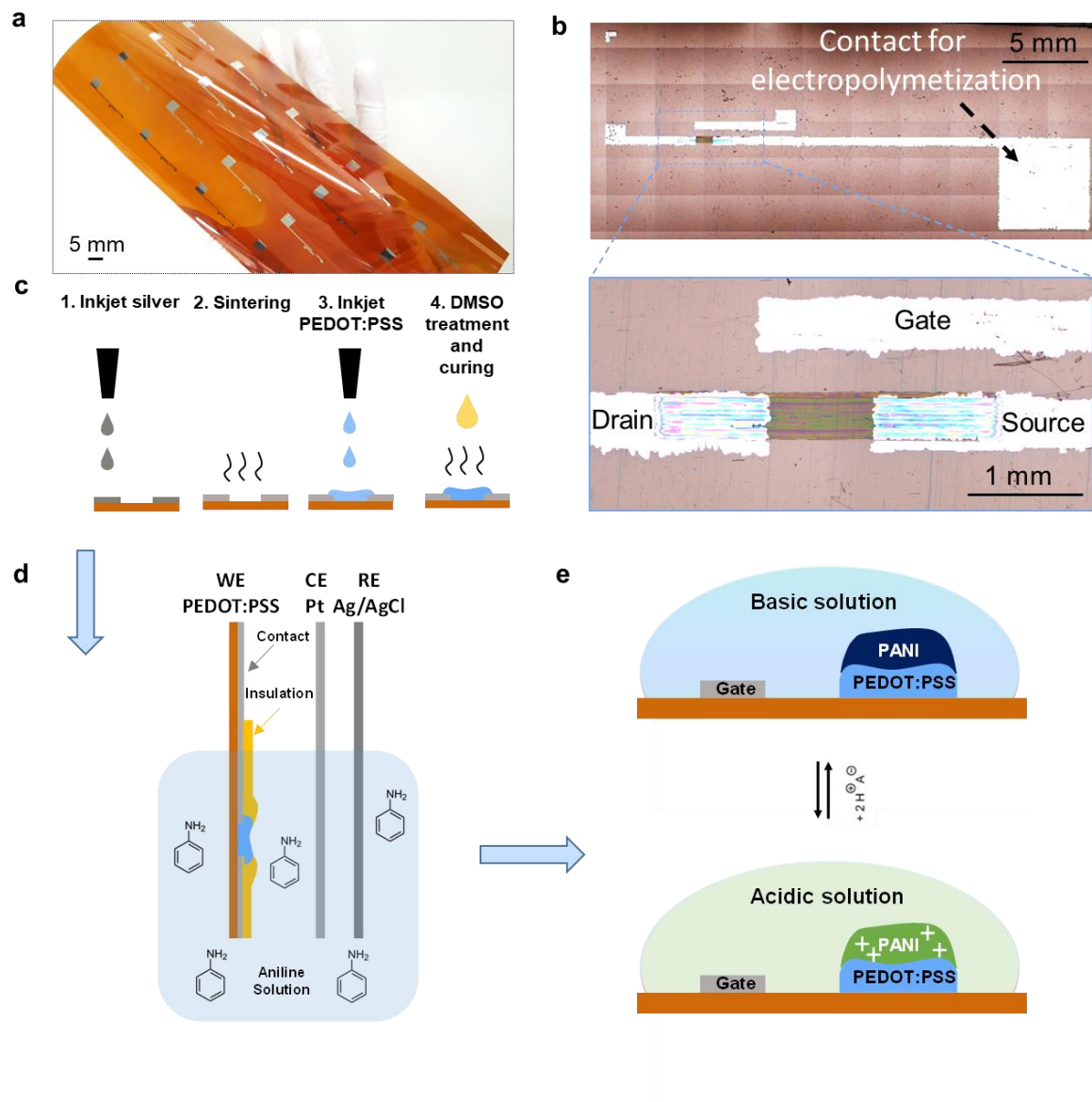


Figure 4-2: Fabrication from digital manufacturing to electropolymerization. (a,b) Optical images of the inkjet-printed organic transistors on the flexible polyimide substrate, (c) schematics of the printing fabrication steps, (d) schematics of the 3-electrode setup used for the aniline electro-deposition, and (e) representation of the pH sensing transistor.

## 4.3 Results and discussion

### 4.3.1 Electropolymerization and morphology of the hybrid PEDOT:PSS-PANI layer

A study analyzing the PANI deposition process with different polymerization cycles equal to 3, 6, and 10 is performed. The OECTs, with only the PEDOT:PSS channel exposed as the working electrode, are electropolymerized in an aniline solution by cyclic voltammetry, as shown in Figure 4-3a. The cycles of electropolymerization from 2 to 10 are reported. It can be seen the oxidation peak around +250 mV, which can be attributed to the conversion from the leucoemeraldine form into the emeraldine form [193]. Also, the current progressively increases with the number of cycles, indicating the growth of the PANI conductive layer on the channel surface. This optimal polymerization is achieved with the PEDOT:PSS layers post-treated with DMSO as working electrodes, while the untreated layers show a less visible growth of material (Figure S4-8). As shown in Figure S4-8b, the untreated layers do not exhibit well-defined peaks in the voltammogram. This behavior is possibly due to the higher resistance of the PEDOT:PSS electrodes without DMSO treatment [192].

Optical images of the electrochemically synthesized layers on the PEDOT:PSS channels are reported in Figure 4-3b, with an increase of the deposited material with the number of cycles. The average heights of the PEDOT:PSS layers were measured with the confocal microscope, and they are equal to  $241 \pm 10$  nm ( $n=2$ ), while after PANI electropolymerization this value increases to  $324 \pm 126$  nm ( $n=4$ ) for 3-cycles electropolymerization,  $423 \pm 61$  nm ( $n=4$ ) for 6-cycles, and  $926 \pm 327$  nm ( $n=3$ ) for 10-cycles (Figure S6-8e). Also, the measured maximum height ( $S_z$ ) is  $473 \pm 72$  nm ( $n=2$ ) for the bare PEDOT:PSS layers,  $1469 \pm 315$  nm ( $n=4$ ) for 3-cycles polymerization,  $2082 \pm 467$  nm ( $n=4$ ) for 6-cycles, and  $4053 \pm 241$  nm ( $n=3$ ) for 10-cycles (Figure 4-3f). The surfaces of the electrodes are analyzed with different microscopy techniques. SEM images without polyaniline (Figure 4-3c) and with polyaniline (Figure 4-3d) demonstrate the formation of a micro-nano structured PANI-layer following electropolymerization. The bare PEDOT:PSS layer shows the presence of nanostructured grains, likely PEDOT crystallites formed during the DMSO post-treatment [170], [194]. Instead, the SEM images of the electropolymerized PANI-layer reveal a porous morphology, with a pores size of about 1  $\mu\text{m}$ . Such a structured film is formed due to the agglomeration of PANI nanowires [194]. Further information on the morphology of the bilayer is obtained through a FIB cross-section (Figure S4-9a,b), where micrometric pores can be seen in the section of the PANI film (Figure S4-9c,d). The formation of the PANI porous microstructures compared to the bare PEDOT:PSS granular structures can be seen also in the SEM and AFM images presented in Figure S4-10.

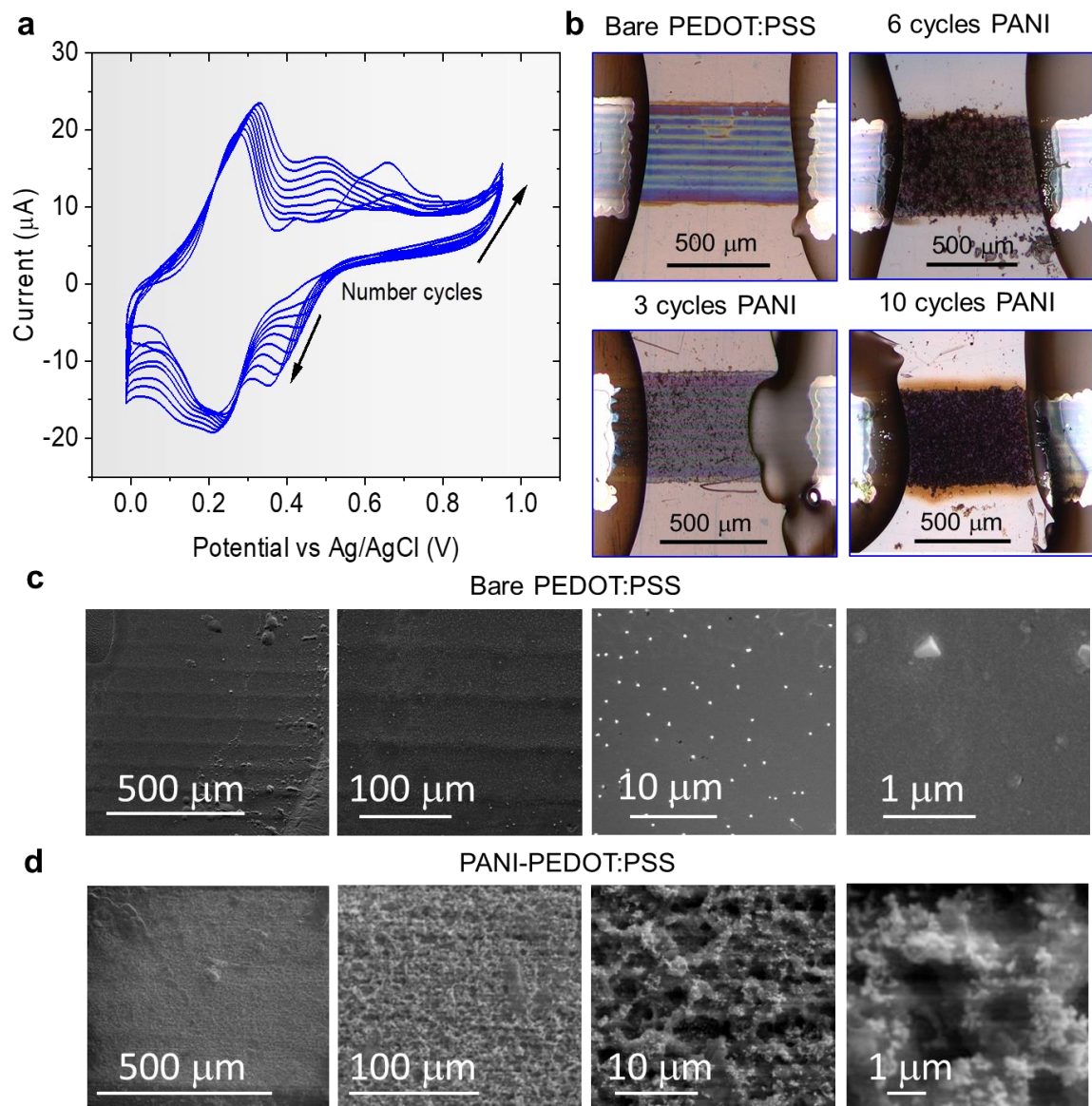


Figure 4-3: Electropolymerization on the PEDOT:PSS layers. (a) Voltammogram of the electrochemical oxidative polymerization of aniline from 2 to 10 cycles, (b) optical images of the PEDOT:PSS-DMSO layers with different polymerized cycles (3, 6, 10), SEM images at different scales without electrodeposited polyaniline in (c) and with polyaniline in (d). The samples in (d) were obtained by 6-cycles electropolymerization.

### 4.3.2 Electrical characterization of the PEDOT:PSS-PANI transistors

The electrical resistance of the conducting polymer channel, equal to  $252 \pm 36$  Ohms ( $n=5$ ) for single PEDOT:PSS layer, increased for the hybrid PANI-PEDOT:PSS layers to  $595 \pm 60$  Ohms ( $n=2$ ) with 3 cycles PANI,  $845 \pm 243$  Ohms ( $n=4$ ) with 6 cycles PANI, and  $1590 \pm 552$  Ohms ( $n=3$ ) with 10 cycles PANI. By using the average dimensions of the layers, the approximate electrical resistivity of the different layers can be extracted. The resistivity of the layers changes from about  $3.04 \pm 0.4$  mOhm·cm without PANI to  $9.64 \pm 0.9$  mOhm·cm with 3 cycles PANI,  $17.9 \pm 5.1$  mOhm·cm with 6 cycles PANI, and  $73.6 \pm 26$  mOhm·cm with 10 cycles PANI. Hence, the hybrid layers show an up to 6X resistivity increase with the higher-PANI content, likely because the PANI layers, when not in acidic solutions, have a very low conductivity of less or equal to  $1 \cdot 10^{-10}$  S/cm [195].

The PEDOT:PSS-PANI transistors with the different number of polymerization cycles are tested electrically in PBS 1X (0.155 M NaCl), with their characteristics shown in Figure 4-4. The transfer curves are acquired with a drain-source voltage at -0.4 V close to the linear regime. As reported in Figure 4-4a, the drain-source current decreases with the number of PANI cycles, particularly for 10-cycles PANI. This effect is possibly due to the increased resistance of the layers. Also, a contribution of this decrease in current may come from the more limited penetration of ions into the PEDOT:PSS layers with the porous PANI interface. This last phenomenon can explain the observed decrease of transconductance, as shown in Figure 4-4b, defined as  $\Delta I_{ds}/\Delta V_{gs}$ , and the fact that even with higher-PANI content (Figure 4-4b and zoom in Figure S4-11a) it is maintained a perfectly bell-shaped transconductance and optimal current modulation (Figure S4-11b) typical of PEDOT:PSS-based OECTs.

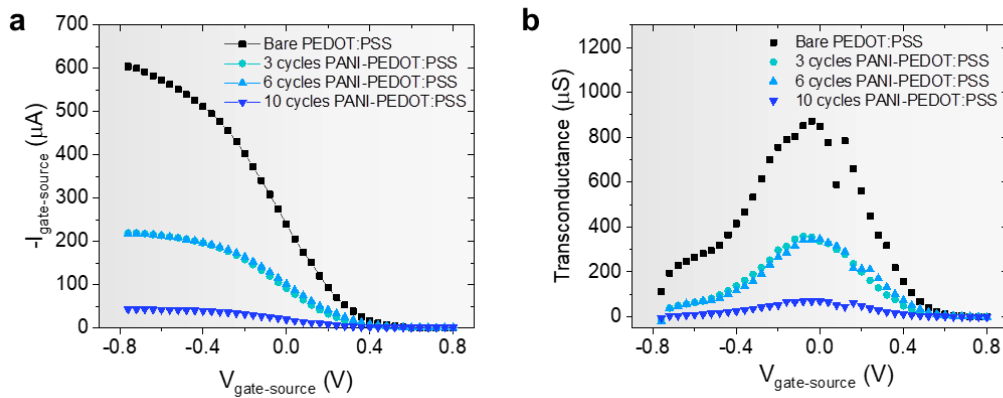


Figure 4-4: Electrical characteristics in PBS 1X with the different electropolymerization cycles. (a) Transfer characteristics and (b) extracted transconductances without PANI and with different PANI-content.  $V_{drain-source} = -0.4$  V in all the transfer curves.

### 4.3.3 Detection of pH variations

We report in Figure 4-5 the effects of pH changes from 10 to 4 on the electrical characteristics of the organic transistors. Such a pH interval includes the pH variations observed in biofluids such as sweat and saliva. The transfer curves ( $V_{\text{drain-source}} = -0.4$  V) show that the hybrid PANI-PEDOT:PSS transistors with the higher-PANI content, notably with 6 and 10 cycles polymerization (Figure 4-5c,d), have very high voltage-shifts, particularly in the positive  $V_{\text{gate-source}}$  range. Within this potential range, the cations ( $\text{H}^+$ ) are injected into the organic channel. On the other hand, for the bare-PEDOT:PSS devices (Figure 4-5a) and the devices with a lower number of PANI-electropolymerization cycles (Figure 4-5b), the curves in the positive  $V_{\text{gate-source}}$  region are very close to each other. This result shows that, at low PANI content, the lower sensitivity observed makes it very difficult to discriminate such pH changes.

For the transistors with the higher number of PANI deposition cycles (6 and 10), the calibration curves are extracted in terms of both the current shift by fixing the voltage in the positive region (at 0.4 V, Figure 4-6a,b), and the voltage shift by fixing the current (correspondent to 0 V at pH 10, Figure 4-6c,d). We found that the sensitivity in terms of voltage shifts is more reproducible than the current shifts. A standard deviation of about 20 % was measured from the average sensitivity in terms of voltage shift, which is reasonable considering the variability of the printing fabrication process and the subsequent electropolymerization step. From the calibration curves, sensitivities of  $102 \pm 22$  mV/pH ( $n=3$ , Figure 4-6a) and  $16 \pm 13$   $\mu\text{A/pH}$  ( $n=3$ , Figure 4-6c) for 6-cycles PANI-devices are calculated, exhibiting very good linearity ( $R^2 \geq 0.98$  in all cases). Hence, 6 cycles of PANI electropolymerization provides a high and linear response within the pH range considered. On the other hand, a different trend was found for the 10-cycles PANI devices, with a higher response of  $226 \pm 50$  mV/pH ( $n=3$ , Figure 4-6b) and  $21 \pm 9$   $\mu\text{A/pH}$  ( $n=3$ , Figure 4-6d) from neutral to low pH values, and the very low response of  $23 \pm 5$  mV/pH and  $5 \pm 1$   $\mu\text{A/pH}$  from neutral to high pH values. Such a different behavior for acidic and basic variations with high-PANI content was previously reported in potentiometric analysis using PEDOT:PSS-PANI indicator electrodes [192]. Herein, the same behavior was observed for a transistor configuration, both in terms of voltage and current variations. The too-high PANI content causes a loss of linearity due to the strong reaction in acidic solutions. Finally, Figure S4-12 shows the transfer curves with 6 and 10 polymerization cycles going from high to low pH (Figure S4-12a,c) and back from low to high pH (Figure S4-12b,d). Going back to pH 10 in Figure S4-12b for 10-cycles PANI and Fig. S5d for 6-cycles PANI, the current decreases close to the initial values (in the positive gate region), proving that the reaction is reversible. For positive gate voltages, the curves are very stable with a low hysteretic effect. Considering the signal at a fixed voltage (0.4 V), we can extract an average current variation between the back and forth pH measurements of less than 8

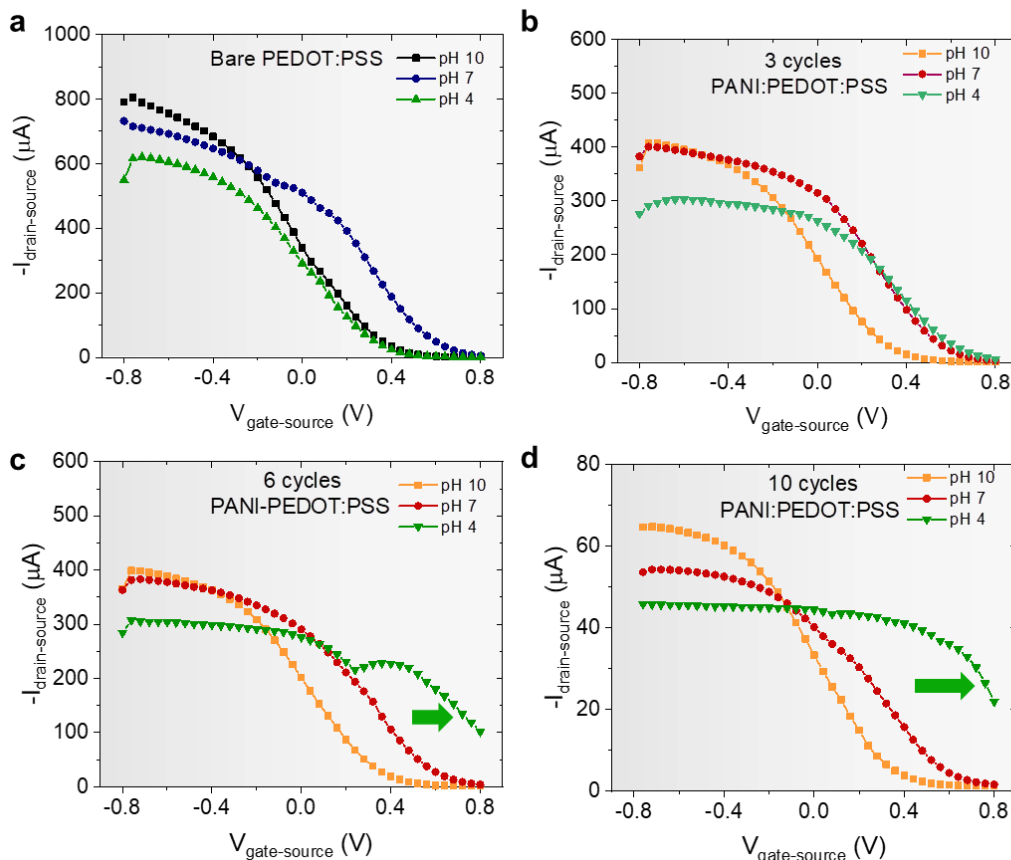


Figure 4-5: pH sensing in the OEETs configuration. Transfer characteristics of the organic transistors: (a) without the PANI layer on the PEDOT:PSS channel, (b) with 3 cycles-PANI, (c) with 6 cycles-PANI, and (d) with 10 cycles-PANI. Tests from pH 10 to pH 4,  $V_{\text{drain-source}} = -0.4$  V in all the cases.

% in the case of PANI-6 cycles and 20 % in the case of PANI-10 cycles. The PANI-PEDOT:PSS devices with 6-cycle polymerization show better stability than the ones with higher PANI-content.

The flexible PANI-PEDOT:PSS devices with high-PANI content show a super-Nernstian sensitivity, so the signal is higher than the theoretical limit obtained from the Nernst equation and equal to 59.2 mV/pH. While it was previously shown in standard 2-electrode potentiometric configurations that PEDOT:PSS devices have sub-Nernstian responses equal to around 10 mV/pH, and PEDOT:PSS-PANI devices have a near-Nernstian behavior equal to around 58 mV/dec [192], our work shows that with the OEETs we have a much higher chemical signal amplification. Compared to the standard potentiometric systems, OEETs can be significantly scaled-down in size and easily integrated into compact arrays onto flexible substrates for multi-parametric analysis. Considering the literature for pH-sensitive and flexible

electrochemical transistors, Table 3 (Supplementary) compares their performances and main characteristics. It has been reported on OECTs with electro-polymerized PANI on a gold-gate electrode (20 cycles), having a sub-Nernstian sensitivity of 44 mV/pH [104]. Another sub-Nernstian response using OECTs with a PEDOT-pH dye gate electrode on a flexible PET substrate was presented, showing a sensitivity of 32 mV/pH [166]. An OECT with a super-Nernstian response of 73 mV/pH was shown employing an IrOx gate [104]. Also, an OECT with an H<sup>+</sup> ion-selective membrane on the PEDOT channel [186] was tested in potentiostatic mode with a sensitivity of about 10 mA/pH. Hence, this work reports on OECTs exhibiting high transduction performances in terms of pH sensitivity for a pH range relevant for biofluids analysis. Finally, considering other devices in the literature, standard potentiometric sensors with a sensitivity up to around 188 mV/dec [196] and with a pH-sensitive charge-coupled device exhibiting a sensitivity of 240 mV/pH [197] were reported. Also, ion-sensitive OECTs with a sensitivity as high as 516 mV/dec [72] were shown. This can be attributed to changes in the Ag/AgCl or Ag pseudo-reference electrodes due to anions [196] or the amplification effects of the transistors or other transducers themselves [72] compared to standard potentiometric detection methods.

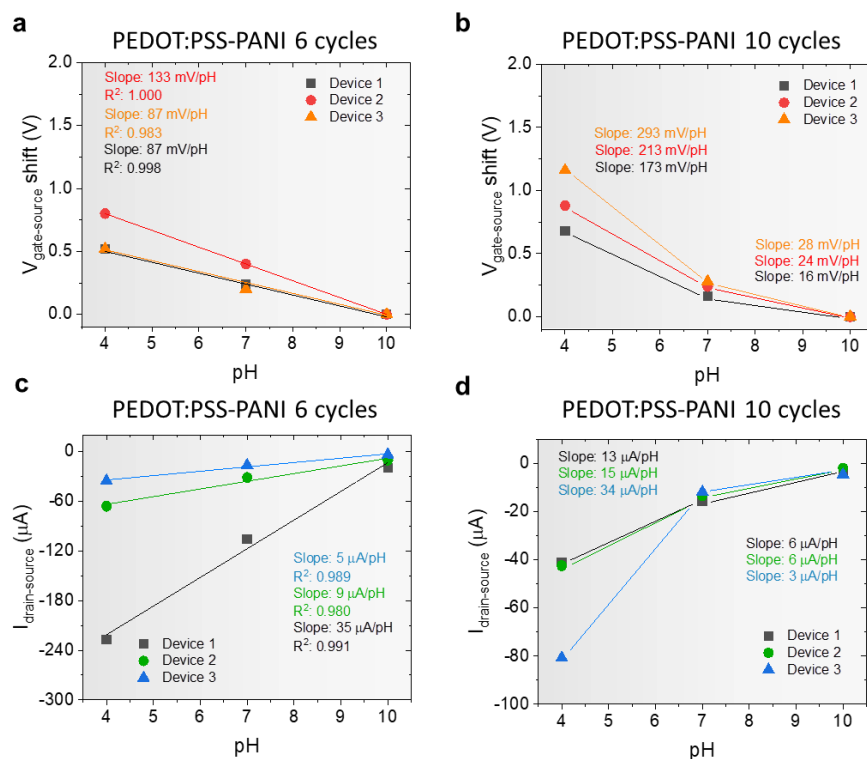


Figure 4-6: Calibration curves of the hybrid OECTs. Calibration curves with 6 cycles of PANI (a,c) and 10 cycles of PANI (b,d). The curves represent the voltage shifts in (a,b) and the current shifts in (c,d). Tests performed going from pH 10 to pH 4,  $V_{\text{drain-source}} = -0.4$  V in all the cases.



#### 4.3.4 Analysis of the sensing mechanism

To bring further insights on the interfacial change with the bare PEDOT:PSS and the hybrid PANI-PEDOT:PSS layers, an electrochemical impedance spectroscopy (EIS) analysis was performed at different pH concentrations. The interface between the charged electrode and the liquid is represented by an electrical double layer (EDL). Since ions and dipole molecules at these interfaces can change the electric field, this separation of electric charges can be modeled with capacitors [198]. Schematics modeling the EDL as a single parallel plate capacitor following the simplified Helmholtz model are very used to qualitatively explain the sensing behavior of OECTs [181].

From the EIS tests, the interfacial capacitances at low frequency were extracted. This was done using the inverse of the slope of the reactance versus the angular frequency, as presented in Figure 4-7a,b where the typical behavior of the devices is reported. The capacitance values for the bare PEDOT:PSS layers were found to be  $9.8 \pm 0.3 \mu\text{F}$  at pH 10,  $11 \pm 0.6 \mu\text{F}$  at pH 7, and  $13 \pm 1 \mu\text{F}$  at pH 4 ( $n=2$  with all the solutions). On the other hand, the extracted capacitances for the PANI-PEDOT:PSS layers with 6-cycles polymerization were higher at  $22 \pm 9 \mu\text{F}$  at pH 10,  $32 \pm 8 \mu\text{F}$  at pH 7, and  $50 \pm 5 \mu\text{F}$  at pH 4 ( $n=2$  with all the solutions), hence finding a  $28 \mu\text{F}$  increase from high to low pH compared to only a  $3.2 \mu\text{F}$  change without the PANI layer (9X lower). This phenomenon is due to the fact that going to higher levels of  $\text{H}^+$  concentration, in particular with PANI on the channel, there is a rise of interfacial charge from the  $\text{H}^+$  doping that increases the capacitance [199]. Also, the porosity of the PANI layer can contribute to the accumulation of ions at the interface, enhancing the capacitive coupling effect. This behavior of a higher increase of capacitance for the PANI-PEDOT:PSS, when increasing the acidity, was observed systematically in our experiments. Considering these capacitance changes, a simplified analysis of the potential distribution between the gate-electrolyte and electrolyte-channel interfaces is proposed in Figure 4-7c. When the capacitance at the electrolyte-channel interface increases, the voltage drop at the electrolyte-channel interface decreases [67]. Hence, there is a shift of the transfer curves towards higher gate voltages because the gate electrode is less effective in controlling the channel. As a result, the organic channel requires a higher gate voltage to obtain the same dedoping [110].



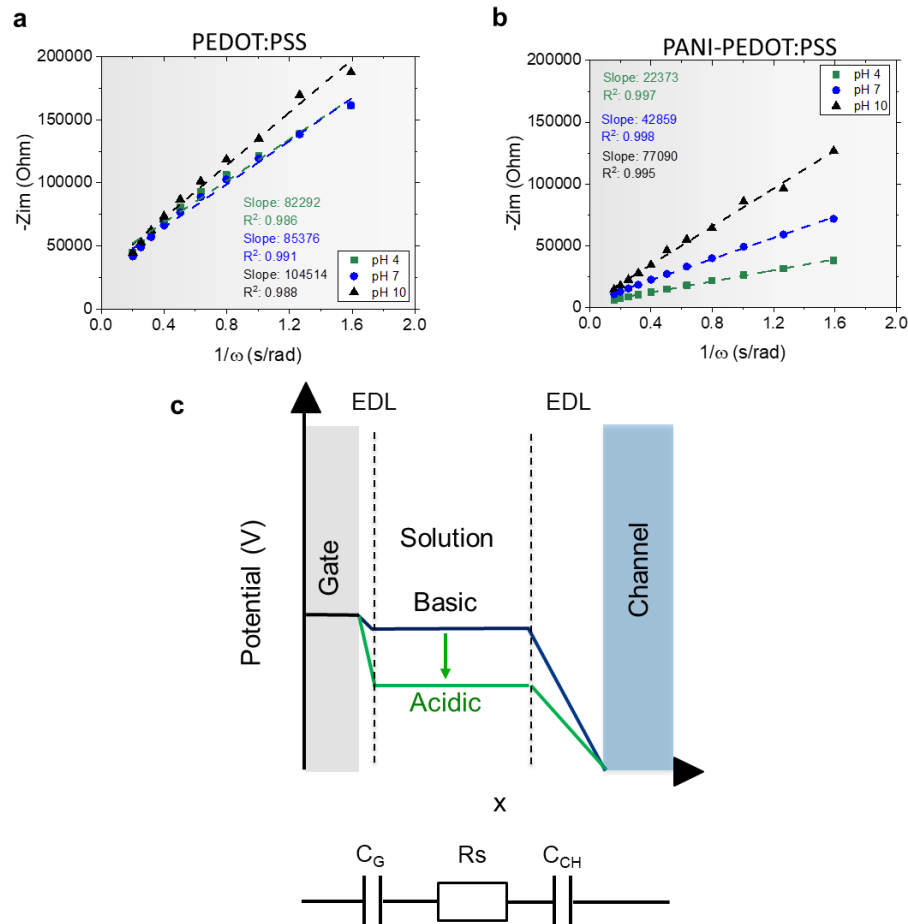


Figure 4-7: Analysis of the sensing mechanism through EIS. EIS analysis including (a) the reactance versus the angular frequency for a PEDOT:PSS-only layer, (b) the reactance versus the angular frequency for a 6-cycles PANI-PEDOT:PSS layer, and (c) a sketch with the simplified electrical circuit and possible sensing mechanism in terms of voltage drops at the two electric double layer (EDL) interfaces.

## 4.4 Conclusions

We have demonstrated for the first time hybrid PANI-PEDOT:PSS organic electrochemical transistors on a polymeric substrate that exhibit improved electrical performances and response to pH variations. The hybrid devices were inkjet printed with a PEDOT:PSS channel integrating an electropolymerized PANI layer on top. 6-cycles of PANI electrodeposition was found to be optimal to achieve a linear sensing response from 10 to 4 pH with a sensitivity equal to  $102 \pm 22$  mV/pH (up to 2X the Nernst limit), extracted from the transfer characteristics of the transistors.

We have also shown that the change of interfacial capacitance when decreasing the pH is 9X higher with the hybrid PANI-PEDOT:PSS layer in comparison to using a single PEDOT-PSS layer, causing a change of potential distribution across the gate-electrolyte and electrolyte-channel interfaces. A complete understanding of the behavior of the hybrid PANI-PEDOT:PSS channel at different pH would require more accurate modeling, notably through the use of 2D drift-diffusion equations and ionic and electronic charge-distribution equations.

Thanks to the simple fabrication process and the high pH-sensing performances, the developed flexible OECTs with hybrid organic channels are promising for being integrated into scalable, low-cost, multi-sensing platforms for wearable applications. To overcome the possible cations interference for real-sensing applications, the next step is to combine the pH sensor with ion-selective OECTs into an array, considering differential measurements and investigating chemometric approaches for the discrimination of the different analytes.

## 4.5 Supporting Information of Chapter 4

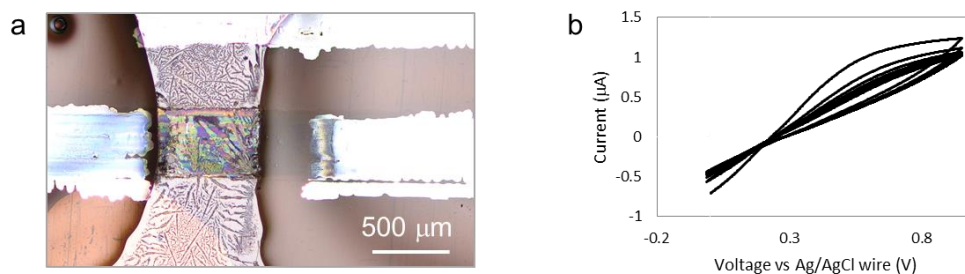


Figure S4-8: Electropolymerization. (a) Optical image with the PEDOT:PSS layer after 10 cycles of polymerization without DMSO treatment, and (b) voltammogram of the polymerization of aniline from 2 to 10 cycles using the PEDOT:PSS channel without DMSO treatment.

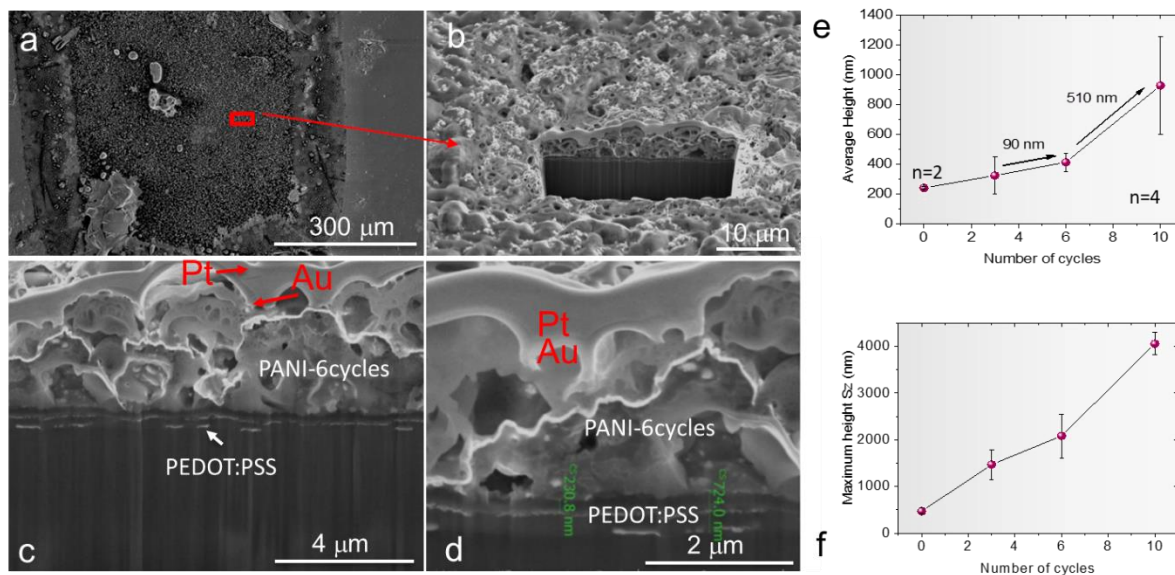


Figure S4-9: Morphological analysis with FIB and confocal microscopes. (a,b) FIB cross-section of a PANI-PEDOT:PSS layer, and (c,d) zoom of the cross-section. (e,f) Analysis of different morphology parameters obtained with the confocal microscope. The measured values in (e,f) include the thickness of the PEDOT:PSS layers.

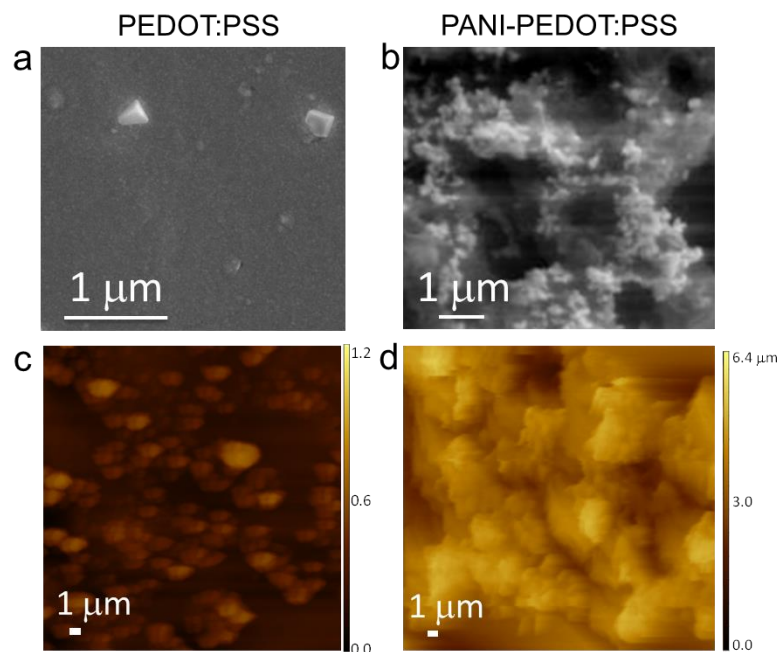


Figure S4-10: Morphological analysis with SEM and AFM. SEM images without PANI in (a) and with PANI in (b), and AFM images without PANI in (c) and with PANI in (d).

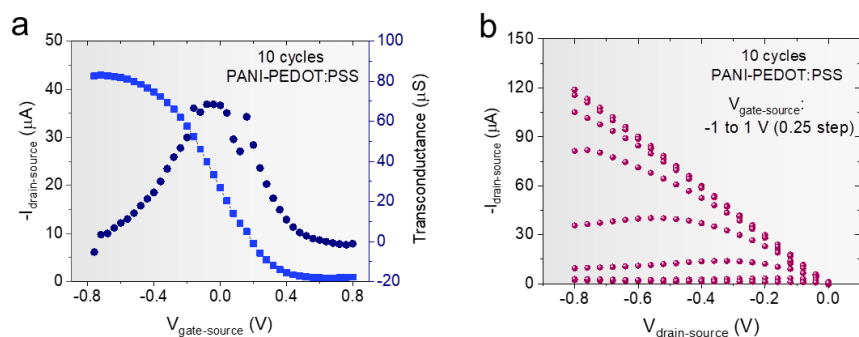


Figure S4-11: Electrical characteristics with high-PANI content. Transfer curve (a) and output curve (b) with 10-cycles of PANI on the PEDOT:PSS channel.  $V_{\text{drain-source}} = -0.4$  V in (a).

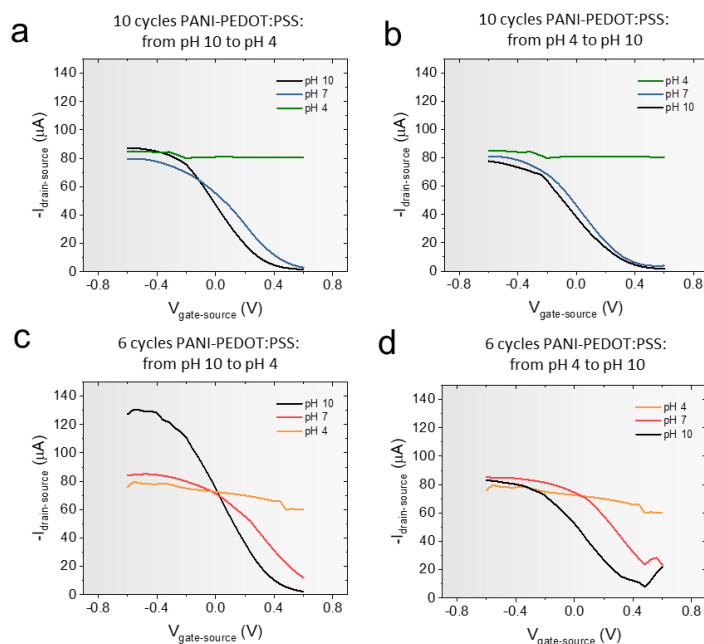


Figure S4-12. Reversibility study. Transfer curves of the hybrid OEETs with 10 cycles of PANI (a,b) and 6 cycles of PANI (c,d). The testing was performed from high to low pH in (a,c) and back from low to high pH in (b,d).  $V_{\text{drain-source}} = -0.4$  V in all the cases.

Table 3: Literature comparison for pH-sensitive organic electrochemical transistors (OEETs) on flexible substrates. The table compares the fabrication method, the gate and channel materials, the sensitivity in terms of current and voltage, and the pH-range tested for different pH-sensitive transistors reported in the literature. ISM stands for Ion-Selective Membrane.

Process and substrate	Gate/Channel Materials	Sensitivity ( $\mu\text{A}\cdot\text{pH}^{-1}$ )	Sensitivity ( $\text{mV}\cdot\text{pH}^{-1}$ )	pH range	Ref.
Lithography, screen printing, electrodeposition, PEN substrate	PANI gate/ PEDOT:PSS channel	5.25	44	5-6.7	[104]
Lithography, screen printing, electrodeposition, PEN substrate	IrOx gate/ PEDOT:PSS channel	9.5	73	5-7.3	[104]
Lithography, Electrodeposition, PET substrate	PEDOT+pH dyes gate/ PEDOT:PSS channel	---	32	5.7-7	[166]
Inkjet-printing, drop-cast, PI substrate	Silver gate/ PEDOT:PSS+ISM channel	11	---	4-7	[186] – My work in Chapter 3
Inkjet-printing, Electrodeposition, PI substrate	Silver gate/ PEDOT:PSS-PANI channel	16	102	4-10	This work

# Chapter 5 Inkjet-printed graphene-gated OECT for enzymatic-based sensing (Paper III)

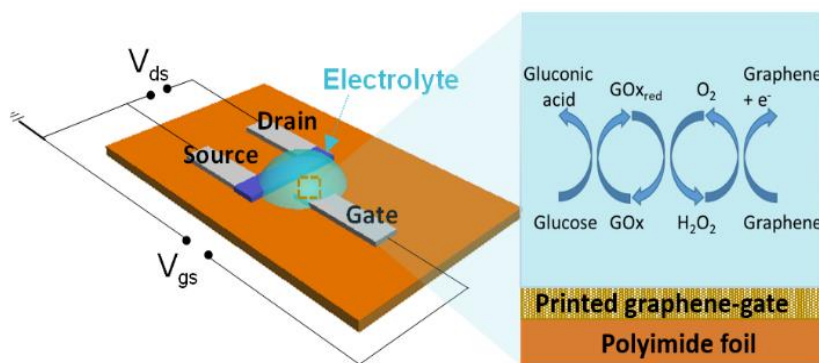


Figure 5-1: Graphical abstract. Organic electrochemical transistors with printed graphene gates for enzymatic-based sensing.

We demonstrate fully inkjet-printed graphene-gated Organic Electrochemical Transistors (OECTs) on polymeric foil for the enzymatic-based biosensing of glucose. The graphene-gated transistors exhibit better linearity, repeatability, and sensitivity than printed silver-gated devices studied in this work and other types of printed devices previously reported in the literature. Their limit of detection is 100 nM with a normalized sensitivity of 20 %/dec in the linear range of 30 to 5000  $\mu\text{M}$  glucose concentrations, hence comparable with state-of-the-art OECT devices made by lithography processes on rigid substrates and with complex multi-layer gates. Electrochemical impedance spectroscopy analysis shows that the improved sensitivity of the graphene-gated devices is related to a significant decrease of the charge-transfer resistance at the graphene electrode-electrolyte interface in the presence of glucose. The optimized sensing method and device configuration are also extended to the detection of the metabolite lactate. This study enables the development of fully-printed high-performance enzymatic OECTs with graphene sensing-gates for multi-metabolites sensing.

## 5.1 Introduction

Innovative electrochemical sensing configurations, electrode-bioreceptor interfaces, and functional materials are currently being studied to develop high-performance biosensors for point-of-care and continuous health monitoring.[2], [149], [166], [200]–[202] Some of the main requirements for the next generation of biosensors include mechanical flexibility for wearable non-invasive applications,[27], [203], [204] digital manufacturing for low-cost disposable devices,[203], [205] enhanced sensitivity, selectivity, short response time in the detection,[46], [202] and facile miniaturization and configurability to realize integrated multi-sensing platforms.[206] Of particular interest is the possibility of non-invasive detection of metabolites in body fluids such as interstitial fluid (ISF), sweat, saliva, and tears.[82], [137], [201], [203], [207]–[209] Recent studies show the correlation between glucose and lactate metabolites in most of the aforementioned body fluids and blood, with some limitations for sweat glucose.[139] This is enabling the development of non-invasive glucose sensors for diabetes management,[8], [24], [139], [201], [209] or non-invasive lactate sensors for anaerobic threshold monitoring and general sport intensity.[25], [201] In the case of sweat and saliva, glucose is present in the  $\mu\text{M}$  range (from 20's to 200's  $\mu\text{M}$ ),[27], [210] hence about 1% of the concentration found in blood plasma,[209], [210] while its concentration in interstitial fluids is similar to the one in blood.[209] Instead, the concentration of lactate is similar to the concentration observed in blood for all these biofluids and equal to 1's-10's mM.[25], [27], [209]

Highly selective enzymes such as glucose oxidase (GOx) and lactate oxidase (LOx) are conventionally used for the electrochemical detection of glucose and lactate, respectively,[201], [210] with the possible use of artificial mediators for improving the electron transfer rate.[90], [203], [211] The enzymes are often immobilized on the working electrode of an amperometric three-electrode system.[13], [201], [212] However, the linear detection range of standard amperometric devices is generally between hundreds of  $\mu\text{M}$ -1 mM to several mM,[13], [212], [213] making glucose detection in some biofluids, such as sweat and saliva, difficult to be achieved. Moreover, the compact integration and fully-printing of standard amperometric cells on flexible substrates is not straightforward.[104], [152], [207]

Organic electrochemical transistors (OECTs)[55], [56], [72], [127] are an interesting alternative to conventional amperometric sensors, overcoming some of their limitations. OECTs are three-terminal devices, with the source and drain electrodes connected by a conjugated polymer-polyelectrolyte channel such as the commonly used poly(3,4-ethylenedioxythiophene):polystyrene sulfonate (PEDOT:PSS). Thanks to the mixed ionic-electronic properties and the mechanical flexibility of PEDOT:PSS, OECTs allow high chemical signal amplification and better mechanical matching of the device with soft

interfaces, such as the human skin, for non-invasive analysis.[20], [57], [62], [155] Also, because digital manufacturing techniques, such as inkjet printing, can be applied for their fabrication, OECTs are promising candidates for the development of low-cost and multi-sensing biochemical platforms on flexible substrates, such as polymeric foil.[126], [186]

OECT-based devices have already proved their accuracy in the detection of multiple analytes such as ions,[78], [186], [214] hormones,[20] proteins,[92] and metabolites.[83] With the use of a specific enzyme, only the desired metabolite will undergo a chemical reaction that leads to a shift of gate voltage, and subsequently a change in the de-doping state of the PEDOT:PSS layer in the OECTs.[4], [81], [89], [121] Organic electrochemical transistors for enzymatic sensing have been mostly reported for devices lithography-processed on rigid glass substrates, implementing platinum-[79], [82], [121] or PEDOT:PSS[83], [90]-based sensing gates. These gates often include nanomaterials such as platinum nanoparticles (Pt-NPs) composites[79], [82], [88] and Pt/multi-wall carbon nanotubes (MWCNTs) composites[79] to enhance the sensitivity and lower the limit of detection for the enzymatic sensing of metabolites. Graphene, a single layer of graphite, is an attractive sensing material in OECTs as it has been shown to enhance the enzyme grafting process and the electrocatalytic activity towards uric acid, cholesterol, and glucose.[81] Precisely, it was used for a multi-layered gate electrode composed of enzymes/graphene oxide/polyaniline/Nafion-graphene/Pt. However, the fabrication involved sputtering of Pt, drop-cast of a Nafion-graphene aqueous solution, and then drop-cast of a polyaniline solution, hence involving a relatively complex and non-sustainable process. More recently, an OECT with source, drain, and gate electrodes made by carbon black and deposited by doctor blade has been reported,[122] but the device shows lower sensing performances compared to the state-of-the-art.

Herein, we report a completely inkjet-printed OECT device for enzymatic sensing integrating a fully-graphene gate electrode, made by printing a defect-free, highly concentrated, biocompatible, and water-based graphene ink.[215], [216] The active channel and the electrical terminals of the devices are made of inkjet-printed PEDOT:PSS and silver ink, respectively. Such graphene-gated OECTs show superior sensing performance for glucose detection in an enzymatic solution, compared to the same device made by printed silver gates, and comparable performance to clean room-processed OECTs, which implemented complex nanomaterial composites on the gate electrode. Electrochemical impedance spectroscopy is used to get insights into the sensing mechanism: we show that the response of the sensor is dominated by a strong decrease of the charge-transfer resistance at the graphene electrode-electrolyte interface in the presence of the analyte to be detected. The fully printed graphene-gated OECTs demonstrate high sensitivity and linearity for the detection of glucose and lactate in the respective physiological ranges.



## 5.2 Experimental section

### 5.2.1 Functional inks

The fully-inkjet-printed organic transistors are shown in Figure 5-2. A silver nanoparticle-ink (Sicrys I30EG-1, PV Nano Cell) is employed for the source and drain electrical contacts, and a PEDOT:PSS ink for the conductive channel. The PEDOT:PSS ink is made by mixing a commercially available aqueous dispersion (PEDOT:PSS 1 S/cm, 1.3 wt % dispersion in H<sub>2</sub>O, from Sigma Aldrich) with 5 vol% of dimethyl sulfoxide (DMSO, from Sigma Aldrich). The latter is added to improve the printability and the electrical conductivity of the organic layers.[130] As shown in Figure 5-2b, the gate electrode was either made with the graphene ink for the active area using the silver ink for its connection (graphene gate) or fully made with the silver ink for comparison (silver gate). The latter devices, made of printed silver gates, were used as reference since silver-based gates provide efficient voltage modulation[72] and silver ink is the most established conductive ink on the printed electronics market[217]. In the graphene gate configuration, the silver used for the gate electrical contact is not touching the electrolyte.

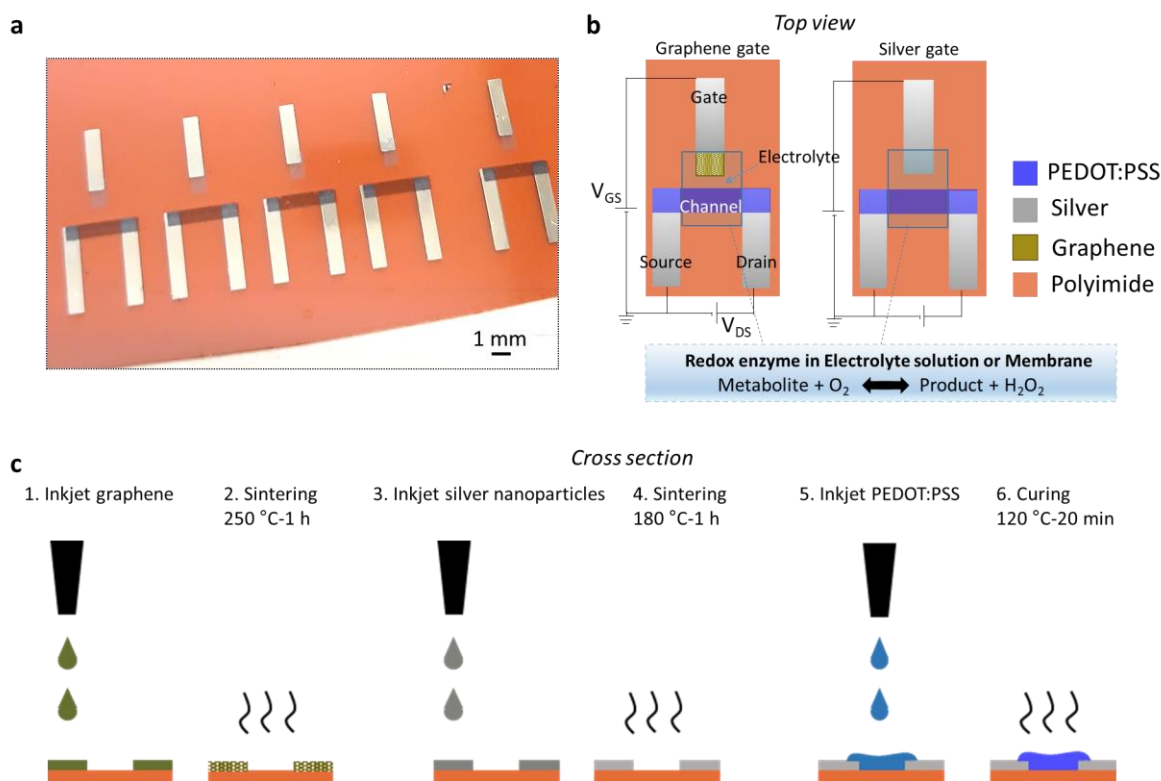
The preparation of inkjet printable graphene and its characterization (e.g. lateral size and thickness distribution of the flakes) has been previously reported.[215], [216] Briefly, the graphene ink is formulated from graphite via ultrasonic-assisted liquid phase exfoliation in water using 1-pyrenesulfonic acid sodium salt (PS1). After removing the un-exfoliated graphite and excess PS1 by centrifugation, the exfoliated graphene was re-dispersed in a water-based printable solvent. The final concentration of printable graphene ink was adjusted to ~2 mg/mL. This graphene formulation is engineered to produce defect-free, inkjet-printable, highly stable (for several months), not-cytotoxic, and concentrated graphene inks.[215]

### 5.2.2 Inkjet printing of the organic electrochemical transistors

The devices are inkjet-printed with a Dimatix DMP-2800 printer (Fujifilm) on a flexible 125  $\mu\text{m}$ -thick polyimide substrate. Before printing, the silver and graphene inks are sonicated for 5 min and the PEDOT:PSS ink (with DMSO added) for 10 min. The silver and PEDOT:PSS inks are filtered with a 1  $\mu\text{m}$  pore-size filter when filling the Dimatix cartridges (10-pL cartridges DMC-11610). The polyimide substrate is treated with oxygen plasma before printing. The Dimatix plate is kept at 40  $^{\circ}\text{C}$  during the printing. For the graphene-gated OECTs, the full fabrication steps are represented in Figure 5-2c and include (1) printing of ten layers of graphene ink (drop-spacing 40  $\mu\text{m}$ , voltage ~20 V, jetting frequency 5 kHz, no cartridge heating), (2) sintering at 250  $^{\circ}\text{C}$  for 1 h, (3) printing of two layers of silver ink for the electrical contacts (drop-spacing 30  $\mu\text{m}$ , voltage ~20 V, jetting frequency 5 kHz, cartridge temperature 35

°C), (4) sintering at 180 °C for 1 h, (5) printing of two layers of PEDOT:PSS ink for the channel (drop-spacing 20  $\mu\text{m}$ , voltage  $\sim 20$  V, jetting frequency 5 kHz, cartridge temperature 30 °C), and (6) curing at 120 °C for 20 min. All the sintering steps were performed in a ventilated oven. For the silver-gated OEETs, the fabrication steps are the same from 3 to 6, using the silver ink also for the active gate area. The design dimensions include a gate active area of about 1 x 1  $\text{mm}^2$  and a channel area of 1 x 3  $\text{mm}^2$ . This design is based on a work we previously reported on OEETs with silver gates applied to multiple ions detection.[186] The gate-channel gap is about 1 mm. The graphene-gated devices have a printed graphene layer of about 1 x 2  $\text{mm}^2$ , including a 1  $\text{mm}^2$  overlap with the silver contact and a 1  $\text{mm}^2$  active area.

The thicknesses of printed layers are measured with a Keyence VK-X1000 Series laser scanning microscope, with 50X magnification for the printed layers and 10X for the enzymatic membrane; we found an average thickness of  $\sim 50$  nm for the graphene electrodes,  $\sim 1$   $\mu\text{m}$  for the PEDOT:PSS channels, and  $\sim 200$  nm for the silver electrodes.



*Figure 5-2: Design, working principle, and fabrication of the devices. (a) Optical image of the OEETs with graphene gates, (b) top-view schematics of a graphene-gated OEET and a silver-gated OEET showing the materials and the simplified enzymatic reaction, and the bias applied during testing, and (c) cross-section with the fabrication steps.*

### 5.2.3 Enzymatic solutions

The OECTs are tested in electrolyte solutions. The enzyme is dissolved in the electrolyte solution or immobilized in a membrane around the gate electrode. Depending on the enzyme used, the targeted metabolite is converted into a different molecule defined as the product, consuming oxygen and producing hydrogen peroxide ( $\text{H}_2\text{O}_2$ ), as shown in Figure 5-2b. For the tests with the enzyme dissolved in solution for glucose detection, the enzymatic solution is freshly made before each experiment by carefully dissolving 10 mg of glucose oxidase (GOx) from *Aspergillus niger* (100,000-250,000 units/g, Sigma Aldrich) in 1 mL of a Phosphate Buffer Saline (PBS) solution. For lactate detection, lactate oxidase (LOx) from *Aerococcus Viridans* (100U, Sigma Aldrich) was dissolved in PBS to a concentration of 10 mg/mL and stored in aliquots before use. The PBS solution used is made of 1 mM monopotassium phosphate ( $\text{KH}_2\text{PO}_4$ , Merck), 155 mM NaCl (Sigma Aldrich), and 2.966 mM disodium phosphate ( $\text{Na}_2\text{HPO}_4$ , Merck). The ferrocene solution is made with 10 mM ferrocene (Sigma Aldrich) in ethanol as previously reported.[90]

### 5.2.4 Membrane preparation

For the tests with the immobilized GOx membrane around the gate, GOx, ferrocene, albumin from bovine serum (BSA, Sigma Aldrich), and glutaraldehyde (Sigma Aldrich) are employed. 10 mg of GOx are dissolved in 120  $\mu\text{L}$  of PBS, and subsequently, 5  $\mu\text{L}$  of ferrocene solution are added. The BSA solution is made by dissolving 80 mg of BSA in 1 mL of PBS, being always freshly made before the experiments. The solution of glutaraldehyde (25 %, Sigma Aldrich) is diluted to 2.5 % in DI water. Then, 50  $\mu\text{L}$  of the GOx solution is mixed with 250  $\mu\text{L}$  of the BSA solution, and 100  $\mu\text{L}$  of glutaraldehyde 2.5 % is added to the previous mixture while carefully stirring, as described in previous methods.[218] About 3  $\mu\text{L}$  of the prepared mixture was pipetted around each gate electrode of the OECTs and left for cross-linking for at least 1 hour at room temperature. The average thickness of the membrane is  $\sim 2 \mu\text{m}$ .

### 5.2.5 Sensing protocol

To confine the electrolyte solutions, a PMMA reservoir is fixed on the OECT's surface defining a gate and channel active area of  $3 \times 4 \text{ mm}^2$ . Glucose and lactate stock solutions are made by dissolving glucose (D-(+)-glucose, Sigma Aldrich) and lactate (sodium L-lactate, Sigma Aldrich) in PBS at different concentrations (3  $\mu\text{M}$ , 1 mM, and 10 mM) and stored in the refrigerator. 30  $\mu\text{L}$  of the enzymatic solution (GOx or LOx) in PBS is first added to the reservoirs, then different volumes of the glucose or lactate stock

solutions are pipetted to have the sensing in time at the different concentrations. Instead, in the tests with the ferrocene mediator, 29  $\mu\text{L}$  of the enzymatic solution and 1  $\mu\text{L}$  of the ferrocene solution are added first to the reservoirs. The latter 29:1 ratio was chosen to have high stability during current recordings since bigger volumes of ferrocene solution caused a higher drift possibly due to ethanol evaporation. In the tests with the GOx membrane, a starting solution of 30  $\mu\text{L}$  PBS, without the enzyme dissolved, is used. For the test with hydrogen peroxide,  $\text{H}_2\text{O}_2$  (30 % w/w in  $\text{H}_2\text{O}$ , Sigma Aldrich) was diluted in PBS at different concentrations (1 mM and 10 mM). Also in the latter case, 30  $\mu\text{L}$  of PBS solution is first added to the reservoirs, then different volumes of the hydrogen peroxide solutions are pipetted to have the sensing in time at the different concentrations.

## 5.2.6 Characterization and testing

The PMMA reservoirs are made by  $\text{CO}_2$  laser (Speedy 300, Trotec) cut of 3 mm-thick PMMA plates with a double-sided silicone adhesive (ARclear 8932EE) laminated on one side. The reservoirs are attached to the sensors removing the plastic cover of the silicone adhesive. The source, drain, and gate silver contacts are insulated using a varnish to avoid possible contact with the testing solutions. The sheet resistance of the graphene electrodes is calculated from graphene resistors made with silver contact electrodes. The OECTs electrical characteristics are acquired with a semiconductor parameter analyzer (Agilent 4155A). For the sensing in time, the  $V_{\text{DS}}$  voltage is fixed to -0.4 V for both the silver and graphene-gated devices, and the  $V_{\text{GS}}$  voltage to 0.1 V for the silver and 1 V for the graphene-gated devices. The latter voltage was chosen to be close to the high-modulation region of the transistor without having water electrolysis. Higher voltages for the silver-gated devices were causing electrode oxidation and unstable sensing behavior. The normalized sensing response is extracted as the absolute value of  $\frac{I_0 - I_{\text{glucose}}}{I_0}$ , with  $I_0$  being the drain current with only the enzyme or enzyme/ferrocene in the solution, and  $I_{\text{glucose}}$  the current obtained upon the addition of a given concentration of the analyte. All the signals are taken after stabilizing the  $I_{\text{ds}}$  current a few minutes after the injections of the different solutions. The Electrochemical Impedance Spectroscopy (EIS) and the cyclic voltammetry (CV) measurements are obtained using a potentiostat/galvanostat (Multi Autolab M204, Metrohm) and employing the graphene-gate or the silver-gate as the working electrodes, and a silver/silver chloride (Ag/AgCl) wire as the reference electrode. The frequency was swept from  $10^5$  Hz to 0.1 Hz at 10 mV of amplitude. In the case of silver, the polarization voltage chosen is equal to 0 V since higher potentials were causing noticeable oxidation. In the case of graphene, a polarization voltage close to the one applied in the transistor configuration is used ( $V_{\text{dc}} = 1$  V). Raman measurements were performed using a Raman spectrometer

(Monovista CRS+, S&I GmbH) equipped with a 514.5 nm laser with 10 mW and 100 mW laser power. The measured graphene samples were printed on a silicon substrate to reduce the background in Raman spectra. The samples measured after H<sub>2</sub>O<sub>2</sub> testing were immersed for 5 minutes in a 1 mM H<sub>2</sub>O<sub>2</sub> solution and then washed with DI water.

## 5.3 Results and discussion

### 5.3.1 Electrical characterization of the OECTs

The silver and graphene-gated OECTs electrical characteristics are analyzed in a PBS 1X solution, of similar ionic content as in biofluids. Figure 5-3a,c shows the output characteristics, and Figure 5-3b,d the transfer characteristics, for both the silver and the graphene-gated devices. The output characteristics of OECTs show a different behavior, with optimal drain currents modulation for the silver-gated OECT, whereas a slight drain current decrease is observed for the graphene-gated ones. From the transfer characteristics, the transconductance  $g_m$  defined as  $\Delta I_{DS}/\Delta V_{GS}$  can be extracted. The transconductance is of extreme relevance in OECTs targeting biosensing applications. The voltage at which the maximum peak appears is generally selected when operating in the detection mode for obtaining the maximum sensitivity.[83], [167], [189] The silver-gated devices show a maximum  $g_m$  of around 1 mS at 0 V while the graphene-gated devices show a continuous increase of  $g_m$  for gate voltages  $>0.8$  V. For graphene-gated devices,  $g_m$  equals  $\sim 50$   $\mu$ S at 1 V. The silver-gated and Ag/AgCl-gated devices described in the literature always show a  $g_m$  peak close to 0 V for a drain-source bias around -0.4 V.[126], [186] The higher voltage modulation of the graphene-gated devices is typical of carbon-based gates, as reported previously for a screen-printed carbon-gated OECT with a  $g_m$  peak at about 1.6 V for a drain-source bias of -0.4 V,[65] and a screen-printed carbon black-gate OECT with a maximum  $g_m$  at 0.7 V and a higher drain-source bias of -0.8 V.[73] Here, the extracted sheet resistance of the patterns with the graphene ink is  $26 \pm 4$  kOhm/sq ( $n=10$  devices), corresponding to what was previously reported for the same material,[215] and with the silver ink is  $3.0 \pm 0.4$  Ohm/sq ( $n=10$  devices). Considering the measured thickness of the patterns, the graphene electrodes have a resistivity of about three orders of magnitude higher than the silver ink-based electrodes. The more resistive nature of the graphene-gated devices compared to the silver-gated ones is the reason for the current modulation at much higher voltages and the difficult switching-off of the devices. Due to this, the gate voltage is fixed at 1 V for the graphene-gated devices and at 0.1 V for the silver-gated ones during the next enzymatic sensing experiments.

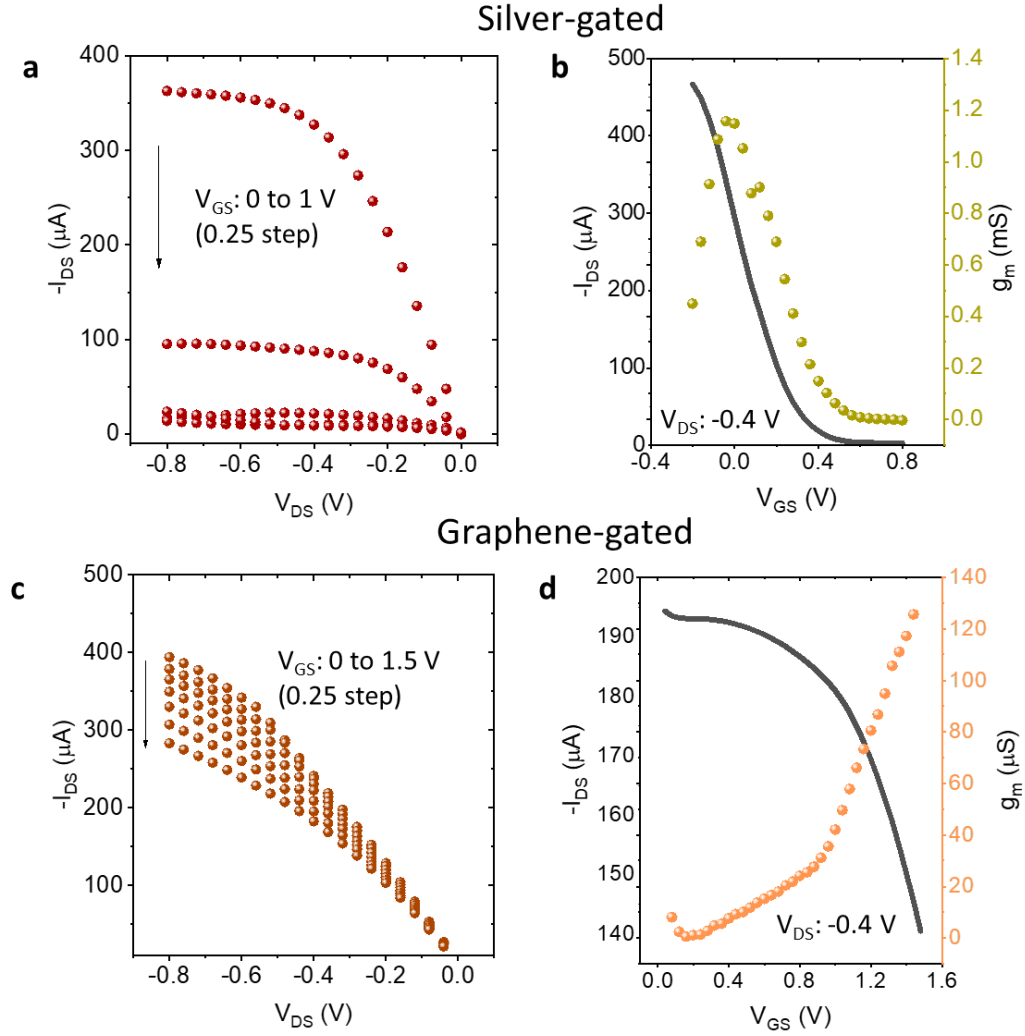


Figure 5-3: Electrical characteristics. Output (a) and (b) transfer characteristics of a silver-gated OEET, and output (c) and transfer (d) of a graphene-gated OEET. Tests in PBS 1X, pH 7.

### 5.3.2 Real-time sensing with the OEETs

The response of the inkjet-printed OEETs is analyzed in real-time for glucose sensing. The sensing is performed in PBS solutions containing the GOx enzyme-only (Figure 5-4a-c) or both the enzyme and ferrocene (Figure 5-4d-f). Ferrocene (Fc) was added in the enzymatic solutions since it is reported to improve the detection.[83], [90], [210] Fc is expected to act as a mediator, competing with the  $O_2/H_2O_2$  redox couple.[219] The response is extracted as the absolute value of  $\frac{I_0 - I_{glucose}}{I_0}$ , with  $I_0$  being the baseline current with only the enzyme or enzyme/ferrocene in the solution, and  $I_{glucose}$  the current obtained upon the injection of the different concentrations of glucose. All the signals are taken after stabilization of the

$I_{ds}$  current after the injections, taking a few minutes to stabilize due to the enzymatic reaction and subsequent PEDOT:PSS dedoping.[89], [189] Multiple successive injections of glucose in the linear range of  $\sim 30$  to  $\sim 5000$   $\mu\text{M}$  are tested, the lower concentrations being in the physiological range for sweat and saliva analysis, and the higher for ISF and blood analysis in healthy subjects. Gate voltages of 0.1 V for the silver and 1 V for the graphene-gated devices are applied, relatively close to the respective transconductance peak. The latter voltage was chosen as a compromise between the  $g_m$  values and water electrolysis. The effect of the voltages applied on the gate is further analyzed using multiple electrochemical analyses in the next paragraph.

The graphene-gated devices, with and without ferrocene, show a much higher signal amplification compared to the silver-gated devices (Figure 5-4c,f). The calibration curves of three different devices per test condition are shown in Figure S5-7. The addition of ferrocene significantly improves the linearity, which increases from a normalized sensitivity value of  $3.0 \pm 1.8$  %/dec with an extracted  $R^2$  coefficient of  $0.94 \pm 0.08$  without ferrocene, to a sensitivity value of  $4.3 \pm 2.3$  %/dec with an  $R^2$  value of  $0.98 \pm 0.01$  for the silver-gated devices ( $n=3$  in both cases). The same applies to the graphene-gated devices, going from sensitivity of  $19.6 \pm 0.7$  %/dec with an  $R^2$  coefficient of  $0.91 \pm 0.05$  without ferrocene, to sensitivity of  $18.8 \pm 1.0$  %/dec with an  $R^2$  coefficient of  $0.98 \pm 0.02$  ( $n=3$  in both cases). Hence, ferrocene does not play a major role in terms of sensitivity, indicating that the enzymatic cycle involves the  $\text{O}_2$  natural mediator more than Fc. Furthermore, the graphene-gated devices with ferrocene in the solution show a 4.4 times higher sensitivity compared to the silver-gated devices also with ferrocene, combined with higher linearity and repeatability.

The more stable and linear behavior in presence of ferrocene in the solution can be attributed to a decrease in the leakage current ( $I_{GS}$ ), as shown in Figure S5-8, where the respective  $I_{GS}$  current of the devices shown in Figure 5-4 is presented. Both for the silver (Figure S5-8a,b) and graphene-gated transistors (Figure S5-8c,d), there is a smaller change in  $I_{GS}$  with the glucose injections in the presence of ferrocene. Also, it is noticeable that both in the presence and absence of ferrocene, the two devices have a different  $I_{GS}$  trend: the silver-gated transistors have a leakage current that goes towards zero when increasing the glucose concentrations, possibly due to oxidation of silver causing a decrease in conductivity. On the other hand, the graphene-gated ones show an increase in current amplitude with the injections. Finally, as shown in Figure S5-9, actuating the graphene-gated transistors at a lower gate voltage (0.1 V, the same used for the silver-gated devices), the sensitivity is lower and more similar to the silver-gate devices. These results suggest that the higher sensitivity with graphene is also related to the fact that its electrical conductivity remains constant at higher voltages, allowing  $\text{H}_2\text{O}_2$  oxidation and hence an increase of Faradaic current with the increase of glucose.

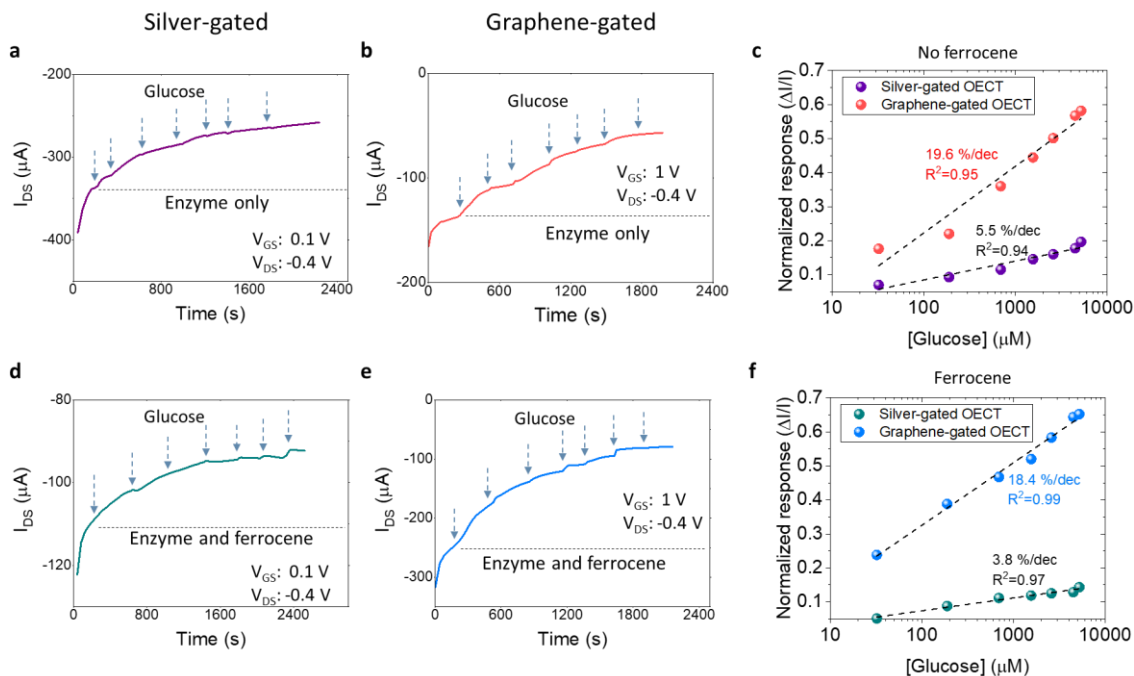


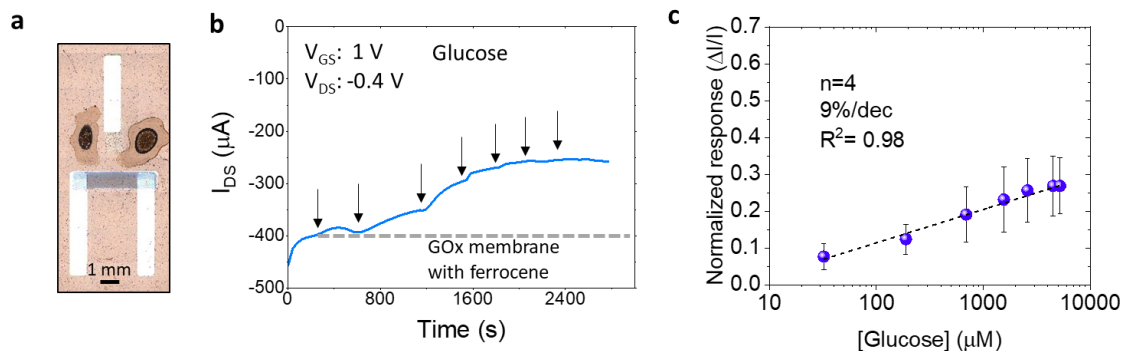
Figure 5-4: Glucose sensing, using only the enzyme for the detection on a silver-gated OECT (a) and on a graphene-gated OECT (b), and corresponding calibration curves (c). Sensing using both the enzyme and ferrocene (29:1 ratio) for a silver-gated OECT (d) and a graphene-gated OECT (e), and corresponding calibration curves (f). The enzyme is dissolved in PBS 1X.

For the best performing devices with graphene gate and ferrocene in solution, the limit of detection was investigated using glucose concentrations in the lower range, starting from  $\sim 100$  nM going up to  $\sim 1$  mM (Figure S5-10). It can be seen that the small concentration of 100 nM glucose can be reliably detected with a signal change from the baseline of about 5 %. The presented sensing performances are compared in Table 4 with state-of-the-art on enzymatic sensing OECT devices. The graphene-gated transistors exhibit a higher sensitivity than previously reported devices with PEDOT:PSS gate electrodes using also the enzyme and ferrocene in solution,[90] platinum gate electrodes with the enzyme linked through graphene oxide,[81] and printed devices with a carbon gate electrode and enzyme in solution,[122] which exhibit similar performances as the silver-gated devices presented in this work. Our fully-printed graphene-gated OECTs are matching the sensing capabilities of those obtained with highly optimized gate electrodes, which are lithographically patterned, and require integration of hybrid nanomaterials or complex multi-layer structures.[81]–[83]



The same optimized devices with graphene and ferrocene are tested also for lactate detection with the LOx enzyme in solution (Figure S5-11). The sensitivity was proven at physiological ranges in biofluids (Figure S5a,b) and lower concentrations (Figure S5-11c,d). Lactate is found at higher concentrations than glucose in most body fluids, hence physiological concentrations from ~2 mM to ~30 mM are used. High sensitivity equal to 21 %/dec (n=3) is also obtained for lactate sensing (Figure S5-11b), with a limit of detection of about 100 nM (Figure S5-11d) corresponding to a signal change of about 5 %, as it has been observed for glucose sensing.

As a first step towards a future implementation for point-of-care monitoring, the devices with the graphene gate are tested with an immobilized GOx membrane (Figure 5-5a).[218] Note that the gate electrode was not covered to not change the potential at the interface with the polymeric membrane. The real-time sensing shows a normalized sensitivity of ~10 %/dec with acceptable repeatability (n=4 devices); a LOD of ~10  $\mu\text{M}$  is extracted (Figure 5-5b,c). The associated leakage current of the device is presented in Figure S5-12. The lower sensitivity and higher LOD may be explained by the number of active enzymes in the membrane. These results could be improved by optimizing the membrane formulation.



*Figure 5-5: Enzymatic immobilization test. (a) Optical image of the OEET with a membrane based on the GOx enzyme immobilized around the graphene-gate, (b) glucose sensing with the device, and (c) calibration curve with standard deviation for 4 devices.*

### 5.3.3 The sensing mechanism

To better understand the sensing mechanism, the transistors are tested with only  $\text{H}_2\text{O}_2$  in the solution (Figure S5-13). The different concentrations tested are the same as the previous glucose concentrations.

Both the silver (Figure S5-13a-c) and the graphene-gated (Figure S5-13d-f) devices show very similar sensing responses as for the devices tested with glucose and the enzyme.

The detection mechanism is further investigated using electrochemical impedance spectroscopy (Figure 5-6a,b). The DC voltage applied during the impedance measurement is close to the one applied during the sensing experiment (close to the transconductance peak). The EIS measurements are performed with the same electrolyte solutions used in the OECT configuration; with only the enzyme dissolved in PBS, then adding ferrocene to the previous solution, and finally adding glucose at a fixed concentration of 700  $\mu$ M. The typical Nyquist plots show that the impedance of the silver gate electrode does not significantly change in the presence of glucose (Figure 5-6a), with some variability among devices due possibly to occurring oxidation processes. Hence, the changes in current observed in the silver-gated OECT configuration during sensing may be due to local variations of pH due to the  $H^+$  produced by the enzymatic reaction,[106] and subsequently de-doping the PEDOT:PSS channel.[127] On the other hand, for the printed graphene electrodes, a significant change in the charge-transfer resistance is observed from the Nyquist plots after the addition of glucose (Figure 5-6b). The values extracted from the fitting with the Randles circuit are reported in Table 5. While the change of charge transfer resistance ( $R_{ct}$ ) before and after the addition of ferrocene is small, from  $5.40 \pm 0.60$  MOhm to  $6.60 \pm 1.20$  MOhm, the addition of glucose strongly decreases the  $R_{ct}$  value to  $1.08 \pm 0.45$  MOhm (6.1 times less). Considering the double-layer capacitance ( $C_{dl}$ ), it only slightly decreases with the addition of glucose, passing from about 220 nF to 200 nF. The initial high interfacial resistance of the graphene electrodes, leading to a large potential drop at the gate-electrolyte interface, is related to the high sensitivity obtained during the enzymatic sensing.[4] In fact, the decrease of the potential drop at the electrolyte/gate interface with the enzymatic reaction leads to an increase of the potential drop at the channel/electrolyte interface and hence a higher influence of  $V_{GS}$  on  $I_{DS}$  resulting in a better modulation.

The role of ferrocene in graphene-gated devices is further investigated by cyclic voltammetry (Figure S5-14a). The measurement is performed with the same experimental conditions as in the previous EIS measurement. The ferrocene/ferrocenium low potential and reversible redox behavior can be seen in the CV. After the addition of glucose, no significant change of the Fc electrochemical signal is observed while an increase of current at high voltages is seen, close to the graphene-electrode polarization voltage in the OECT configuration and the EIS test (1 V); this current is probably due to  $H_2O_2$  oxidation. In fact, a similar increase of current in the CV at high voltages can be seen in Figure S5-14b, where the graphene electrodes are tested with only  $H_2O_2$  in the solution. Hence, the sensing is unlikely related to an Fc-mediated electron transfer,[83] confirming that the transduction of the enzymatic activity is based on the

detection of  $\text{H}_2\text{O}_2$ . The more linear and reproducible sensing behavior with ferrocene can be explained by the fact that this redox couple can stabilize the solution potential, acting as a redox buffer.[220]

The proposed detection mechanism is that the produced  $\text{H}_2\text{O}_2$  from the enzymatic reaction is oxidized at the sensing graphene-electrode interface, and the current produced is proportional to the glucose amount in solution (Figure 5-6c,d). Electrons are likely transferred from the reduced enzyme to the graphene electrode thanks to the  $\text{O}_2/\text{H}_2\text{O}_2$  redox couple, leading to a decrease of the  $R_{\text{ct}}$  resistance at the gate, which results in the rise of the voltage at the gate-electrolyte interface (Figure 5-6e,f). Even if the silver-gated transistors have superior electrical characteristics, this electrochemical reaction at the graphene-gate interface is the reason for the improved sensitivity with the graphene-gated devices. This transduction principle was previously reported for other enzymatic-based OECTs.[83], [121] To analyze if a change of material composition could also play a role in the sensing process, Raman spectroscopy was performed on the graphene layers at different conditions (Figure S5-15). The Raman spectra show that the D and G peaks of the graphene stay constant after exposure to  $\text{H}_2\text{O}_2$ , demonstrating that the  $\text{H}_2\text{O}_2$  produced from the enzymatic reaction does not alter the graphene layers.[216] The insignificant change observed after sintering and after  $\text{H}_2\text{O}_2$  exposure confirms the stability of the printed graphene layers (Figure S5-15a,b).

Finally, the amplification effect of the OECTs is demonstrated in Figure S5-16, where the OECT configuration (Figure S5-16a) is compared to a 2-electrode amperometric system composed of the graphene electrode as a working electrode and an Ag wire as the auxiliary electrode (Figure S5-16b). The current values in the OECT configurations for glucose sensing are about three orders of magnitude higher compared to the 2-electrode amperometric measurement. The values in the 2-electrode mode are in the same order of magnitude as the leakage current. While the variations of normalized current in the 2-electrode mode are higher than the OECT mode as previously reported,[221] the capability of producing an amplified current signal with OECT allows a much lower limit of detection and higher sensitivities for low-concentrated molecules.

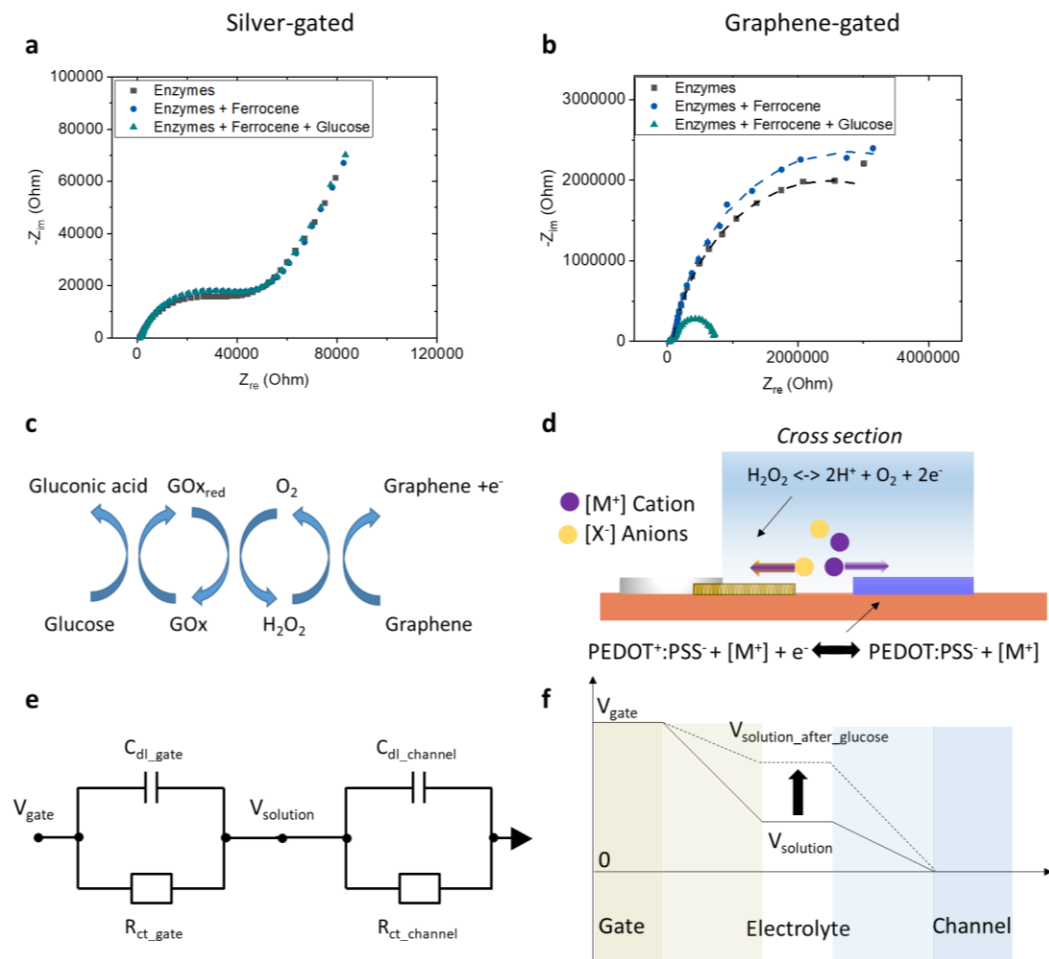


Figure 5-6: Electrochemical impedance spectroscopy analysis. Nyquist plots of the silver-gate electrode (a) and the graphene-gate electrode (b) versus an Ag/AgCl reference, with only the enzyme in PBS, the enzyme and ferrocene (29:1 ratio), and adding 700  $\mu\text{M}$  of glucose. (c) Enzymatic reaction with the detection at the graphene electrode interface, (d) cross-section showing the potential transduction principle of OECTs and the electrochemical reactions, (e) schematics of the extracted model with the graphene-gate electrode, and (f) the detection mechanism in terms of voltage change.

## 5.4 Conclusions

This work demonstrates highly sensitive and fully-inkjet-printed enzymatic organic electrochemical transistors based on graphene gates. The printed graphene-gated OECTs show sensing performances for glucose and lactate detection in enzymatic solutions comparable to those obtained with lithography processed devices on rigid substrates and integrating complex materials as sensing gate electrodes. The

OECTs with inkjet-printed graphene gates show higher sensitivity and linearity than OECTs with silver-nanoparticles gate electrodes. The repeatability of the OECT devices with graphene gates and adding ferrocene in solution is demonstrated both for glucose and lactate sensing in enzymatic solutions. The operation of the sensor with the immobilized enzyme using a membrane around the gate is demonstrated for future implementations in point-of-care analysis. Moreover, the sensing mechanism is analyzed through cyclic voltammetry and electrochemical impedance spectroscopy, and with the latter, a 6 times decrease of the charge-transfer resistance at the graphene electrode-electrolyte interface in the presence of glucose at a concentration of interest is extracted. This voltage change at the gate electrode is amplified in terms of current thanks to the modulated organic channel.

The simplicity of the fabrication process, with the optimized inkjet-printed graphene active-gate material, enables digital manufacturing of performing enzymatic OECT based sensors on polymeric foil for the realization of disposable and configurable biosensing platforms. For future applications with real biofluids, further stability and interference studies are required, including OECTs with different selective bio-layers in the same platform for multi-parametric analysis.

## 5.5 Supporting Information of Chapter 5

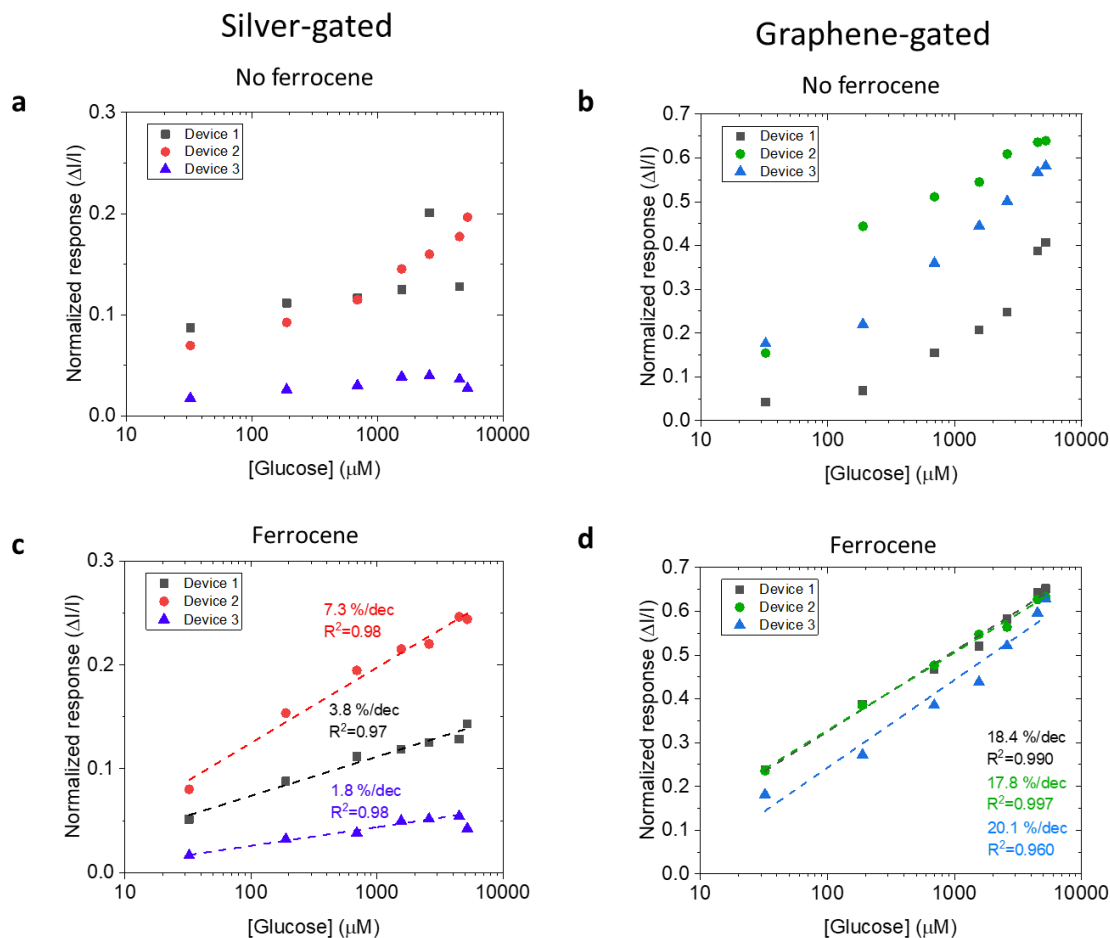


Figure S5-7: Repeatability study. Calibration curves using only the enzyme for the detection with a silver-gated OECT (a) and with a graphene-gated OECT (b). Calibration curves using both the enzyme and ferrocene (29:1 ratio) with a silver-gated OECT (c) and with a graphene-gated OECT (d). Each calibration shows the results for three different devices. The GOx enzyme is dissolved in PBS 1X.

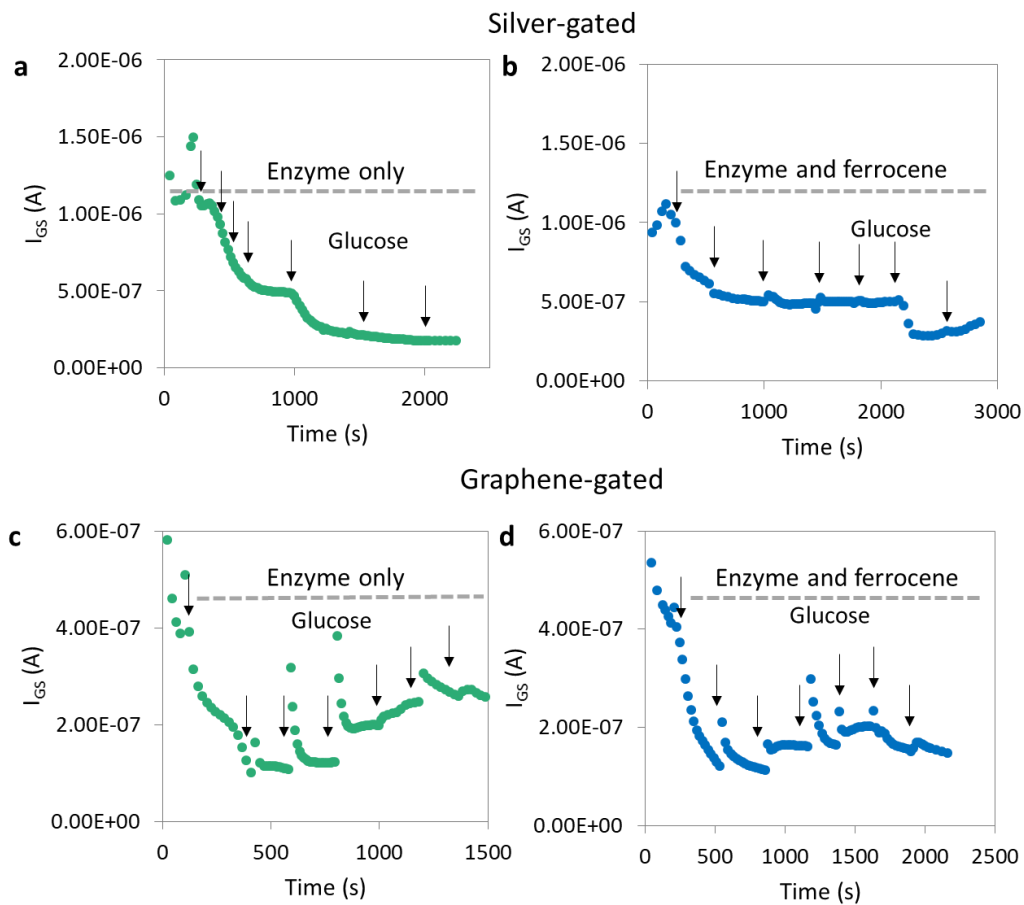
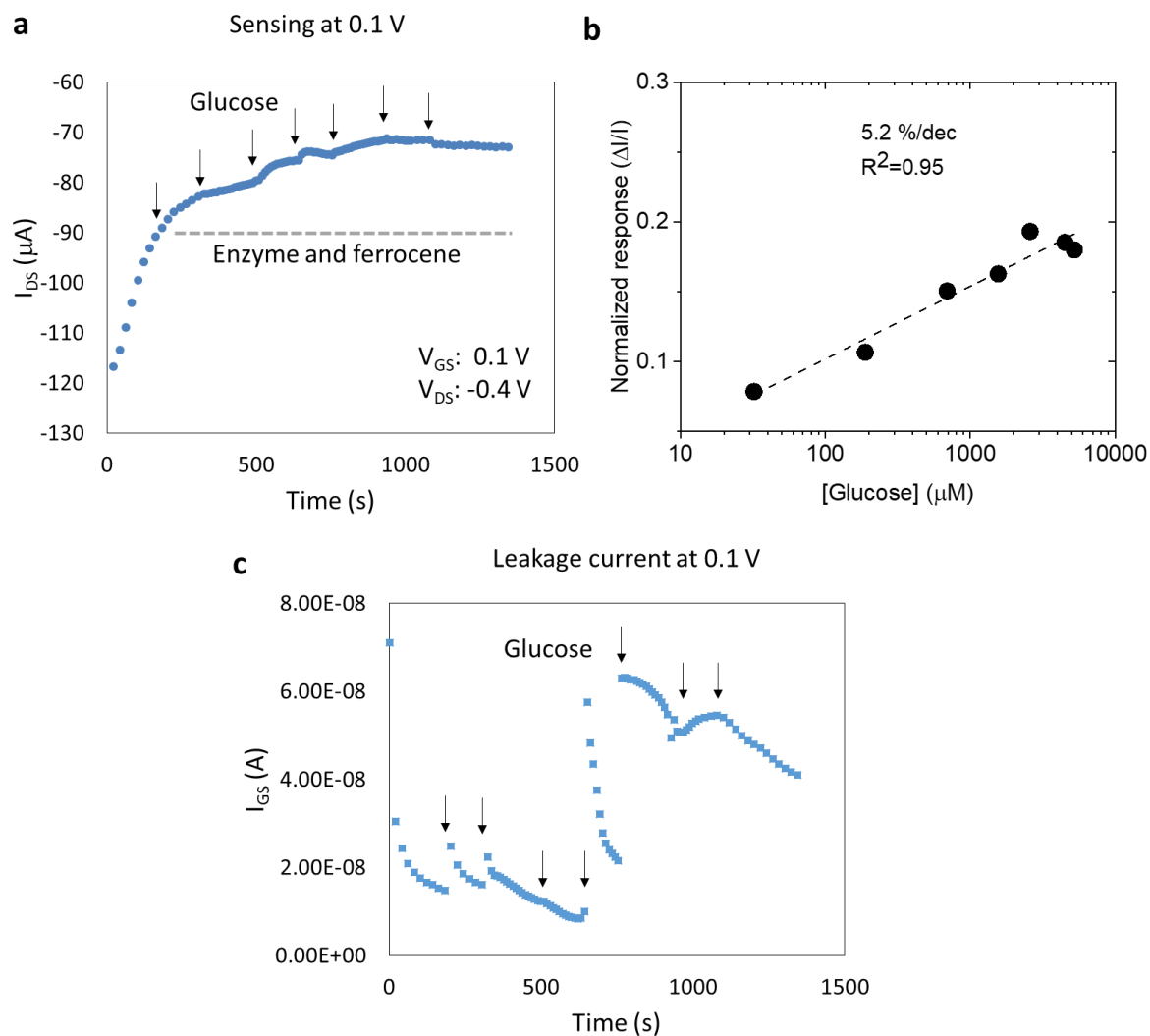


Figure S5-8: Leakage current in the OECTs during sensing. (a) OECT with a silver gate using only the GOx enzyme for the glucose detection and (b) using the enzyme and ferrocene. (c) OECT with a graphene gate using only the enzyme for the detection and (d) using the enzyme and ferrocene.



*Figure S5-9: Sensing comparison. Glucose sensing with a graphene-gated device, with a fixed gate voltage of 0.1 V (far from the transconductance peak) in (a), relative calibration curve in (b), and relative leakage current in (c).*



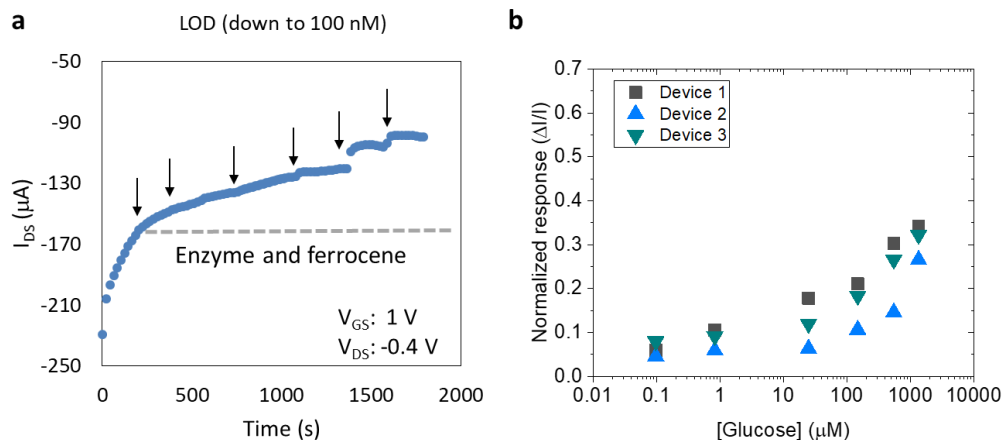


Figure S5-10: Limit of detection for glucose sensing. Typical sensing characteristics with the graphene-gated OECTs for glucose detection at low concentrations in (a) and calibration curves (b).

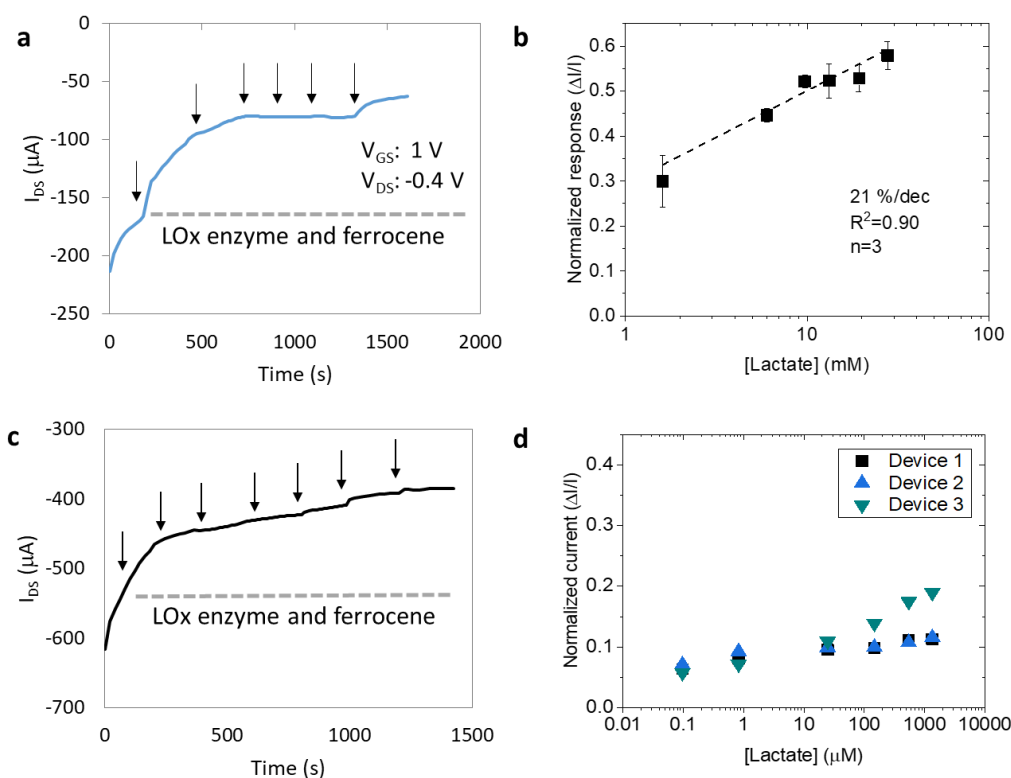


Figure S5-11: Lactate sensing. (a) Sensing lactate in the sweat concentration range using both the LOx enzyme and ferrocene (29:1 ratio) and (b) corresponding calibration curves. (c) Sensing characteristics for lactate detection at low concentration using both the enzyme and ferrocene (29:1 ratio) and (d) calibration curves for three devices.

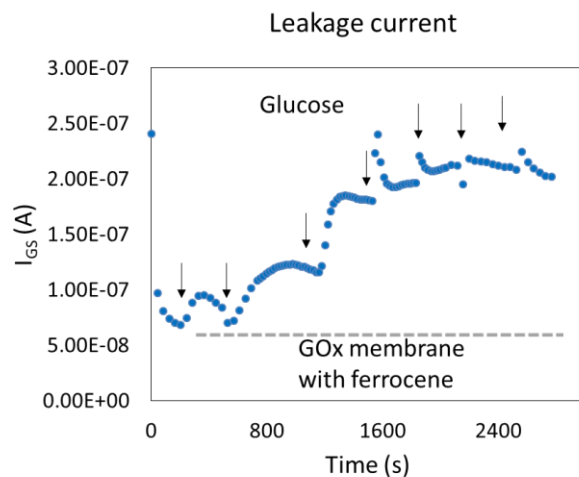


Figure S5-12: Leakage current with the membrane. Typical leakage current of the graphene-gated devices during glucose sensing with the GOx membrane immobilized around the gate electrode.

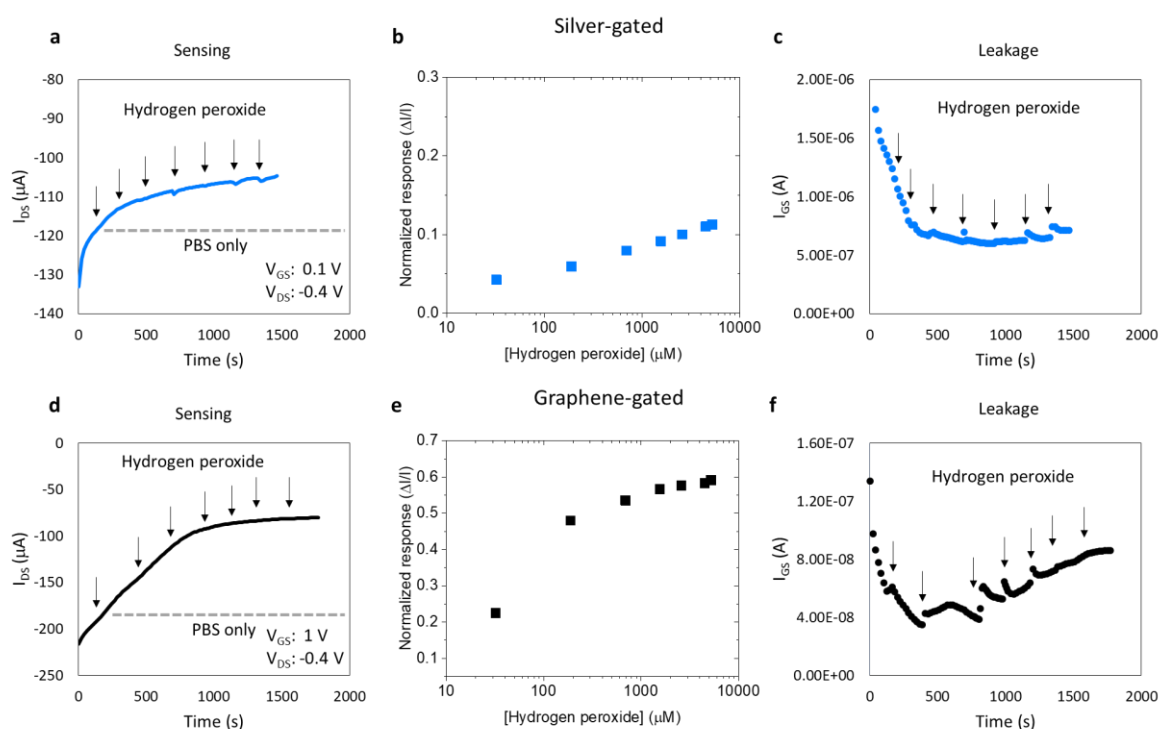


Figure S5-13: Test with hydrogen peroxide. Sensing in time at different hydrogen peroxide concentrations with the silver-gated OECT in (a), with the corresponding calibration curve in (b), and the leakage current in (c). Sensing in time with the graphene-gated OECT in (d), with the corresponding calibration curve in (e), and the leakage current in (f). The hydrogen peroxide is diluted in PBS 1X.

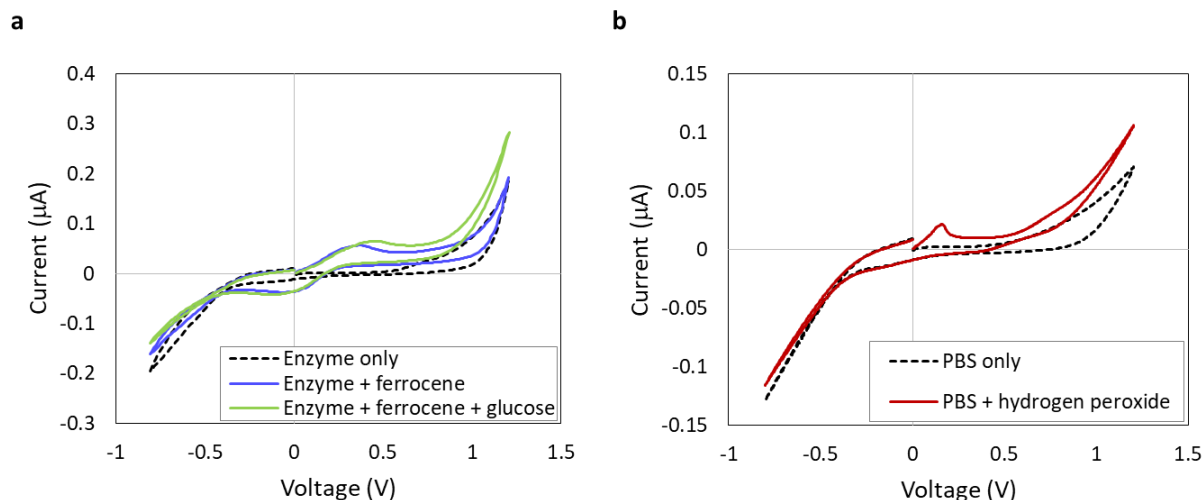


Figure S5-14: Cyclic voltammetry measurement. CV measurement for the graphene-gate electrode versus an Ag/AgCl reference, with only the GOx enzyme in PBS, the enzyme and ferrocene (29:1 ratio), and adding 700 μM of glucose in (a), and with only PBS and adding 700 μM of hydrogen peroxide ( $H_2O_2$ ) in (b). Scan rate 10 mV/s.

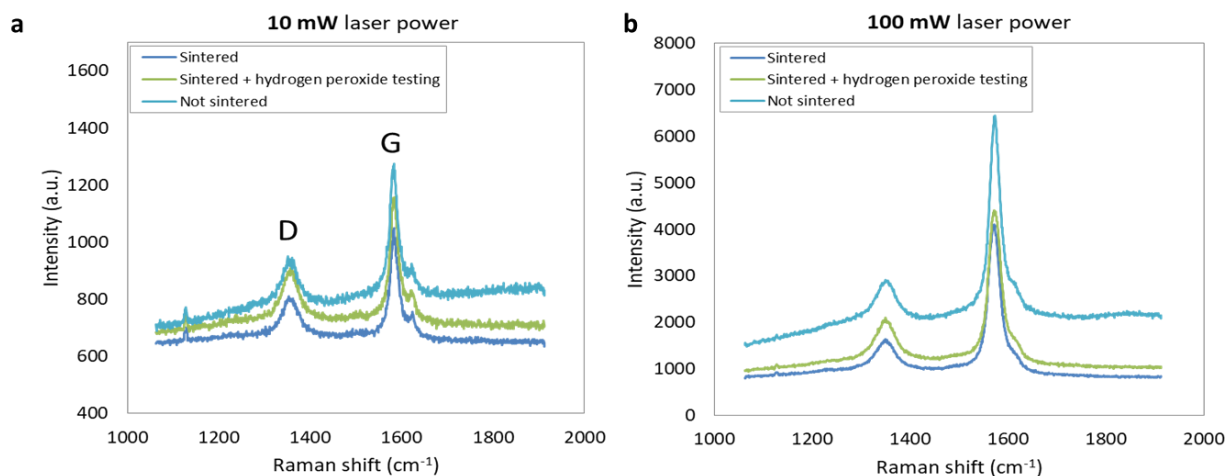


Figure S5-15: Raman spectroscopy. Raman spectra of the graphene layers before sintering, after sintering (250°C for 1 hour), and after the testing with hydrogen peroxide. The measurements are performed at 10 mW (a) and 100 mW (b) laser power.

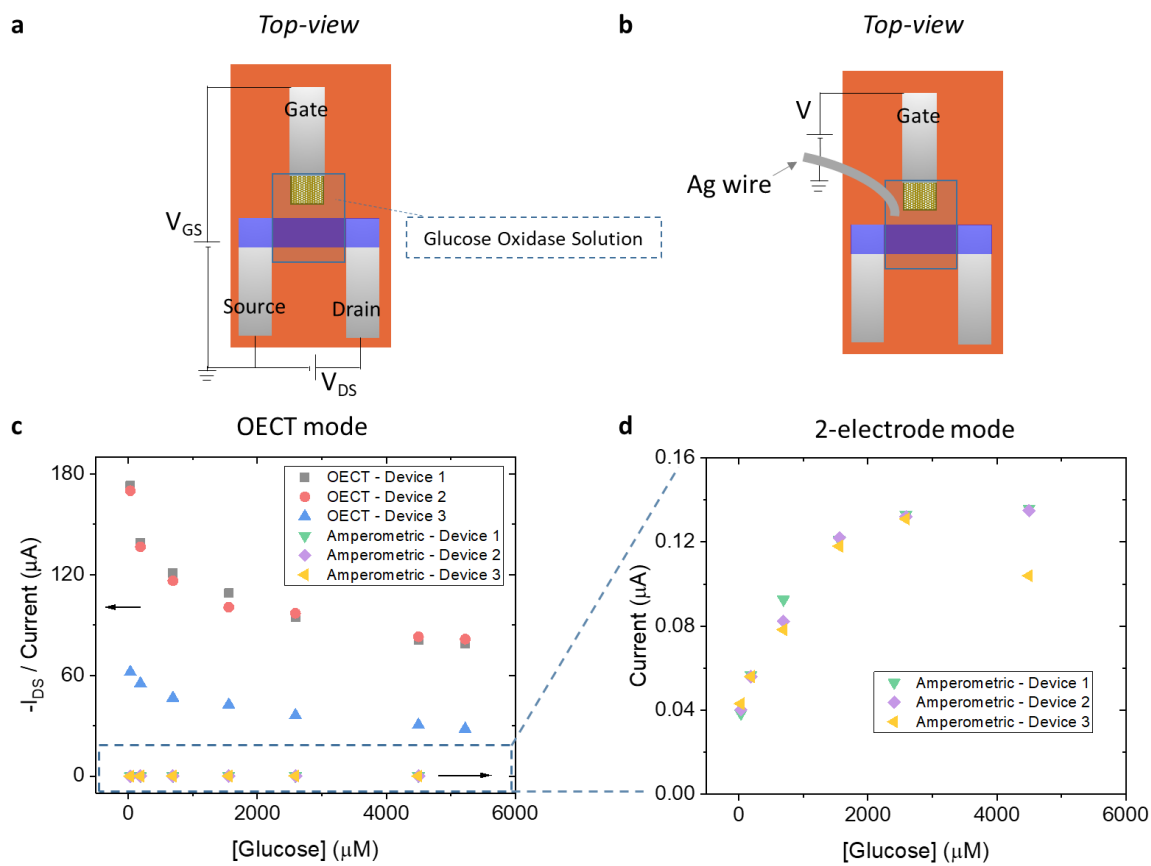


Figure S5-16: Amplification mechanism. (a) Schematic of an OEET, and (b) schematic of the 2-electrode configuration. Glucose sensing tests with a graphene-gated OEET compared to the sensing tests in the 2-electrode mode (c), and zoom on the latter (d). Tests with the GOx enzyme and ferrocene in solution (29:1 ratio). The results for three different devices are reported for each configuration. In the OEET mode:  $V_{gs} = 1 \text{ V}$ ,  $V_{ds} = -0.4 \text{ V}$ . In the amperometric mode: Voltage = 1 V.

Table 4: Literature comparison. Glucose sensing performances compared with the literature for organic electrochemical transistors.

Device	Sensitivity ( $\Delta I/I$ )	Linear range ( $\mu M$ )	LOD ( $\mu M$ )	Conditions (Enzymes)	Gate electrode material	Fabrication/ Substrate	Ref.
OECT	~6%/dec	1-1000	---	GOx + ferrocene in solution	PEDOT:PSS	Lithography/ Glass	[90]
OECT	~30%/dec	20-1000	10	GOx+ferrocene in chitosan on the gate	Gold- PEDOT:PSS	Lithography/ Glass	[83]
OECT	~30%/dec	5-100	0.1	GOx+Pt NPs in chitosan on the gate	Gold-Pt NPs	Lithography/ Glass	[82]
OECT	~1%/dec	1-100	5	GOx in graphene oxide linker	Pt	Lithography/ PET	[81]
OECT	~10%/dec	0.1-30	0.03	GOx in graphene oxide linker	Pt-Nafion- Graphene flakes-PANI	Lithography& drop-cast/ PET	[81]
OECT	~3%/dec	1-100000	---	GOx in solution	Carbon black	Inkjet& doctor blade coating/ Clarifoil	[73]
OECT	~4%/dec	30-5000	---	GOx + ferrocene in solution	Silver NPs	All-inkjet printing/ Polyimide	This work
OECT	~20%/dec	30-5000	0.1	GOx + ferrocene in solution	Graphene nanosheets	All-inkjet printing/ Polyimide	This work

Table 5: EIS fitting for the graphene electrodes. The charge transfer resistance ( $R_{ct}$ ) and double-layer capacitance ( $C_{dl}$ ) with the relative constant-phase element number ( $n$ ). The values are reported for two devices for each testing conditions. The glucose concentration is fixed at 700  $\mu M$ .

Condition	$R_{ct}$	$C_{dl}$
GOx enzyme only	Device 1) 4.81 MOhm Device 2) 6.00 MOhm	Device 1) 254 nF ( $n=0.88$ ) Device 2) 234 nF ( $n=0.89$ )
GOx enzyme + ferrocene	Device 1) 5.38 MOhm Device 2) 7.78 MOhm	Device 1) 241 nF ( $n=0.92$ ) Device 2) 205 nF ( $n=0.89$ )
GOx enzymes + ferrocene + glucose	Device 1) 0.63 MOhm Device 2) 1.52 MOhm	Device 1) 196 nF ( $n=0.92$ ) Device 2) 196 nF ( $n=0.85$ )

# Chapter 6 OECTs with antibody-coated gates for cortisol sensing in human sweat (Paper IV)

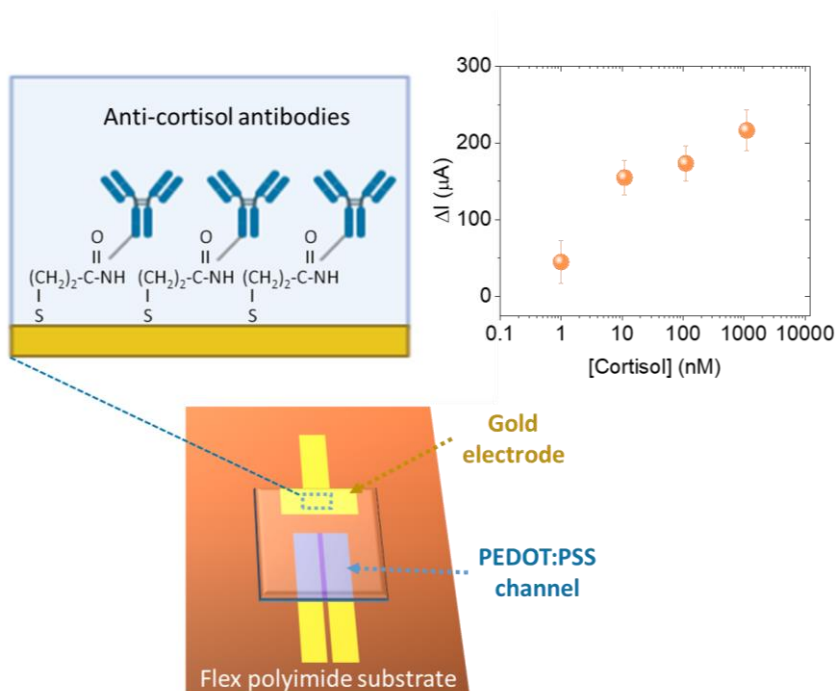


Figure 6-1: Graphical abstract. Flexible OECTs with antibody-coated gates for cortisol detection.

The dysregulation of the hormone cortisol is related to several pathological states, and its monitoring could help prevent severe stress, fatigue, and mental diseases. While wearable antibody-based biosensors could allow real-time and simple monitoring of antigens, an accurate and low-cost antibody-based cortisol detection through electrochemical methods is considerably challenging due to its low concentration and the high ionic strength of real biofluids. Here, a label-free and fast sensor for cortisol detection is proposed based on antibody-coated organic electrochemical transistors. The developed devices show unprecedented high sensitivities of 50  $\mu A/dec$  for cortisol sensing in high-ionic strengths solutions with effective cortisol detection demonstrated with real sweat. The sensing mechanism is analyzed through impedance spectroscopy and confirmed with electrical models. Compared to existing methods requiring bulky and expensive laboratory equipment, these wearable devices enable point-of-care cortisol monitoring in 5 minutes with direct sweat collection for personalized well-being monitoring.

## 6.1 Introduction

Wearables for the real-time monitoring of cortisol levels in human sweat have great potential for maintaining a healthy mental and physical condition[19]. Compared to standard methods of measurement, such as enzyme-linked immunosorbent assay (ELISA) or liquid chromatography-tandem mass spectrometry (LC-MS/MS)[222], a sensitive, selective, and simple to use wearable cortisol sensor for direct sweat collection on the skin could provide consistent measurements due to reduced sweat evaporation and the possibility of performing point of care monitoring,[21], [28], [167] for analyzing subjective physiological or stress-related variations[223]–[225].

Cortisol, a glucocorticoid hormone, is a biomarker regulated by the hypothalamic-pituitary-adrenal axis[19], [95]. This hormone has a distinct circadian rhythm essential for human health, with the highest levels in the morning and the lowest at night[37]. Short-term modification of cortisol secretion can be adaptive responses of the body; however, chronic dysregulations are associated with a disrupted circadian rhythm and pathological conditions such as anxiety, depression, burnout, weaker immune system, chronic fatigue, and cardiovascular complications[19], [37], [95], [167]. A non-invasive and “stress-free” way being explored to determine cortisol is by analyzing the biofluid sweat[19], [226]–[228]. Compared to the other non-invasively available fluids, such as urine and saliva, sweat is the only one that can allow a continuous collection without human intervention with a wearable device[222]. Cortisol has a passive sweat transport, and its concentration in sweat is sweat-rate independent[29], and a good correlation between cortisol sweat and serum levels has previously been reported[19]. However, the correct quantification of normal and abnormal cortisol levels in sweat is challenging due to the high dilution of this steroid hormone, the high sweat ionic strength, and possible interferents[101], [123].

Recent technological advances with organic transistor-based biosensors are allowing the detection of molecules at low concentrations without the need for enzymatic labels and complex preparation procedures[37], [38], [167]. Transistors can play an essential role in wearable applications, thanks to their ability to amplify signals, and since they are simple to miniaturize and integrate into portable electronic devices. Organic electrochemical transistors (OECTs), which have an electrolyte coupling the gate with a conducting polymer channel, were proposed as biosensors for low-cost and fast diagnosis[69], [93]. Compared to other types of transistors, in OECTs, the ions from the electrolyte permeate into the channel, typically made of poly(3,4-ethylenedioxythiophene) doped with poly(styrene sulfonate) (PEDOT:PSS), once a gate voltage is applied[42]. This phenomenon causes a volumetric change of the doping state, with significant modulations of drain current at low gate voltages and very high signal amplification[50]. The

devices can be used as biosensors by integrating a biorecognition layer either at the gate/electrolyte or at the electrolyte/channel interfaces[4], [46].

OECTs with antibodies or aptamers immobilized on the gate electrode are reported as promising biosensor configurations for sensing COVID-19 spike proteins or immunoglobulin G (using nanobody[69] or standard antibody[93]), rabbit immunoglobulin G (standard antibody)[67], interleukin-6 (standard antibody)[92], epinephrine (aptamers)[102]. The main advantage of using antibodies is that they can be produced easily for a wide range of sensing applications, while producing aptamers for several targets is still challenging[124]. One of the main difficulties for cortisol detection using antibodies is that cortisol does not carry any electrical charge[20], [37], making its detection particularly problematic. Cortisol detection with an OECT transducer was only achieved so far by using a molecularly imprinted membrane (MIP) as functionalization, not located on the gate but on the PEDOT:PSS channel, exhibiting a sensitivity of 2.68  $\mu\text{A}/\text{dec}$  in the range of 10 – 10000 nmol/L (nM)[167]. The device was tested by collecting sweat on the skin of one subject during exercise, measuring two relatively high cortisol concentrations equal to ~400 nM, with these values confirmed using a standard ELISA measurement on sweat samples collected simultaneously.

Here, we report on fully-integrated and flexible OECTs with monoclonal anti-cortisol antibody-coated gold gate electrodes to detect low concentrations of cortisol in 5 minutes. Our OECT sensors are optimized for enhanced current amplification, reaching a high sensitivity to cortisol of about 50  $\mu\text{A}/\text{dec}$  in the 1 – 1000 nM concentration, with a limit of detection of 100 pM, making them relevant for real sweat analysis[19], [222]. Through electrochemical impedance spectroscopy measurements on the biofunctionalized gate electrodes, we have identified as the main transducing mechanism that the cortisol binding events result in a variation of double-layer capacitances at the gate interface. By implementing the capacitance values into an electrical analytical model for the electrochemical transistors, we show that the predicted sensitivity matches the experimental data. Finally, the OECT sensors were used to determine cortisol in real sweat samples, with results compared to a method using LC-MS/MS. The wearable sensors can be implemented as stickers-on-the-skin for direct sweat collection and fast measurements of the stress-biomarker cortisol in sweat.



## 6.2 Results

### 6.2.1 Devices and electrical measurements

The architecture of the all-integrated, planar organic transistors on flexible foil and their biosensing principle is presented in Figure 6-2. The sensing part of the devices is composed of an evaporated gold gate, functionalized through a standard thiol process for the binding of antibodies[229], and the amplification part comprises an inkjet-printed PEDOT:PSS organic channel[135]. The antibody employed is a commercial monoclonal anti-cortisol antibody, but the same process and device structure could be used for any other sensing applications involving antibodies.

Our devices on flexible foils can be easily processed, separating the gate to the channel during the gate functionalization steps and subsequently assembling them through double-sided adhesives (Figure S6-7a,b). The separation of the gate prevents damaging the organic PEDOT:PSS channel during the multiple incubation and washing steps required for the antibody immobilization. A flexible microfluidic system can be implemented, through the lamination of a combination of plastic and adhesive layers, for sweat collection on people (Figure 6-2b and Figure S6-7c,d), or a rigid reservoir can be added to confine the electrolyte solution during laboratory experiments (Figure S6-7c,e). The OECT sensors with the microfluidics integrated can be applied as skin-sticker to collect the electrolyte thanks to the presence of multiple inlets on the surface, trapping the liquid through capillary action (Figure S6-7f,g).

To confirm the formation of the thiol monolayer and the binding of the antibodies, the gates are characterized with X-ray photoelectron spectroscopy (XPS) (Figure S6-8). The significant increase of the S2p peak (Figure S6-8a) and the N1s peak (Figure S6-8b) with thiols and antibody on the surface confirm the successful surface modification and immobilization of the capture antibody on the gold gates[19]. Two inert gold electrodes, used as source and drain, establish contact with the PEDOT:PSS material defining the channel length.

Modifying the PEDOT:PSS geometry by varying the ratio of channel width (W) versus length (L) (Figure 6-2a) leads to a modulation of the current amplification for the same binding events at the gate electrode. Three different channel  $\frac{W}{L}$  ratios were evaluated, equal to 0.25 ( $W=1$  mm,  $L=4$  mm), 1.5 ( $W=3$  mm,  $L=2$  mm), and 12.5 ( $W=3$  mm,  $L=0.24$  mm), namely called long-channel, short-channel, and very-short channel. The thickness ( $t$ ) of the PEDOT:PSS layer was  $101 \pm 17$  nm ( $n=3$ ).

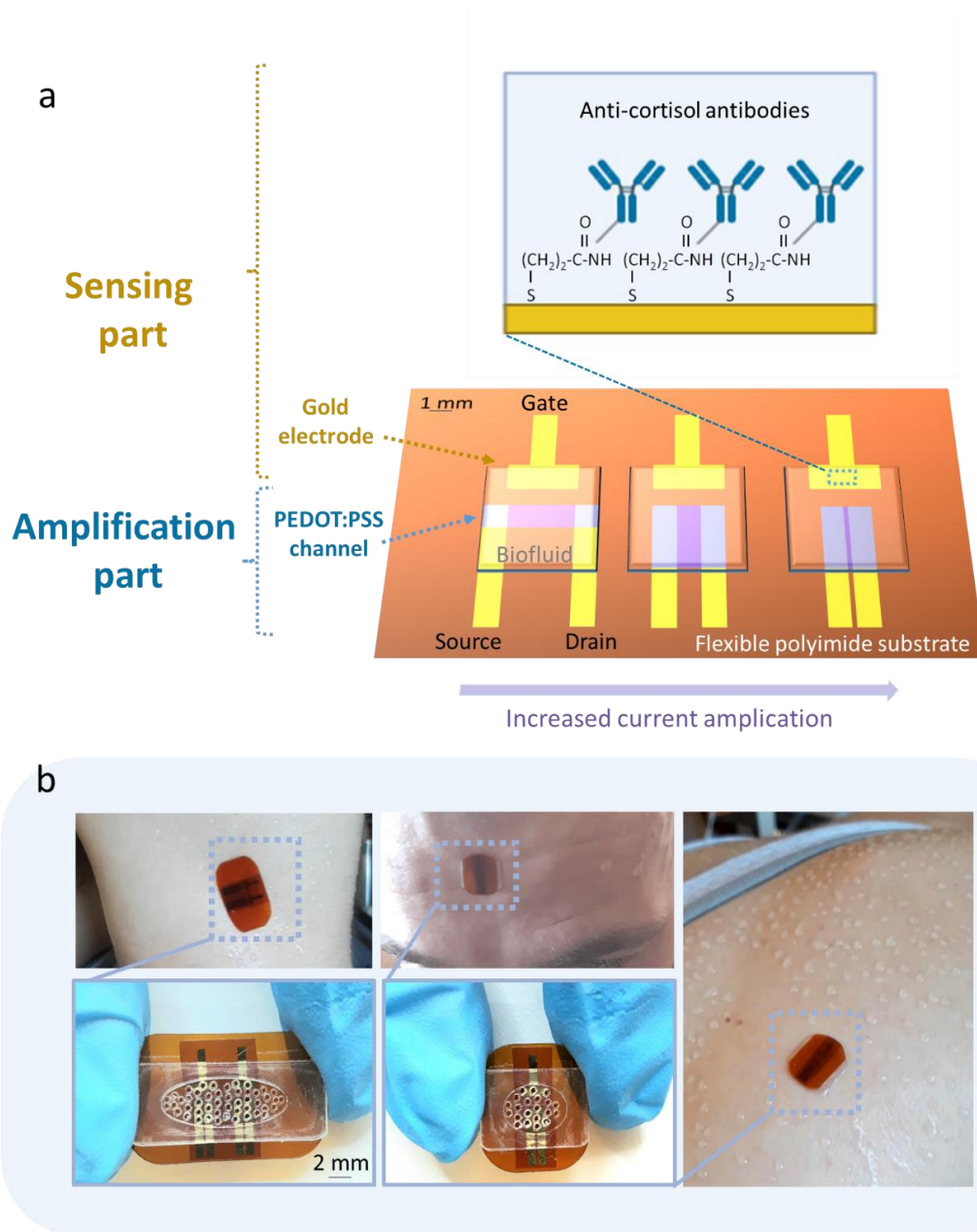


Figure 6-2: Organic transistor structure and sticker application. (a) Schematic of the biosensing principle involved and structure of the OECT devices, including antibody-coated gate electrodes and the organic PEDOT:PSS channel for current amplification; the latter shows three OECT devices with different PEDOT:PSS channels of an increased width per length ratio. (b) Application of cortisol sensing sticker on the human skin for sweat collection during sports activities; the microfluidic part with the multiple inlets is placed in contact with the skin.

In the presence of PBS electrolytic solution and with the conducting channel biased at a potential ( $V_{ds}$ ), the  $I_{ds}$  current decreases once a positive voltage is applied at the gate ( $V_{gs}$ ). This behavior can be well observed in the electrical characteristics of the fabricated devices reported in Figure 6-3 and Figure S6-7, including the output (Figure 6-3a, Figure S6-7g,h) and transfer (Figure 6-3b,c) characteristics and the amplification of the devices (Figure 6-3d). The latter intrinsic amplification is defined as the transconductance  $g_m$ , equal to  $\frac{\Delta I_{ds}}{\Delta I_{gs}}$ .

It can be observed from the transfer characteristics of the gold gated OECTs that the maximum transconductance peak ( $g_{m,max}$ ) and its relative voltage ( $V_{gs,max}$ ) increase with the geometrical factor  $\frac{W}{L}$ , as previously reported for silver-gated devices[135]. Here we push these analyses by comparing gold gates with and without immobilized antibodies. Interestingly, the presence of antibodies on the gate electrode does not modify the current modulation effect of the transistors (Figure 6-3a, Fig 2b). However, it can be seen that there are two  $g_m$  peaks (Figure 6-3d), with a small peak between 0.2 – 0.3 V. This small peak is due to the formation of the thiols monolayers on the surface,[65] while before the thiol functionalization, there is only the main  $g_m$  peak at  $V_{gs,max}$  close to 0.6 V, as can be seen in Figure S6-9. The devices functionalized with antibodies had a thiol activation of the carboxylic groups with the chemical 1-ethyl-3-(3-diamino)propyl-carbodiimide (EDC) and the use of both EDC and N-hydroxysulfosuccinimide (NHS) chemistry did not modify the electrical properties of the devices (Figure S6-10).

Between the long to short channels, the geometrical factor  $W/L$  is increased by 6 times, and for short to very short by 8 times. The  $g_m$  increased by approximately 5 times (~400 mS to ~2 mS) and 4 times (~2 mS to ~6 mS), for these respective channel variations. While the initial variation of  $g_{m,max}$  is almost linear with the  $\frac{W}{L}$  ratio as generally reported[57], a saturation of  $g_m$  from short to very-short channels occurs. Such a  $g_{m,max}$  saturation phenomenon was observed and confirmed with simulations with unfunctionalized devices already [135]. It was shown to be related to the more significant parasitic contact resistance for small channel designs.

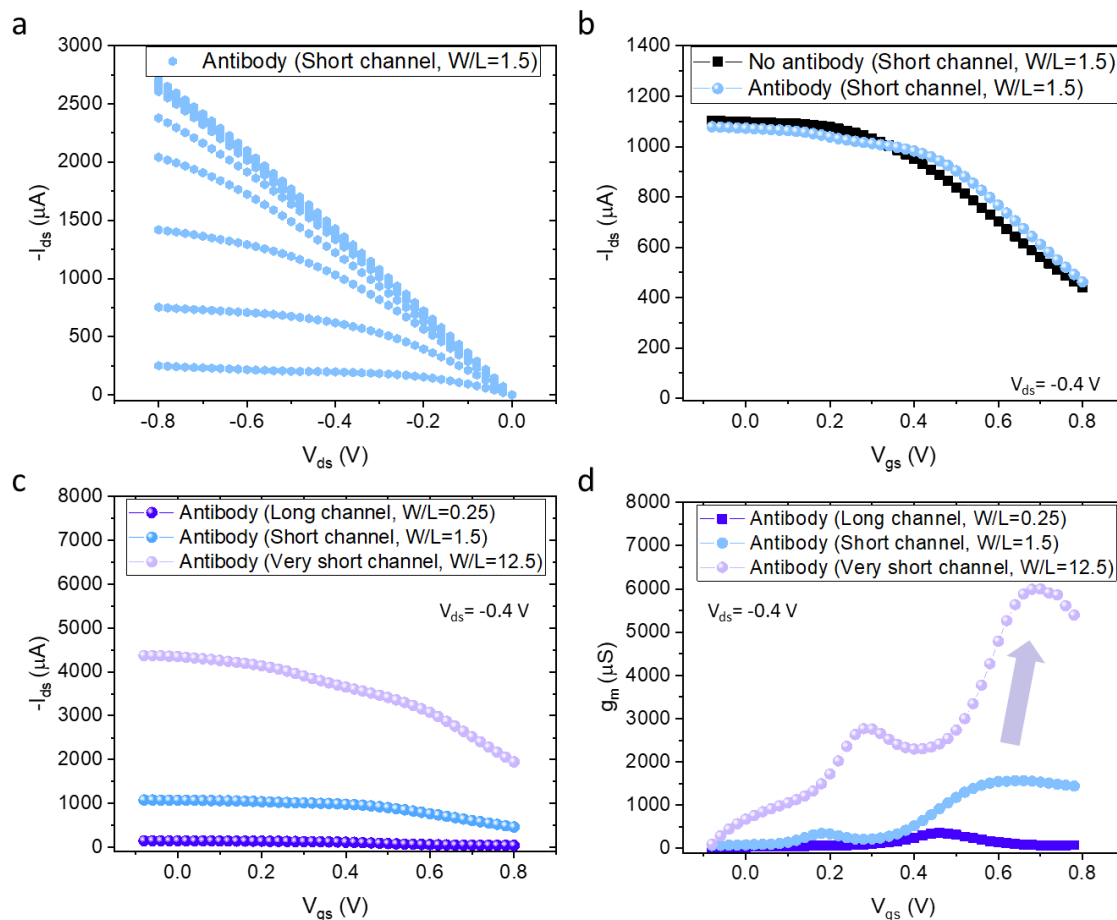


Figure 6-3: Organic transistor electrical characteristics. (a) Output characteristics with a  $V_{gs}$  voltage sweep from -1 to 1 V with a step of 0.25 V for devices having the anti-cortisol antibody on the gate electrode and a PEDOT:PSS W/L=1.2. (b) Comparison of transfer characteristics without and with antibodies, for a fixed PEDOT:PSS W/L=1.2 and a fixed drain voltage  $V_{ds}=-0.4$  V. (c) Multiple transfer characteristics for devices with all the different W/L and antibody on the gate, and (d) respective transconductance  $g_m$ . The tests are in PBS IX (0.15 M), pH 7.

## 6.2.2 Cortisol biosensing

The OECTs with the multiple PEDOT:PSS channel designs (long, short, and very-short channels) were tested in real-time at different cortisol concentrations (Figure 6-4) to study how the geometrical and  $g_m$  variations influenced the sensitivity of the devices. All the sensors had an EDC thiol activation before the antibody immobilization on the gate, while the devices with NHS on the label had both an EDC/NHS chemistry. Some devices were tested without antibodies on the gate and PBS-only blank solutions as

control measurements. The devices were operated at  $V_{gs}$  equal to 0.6 V, close to the  $V_{gs,max}$ , and  $V_{ds}$  -0.4 V. The cortisol concentrations tested were 1 nM, 10 nM, 100 nM, and 1000 nM in PBS 1X (0.15 M, pH 7). The measurement starts in PBS-only as a baseline, and then cortisol in PBS was added each time for 5 minutes per injection. The tests were performed with a reservoir fixed on the sensor, exposing the sensor to 50  $\mu$ L of solution at the fixed concentration after removing the previous solution.

Roughly one minute following an increase in cortisol concentration, a significant decrease of  $I_{ds}$  current was observed in real-time for the sensing devices with the anti-cortisol antibody on the gold gate (Figure 6-4a,b,d,e). The sensitivity for the real-time cortisol measurements was extracted as the variation of drain current from the baseline,  $\Delta I = I_{ds,cortisol} - I_{ds,0}$ , per order of magnitude of cortisol concentration, as reported in Figure 6-4g. The error bars in the graphs (Fig 3g,h) represent the standard deviation from the average obtained from multiple devices, with the exact number (n) written for each case in the following lines.

The increase of sensitivity with the increase of the ratio  $\frac{W}{L}$  matched well the variation of transconductance, with an increase of sensitivity of  $\sim 3$  and 5 times, from long to short and from short to very-short channels, respectively. Sensitivities of  $3.7 \pm 0.4 \mu A/dec$  ( $R^2=0.99$ ,  $n=4$ ) and  $17.7 \pm 2 \mu A/dec$  ( $R^2= 0.99$ ,  $n=3$ ) were obtained from fitting the short channel and the long channel responses in Figure 6-4g, respectively. The extracted sensitivities for the very-short channel devices ( $n=4$ ) were similar for both the tested chemical processes, reaching high values of  $51.0 \pm 14 \mu A/dec$  ( $R^2= 0.9$ ) when functionalized with EDC/NHS and  $51.2 \pm 8 \mu A/dec$  ( $R^2= 0.95$ ) with EDC-only. All the devices exhibited a leakage current  $I_{gs}$  of  $\sim 100$  nA, four orders of magnitude lower than the  $I_{ds}$  current for very-short channels, remaining stable or observing a small increase with the first cortisol injection while experiencing a slight decrease after the stabilization phase of 5 minutes, as reported in Figure S6-11.

Multiple measurements performed on control devices with and without antibodies show that the high current variations originate from the antibody-antigen binding events. The devices with antibodies showed a small change of current for multiple PBS injections without cortisol (Figure 6-4c,f,h) and without antibodies for the different cortisol concentrations (Figure 6-4h). These variations are reported in absolute values since the control devices showed an increase or a decrease of current with the injections depending on the device. Without antibodies, the variations were  $1.9 \pm 1 \mu A/dec$  ( $n=5$ ), while the changes observed on devices having the gate functionalized and tested following multiple blank injections were  $6 \pm 2 \mu A$  for the long channels ( $n=2$ ),  $6 \pm 7 \mu A/dec$  for the short channel ( $n=2$ ), and  $7 \pm 1 \mu A/dec$  for the very-short channel ( $n=5$ ). These current variations observed on the control devices are considerably lower than the sensitivity reported for the very short (7X) and the short channel devices (3X), but comparable to the long

channel devices. Among all the tested conditions, the sensors implementing a very-small W/L ratio and an EDC/NHS chemistry showed the highest sensitivity and thus to be the least influenced by the observed current variations in the control experiments, making them therefore the most suitable for being applied for real sweat analysis.

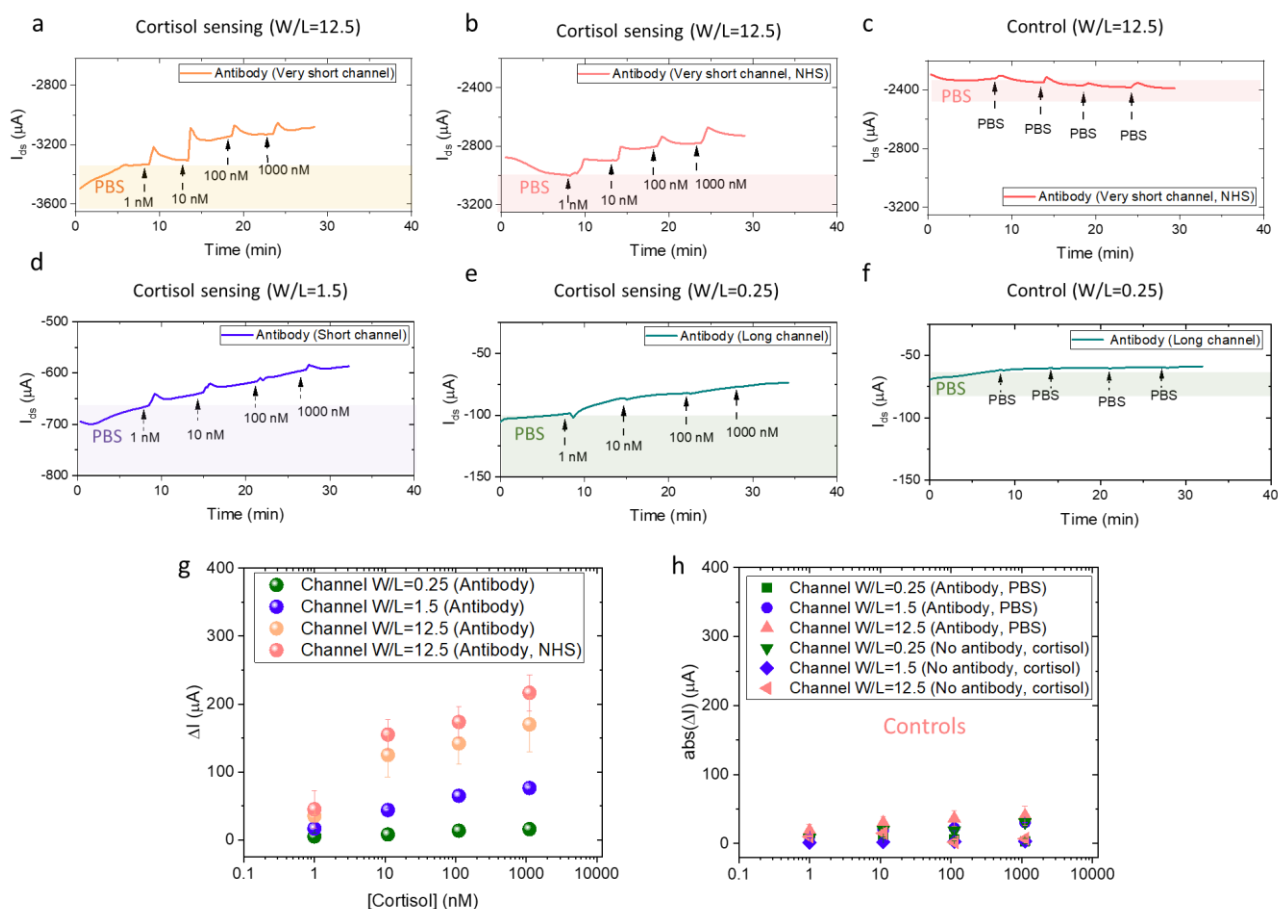


Figure 6-4: Real-time cortisol sensing. (a) Cortisol measurement with PEDOT:PSS W/L=12.5 and thiol/EDC/antibody gate chemistry. (b) Cortisol measurement with PEDOT:PSS W/L=12.5 and thiol/EDC/NHS/antibody gate chemistry. (c) Control measurement with multiple PBS injections with PEDOT:PSS W/L=12.5 and thiol/EDC/antibody gate chemistry. (d) Cortisol measurement with PEDOT:PSS W/L=1.5 and thiol/EDC/antibody gate chemistry. (e) Cortisol measurement with PEDOT:PSS W/L=0.25 and thiol/EDC/antibody gate chemistry. (f) Control measurement with multiple PBS injections with PEDOT:PSS W/L=0.25 and bare gold gates. (g) Calibration curves at the multiple sensing conditions, and (h) multiple control measurements. The error bars represent the standard deviation from the average obtained from multiple devices. The tests are at  $V_{ds}=-0.4$  V and  $V_{ds}=0.6$  V.

### 6.2.3 Sensing mechanism

To investigate the detection mechanism of the OEET devices, we analyzed the antibody-coated gate electrodes by electrochemical impedance spectroscopy (EIS) (Figure 6-5a).

The Nyquist plots show a significant impedance change at the gate interface at the different cortisol concentrations after 5-minute incubations. We can observe a considerable impedance variation at 0.1 Hz (lowest frequency, Figure 6-5b) of ~60 kOhm/dec ( $R^2=0.93$ ,  $n=3$ ). The error bars represent the standard deviation from the average obtained from the three tested devices. These variations in the Nyquist plot are similar as previously reported for the antibody-antigen detection of cortisol for a different electrode material (molybdenum disulfide)[230]. On the other hand, control devices incubated with PBS-only for 5 minutes exhibited a minimal impedance change at the same conditions (Figure S6-12a).

A typical Bode plot for the sensing devices is shown in Figure S6-12b, where there is a clear variation of phases at low frequency. Using the equivalent circuit in Figure S6-13a, with a constant phase element for taking double-layer non-idealities and a Warburg element representing the ionic diffusion[192], [231], the CPE values before and after the multiple cortisol concentrations were extracted (Figure S6-13b). From this, the double-layer capacitance ( $C_{dl}$ ) values were calculated using the following formula:

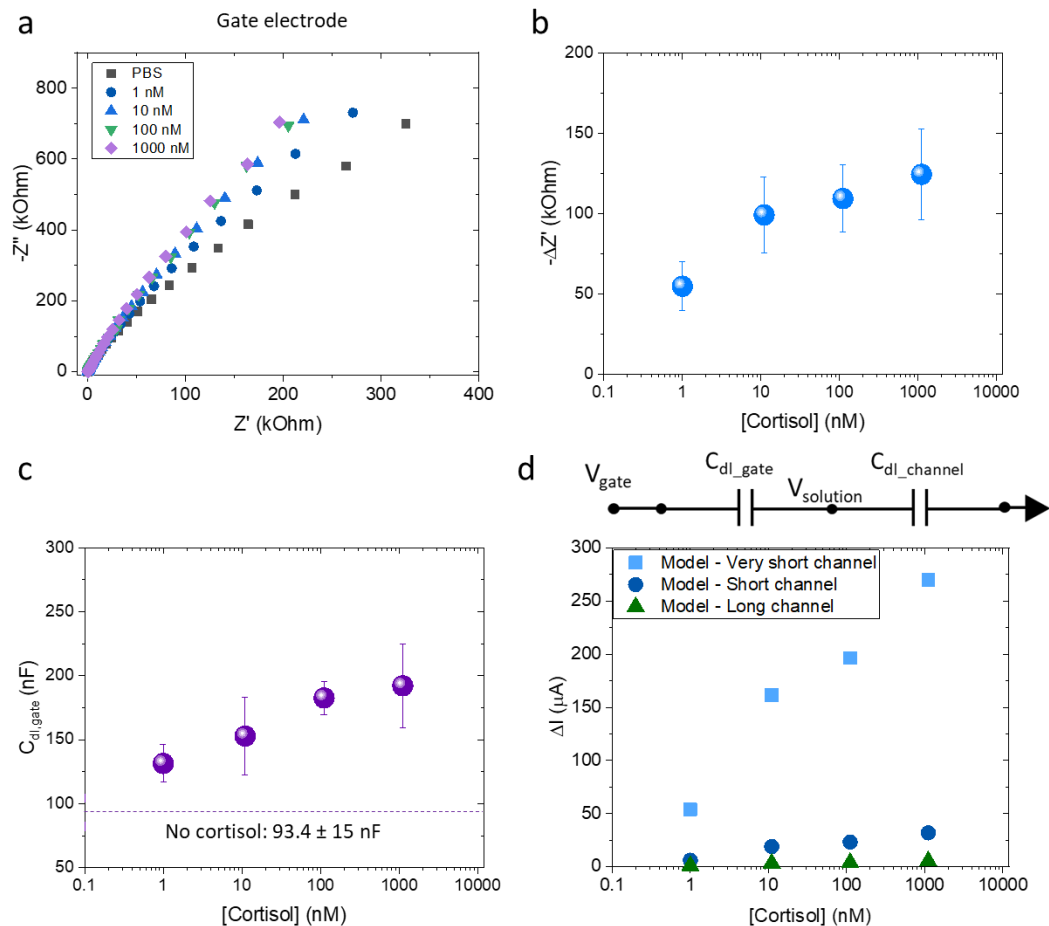
$$C_{dl} = \frac{(R_{ct} CPE)^n}{R_{ct}} \quad (1)$$

In Eq. 1,  $n$  is the phase angle of the CPE element and  $R_{ct}$  the charge-transfer resistance in parallel. The extracted  $C_{dl}$  values for each cortisol injection are reported in Figure 6-5c, showing an increase of capacitance with the injections equal to  $25 \pm 2$  nF/dec ( $n=3$ ). Considering that the gate area is  $0.3 \times 0.1$  cm<sup>2</sup>, the variation of capacitance is  $0.8 \pm 0.07$  μF/cm<sup>2</sup>dec, similar as previously reported using other types of electrodes coated with antibodies for cortisol detection[232].

To analyze how the variation of double-layer capacitance is amplified in the OEET configuration, a simplified OEET capacitive model can be employed to calculate the theoretical voltage in the solution considering the measured changes in gate capacitance and the capacitance of the channel[60], [128]. This model, introduced by Bernards and Malliaras[233], allows to use of standard thin-film transistor theory to calculate the theoretical  $I_{ds}$  current variations depending on the measured gate capacitance variations, applying the following formula in the linear regime[126]:

$$I_{ds} = \frac{Wt}{L} \mu C_v [(V_T - V_{gs})V_{ds} + \frac{V_{ds}^2}{2}] \quad (2)$$

where  $\frac{Wt}{L}$  is the geometrical factor,  $\mu$  the hole mobility,  $C_v$  the volumetric capacitance, and  $V_T$  the threshold voltage, defined as  $V_T = V_{pinch-off} - V_{solution}$ . The pinch off voltage  $V_{pinch-off}$  in Eq. 2 is equal to  $\frac{qp_0}{C_v}$ , with  $q$  being the elementary charge ( $1.6 \times 10^{-19}$  C) and  $p_0$  the intrinsic doping of the organic material ( $1.8 \times 10^{20} \text{ cm}^{-3}$ )[67].



*Figure 6-5: Sensing mechanism analysis. (a) Nyquist plots of the gate electrode tested at the different cortisol concentrations versus an Ag/AgCl wire ( $V_{dc}=0.6$  V,  $V_{ac}=10$  mV, frequency= $10^5$ -0.1 Hz). (b) Extracted variations of the real part of the impedance from the Nyquist plots at 0.1 Hz ( $n=3$ ). (c) Extracted variations of double-layer capacitances from the equivalent circuit. (d) Simulated current variations per decade of cortisol concentrations extracted from the simplified OECT capacitance model. The error bars represent the standard deviation from the average obtained from three devices. The impedance spectroscopy was performed in PBS 1X (0.15 M) following 5 minutes of incubation at the desired cortisol concentration. The gate electrodes had thiols/EDC/NHS/antibody on their surfaces.*



The capacitive model is reported in Figure 6-5d, and the solution voltage to be included in Eq. 2 can be calculated using the formula for a voltage divider:

$$V_{solution} = \frac{Z_{channel}}{Z_{gate} + Z_{channel}} V_{gs} = \frac{V_{gs}}{1 + \frac{C_{dl,channel}}{C_{dl,gate}}} \quad (3)$$

where  $Z_{channel/gate}$  is the respective impedance at the interface, simplified as a purely capacitive element. The volumetric capacitance  $C_v$  of the PEDOT:PSS material was also extracted from the impedance spectroscopy measurements (Figure S6-14), and it is equal to about 24 F/cm<sup>3</sup>, in agreement with previously reported values[67]. Considering that the term  $\frac{Wt}{L} \mu C_v$  in Eq. 2 is equivalent to  $\frac{G}{V_p} = \frac{g_m}{V_d}$ , and  $G = \frac{Wt}{L} \mu q p_0$  being the conductance of the organic material[234], the hole mobility was estimated to be 6 cm<sup>2</sup> Vs<sup>-1</sup>, similar to previously reported PEDOT:PSS values[67]. For the different channel geometries, the  $C_{dl,channel}$  values are then 2 μF for the very-short channel (volume 0.072 cm<sup>3</sup>), 14 μF for the short channel (volume 0.6 cm<sup>3</sup>), and 10 μF for the long channel (volume 0.4 cm<sup>3</sup>). Substituting the extracted  $C_{dl,channel}$  values and the  $C_{dl,gate}$  gate values for multiple cortisol concentrations in Eq. 3, and the previously mentioned parameters into the drain current Eq. 2, the  $\Delta I_{ds}$  variations per decade of cortisol changes in Figure 6-5d are obtained.

The extracted  $\Delta I_{ds}$  from the model are equal to  $67 \pm 9$  μA/dec for the very-short channel,  $8 \pm 1$  μA/dec for the short channel, and  $1 \pm 0.2$  μA/dec for the long-channel OECTs. The R<sup>2</sup> coefficient from the linear fitting is equal to 0.97 in all cases. The values are similar to experimental ones, particularly for the very-short channel designs (~50 μA/dec), as shown by superimposing the results in Fig. S9a. The smaller values obtained for short channels (Fig. S9b) could be due to the simplified capacitive model at the gate interface. On the other hand, the results confirm that an increase in double-layer capacitance causes the variation in drain current,  $\Delta I_{ds}$ , measured for our OECT configuration while experiencing cortisol binding events. These events transduce into a higher coupling with the PEDOT:PSS channel, decreasing the drain current due to the higher dedoping.

## 6.2.4 Sweat analysis

OECTs with very-short channels and EDC/NHS chemistry on the gate are validated with real sweat samples extracted during an indoor-cycling session (Figure 6-6). The testing protocol consists of first

measuring the baseline current of the OECT devices in PBS 1X, incubating the integrated devices for 5 minutes with sweat samples, and finally measuring the baseline shift in PBS 1X (Figure 6-6a). The sweat cortisol concentrations were previously measured by liquid chromatography-tandem mass spectrometry (LC-MS/MS) to validate our  $I_{ds}$  measurements. The samples are defined as high-concentrated if the cortisol concentration is above 10 nM or low-concentrated below 10 nM.

The time responses for two devices tested with low-concentrated (Figure 6-6b) and high-concentrated sweat cortisol (Figure 6-6c) are reported. The corresponding extracted  $\Delta I_{ds}$  are reported in Figure 6-6d at different stabilization times. The responses,  $\Delta I_{ds}$ , of the OECT sensors (at 250 seconds of stabilization) for several sweat samples are compared in Figure 6-6e with the results obtained using liquid chromatography-tandem mass spectrometry. The value for each sweat sample corresponds to a measurement performed with a fresh OECT device.

The antibody-coated flexible OECT devices correlate well with the sweat samples measured by LC-MS/MS. The t-test (1-tailed), considering all the measured current variations and the respective measured values by LC-MS/MS, shows a p-value  $<0.001$ ; hence the correlation between the variation in the OECTs and the LC-MS/MS measurements has high statistical significance. Then, the extracted Pearson coefficient of correlation ( $r$ ) equals 0.84. It increases to 0.93, excluding the one less correlated point below the line (Figure 6-6e). Our approach effectively demonstrates the potential of our wearable OECT biosensor for the point of care monitoring of cortisol concentration in sweat with direct sweat collection on the skin.

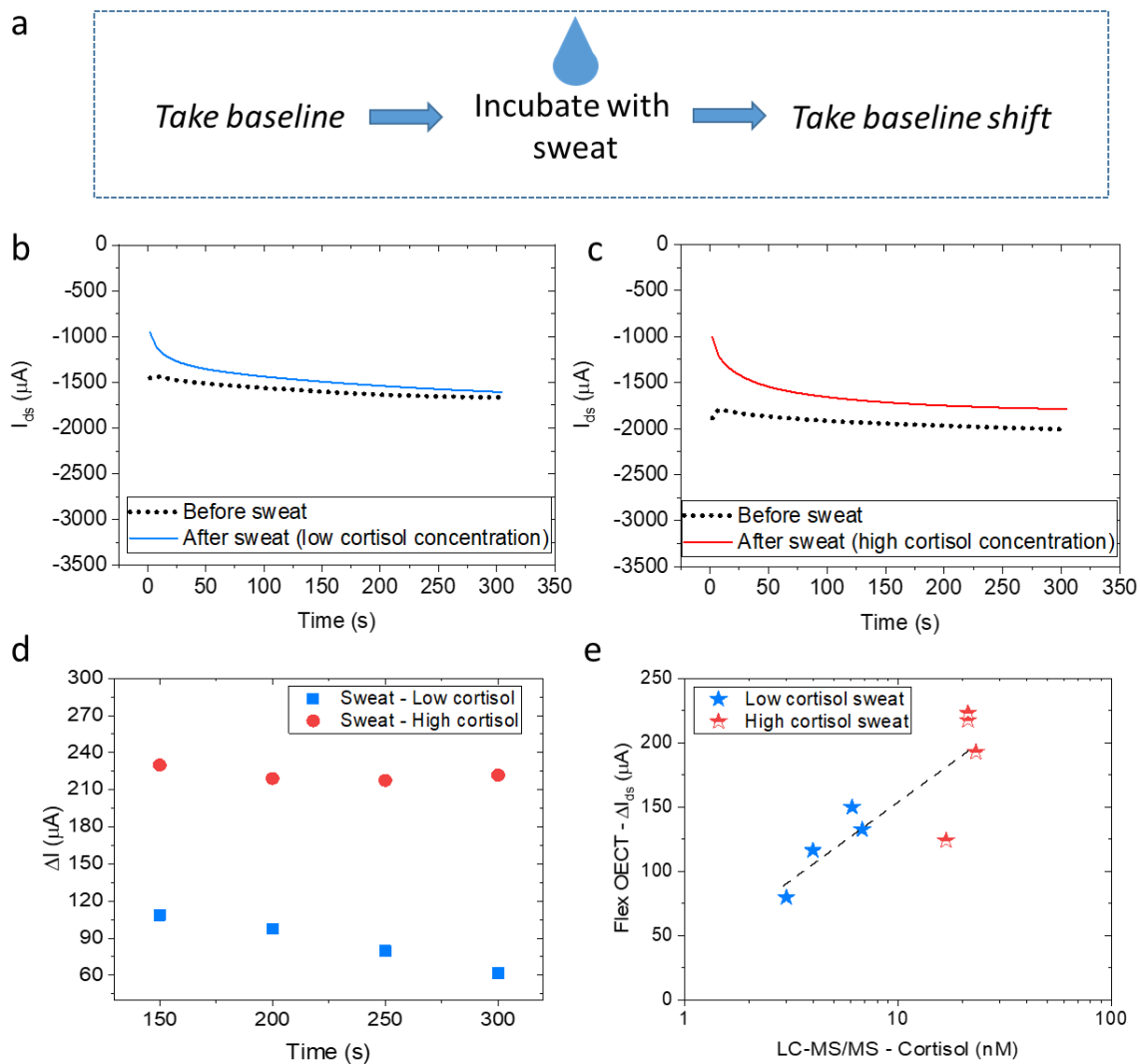


Figure 6-6: Real sweat testing. (a) Schematic of the protocol followed to test real sweat samples collected during indoor cycling and validated with liquid chromatography-tandem mass spectrometry. (b) Time response of the device at low cortisol concentration. (c) Time response of the device at high cortisol concentration. (d) Extracted variations drain current through the baseline shift before and after the sweat sample. (e) Comparison with the values measured by LC-MS/MS and the OECTs current variations measured after 250 s of stabilization. The OECT tests are at a fixed drain voltage  $V_{ds} = -0.4$  V and gate voltage  $V_{gs} = 0.6$  V.

## 6.3 Discussion

This work reports on integrated, antibody-coated organic electrochemical transistors for cortisol detection. Compared to the OECT state-of-the-art,[167] our optimized sensors exhibit a higher sensitivity (20X at 50  $\mu\text{A}/\text{dec}$ ) and a wider dynamic range of 1 – 1000 nM, making them relevant for real sweat analysis.[222] The sensitivity of the wearable OECT sensor was demonstrated after only 5 minutes of incubation using a fully-integrated sensor, both with standard cortisol solutions and real sweat. The correlation found between the OECT electrical models and the extracted impedance variations at the antibody-coated gate interface highlights the sensing mechanism involved, providing useful information for further optimization. These impedance variations at the gate interface, possibly due to conformational changes during the binding[101], need to be further investigated towards a more standardized electrical modeling of antibody-antigen binding events for these particular devices.

Considering our calibration measurements performed at different cortisol concentrations in PBS (n=4), a plot including the extracted  $I_{\text{ds}}$  variations with the sweat samples measured by LC-MS/MS and our calibration curve is presented in Figure S6-70. The limit of detection of our OECT sensors was measured to be 100 pM in PBS. The sensitivity slope measured detecting cortisol in real sweat (Figure 6-6e) is about two times higher than in PBS (Figure S6-70) for the flexible OECT devices. This increase is measured because there are potential interfering species in sweat (steroids, metabolites, drugs, or similar isomers), making it difficult to accurately calibrate the OECT sensors in standard PBS. The values reported using portable electrochemical or colorimetric techniques are generally higher than values obtained with LC-MS/MS technique[222], [235], similarly to ELISA methods[21], [167], [226], possibly due to the mentioned interfering species. Hence, our approach of measuring the  $\Delta I_{\text{ds}}$  current variations in relation to LC-MS/MS measurements (Figure 6-6e) can be used to calibrate precisely anti-cortisol antibody-coated devices for real sweat applications. The flexible OECT sensor combined with the integrated microfluidic collection reservoir could effectively determine the concentration of the stress-biomarker cortisol with direct *in situ* sweat collection and measurement in a wearable fashion.

Finally, this work also shows strategies to functionalize the devices without damaging the organic layer and integrate them into a fluidic system, which could also be applied to measure other antigens. Multiple organic transistors could be integrated into the same platform, including unfunctionalized and functionalized with different bio-layers, towards multiplexed monitoring of analytes in various biofluids.[78], [83], [186], [236]

## 6.4 Methods

### 6.4.1 Biofunctionalization

All the chemicals have been purchased from Sigma Aldrich unless otherwise stated. The thiol monolayers on the gold electrodes were formed using 3-mercaptopropionic acid (3-MPA,  $\geq 99\%$ ). A solution of 250 mM was always freshly prepared, adding 418  $\mu\text{L}$  of 3-MPA in a total volume of DI water equal to 20 mL. About 50  $\mu\text{L}$  of the diluted solution was left on the electrodes overnight. This step was followed by cleaning the electrodes with DI water and drying with a nitrogen gun. Then, the activation of the carboxylic groups for an amine reaction was performed, adding either 0.05 M of EDC (N-(3-Dimethylaminopropyl)-N-ethylcarbodiimide hydrochloride) or 0.05 M EDC + 0.03 M NHS (N-hydroxysuccinimide) in PBS, on the gold electrodes for 2 hours. Precisely, 95.8 mg of EDC, with or w/o 34.5 mg of NHS, were added in a total volume of 10 mL of PBS. Subsequently, the electrodes were quickly rinsed with PBS and dried with a nitrogen gun, finally adding 5  $\mu\text{L}$  of anti-cortisol antibody solution. The electrodes were left for two hours at  $4^\circ\text{C}$  in this condition. The anti-cortisol antibody was purchased from Abcam (Mouse monoclonal [XM210] to cortisol, AB1949) and diluted to a 300 mg/ml concentration in PBS.

The diluted antibody solution was separated into several aliquots and frozen before use. Then, after a washing step with the same PBS, the devices were tested for cortisol sensing. The PBS 1X solution was made using 0.001 M of monopotassium phosphate ( $\text{KH}_2\text{PO}_4$ ), 0.15 M of NaCl, and 0.003 M of disodium phosphate ( $\text{Na}_2\text{HPO}_4$ ). The X-ray photoelectron spectroscopy (XPS) measurements at the different functionalization steps were carried out on an Axis Supra (Kratos Analytical) using the monochromated Ka X-ray line from an aluminum anode. The samples were electrically insulated from the sample holder and an electron flood gun was used to compensate for charging effects. The data were referenced at 84 eV with the Au 4f peak.

### 6.4.2 Device fabrication

The OECTs are fabricated on a thin polyimide substrate (125  $\mu\text{m}$ -thick, DuPont Kapton HN) using a PEDOT:PSS ink for their organic channels (2 printed layers of  $\sim 100$  nm in thickness). Gold was evaporated for the gate and the source/drain contacts through a shadow mask ( $\sim 20$  nm-thick titanium or chromium adhesion layer/ $\sim 100$  nm-gold layer). The titanium layer showed higher stability in the transfer and impedance measurements compared to a chromium layer hence it was chosen for the final tests. After the gold evaporation, the PEDOT:PSS ink is deposited using a Dimatix DMP-2800 printer (Fujifilm) with 10 pL cartridges (DMC-11610). The ink is prepared by mixing a PEDOT:PSS solution (1.3 wt % in  $\text{H}_2\text{O}$ )

with 5 vol % of dimethyl sulfoxide (DMSO). The mixture is sonicated for 10 min and then filtered with a 1  $\mu\text{m}$  pore-size filter when filling the Dimatix cartridges. The substrate is treated with oxygen plasma before printing. The Dimatix plate is kept at 40 °C during the printing and an annealing step is performed after at 120°C for 20 min. The design includes a gate active area of about 3 x 1 mm<sup>2</sup> and three different channel areas of 1 x 4 mm<sup>2</sup>, 3 x 2 mm<sup>2</sup>, and 3 x 0.24 mm<sup>2</sup>. The gap between the gate and the channel is about 1 mm, and the gold source and drain contacts have a respective length of 1 mm. The thickness of printed layers are measured with a Keyence VK-X1000 Series laser scanning microscope, with 150x magnification and laser mode. The gold gates on polyimide were made separately for their functionalization, and subsequently assembled in the OECT configuration using a double-sided acrylic adhesive (ARcare 92712) on polyimide. The OECTs are integrated into a flexible microfluidic system composed of PET foils (125  $\mu\text{m}$ -thick) and acrylic adhesives for the demonstrator on the skin. The PET foils were patterned using a CO<sub>2</sub> laser cutter (Trotec Speedy300) to define the shape of the micro-fluidic channel and the cover with the inlets (500  $\mu\text{m}$ -diameter). The PET fluidics system was made by lamination of the patterned PET channel with the PET top cover, bonded using the double-side acrylic adhesive. The adhesive was used also to fix the fluidics system to the organic transistor arrays on polyimide substrate. On top of the multi-inlets cover, a double-sided medical-grade adhesive (ARcare 90445) shaped as the fluidic channel was added to contact the skin.

### 6.4.3 *Electrochemical testing*

Cortisol (hydrocortisone, AB141250, Abcam) was used for the sensing measurements. An initial stock solution of 0.01 M was prepared in ethanol, then multiple concentrations (1 nM – 1  $\mu\text{M}$ ) of cortisol were prepared in PBS 1X, divided into aliquots, and frozen before use at -20 °C. The devices are tested using PMMA reservoirs containing the different electrolytes. The PMMA plates (3 mm thick) were cut with the CO<sub>2</sub> laser into a rectangular shape with 5 x 3 mm<sup>2</sup> gap, and fixed onto the polyimide substrate through the double-sided acrylic tape. A total volume of 50  $\mu\text{L}$  of solution in the reservoir was employed in all the tests. The protocol for the testing in real-time included an initial stabilization of the devices for ~500 s in PBS 1X-only (no cortisol), then the removal of the solution with a pipette, and the addition of the PBS solutions containing cortisol for ~300 s/concentration. Multiple cortisol solutions were tested in real-time with the same device, removing the previous solution and adding the new solution of an increased cortisol concentration. For the testing of the real sweat samples, the devices were first stabilized for ~300 s in PBS-only, then incubated with the desired sweat sample (1 device/sweat sample) for ~300 s, washed with DI water, and then ~300 s in PBS-only was added again for measuring current shift. The OECTs electrical measurements (electrical characteristics and time measurements) were acquired using a semiconductor parameter analyzer (Agilent 4155A). For the electrochemical impedance spectroscopy (EIS)

measurements, a potentiostat/galvanostat (Multi Autolab M204, Metrohm) is employed. A gold electrode or a PEDOT:PSS electrode (with a gold contact) was used as the working electrode and a silver/silver chloride (Ag/AgCl) wire as the reference electrode. The frequency was swept from  $10^5$  to 0.1 Hz at an amplitude of 10 mV ( $V_{AC}$ ). A polarization voltage ( $V_{DC}$ ) of 0.6 V was used for the gold gate as the applied gate voltage during the sensing measurements. A  $V_{DC}$  of 0.1 V was used for the PEDOT:PSS electrode.

#### *6.4.4 Sweat collection*

All eccrine sweat samples were handled in accordance with the approved ethical agreement N° 2019 01235 of the Canton of Vaud, Switzerland. Sweat collection was done in an environment at  $25.7 \pm 1.1^\circ\text{C}$  and  $49 \pm 5\%$  humidity. All sweat samples were collected using the absorbent patch method on the middle back of the subject. The sweat collection started after 10 minutes of biking to initiate sweating. The body regions were cleaned with alcohol, then deionized water, and dried with gauze pads before applying the absorbent patches onto these body regions. Each patch consisted of a sterilized nonwoven compress with a covered area of  $112.5\text{ cm}^2$  and an absorbing capacity of around 8.0 g (Promedical AG, Glarus, Switzerland). The patches are covered with an impermeable fabric and were fixed onto the skin in an airtight manner using a porous adhesive on top (nonwoven micropore tape 3M™ Micropore™, 3M Company, St. Paul, USA). After 20 min of continuous cycling, to extract the sweat samples, patches were placed in the barrel of a plastic syringe and squeezed with a syringe plunger. Sweat was then conserved into a sealed tube at  $-20^\circ\text{C}$  before chemical analysis.

#### *6.4.5 Liquid chromatography-tandem mass spectrometry*

Calibrators, samples, and controls (1000  $\mu\text{L}$ ) were placed in Eppendorf tubes (2.0 ml); under a fume hood, the IS solution was then added to each tube (1000  $\mu\text{L}$ ), each one undergoing a short vortex. The tubes were centrifuged (20160 g, 5 min,  $4^\circ\text{C}$ ) then shortly stored at  $-80^\circ\text{C}$  (10 min). The resulting upper organic phase (800  $\mu\text{L}$ ) was transferred to a 96-well microplate; the samples were completely dried down under  $\text{N}_2$  and then reconstituted by adding a solution of methanol:ultrapure  $\text{H}_2\text{O}$  4:6 (75  $\mu\text{L}$ ), briefly agitated, and then centrifuged (3220 g, 5 min, RT). Samples were transferred to another 96-well microplate (700  $\mu\text{L}$  well volume), sealed with a sealing mat, centrifuged (3220 g, 5 min, RT), and placed in the autosampler for liquid chromatography-tandem mass spectrometry (LC-MS/MS) analysis. The LC-MS/MS system is comprised of an ExionLC system coupled to a 6500+ Q-Trap mass spectrometer (SCIEX) with electrospray ionization operating in positive ion mode and operating in the multiple reaction monitoring (MRM) mode. The system was piloted by Analyst software (version 1.7.2). Samples were injected onto a Zorbax Eclipse Plus C18 column (2.1 x 50 mm, 1.8  $\mu\text{m}$ , Agilent). The flow rate was 400  $\mu\text{L}/\text{min}$ , and the column was placed in a column oven ( $30^\circ\text{C}$ ). The mobile phase comprised ultrapure  $\text{H}_2\text{O}$

(A) and methanol with 0.001% formic acid (B). The starting mobile phase conditions were A = 60% and B = 40%, gradients were immediately employed: A = 50% and B = 50% (1.00 min), then A = 42% and B = 58% (5.50 min), A = 20% and B = 80% (7.00 min), A = 0% and B = 100% (8 min) which was held for a further 2 min, then back to A = 60% and B = 40% (12.00 min) held for a final 2 minutes. The mass spectrometer ion spray voltage was set to 5500 V, with a curtain gas of 20.0 and a temperature of 600 °C. The transitions used in the scheduled MRM mode were as follows: 363.2 / 121.1 and 363.2 / 91.1 (quantifier and qualifier for cortisol, respectively) and 367.3 / 121.1 (d4-cortisol). The declustering potential was 76 V, and the collision energy was 29 V for the quantifier transitions and 83 V for the qualifier. LC-MS/MS data processing was performed using SCIEX OS software (version 1.7.0.36606).



## 6.5 Supporting Information of Chapter 6

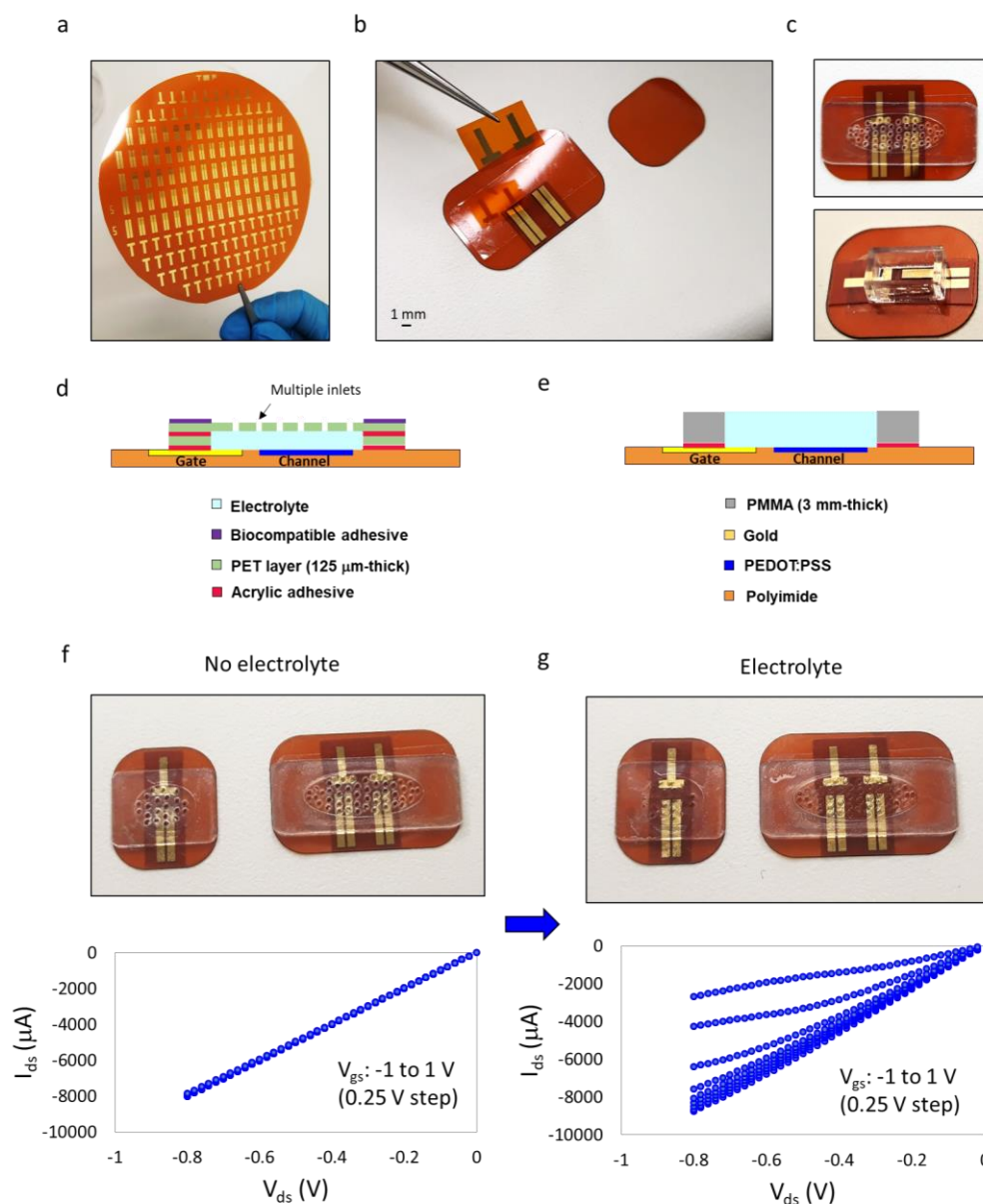


Figure S6-7: OECT sensors fabrication and assembly. (a) Wafer-like polyimide substrate with the fabricated devices. (b) Assembly of the gate electrode on the substrate through acrylic adhesive. (c) Assembly of the microfluidics to form the wearable sticker and assembly of the reservoir. (d) Cross-section with the multiple plastic layers and adhesives for the microfluidics, and (e) for the reservoirs. (f) Image and output characteristics of the integrated devices into the microfluidics without the electrolyte and (g) with the electrolyte (PBS 1X, W/L=12.5).

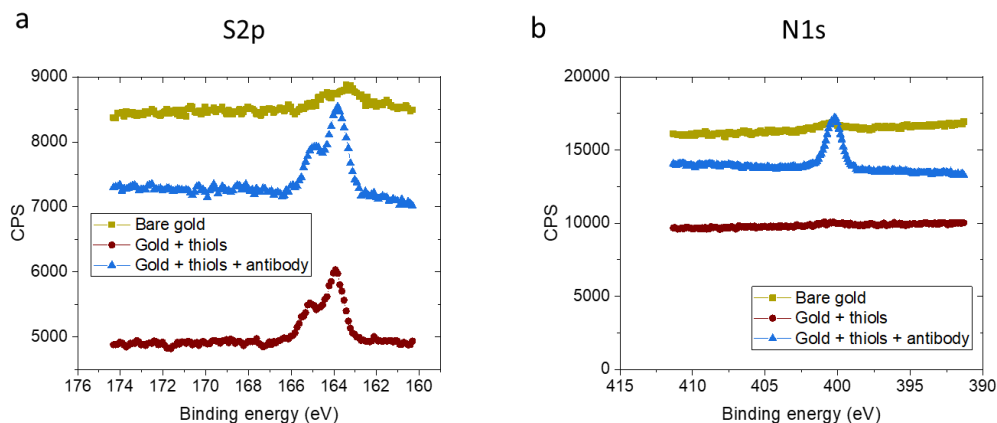


Figure S6-8: X-ray photoelectron spectra on gold gates. (a) S2p and (b) N1s peaks of bare gold electrodes, gold electrodes with thiol monolayers, and gold electrodes with capture antibody after thiol activation. The thiol activation was done using EDC chemistry.

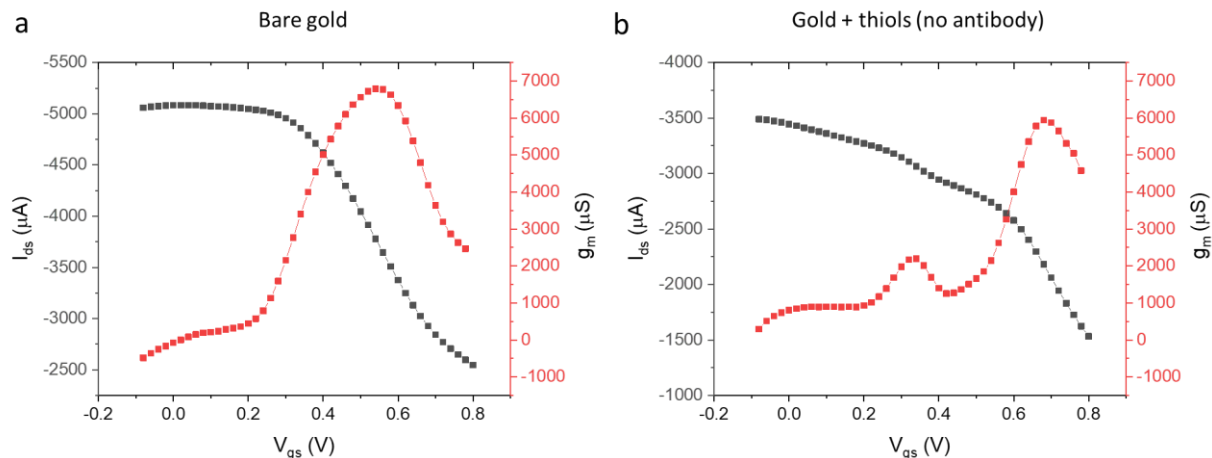


Figure S6-9: Thiol functionalization and characteristics. (a) Transfer characteristics of the transistors with bare gold gate electrodes. (b) Transfer characteristics of the transistors with gate electrodes and thiol monolayer (without antibody and thiol activation). The devices have a  $W/L=12.5$  (very short channel), and a drain voltage  $V_{ds} = -0.4$  V. The tests are performed in PBS 1X (0.15 M), pH 7.

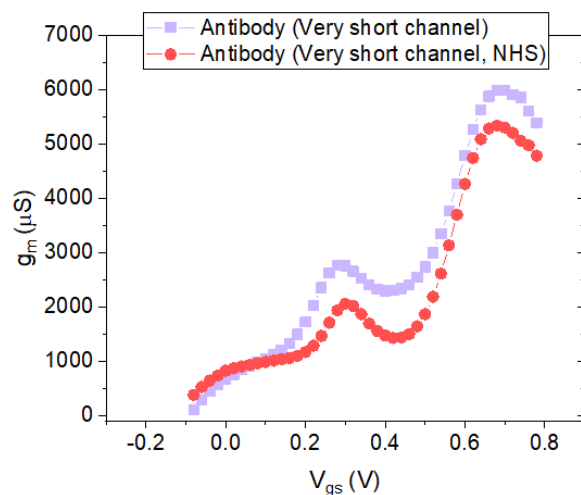


Figure S6-10: Different thiol activation. Transfer characteristics of the transistors with the antibody on the gold gates and two different thiol activations before the antibody are immobilized. The device for which NHS is specified in the label had an EDC/NHS chemistry. The devices have a  $W/L=12.5$  (very short channel), and a drain voltage  $V_{ds} = -0.4$  V. The tests are performed in PBS 1X (0.15 M), pH 7.

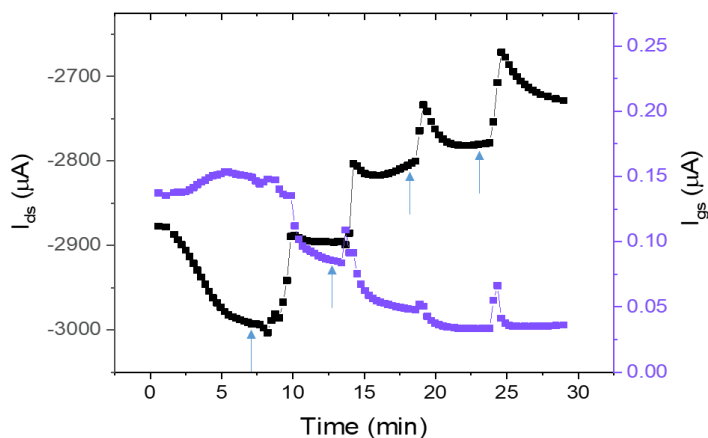


Figure S6-11: Leakage current. Simultaneous  $I_{ds}$  and  $I_{gs}$  current variation during the real-time sensing measurement with multiple subsequent cortisol injections (1, 10, 100, and 1000 nM). The devices have a  $W/L=12.5$  (very short channel), an EDC/NHS chemistry for the thiol activation and antibody immobilization. They are biased by applying a drain voltage  $V_{ds} = -0.4$  V and a gate voltage  $V_{gs} = 0.6$  V. The tests are performed in PBS 1X (0.15 M), pH 7.

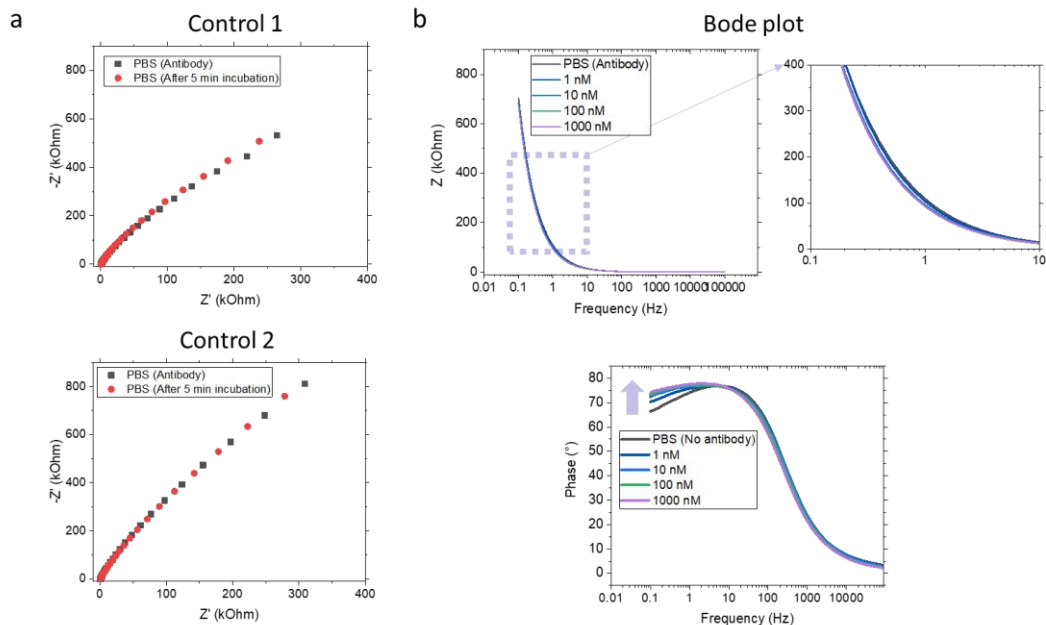


Figure S6-12: Impedance spectroscopy. (a) Control experiments showing the Nyquist plots of two control gates, having the antibody on the gates and incubated with only PBS (no cortisol) for 5 minutes. (b) Example of the Bode plot for different cortisol concentrations. The measurements are performed at  $V_{dc}=0.6$  V,  $V_{ac}=10$  mV, frequency= $10^5$ -0.1 Hz with a two-electrode setup versus an Ag/AgCl wire.

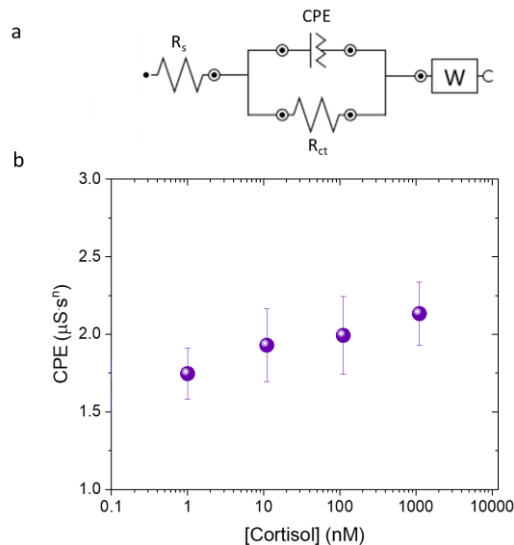


Figure S6-13: Impedance spectroscopy on the gate electrode. (a) Equivalent circuit used to fit the impedance spectra, including a constant phase element (CPE). (b) The extracted double layer capacitance from the model for three devices. All the CPE elements had a constant phase equal to 0.9 or higher.

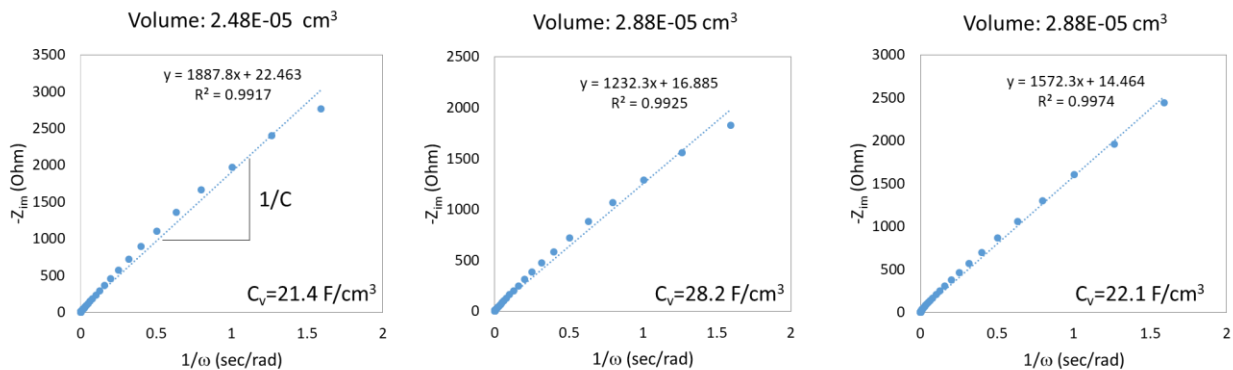


Figure S6-14: PEDOT:PSS impedance. Extraction of the double-layer capacitance and the relative volumetric capacitance ( $C_v$ ) of three different PEDOT:PSS electrodes from the imaginary impedance versus the inverse of the angular frequency. The measurements are performed at  $V_{dc}=0.1$  V,  $V_{ac}=10$  mV, frequency= $10^5$ -0.1 Hz with a two-electrode setup versus an Ag/AgCl wire.

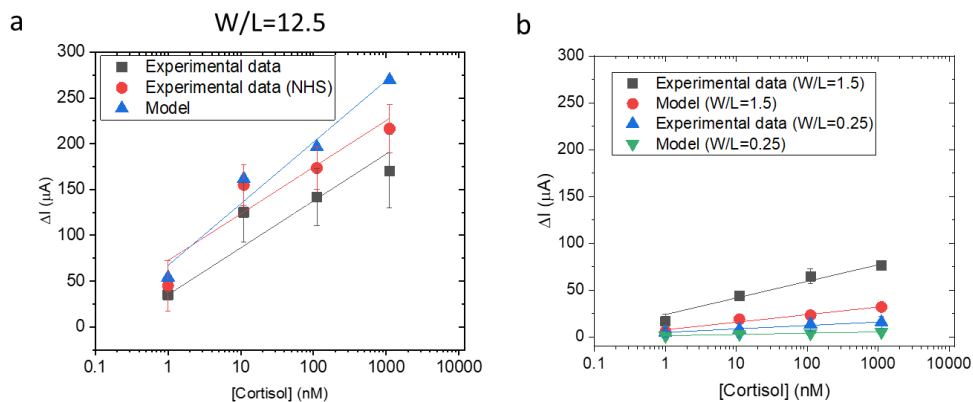


Figure S6-15: OECT electrical model for cortisol sensing and experimental results. (a) Extracted  $\Delta I_{ds}$  per cortisol concentration from the OECT electrical model and corresponding experimental values for OECTs with very-short channels ( $W/L=12.5$ ), and (b) with short-channels ( $W/L=1.5$ ) and long-channels ( $W/L=0.25$ ). The graphs include the linear fitting of the sensing results for each condition.

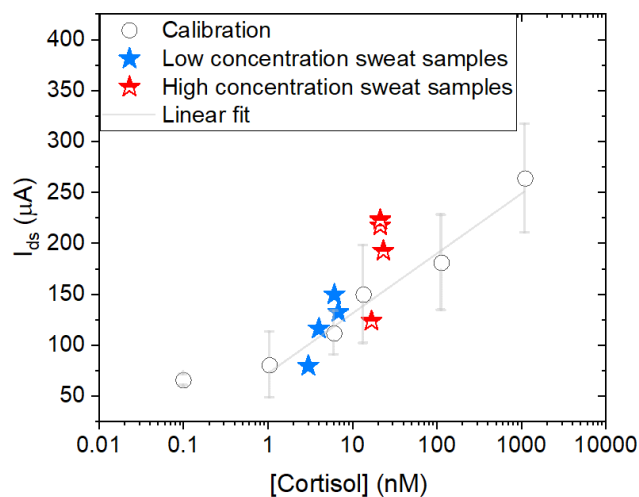


Figure S6-16: Comparison with the values measured by liquid chromatography-tandem mass spectrometry and the OECTs, considering the current variations measured from the OECT devices (at 250 s), and the calibration curve with a standard deviation for  $n=4$  OECTs. The calibration includes a correction due to noise variations of the sensors during the injections, shifting upwards the calibration of 6  $\mu\text{A}/\text{dec}$ . The linear fitting is performed excluding the calibration point at 100 pM. The OECT tests are at a fixed drain voltage  $V_{ds}=-0.4$  V and gate voltage  $V_{gs}=0.6$  V.

## Chapter 7 Integrated multi-OECT platform for multiplexed sweat analysis (Paper V)

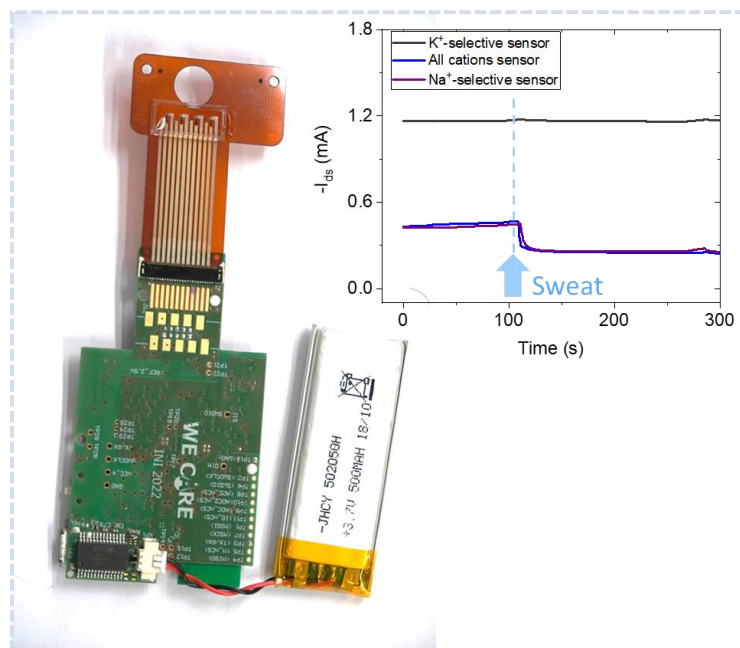


Figure 7-1: Graphical abstract. Integrated multi-ion OECT platform for multiplexed sweat analysis.

Organic electrochemical transistors are emerging as prominent biochemical sensors for multi-analyte detection, including ions, metabolites, hormones, or viruses. However, the implementation of the devices is mainly limited to a single-analyte detection and a single-shot measurement in a non-integrated, rigid configuration. Here, optimized technology and integration processes enable fully-integrated inkjet-printed OECT platforms on flexible substrates for simultaneous and real-time multi-ion sensing. The combination of miniaturized OECTs, including sensors covered with potassium-selective and sodium-selective membranes, as well as sensors with a bare PEDOT layer, and the development of a portable board for sensor read-out, allows the multiplexed discrimination of different cations in the same electrolytic solution. The devices exhibit high sensitivities of  $\sim 10$ - $20$  %/dec of ionic concentrations in the respective sweat concentration ranges. The platforms effectively quantify ions in real human sweat samples, with values correlated with commercial ion sensors. The developed OECT sensors could be used as a wearable system to enable the real-time monitoring of the hydration status of individuals.

## 7.1 Introduction

The monitoring of biofluids that can be non-invasively accessed, such as sweat, tears, and saliva, could allow the continuous or point-of-care analysis of various physiological and health parameters.[5] Sweat is one of the main biofluids of interest since it is the easiest to access non-invasively with a wearable patch integrating biochemical sensors.[6]

Among sweat analytes, sodium ( $\text{Na}^+$ ) and chloride ( $\text{Cl}^-$ ) ions are concentrated in sweat, going from  $\sim 10$  mM to  $\sim 100$  mM.[27] The clinical relevance of monitoring these sweat ions could be assessed only with a personalized and continuous analysis, taking into account multiple parameters depending on the individual (genetics, sweat losses, sweat rate, hydration, sports effort, and so on).[18], [28], [29], [144] It is known that genetics plays an important role in the sweat reabsorption. After prolonged endurance exercise, the so-called “salty sweaters”, which lose high quantities of  $\text{Na}^+$  and  $\text{Cl}^-$ , could suffer from hyponatremia,[144] and personalized wearable sensors could be advantageous to monitor these losses and prevent dangerous situations. On the other hand, sweat potassium ( $\text{K}^+$ ) ion has a passive transport and a lower concentration in sweat (from  $\sim 1$  mM up to  $\sim 10$  mM),[27] and recent studies show that it is better correlated with blood levels.[34] Overall, novel wearable technologies for continuous monitoring could help to highlight the clinical relevance of ion measurements in sweat during exercise.

Electrochemical sensors, based on the amperometric[10], [12], [13] and potentiometric principles,[6], [12], [14] have been mainly considered for wearable applications. They are often integrated into flexible, wearable platforms on the skin,[6]–[8] eyeglasses,[9] or textiles.[11] However, transistors are gaining interest for wearable applications thanks to their simple miniaturization, integration into portable electronic devices, low output impedance, and high sensitivities.[4], [20], [39], [40] Among them, the unique mixed ionic-electronic charges interaction in Organic Electrochemical Transistors (OECTs) sets them apart from conventional transistor-based sensors. The devices are composed of an organic channel with source and drain contacts and a gate electrode, and the channel and the gate are in contact with the electrolyte solution. While standard field-effect transistors form an electrical double-layer between the channel and the electrolyte in the presence of ions, in OECTs, the ions permeate the organic channel.[42] This phenomenon causes a volumetric change of the doping state of the organic material, with significant modulations of drain current at very low gate voltages and very high current amplification.[50]

OECT devices are generally fabricated on glass, with lithography-patterned organic channels (generally made of poly(3,4-ethylenedioxythiophene):poly(styrene sulfonate), PEDOT:PSS) and contacts and external gate electrodes not integrated into the substrate.[68], [69], [72], [77], [79], [107], [108], [110] One of the highest integration levels in OECTs devices was achieved by combining flexible ion-selective



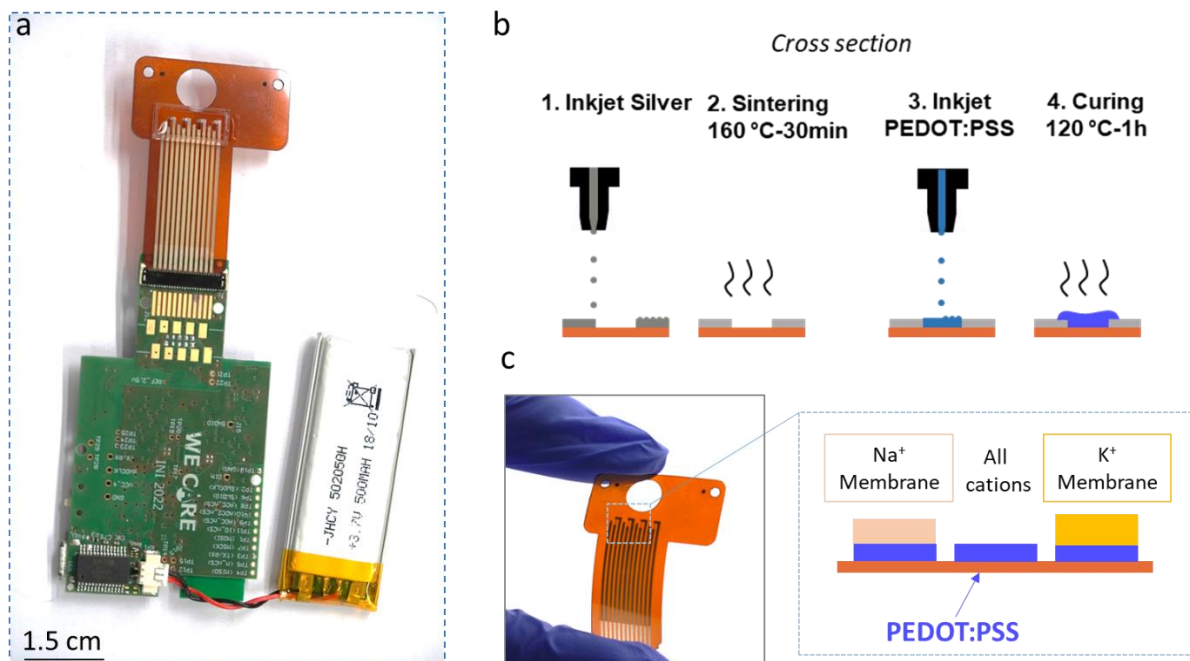
OECTs with standard thin-film transistors.[78] The voltage at the output of a multiplexer circuit was measured at increased ion concentrations, but the real-time sensing characteristics were not studied and reported. Another work showed ion-selective OECT devices for calcium and ammonium ions detection, integrating the pseudo-reference gate electrodes into the substrate and the ion-selective membranes on the PEDOT:PSS channel.[75] They performed single-shot time measurements on the skin for a few seconds. Also, the use of flexible and inkjet-printed OECTs for  $\text{Na}^+$ ,  $\text{K}^+$ , and  $\text{H}^+$  sensing was reported with selective membranes and real-time sensing characteristics, but without simultaneous sensing with multiple OECTs and no proof of sensing in real biofluids.[186]

Herein, we report on flexible and printed platforms integrating OECT sensor arrays for simultaneous  $\text{Na}^+$  and  $\text{K}^+$  discrimination in human sweat. In combination with a custom-made wireless read-out electronic board, the sensing responses of the OECT devices are measured in real-time for common electrolyte solutions. The sensors are fully printed for simple digital integration onto flexible substrates, with the ion-selective membranes integrated through a simple stencil-printing process on the PEDOT:PSS channel. The platforms, including sensors covered with  $\text{K}^+$ -selective and  $\text{Na}^+$ -selective membranes, as well as sensors with a bare PEDOT layer, show high sensitivities (10-20 %/dec) and could successfully discriminate  $\text{K}^+$  and  $\text{Na}^+$  concentrations in real sweat samples extracted during sports conditions. Compared to standard potentiometric ion sensors, the OECT devices are more compact and miniaturized, and by the addition of other functional layers, a wider range of analytes could be easily targeted. The developed platforms could be used in a wearable fashion with an integrated microfluidic system for real-time and continuous sweat analysis.

## 7.2 Results and Discussion

### 7.2.1 OECT platforms

To address the challenge of continuous multi-ions monitoring for dehydration studies, we integrated four miniaturized organic transistors into the same flexible platform (Figure 7-2a). As the image shows, the sensing patch is designed to be integrated with a small read-out PCB (65 mm x 35 mm), enabling real-time measurements on the human skin. The electrodes are inkjet-printed (Figure 7-2b), using a silver nanoparticle ink for the source and drain and gate of the devices, and the conducting polymer PEDOT:PSS for their channel.



*Figure 7-2: OECT array for multi-ion sensing. (a) Picture showing the integrated patch with four organic electrochemical transistors and the wearable read-out electronics. (b) Cross section with the inkjet printing and sintering fabrication steps. (c) Application for ion-selective sensing by coating some OECTs with ion-selective membranes and optical image of the respective membrane.*

PEDOT:PSS has two phases, one with electronic charge carriers in the form of polarons (PEDOT phase) and one with the ionic charge carriers (PSS phase).[52] Once a positive gate voltage is applied, the current flowing in the organic channel decreases due to the volumetric de-doping derived from the injections of cations from the electrolyte into the channel.[50] But, with the addition of ion-selective membranes, only the cations of interest can, with a certain selectivity, contribute to the de-doping of the channel.[186] In this work, we originally combine OECT sensors with bare PEDOT:PSS channels (sensitive to all cations in solutions) and with ion-selective membranes (ISMs) for  $\text{Na}^+$ , and  $\text{K}^+$ , to have simultaneous signal patterns from multiple ions.

The integrated inkjet-printed Ag gate electrodes are oxidized into Ag/AgCl to provide higher stability, acting as pseudo-references for the multi-ion OECTs.[78] The chloridation was performed electrochemically, with the application of scanning voltages up to 1 V in solutions containing 140 mM of chloride. To investigate the AgCl formation, scanning electron microscopy (SEM)/Energy Dispersive Spectroscopy (EDS) is performed on the silver gate before (Figure 7-3a,c) and after (Figure 7-3b,d) the electrochemical process. As seen from the SEM images, the surface of the printed Ag electrodes is oxidized, forming AgCl crystals.[237] The calculated element weight percentage after the partial

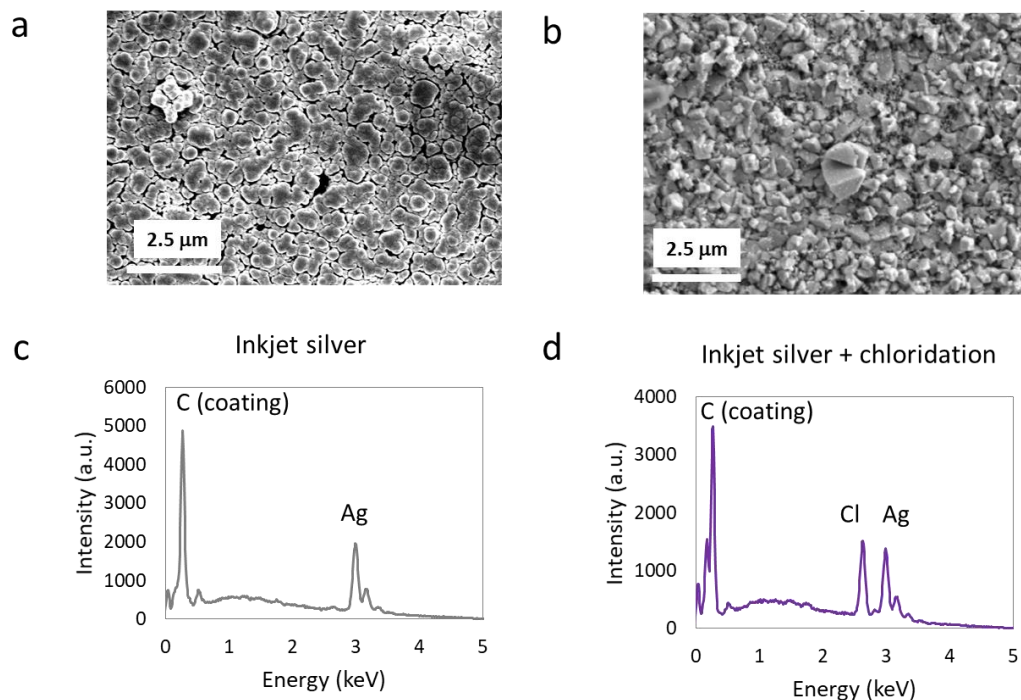


Figure 7-3: Pseudo-reference OECT gate electrode. SEM images before (a) and after (b) chloridation of the gate electrodes, and respective EDS measurements (c,d).

chloridation is measured by EDS to be 18.7 wt% Cl and 73.5 wt% Ag. The experiment confirms that the printed Ag is converted to Ag/AgCl through the electrochemical experiment.

### 7.2.2 Characterization of ion-sensitive and ion-selective OECTs

The integrated multi-ion OECT devices are characterized in an electrolyte solution containing 120 mM NaCl and 20 mM KCl by using the portable electronic board (Figure 7-4). The output characteristics (drain-source current  $I_{\text{ds}}$  versus drain-source voltage  $V_{\text{ds}}$ ) can be seen in Figure 7-4a-c, and the transfers characteristics ( $I_{\text{ds}}$  versus gate-source voltage  $V_{\text{gs}}$ ) in Figure 7-4d, for devices without and with ISMs on the PEDOT:PSS channels. The respective characteristics are acquired simultaneously for the different OECTs. As it can be seen from the output characteristics, the devices show an effective  $I_{\text{ds}}$  current modulation when changing the gate voltages through the integrated pseudo-reference gate, similarly without (Figure 7-4a) or with (Figure 7-4b,c) the membranes.

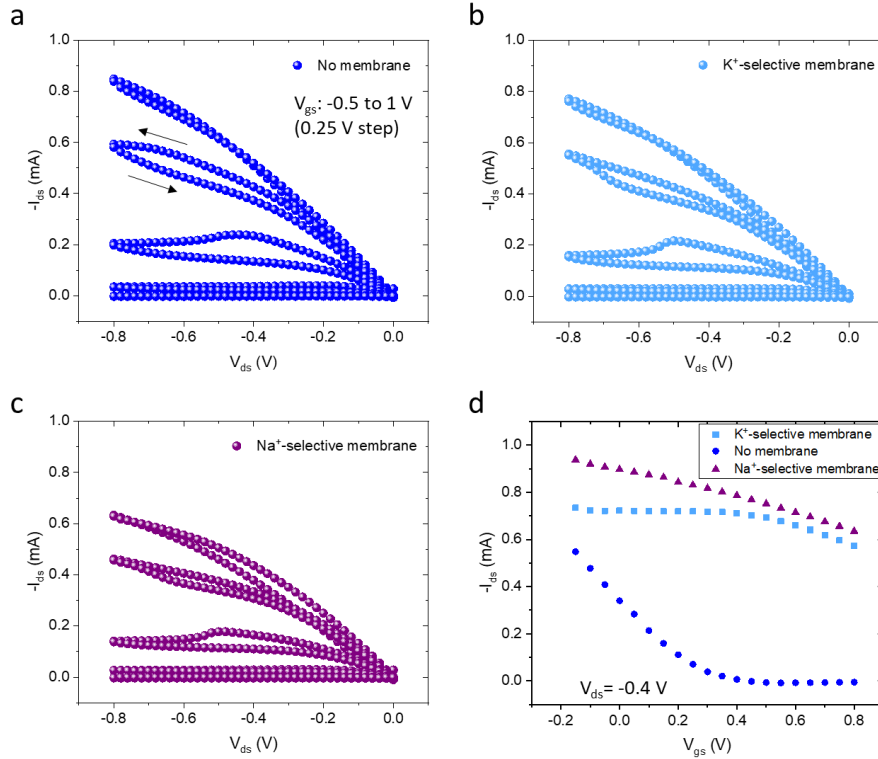


Figure 7-4: Electrical characterization of the organic electrochemical transistors with and without different ion-selective membranes. (a) Output characteristics without any membrane, (b) output characteristics with the  $K^+$  membrane, (c) output characteristics with the  $Na^+$  membrane, and (d) transfer characteristics with and without membranes. The measurements are performed with the portable electronics in a solution containing 120 mM NaCl and 20 mM KCl.

Considering the transfer characteristics, the OECTs devices without the membranes have a high current modulation close to 0 V, while for the devices with the membranes starts at higher voltages (after 0.6 V, Figure 7-4d). The reason for this shift is that the transfer characteristics were acquired three times faster than the output characteristics (208 mV/s compared to 80 mV/s) with the electronics, and the presence of the membranes increases the time response of the devices.[238] The transconductance can be calculated as  $g_m = \Delta I_{ds} / \Delta I_{gs}$ , as reported in Figure S7-7. Considering the results from multiple devices, the  $g_m$  was extracted to be  $0.7 \pm 0.4$  mS ( $n=4$ ) without the membrane,  $0.7 \pm 0.5$  mS ( $n=3$ ) with the  $Na^+$  membrane and  $0.3 \pm 0.2$  mS ( $n=4$ ) with the  $K^+$  membrane. The high standard deviation in these measurements is due to the printing fabrication process[238] since it includes integrated devices from three different fabrication batches.

It was observed that the  $g_m$  peak was shifted for some of the tested OECTs with the membranes, possibly due to variability in the deposition process, which requires further optimization. Different

membranes thicknesses were shown to influence the shift of the transconductance peak.[238] An example with the optical images of the  $\text{Na}^+$  and  $\text{K}^+$  membranes after the casting process is shown in Figure S7-7b,d. The thickness of the  $\text{K}^+$ -selective membrane is measured to be  $\sim 40 \mu\text{m}$  (Figure S7-7c), and the thickness of the  $\text{Na}^+$ -selective membrane  $\sim 30 \mu\text{m}$  (Figure S7-7d). Further studies will be necessary to measure the thickness variability after multiple deposition processes and the relative influence on the  $g_m$  repeatability.

### 7.2.3 Multi-analyte detection using the integrated OECT array

The sensing platform, including an OECT with a  $\text{K}^+$ -membrane, a  $\text{Na}^+$  membrane, and a device without any membrane, are tested operating in common electrolyte solutions at the relevant sweat concentration ranges, as shown in Figure 7-5.

The recordings are performed simultaneously, always starting with deionized water (DI) to record the baseline signal. Then, the tests are carried out with NaCl solutions-only (Figure 7-5a), KCl solutions-only (Figure 7-5b), and solutions with a mix of KCl and NaCl (Figure 7-5c). From these signals, the normalized response of the devices, calculated as  $(I_{ds,DI} - I_{ds,concentration})/I_{ds,DI}$ , can be extracted. These normalized signals are calculated from the real-time multiplexed sensing patterns of several platforms from multiple fabrication batches to analyze the reliability of the devices and reported in Figure S7-8. In all the cases, with the membranes, the normalized signals are higher for the ion of interest (Figure S7-8a,b) than for the interfering ion (Figure S7-8d,e) for the tested concentrations in the sweat range. The extracted sensitivities are  $14 \pm 9 \text{ \%/dec}$  for KCl with the  $\text{K}^+$  membranes ( $n=5$ ) and  $20 \pm 5 \text{ \%/dec}$  ( $n=3$ ) for NaCl with the  $\text{Na}^+$  membranes.

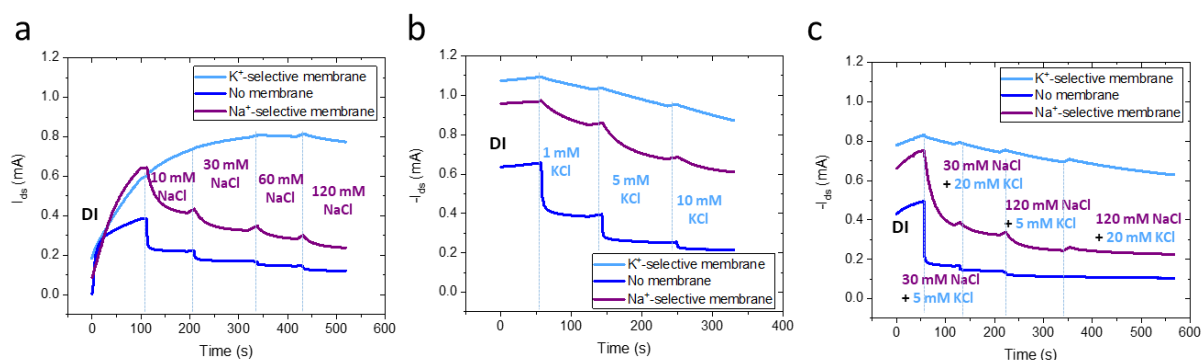


Figure 7-5: Multi-analyte detection with the OECT arrays. (a) Variations of the multiple OECT sensors to  $\text{Na}^+$  concentrations, (b) to  $\text{K}^+$  concentrations, and (c) to mixed  $\text{Na}^+$  and  $\text{K}^+$  concentrations.  $V_{ds} = -0.4 \text{ V}$ ,  $V_{gs} = 0.1 \text{ V}$  in all the cases.

Without any membrane, the sensitivity for  $\text{Na}^+$  (Figure S7-8c) and  $\text{K}^+$  (Figure S7-8f) ions was equal to  $24 \pm 7 \text{ \%/dec}$ . These sensing values are similar to those recorded with a standard semiconductor parameter analyzer (Figure S7-9).

From the multiplexed studies with mixed solutions such as the ones in Figure 7-5c, it can be seen that  $\text{K}^+$  variations in the sweat concentration range have a small influence on the  $\text{Na}^+$  sensor due to the very low concentrations of  $\text{K}^+$  compared to  $\text{Na}^+$ . On the other hand, the  $\text{K}^+$  sensor seems to have some small responses for high  $\text{Na}^+$  variations (from 30 to 120 mM) but lower than for the respective ion and concentration of interest (from 5 to 20 mM). Finally, the sensors without any membrane show the highest de-doping effects, having cumulative  $\text{K}^+$  and  $\text{Na}^+$  sensitivities. These studies show that the developed patches could be used to effectively discriminate multiple ions in the sweat concentration ranges. Nevertheless, machine-learning algorithms could be developed to overcome the semi-selectivity when the interfering ion is highly concentrated.

## 7.2.4 Calibration and sweat analysis with the multi-ion OECTs

We demonstrate for the first time the analysis of real sweat samples with an OECT array composed of two  $\text{K}^+$ -selective sensors, one  $\text{Na}^+$ -selective sensor, and one sensor without any membrane in Figure 7-6. The implementation included two  $\text{K}^+$  sensors to detect low sweat concentrations (1s-10s mM), and one  $\text{Na}^+$  and one uncoated to detect high sweat concentrations (10s-100s mM  $\text{K}^+$ ). With this approach, two sensors were used to measure the low-concentrated ionic content as reference values, the  $\text{Na}^+$  sensor to measure the higher-concentrated content, and the uncoated device to have a signal containing the total ionic content to enable multiplexed analysis. The devices are initially calibrated with DI water, followed by low and high-concentrated solutions containing mixed  $\text{K}^+$  and  $\text{Na}^+$  ions (Figure S7-10). The sweat samples are injected successively, and the  $\text{Na}^+$  and  $\text{K}^+$  concentrations were previously measured with commercial sensors. The tested concentrations included various sweat samples with low ( $\sim 5\text{-}6 \text{ mM}$ ) and higher ( $\sim 8\text{-}9 \text{ mM}$ )  $\text{K}^+$ , and low ( $\sim 50\text{-}70 \text{ mM}$ ) and higher ( $\sim 90\text{-}100 \text{ mM}$ )  $\text{Na}^+$ , with the full values tabulated in Figure 7-6a. The real-time testing with the multiple OECT sensors through several injections of the different sweat samples is presented in Figure 7-6b. The extracted  $\text{K}^+$  concentrations with the  $\text{K}^+$ -selective OECT versus the concentrations measured with the  $\text{K}^+$  commercial sensor are presented in Figure 7-6c for two different patches. Then, the  $\text{Na}^+$  concentrations with the  $\text{Na}^+$ -selective OECTs versus the concentrations measured with the  $\text{Na}^+$  commercial sensor for two different patches, or the cumulative signal obtained without any membrane versus the cumulative  $\text{K}^+$  and  $\text{Na}^+$  concentrations measured with the respective commercial sensors, are presented in Figure 7-6d.

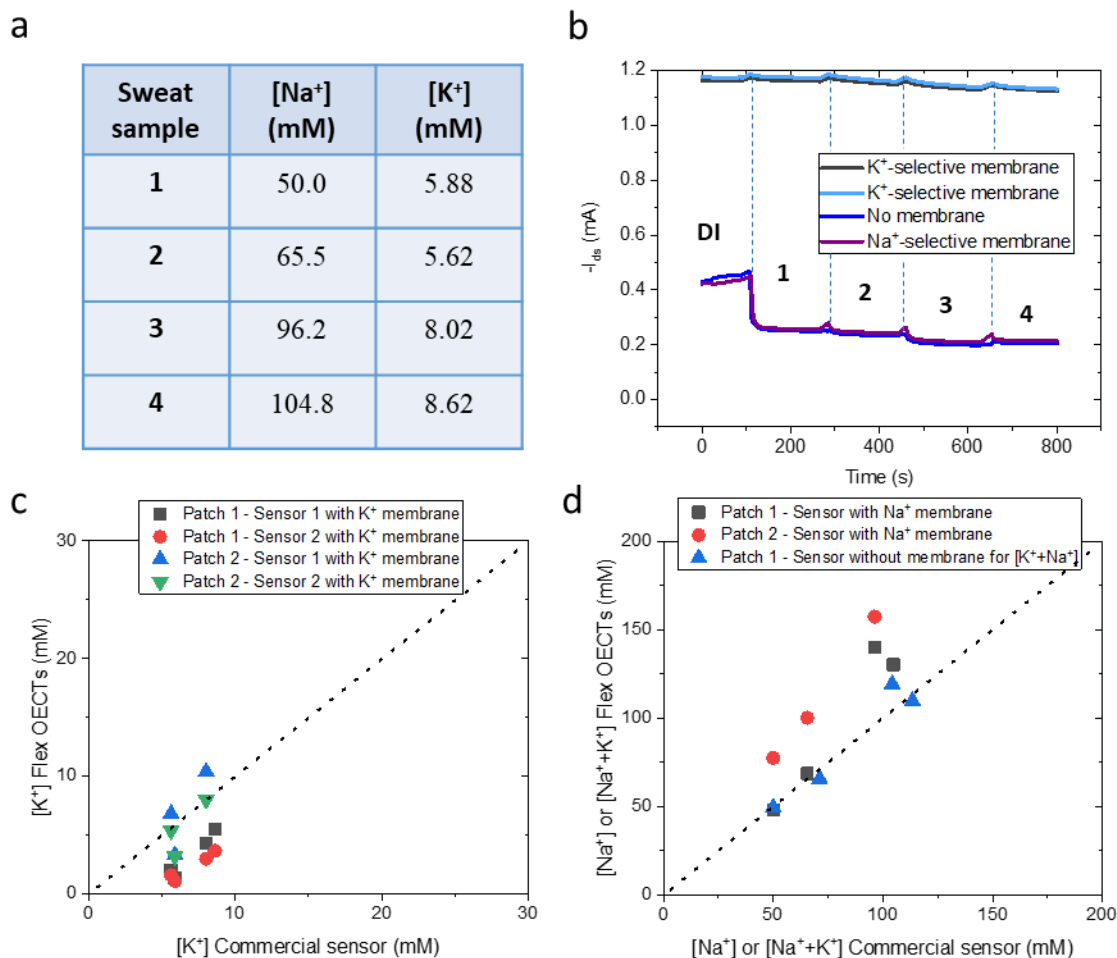


Figure 7-6: Sweat analysis with the OECT arrays. (a) Table with the Na<sup>+</sup> and K<sup>+</sup> concentrations of the sweat samples measured by commercial sensors and tested with the OECTs. (b) Testing of real sweat samples after the calibration of the OECT devices. (c) Comparison of the extracted concentrations from the K<sup>+</sup>-selective OECT sensors versus the the standard commercial sensors for K<sup>+</sup> sensing. (d) Comparison of extracted concentrations from the Na<sup>+</sup>-selective OECT sensors versus the standard commercial sensors for Na<sup>+</sup> sensing, or the OECT sensor without any membrane versus the results for both Na<sup>+</sup> and K<sup>+</sup> sensing with commercial sensors.  $V_{ds} = -0.4$  V,  $V_{gs} = 0.1$  V in all the cases.

As can be seen in Figures 5c,d, the devices show a good correlation with the extracted concentration values obtained from commercial ionic sensors. The developed platform is effectively able to discriminate ions in real sweat and it would be of interest to perform further tests with more platforms and on people to confirm the suitability of the devices for continuous sweat analysis. Developing classification methods

based on pattern recognition algorithms for the desired analyte could further improve the measured correlation.

## 7.3 Conclusions

This work shows multi-OECT array platforms operating simultaneously to measure in real-time sweat ion concentrations. The multiplexed sensing of  $K^+$ ,  $Na^+$ , and all-cations content are recorded thanks to the custom-made wearable read-out electronics. The sensing devices include an integrated pseudo-reference Ag/AgCl gate electrode made by inkjet-printed silver nanoparticle inks and electrochemical chloridation. The thin-film PEDOT:PSS are coated through a stencil printing process with ion-selective membranes, directly cast onto the organic layer. The ion sensing capabilities of the developed platform are validated with standard ionic solutions and with real human sweat samples. The measured ionic concentrations by the OECTs correlate well with the values determined by a standard commercial method. The compact integrated devices could be used with other functional materials and bio-layers for the multiplexed analysis of various analytes. The platforms are flexible and fully printed, towards the next generation of digitally-manufactured and configurable multi-sensing systems.

## 7.4 Experimental Section

### 7.4.1 Sensors platform materials and processing

The fabrication was performed with a Dimatix DMP inkjet printer (Fujifilm) on a polyimide substrate (125  $\mu\text{m}$ -thick, DuPont Kapton HN) for the silver gate electrode, silver source-drain electrode and PEDOT:PSS channel. The polyimide substrate was treated with oxygen plasma (Diener electronic GmbH + Co. KG, ATTO, 13.56 MHz with 300 W power for 2 min at 75 %) prior printing the PEDOT:PSS (1 S  $\text{cm}^{-1}$ , 1.3 wt. % dispersion in  $\text{H}_2\text{O}$ , Sigma Aldrich) ink was printed with 10 pL cartridges (DMC-11610), and prepared by mixing PEDOT:PSS solution (1.3 wt. % in  $\text{H}_2\text{O}$ ) with 5 vol % of dimethyl sulfoxide (DMSO). The mixture was sonicated for 10 min and then filtered with a 1  $\mu\text{m}$  pore-size filter when filling the cartridge. The silver nanoparticle ink is commercially available (PV Nano Cell, Sicrys<sup>TM</sup> I20DM-206), and it was printed by using the 2.5 pL cartridges (Samba). The silver ink was sonicated for 5 min prior to printing and subsequently filtered when filling the respective cartridge. The Dimatix substrate holder was kept at 35 °C. The process started with the printing of 4 layers stack of the silver gate, source and drain electrodes and subsequent sintering at 160 °C for 30 minutes. Then, the PEDOT:PSS layers were printed



(2 layers) and subsequently cured at 120 °C for 20 min. Subsequently, a polyurethane-based insulator layer (30 wt. % SMP Technologies Inc, MM4520 dissolved in 70 wt. % dimethylformamide) was stencil-printed on top of the silver contacts and the interconnections through a laser-cut mask (Nexus, 95 µm-thick GP20) by laser cutter (Trotec Speedy300, CO<sub>2</sub> laser), and cured at 80 °C for 10 minutes. The final printed platform contains four OECT devices, each OECT having a channel width/length (W/L) ratio of 0.3 (W=0.5 mm, L=1.5 mm) and a gate area of 0.3 x 0.5 mm<sup>2</sup>.

### 7.4.2 Ion-selective membranes preparation

All the chemicals were purchased from Sigma Aldrich unless otherwise stated. K<sup>+</sup> and Na<sup>+</sup> ISM mixtures were obtained by preparing two separate solutions per membrane, one solution dissolving the ionophores with the sodium tetrakis[3,5-bis(trifluoromethyl) phenyl] borate (Na-TFPB) salt in cyclohexanone, and the other solution with the bis(2- ethylehexyl) sebacate (DOS) and polyvinyl chloride (PVC) in cyclohexanone. The DOS and PVC solution was thoroughly mixed overnight to get the homogenous membrane solution, and the ionophore-salt complex was let to form overnight in the refrigerator. Then, the two solutions are mixed in a 1:1 ratio to get the final membrane solution. The K<sup>+</sup> membrane solution contains  $5.142 \times 10^{-3}$  M potassium ionophore,  $4.174 \times 10^{-3}$  M NaTFPB,  $433.25 \times 10^{-3}$  m DOS, and PVC (5 wt. %/vol%) in cyclohexanone. The Na<sup>+</sup> membrane solution contains  $1.5 \times 10^{-3}$  m sodium ionophore X,  $0.940 \times 10^{-3}$  m Na-TFPB,  $232.420 \times 10^{-3}$  m DOS, and PVC (2.5 wt. %/vol%). All the prepared ISE membrane solutions were tightly sealed and stored at 4 °C until further use. Each membrane was stencil printed separately onto the PEDOT:PSS layers using 160 µm-thick polyimide tape laser-cut mask after a moderate oxygen plasma treatment (Diener electronic GmbH + Co. KG, ATTO, 13.56 MHz with 300 W power for 2 min at 50 %) to improve the adhesion. After printing, a drop of  $10 \times 10^{-3}$  M KCl or  $60 \times 10^{-3}$  M NaCl solution in DI water was left on the K<sup>+</sup> or Na<sup>+</sup> membrane, respectively, for 30 minutes as a preconditioning.

### 7.4.3 Electronics readout

The WeCare-UZH-INISensors printed circuit board (PCB) was constructed to measure the currents from up to 4 OECT sensors at the same time. The PCB is composed of two 24-bit Analog to Digital Converters (ADCs) with four differential channels each and a 14-bit, 8-channel Digital to Analog Converter (DAC) to drive the terminal voltages of the OECT. It can source up to 3 mA per channel in parallel for all channels. The first ADC measures the source current of all 4 OECT sensors; the second ADC sequentially measures the gate current of one OECT and the common drain current. The drain voltage is common to all four sensors and is set to a fixed voltage (0.5 V). The source and gate voltages can be set independently to a value between 0 to 2.5 V. The measured source current of the OECT is then

converted to a voltage and filtered with a second-order low-pass filter with a cutoff frequency of 10 Hz. The filtered signal is digitized at a rate of 2 samples/sec, and the data samples are transmitted wirelessly to a laptop using Bluetooth. The board can be powered by an embedded Li-Polymer (> 500 mAh) battery depending on the usage time or USB. A commercial connector (FH62-55S-0.25SHW, Farnell) was used to interface the PCB to the printed sensors. The silver interconnection part of the sensors was designed, as shown in the zoomed image in Figure S7-11 to be compatible with the PCB connector.

#### *7.4.4 Sensors characterization and analyte measurements*

The devices were tested using PMMA reservoirs containing the different electrolytes. The PMMA plates (3-mm thick) were cut with a CO<sub>2</sub> laser into a rectangular shape of 15 x 5 mm<sup>2</sup>, and fixed onto the polyimide substrate through a double-sided acrylic tape (ARcare 92712). A total volume of 100 µL of solution in the reservoir was employed in all the tests, removing each time the previous solution through pipetting. All the characterizations of the ion-selective sensors were executed using the WeCare-UZH-INISensors PCB. A comparison with a standard semiconductor parameter analyzer (Agilent 4155A) is presented in the Supplementary. For the output and transfer characteristics, a solution containing 120 mM NaCl and 20 mM KCl in deionized water (DI) was used. For the sensitivity and selectivity studies of K<sup>+</sup> and Na<sup>+</sup> sensors, KCl concentration from 1 mM to 20 mM and NaCl concentration from 10 mM to 120 mM in DI water were used. Mixed concentrations of 30-120 mM NaCl and 5-20 mM KCl in DI water were also employed, mixing low and high concentrations of the sensing and interfering ions. For the sensor calibration before the sweat measurements, the protocol includes the use first of DI water (to normalize the signal), and then a two-point calibration with a low-concentrated solution containing 10 mM NaCl and 2 mM KCl, and a highly concentrated solution with 160 mM NaCl and 32 mM KCl. The EDS analyses were performed with an SEM GemniSEM450 equipped with a Symmetry EBSD camera and UltimMax EDS detector. A thin layer of carbon was deposited on top of the silver-based electrodes before the EDS measurements. The accelerating voltage for the EDS analysis was 5 kV. The thickness measurements are performed with a Keyence VK-X1000 Series laser scanning microscope.

#### *7.4.5 Sweat samples*

All eccrine sweat samples were handled in accordance with the approved ethical agreement N° 2019 01235 of the Canton of Vaud, Switzerland. Sweat collection was done in an environment at 25,7 ± 1,1°C and 49 ± 5 % humidity. All sweat samples were collected using the absorbent patch method on the middle back of the subject. The sweat collection started after 10 minutes of biking to initiate sweating. The body regions were cleaned with alcohol, then deionized water, and dried with gauze pads before applying the absorbent patches onto these body regions. Each patch consisted of a sterilized nonwoven compress with

a covered area of 112.5 cm<sup>2</sup> and an absorbing capacity of around 8.0 g (Promedical AG, Glarus, Switzerland). The patches are covered with an impermeable fabric and were fixed onto the skin in an airtight manner using a porous adhesive on top (nonwoven micropore tape 3M™ Micropore™, 3M Company, St. Paul, USA). After 20 min of continuous cycling, to extract the sweat samples, patches were placed in the barrel of a plastic syringe and squeezed with a syringe plunger. The analysis of the K<sup>+</sup> and Na<sup>+</sup> concentrations was performed using LAQUAtwin (Horiba) pocket meters with fresh samples. Sweat was then conserved into a sealed tube at -20 °C before analysis with the OECTs.

## 7.5 Supporting Information of Chapter 7

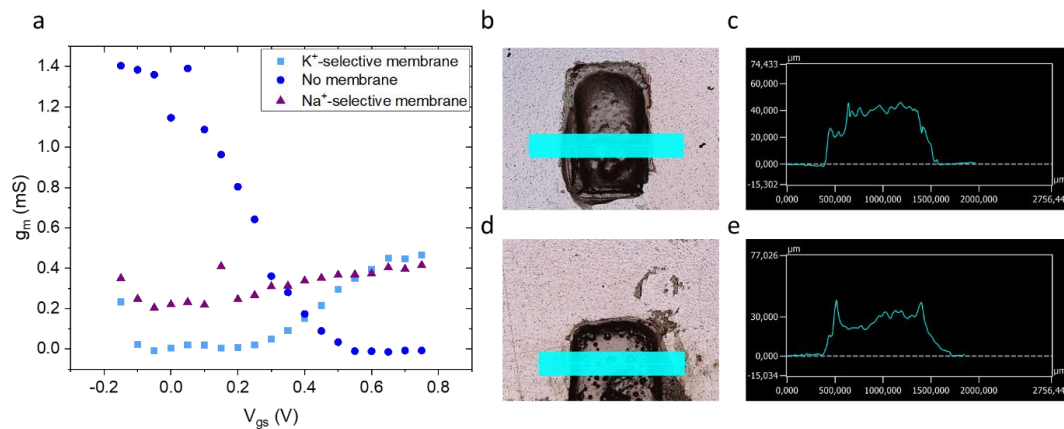


Figure S7-7: The transconductance of the OECTs. (a) Transconductance of the OECTs measured with the portable electronics. (b) Optical image of the  $K^+$  membrane, and (c) the respective thickness profile. (d) Optical image of the  $Na^+$  membrane, and (e) the respective thickness profile.

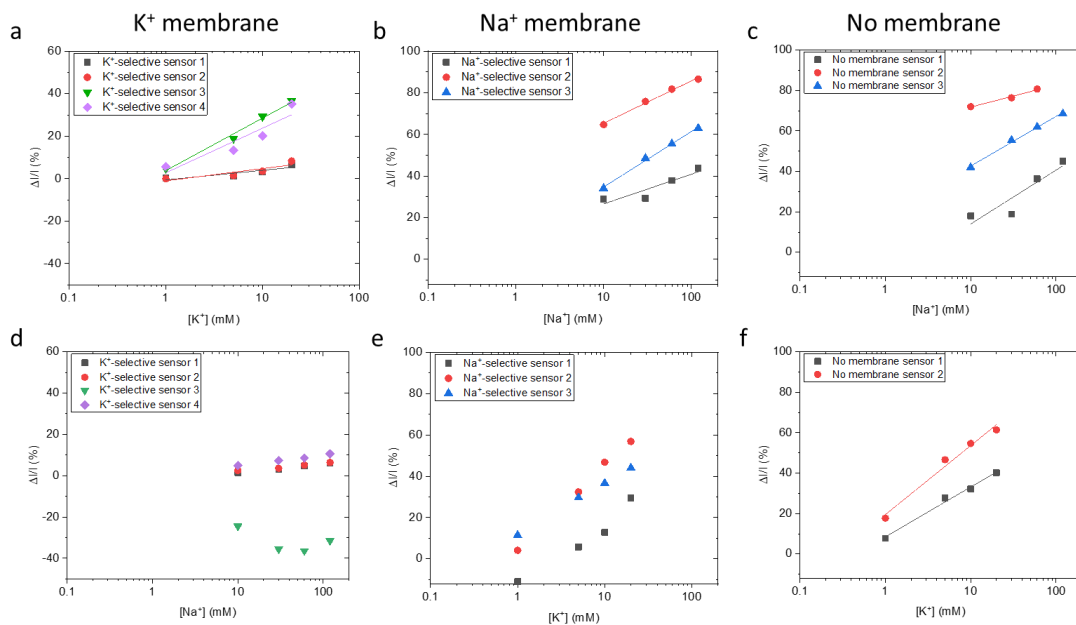


Figure S7-8: Sensitivity and selectivity. (a) Sensitivity with the  $K$ -selective membrane versus  $KCl$ . (b) Sensitivity with the  $Na$ -selective membrane versus  $NaCl$ . (c) Sensitivity without membrane versus  $NaCl$ . (d) Selectivity with the  $K$ -selective membrane versus  $NaCl$ . (e) Selectivity with the  $Na$ -selective membrane versus  $KCl$ . (f) Sensitivity without membrane versus  $KCl$ .

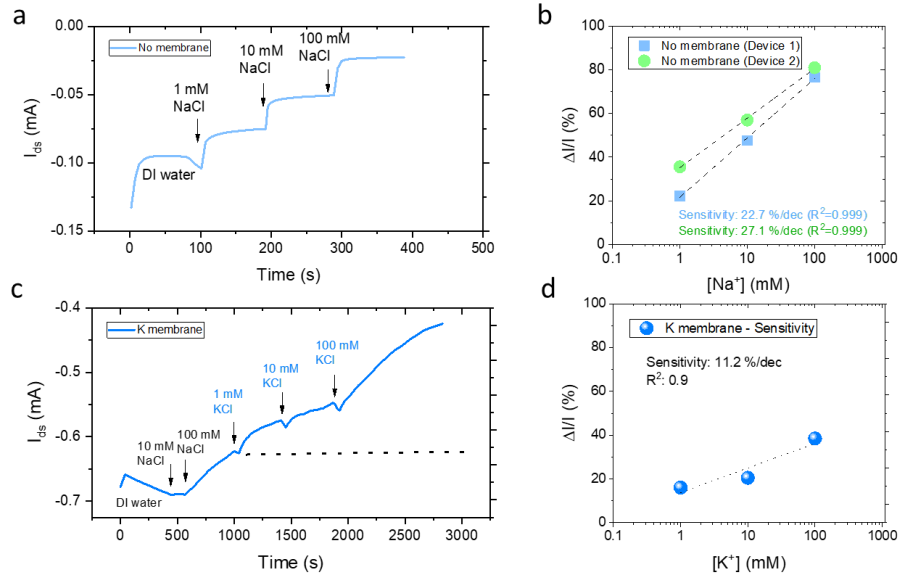


Figure S7-9: Ion sensing with the semiconductor parameter analyzer. (a) Time characteristics of an OECT without any membranes, and relative calibration curves in (b). (c) Time characteristics with a K<sup>+</sup>-selective membrane, and (d) relative calibration curve.

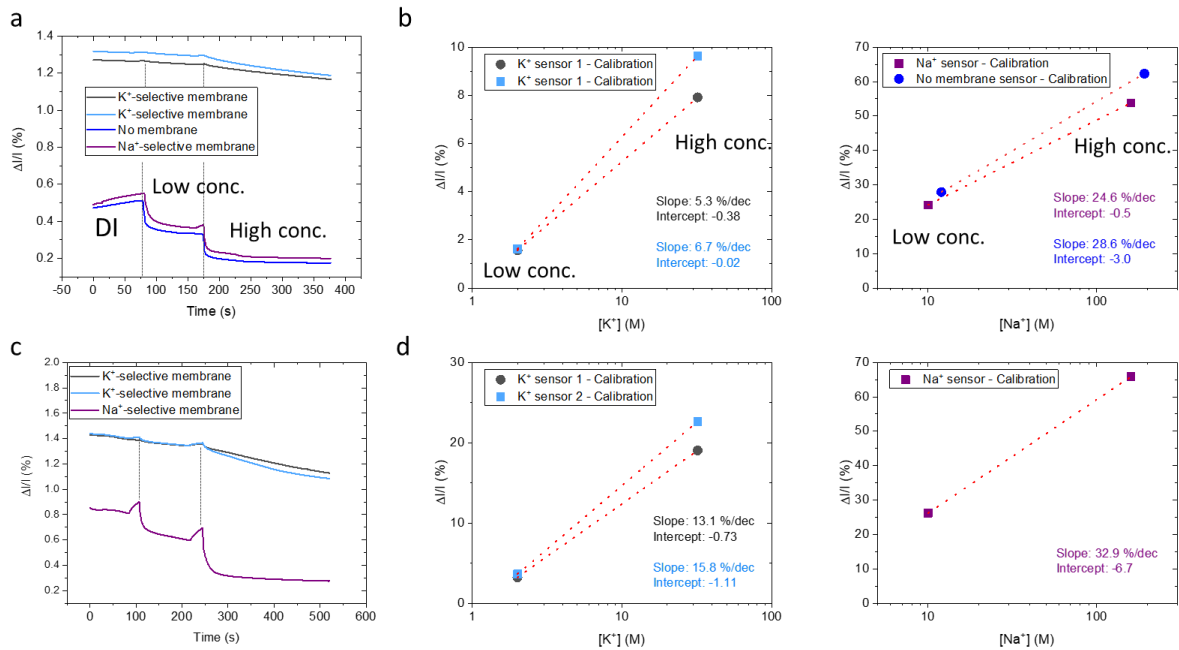
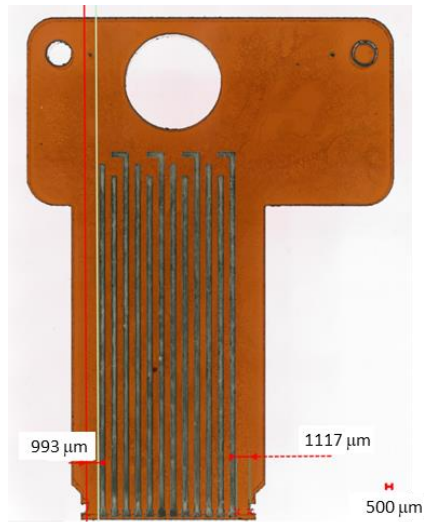


Figure S7-10: Calibration for sweat analysis. (a,c) Calibration of two integrated patches before sweat analysis with low and high concentrations, and (b,d) calibration curves of the K<sup>+</sup> and Na<sup>+</sup> sensors and the sensor without the membrane.



*Figure S7-11: Design and connections. Optical microscopy image with relevant dimensions for the interconnection part of the patches.*

# Chapter 8    **Conclusions and outlook**

## **8.1    Conclusions**

The thesis overcomes several challenges for OECT biosensors and sweat analysis.

**OECT sensors.** Different OECTs for sensing multiple analytes in the sweat physiological concentration ranges are proposed throughout the thesis chapters. Various functionalization strategies were explored according to the type of analyte targeted. First, the development of multi-ion sensitive and selective OECTs was enabled by ISMs or polyaniline (PANI) coatings directly integrated onto the PEDOT:PSS channels. This resulted in high-sensitivity ion sensors with integrated silver-based pseudo-reference gates. Then, enzymatic-based and antibody-based OECTs were demonstrated with the sensing reactions occurring on the gate electrodes. The enzymatic sensors showed optimal sensing performance with integrated functional graphene gates to detect  $\mu\text{M}$  concentrations of glucose and  $\text{mM}$  concentrations of lactate. Finally, antibody-based functionalization was performed on gold gates, which, in combination with an optimization of the transducer, enabled the effective cortisol detection in the  $\text{nM}$  concentration ranges.

For each biosensing method explored, the sensing mechanisms were analyzed with electrical measurements and electrochemical impedance spectroscopy (EIS), highlighting the capacitive and resistive variations at the functionalized electrode/electrolyte interface during the sensing. For the pH sensors with the PEDOT:PSS/PANI layers, their increased sensitivity is attributed to the larger increase in the interfacial capacitance when decreasing the pH compared to bare PEDOT:PSS devices. This mechanism is possibly due to an increase of interfacial charge from the  $\text{H}^+$  doping, which causes a less-efficient dedoping at low pH values, leading to an increase in drain current. For the glucose and lactate sensors, a strong decrease in charge-transfer resistance is measured at the graphene gate interface due to the enzymatic reaction and  $\text{H}_2\text{O}_2$  oxidation at the interface. This reaction increases the current modulation of the devices, decreasing the current, in agreement with the theory on enzymatic-based sensing. This work also shows the importance of the mediator ferrocene for controlling the solution potential in the OECT configurations for reliable enzymatic measurements. Finally, the sensing mechanism with antibodies on the gate electrode was related to an increase in double-layer capacitance at the gate interface during the binding events. These experimental findings were also confirmed with OECT electrical models, showing an excellent correspondence. The insights here presented shed light on the sensing mechanisms in OECTs devices and pave the way for their future improvement and development.

**Integrated technology for wearables.** The OECT devices proposed in this thesis are digitally-configurable, thanks to the use of additive manufacturing technologies (i.e., inkjet printing and laser cutting), which facilitate the integration of multiple OECTs into the same platform. Sensing of ions, pH, glucose, and lactate in the relevant concentration ranges for sweat analysis is achieved by modifying the inkjet-printed gate material and the functionalization process. For ion sensing, the respective ion-selective membranes or ion-sensitive polymers were directly in contact with the printed PEDOT:PSS channels and the pseudo-reference silver-based gates are integrated onto the same substrate. For enzymatic-based sensing, a replacement of the conventional pseudo-reference gates with a functional graphene printed electrode allowed obtaining high sensitivity for glucose and lactate detection. For antibody-based sensing, the evaporated gold gate was separated from the channel to avoid any damage during the multiple functionalization steps. The gate was subsequently integrated with the transducer to form the complete devices through adhesive lamination for testing. Thanks to the use of thin-film technologies on flexible substrates, the developed devices were integrated into a flexible, wearable microfluidic system patterned by CO<sub>2</sub> laser to enable a direct sweat collection. Finally, multiple OECTs were miniaturized to form a sensor array and were tested simultaneously, thanks to the use of custom-made portable electronics. These results demonstrate the great potential of the OECT platform to realize flexible and fully-integrated multi-sensor arrays towards wearable applications.

**Multi-sensing and sweat analysis.** This thesis reports on the development of multi-sensing OECTs, including ion-selective (Na<sup>+</sup>, K<sup>+</sup>), pH-sensitive, enzymatic-based, and antibody-based sensors involving novel fabrication protocols. The integration of multiple biosensors developed in this thesis could provide a collective signal, fundamental for generating reliable multiplexed sensing patterns. Proper sensing of the main analytes in human sweat, including ions, glucose, lactate, and cortisol, are shown. The devices are optimized for the relevant concentration ranges for analysis in human sweat. With ion-selective membranes for ions, polyaniline for pH, and enzymatic solutions or membranes for glucose and lactate, high sensitivities of 20 %/dec of concentration were achieved. These values were extracted in the relevant concentration ranges in human sweat, being 1 – 100 mM for ions, 4 – 10 for pH, 10s – 100s  $\mu$ M for glucose, and 1 – 10s mM for lactate. All the sensing results are shown based on real-time drain current measurements. In the case of cortisol sensing, the antibody-coating on the OECT gate enabled the detection of very low concentrations in the 0.1 – 1000 nM range with a large corresponding current variation of 50  $\mu$ A/dec after 5 minutes of incubation. Finally, the devices with K<sup>+</sup> and Na<sup>+</sup> ion-selective membranes and the devices with antibodies were successfully tested with real sweat samples, confirming the suitability of the developed technologies to measure the concentrations of various analytes. Multiple



ion sensors were then integrated into a single platform to achieve a potentially wearable, multi-sensing array. Preliminary results show the potential of this approach to provide simultaneous and selective sensing of multiple analytes in human sweat, paving the way to real-time, non-invasive health monitoring in athletes during sports conditions.

## 8.2 Outlook

Based on the presented results in this thesis, the following future research directions are suggested.

**OECT sensors sensing mechanism and stability.** This thesis work analyzed through impedance spectroscopy and basic electrical modeling the sensing mechanism of the devices depending on the bio-layers and materials. For complex bio-receptors such as antibodies or aptamers, more studies are required. Depending on the charge carried by the different antibody/antigen and self-assembly monolayers for the crafting,[92] and due to the shorter length of receptors such as aptamers,[37] the electrical effects and impedance variations measured through the electrochemical impedance spectroscopy analysis could change. This would require the use of other electrical models at the interface for understanding and optimizing the devices. The use of custom-made bio-receptors, such as aptamers or nanobodies,[69] could enhance the sensitivity of the devices for point-of-care applications, but correlation with experimental work and electrical modeling is required to develop these implementations. Practically, studies on other types of transistors, such as EGOFETs,[101] showed that through the use of highly-packed bio-receptors on gate electrodes and interdigitated channel, single-molecules detection could be achieved. These insights could be applied to OECTs sensors as well and enable ultra-low detection (pico-molar) of molecules such as interleukins in biofluids.[209], [239] Hence, studies with other bio-receptors are needed.

This thesis also showed that the OECT could be used to analyze variations of cortisol and ions in real sweat samples for a few minutes. For future accurate testing and quantification of the sweat content for the continuous monitoring (at least 1-2 hours) of ions and metabolites, more extensive testing and possible modification of the bio-functionalization layers are still necessary. To make sure to have a repeatable deposition with good coverage and thickness control using the enzymatic membranes and ion-selective membranes for long-term operation in solutions, a more reproducible deposition process of the membranes is required. In practice, the membranes could be inkjet, aerosol-jet, or 3D-printed.[240]

Further studies of the stability of the organic materials, particularly for the detection of low-concentrated molecules (nM-pM ranges or below) or for the aforementioned testing for a few hours

continuously, are still needed. To avoid false-positive measurements, a minimal current change due to the testing conditions (incubations and injections of multiple solutions) should be achieved.[76] Reliability tests should be performed in artificial biofluids (containing several interfering analytes[241]) for several minutes up to hours to understand the limitations of the OECT sensors. A setup with an integrated fluidic pump that allows the injection of several solutions into the sensors with a controlled flow rate should be implemented. The chemical structure of the organic layers, such as the PEDOT:PSS channels, should be modified with chemicals such as GOPS[76] or sulfuric acid treatments for improving the cross-linking or crystallinity if needed.[132]

Another possible solution to prevent the damaging of the organic channels in real biofluids is the use of custom-made molecularly-imprinted membranes (MIPs) for various molecules[167] or other membranes and hydrogels directly on the channels to prevent interactions of all the interfering molecules/multiple analytes with the organic materials. The membrane could be used just as a diffusion barrier so that a few ions could arrive at the PEDOT:PSS material to enable the transduction principle/dedoping of the devices but possibly enhance the lifetime by protecting the organic channel. Overall, further research should be done on bio-receptors embedded in membranes (ions and enzymes), membranes or coatings on the PEDOT:PSS layers, and the chemical structure of the PEDOT:PSS layer itself for long-term testing.

**OECT wearable patch for sweat sensing.** In this work, the sensors are developed directly on flexible substrates and can be simply integrated by lamination with microfluidics. This could allow the real-time analysis of sweat on the skin.

For real sweat applications, the direct sweat uptake and continuous filling of the microfluidic system in real-time with the integrated OECT arrays need to be validated.[242] Depending on the sweat rate of individuals and the overall dimension of the microfluidic channel, the sweat flow reaching the sensors can vary significantly. The effect of this continuous sweat flow for several minutes on the OECT sensors needs to be characterized. In addition, the sweat replacement in the sensor area with new sweat during continuous monitoring depends on the individual sweat rate and on the evacuation and evaporation of the old sweat through the microfluidic outlet.[18] Moreover, the concentration of some analytes (such as sodium),[34] could also be correlated in real-time with the sweat rate variations. All these factors add complexity to the measurement and should be carefully considered. A possible solution consists of adding a sweat-rate sensor inside the microfluidic chamber together with the OECT devices to enable continuous and real-time monitoring of the analytes depending on the sweat flow.[18] To optimally interpret this

complex set of data, including the sweat rate and the signal from the analytes, machine learning algorithms would be needed for accurate and reliable on-skin continuous analysis. Also, the effect of movement on the integrated sensors/electronics system on the skin should be evaluated.. The suggested locations to carry out these tests are either on the back or forehead, where there is a high sweat rate and limited movement during cycling and running conditions.

Hence, further research will be necessary on printed, wearable, and simple integrated sweat-rate sensors, combined with microfluidic design optimizations, data analysis, and the final evaluation of the integrated OECT platform and electronics on the skin.[243]

**Multi-sensing with OECTs in biofluids.** In this thesis, multiple sensors for sensing different analytes are presented. Combining all these OECTs sensors with the different bio-functionalization layers could have a high impact on the biosensing field, not only for sweat analysis but for multiple applications (point-of-care testing of saliva, blood, urine, tears, and so on).[5] The multiplexed sensing of the enzymatic sensors for glucose and lactate with pH and ions could help to generate patterns to compensate for the enzymatic activity variation due to pH,[8] and the enzymatic signal changes due to possible dedoping variations into the PEDOT:PSS (changes in ionic concentrations).[47] Also, the influence of the  $H_2O_2$  produced through the enzymatic reaction on the response of other integrated sensors should be investigated. In the case of the biofluid sweat, adding a potassium-selective OECT in the platform, being potassium sweat rate-independent (i.e., it should be constant during the measurement),[34] can be extracted if a change in the sensor signal comes from real changes in the analyte concentration, the sweat rate, or external noise. Also, the combination of ion-selective OECTs and antibody-based sensors can be implemented to see the actual antigen variation in real-time on the skin, also compensating for the dedoping variations in the PEDOT:PSS due to changes in ionic concentrations. These patterns with multiple sensors still require many tests performed in the laboratory environment with artificial biofluids and training machine learning algorithms to correlate the variations from the sensors to actual concentration variations. All the tests should be performed with specifically designed read-out electronics for the simultaneous measurement of multiple OECT sensors, which can be integrated in a compact and wearable way.[85] This multiplexed analysis could open the door for personalized medicine techniques for continuous and point-of-care applications in multiple biofluids such as sweat, tears, and saliva.

# References

- [1] “PAC,” *Gloss. Chem. terms used Biotechnol. (IUPAC Recomm. 1992)*, vol. 64, no. 143, p. 148, 1992.
- [2] A. M. Pappa, O. Parlak, G. Scheiblin, P. Mailley, A. Salleo, and R. M. Owens, “Organic Electronics for Point-of-Care Metabolite Monitoring,” *Trends Biotechnol.*, vol. 36, no. 1, pp. 45–59, 2018.
- [3] L. C. J. Clark and C. Lyons, “Electrode systems for continuous monitoring in cardiovascular surgery,” *Ann. N. Y. Acad. Sci.*, vol. 102, pp. 29–45, 1962.
- [4] L. Kergoat, B. Piro, M. Berggren, G. Horowitz, and M. C. Pham, “Advances in organic transistor-based biosensors: From organic electrochemical transistors to electrolyte-gated organic field-effect transistors,” *Analytical and Bioanalytical Chemistry*. pp. 1813–1826, 2012.
- [5] J. Kim, A. S. Campbell, B. E. F. de Ávila, and J. Wang, “Wearable biosensors for healthcare monitoring,” *Nat. Biotechnol.*, vol. 37, no. 4, pp. 389–406, 2019.
- [6] W. Gao *et al.*, “Fully integrated wearable sensor arrays for multiplexed in situ perspiration analysis,” *Nature*, vol. 529, pp. 509–514, 2016.
- [7] A. Koh *et al.*, “A soft, wearable microfluidic device for the capture, storage, and colorimetric sensing of sweat,” *Sci. Transl. Med.*, vol. 8, no. 366ra165, pp. 1–13, 2016.
- [8] H. Lee *et al.*, “A graphene-based electrochemical device with thermoresponsive microneedles for diabetes monitoring and therapy,” *Nat. Nanotechnol.*, vol. 11, pp. 566–572, 2016.
- [9] J. R. Sempionatto *et al.*, “Eyeglasses based wireless electrolyte and metabolite sensor platform,” *Lab Chip*, vol. 17, no. 10, pp. 1834–1842, 2017.
- [10] J. Kim *et al.*, “Wearable salivary uric acid mouthguard biosensor with integrated wireless electronics,” *Biosens. Bioelectron.*, vol. 74, pp. 1061–1068, 2015.
- [11] I. Jeerapan, J. R. Sempionatto, A. Pavinatto, J. M. You, and J. Wang, “Stretchable biofuel cells as wearable textile-based self-powered sensors,” *J. Mater. Chem. A*, vol. 4, pp. 18342–18353, 2016.
- [12] J. Min, J. R. Sempionatto, H. Teymourian, J. Wang, and W. Gao, “Wearable electrochemical biosensors in North America,” *Biosens. Bioelectron.*, vol. 172, p. 112750, 2021.

- [13] W. Jia *et al.*, “Electrochemical tattoo biosensors for real-time noninvasive lactate monitoring in human perspiration,” *Anal. Chem.*, vol. 85, p. 6553–6560, 2013.
- [14] M. Parrilla, I. Ortiz-Gómez, R. Cánovas, A. Salinas-Castillo, M. Cuartero, and G. A. Crespo, “Wearable Potentiometric Ion Patch for On-Body Electrolyte Monitoring in Sweat: Toward a Validation Strategy to Ensure Physiological Relevance,” *Anal. Chem.*, vol. 91, no. 13, pp. 8644–8651, 2019.
- [15] J. T. Reeder *et al.*, “Resettable skin interfaced microfluidic sweat collection devices with chemesthetic hydration feedback,” *Nat. Commun.*, vol. 10, no. 1, p. 5513, 2019.
- [16] A. Alizadeh *et al.*, “A wearable patch for continuous monitoring of sweat electrolytes during exertion,” *Lab Chip*, vol. 18, no. 17, pp. 2632–2641, 2018.
- [17] K. Kwon *et al.*, “An on-skin platform for wireless monitoring of flow rate, cumulative loss and temperature of sweat in real time,” *Nat. Electron.*, 2021.
- [18] H. Yin *et al.*, “A Wearable Microfluidic Sensing Patch for Dynamic Sweat Secretion Analysis,” *ACS Sensors*, vol. 3, p. 944–952, 2018.
- [19] R. M. Torrente-Rodríguez *et al.*, “Investigation of Cortisol Dynamics in Human Sweat Using a Graphene-Based Wireless mHealth System,” *Matter*, vol. 2, no. 4, pp. 921–937, 2020.
- [20] O. Parlak, S. T. Keene, A. Marais, V. F. Curto, and A. Salleo, “Molecularly selective nanoporous membrane-based wearable organic electrochemical device for noninvasive cortisol sensing,” *Sci. Adv.*, vol. 4, no. eaar2904, pp. 1–10, 2018.
- [21] S. Kim *et al.*, “Soft, skin-interfaced microfluidic systems with integrated immunoassays, fluorometric sensors, and impedance measurement capabilities,” *Proc. Natl. Acad. Sci.*, vol. 117, no. 45, pp. 27906–27915, 2020.
- [22] B. Jagannath, K. C. Lin, M. Pali, D. Sankhala, S. Muthukumar, and S. Prasad, “Temporal profiling of cytokines in passively expressed sweat for detection of infection using wearable device,” *Bioeng. Transl. Med.*, no. December 2020, pp. 1–14, 2021.
- [23] F. Criscuolo *et al.*, “Wearable multifunctional sweat-sensing system for efficient healthcare monitoring,” *Sensors Actuators, B Chem.*, vol. 328, no. 129017, pp. 1–9, 2021.
- [24] J. R. Sempionatto, J.-M. Moon, and J. Wang, “Touch-Based Fingertip Blood-Free Reliable Glucose Monitoring: Personalized Data Processing for Predicting Blood Glucose Concentrations,”

*ACS Sensors*, vol. 6, p. 1875–1883, 2021.

- [25] Y. Seki *et al.*, “A novel device for detecting anaerobic threshold using sweat lactate during exercise,” *Sci. Rep.*, vol. 11, no. 1, pp. 1–11, 2021.
- [26] S. Krishnan *et al.*, “Waterproof, electronics-enabled, epidermal microfluidic devices for sweat collection, biomarker analysis, and thermography in aquatic settings,” *Sci. Adv.*, vol. 5, no. 1, p. eaau6356, 2019.
- [27] M. Bariya, H. Y. Y. Nyein, and A. Javey, “Wearable sweat sensors,” *Nat. Electron.*, vol. 1, pp. 160–171, 2018.
- [28] B. Zhong, K. Jiang, L. Wang, and G. Shen, “Wearable Sweat Loss Measuring Devices: From the Role of Sweat Loss to Advanced Mechanisms and Designs,” *Adv. Sci.*, vol. 9, no. 2103257, pp. 1–27, 2022.
- [29] Z. Sonner *et al.*, “The microfluidics of the eccrine sweat gland, including biomarker partitioning, transport, and biosensing implications,” *Biomicrofluidics*, vol. 9, no. 3, pp. 1–19, 2015.
- [30] R. Ghaffari, J. A. Rogers, and T. R. Ray, “Recent progress, challenges, and opportunities for wearable biochemical sensors for sweat analysis,” *Sensors Actuators, B Chem.*, vol. 332, p. 129447, 2021.
- [31] E. Garcia-Cordero *et al.*, “Three-Dimensional Integrated Ultra-Low-Volume Passive Microfluidics with Ion-Sensitive Field-Effect Transistors for Multiparameter Wearable Sweat Analyzers,” *ACS Nano*, vol. 12, pp. 12646–12656, 2018.
- [32] F. Vermeulen, C. Le Camus, J. C. Davies, D. Bilton, D. Milenković, and K. De Boeck, “Variability of sweat chloride concentration in subjects with cystic fibrosis and G551D mutations,” *J. Cyst. Fibros.*, 2017.
- [33] K. K. Yeung, T. Huang, Y. Hua, K. Zhang, M. M. F. Yuen, and Z. Gao, “Recent Advances in Electrochemical Sensors for Wearable Sweat Monitoring: A Review,” *IEEE Sens. J.*, vol. 21, no. 13, pp. 14522–14539, 2021.
- [34] D. Vairo *et al.*, “Towards Addressing the Body Electrolyte Environment via Sweat Analysis: Pilocarpine Iontophoresis Supports Assessment of Plasma Potassium Concentration,” *Sci. Rep.*, vol. 7, no. 1, pp. 1–7, 2017.
- [35] J. Bolinder, R. Antuna, P. Geelhoed-Duijvestijn, J. Kröger, and R. Weitgasser, “Novel glucose-

- sensing technology and hypoglycaemia in type 1 diabetes: a multicentre, non-masked, randomised controlled trial,” *Lancet*, vol. 388, no. 10057, pp. 2254–2263, Nov. 2016.
- [36] H. Zafar, A. Channa, V. Jeoti, and G. M. Stojanovi, “Comprehensive Review on Wearable Sweat-Glucose Sensors for Continuous Glucose Monitoring,” *Sensors*, vol. 22, no. 638, pp. 1–35, 2022.
  - [37] S. Sheibani *et al.*, “Extended gate field-effect-transistor for sensing cortisol stress hormone,” *Commun. Mater.*, vol. 2, no. 10, pp. 1–10, 2021.
  - [38] B. Wang *et al.*, “Wearable aptamer-field-effect transistor sensing system for noninvasive cortisol monitoring,” *Sci. Adv.*, vol. 8, no. eabk0967, pp. 1–16, 2022.
  - [39] S. Demuru, K. Chennit, V. Noël, B. Piro, G. Mattana, and D. Briand, “An integrated flexible platform with printed organic electrochemical and field-effect transistors for biochemical sensing,” *MicroTAS 2020 - 24th Int. Conf. Miniaturized Syst. Chem. Life Sci.*, no. 978-1-7334190-1-7/ $\mu$ TAS 2020/\$20©20CBMS–0001, pp. 284–285, 2020.
  - [40] T. Someya, Z. Bao, and G. G. Malliaras, “The rise of plastic bioelectronics,” *Nature*, vol. 540, no. 7633, pp. 379–385, 2016.
  - [41] C. Jimenez-Jorquera, J. Orozco, and A. Baldi, “ISFET based microsensors for environmental monitoring,” *Sensors*, vol. 10, no. 1, pp. 61–83, 2010.
  - [42] K. D. Dorfman, D. Z. Adrahtas, M. S. Thomas, and C. D. Frisbie, “Microfluidic opportunities in printed electrolyte-gated transistor biosensors,” *Biomicrofluidics*, vol. 14, no. 1, pp. 1–15, 2020.
  - [43] X. Yongzhao *et al.*, “Silicon-Based Sensors for Biomedical Applications: A Review,” *Sensors*, vol. 19, no. 2908, pp. 355–376, 2019.
  - [44] P. Andersson Ersman *et al.*, “All-printed large-scale integrated circuits based on organic electrochemical transistors,” *Nat. Commun.*, vol. 10, no. 1, pp. 1–9, 2019.
  - [45] A. Cazalé *et al.*, “Physiological stress monitoring using sodium ion potentiometric microsensors for sweat analysis,” *Sensors Actuators, B Chem.*, vol. 225, pp. 1–9, 2016.
  - [46] R. A. Picca *et al.*, “Ultimately Sensitive Organic Bioelectronic Transistor Sensors by Materials and Device Structures’ Design,” *Adv. Funct. Mater.*, vol. 30, no. 1904513, pp. 1–23, 2019.
  - [47] P. Lin, F. Yan, and H. L. W. Chan, “Ion-Sensitive Properties of Organic Electrochemical Transistors,” *ACS Appl. Mater. Interfaces*, vol. 2, no. 6, pp. 1637–1641, 2010.

- [48] L. Groenendaal, G. Zotti, P. H. Aubert, S. M. Waybright, and J. R. Reynolds, “Electrochemistry of poly(3,4-alkylenedioxythiophene) derivatives,” *Adv. Mater.*, vol. 15, no. 11, pp. 855–879, 2003.
- [49] F. Torricelli *et al.*, “Electrolyte-gated transistors for enhanced performance bioelectronics,” *Nat. Rev. Methods Prim.*, vol. 1, no. 66, pp. 1–24, 2021.
- [50] G. G. Malliaras, M. Berggren, R. M. Owens, J. Rivnay, S. Inal, and A. Salleo, “Organic electrochemical transistors,” *Nat. Rev. Mater.*, vol. 3, no. 2, p. 17086, 2018.
- [51] H. S. White, G. P. Kittlesen, and M. S. Wrighton, “Chemical Derivatization of an Array of Three Gold Microelectrodes with Polypyrrole: Fabrication of a Molecule-Based Transistor,” *J. Am. Chem. Soc.*, vol. 106, no. 18, pp. 5375–5377, 1984.
- [52] K. Tybrandt, I. V. Zozoulenko, and M. Berggren, “Chemical potential – electric double layer coupling in conjugated polymer – polyelectrolyte blends,” *Sci. Adv.*, vol. 3, no. eaao3659, pp. 1–7, 2017.
- [53] L. Contat-Rodrig, C. Pérez-Fuster, J. V. Lidón-Roger, A. Bonfiglio, and E. García-Breijo, “Characterization of screen-printed organic electrochemical transistors to detect cations of different sizes,” *Sensors*, vol. 16, no. 1599, pp. 1–11, 2016.
- [54] J. T. Friedlein, S. E. Shaheen, G. G. Malliaras, and R. R. McLeod, “Optical Measurements Revealing Nonuniform Hole Mobility in Organic Electrochemical Transistors,” *Adv. Electron. Mater.*, vol. 1, no. 1500189, pp. 1–9, 2015.
- [55] J. Rivnay, S. Inal, A. Salleo, M. Berggren, and G. G. Malliaras, “Organic electrochemical transistors,” *Nat. Rev. Mater.*, vol. 3, no. 17086, pp. 1–13, 2018.
- [56] D. Khodagholy *et al.*, “High transconductance organic electrochemical transistors,” *Nat. Commun.*, vol. 4, pp. 1–6, 2013.
- [57] J. Rivnay *et al.*, “High-performance transistors for bioelectronics through tuning of channel thickness,” *Sci. Adv.*, vol. 1, no. 4, pp. 1–6, 2015.
- [58] E. Zeglio and O. Inganäs, “Active Materials for Organic Electrochemical Transistors,” *Adv. Mater.*, vol. 30, no. 1800941, pp. 1–18, 2018.
- [59] J. T. Friedlein, R. R. McLeod, and J. Rivnay, “Device physics of organic electrochemical transistors,” *Org. Electron.*, vol. 63, no. September, pp. 398–414, 2018.
- [60] R. Colucci, H. F. D. P. Barbosa, F. Günther, P. Cavassin, and G. C. Faria, “Recent advances in



- modeling organic electrochemical transistors,” *Flex. Print. Electron.*, vol. 5, no. 1, 2020.
- [61] V. N. Prigodin, F. C. Hsu, Y. M. Kim, J. H. Park, O. Waldmann, and A. J. Epstein, “Electric field control of charge transport in doped polymers,” *Synth. Met.*, vol. 153, no. 1–3, pp. 157–160, 2005.
  - [62] V. Kaphle, P. R. Paudel, D. Dahal, R. K. Radha Krishnan, and B. Lüssem, “Finding the equilibrium of organic electrochemical transistors,” *Nat. Commun.*, vol. 11, no. 2515, pp. 1–11, 2020.
  - [63] L. B. Baker, “Physiology of sweat gland function: The roles of sweating and sweat composition in human health,” *Temperature*, vol. 6, no. 3, pp. 211–259, 2019.
  - [64] F. Cicoira, M. Sessolo, O. Yaghmazadeh, J. A. Defranco, S. Y. Yang, and G. C. Malliaras, “Influence of device geometry on sensor characteristics of planar Organic electrochemical transistors,” *Adv. Mater.*, vol. 22, no. 9, pp. 1012–1016, 2010.
  - [65] M. Sensi *et al.*, “Modulating the Faradic Operation of All-Printed Organic Electrochemical Transistors by Facile in Situ Modification of the Gate Electrode,” *ACS Omega*, vol. 4, no. April, pp. 5374–5381, 2019.
  - [66] D. A. Koutsouras, F. Torricelli, P. Gkoupidenis, and P. W. M. Blom, “Efficient Gating of Organic Electrochemical Transistors with In-Plane Gate Electrodes,” *Adv. Mater. Technol.*, vol. 2100732, p. 2100732, 2021.
  - [67] E. Macchia *et al.*, “Ultra-sensitive protein detection with organic electrochemical transistors printed on plastic substrates,” *Flex. Print. Electron.*, vol. 3, no. 034002, pp. 1–9, 2018.
  - [68] M. Sessolo, J. Rivnay, E. Bandiello, G. G. Malliaras, and H. J. Bolink, “Ion-selective organic electrochemical transistors,” *Adv. Mater.*, vol. 26, no. 28, pp. 4803–4807, 2014.
  - [69] K. Guo *et al.*, “Rapid single-molecule detection of COVID-19 and MERS antigens via nanobody-functionalized organic electrochemical transistors,” *Nat. Biomed. Eng.*, vol. 5, pp. 666–677, 2021.
  - [70] G. Tarabella *et al.*, “A single cotton fiber organic electrochemical transistor for liquid electrolyte saline sensing,” *J. Mater. Chem.*, vol. 22, pp. 23830–23834, 2012.
  - [71] N. Coppedè, G. Tarabella, M. Villani, D. Calestani, S. Iannotta, and A. Zappettini, “Human stress monitoring through an organic cotton-fiber biosensor,” *J. Mater. Chem. B*, vol. 2, pp. 5620–5626, 2014.
  - [72] M. Ghittorelli *et al.*, “High-sensitivity ion detection at low voltages with current-driven organic electrochemical transistors,” *Nat. Commun.*, vol. 9, no. 1441, pp. 1–10, 2018.

- [73] S. Khan, S. Ali, A. Khan, B. Wang, and A. Bermak, "Printing Sensors on Biocompatible Substrates for Selective Detection of Glucose," *IEEE Sens. J.*, no. c, pp. 1–1, 2020.
- [74] B. Piro *et al.*, "Fabrication and Use of Organic Electrochemical Transistors for Sensing of Metabolites in Aqueous Media," *Appl. Sci.*, vol. 8, no. 928, pp. 1–33, 2018.
- [75] S. T. Keene, D. Fogarty, R. Cooke, C. D. Casadevall, A. Salleo, and O. Parlak, "Wearable Organic Electrochemical Transistor Patch for Multiplexed Sensing of Calcium and Ammonium Ions from Human Perspiration," *Adv. Healthc. Mater.*, vol. 8, no. 24, pp. 1–8, 2019.
- [76] S. L. Bidinger, S. Han, G. G. Malliaras, and T. Hasan, "Highly stable PEDOT:PSS electrochemical transistors," *Appl. Phys. Lett.*, vol. 120, no. 073302, pp. 1–5, 2022.
- [77] M. Sessolo, J. Rivnay, E. Bandiello, G. G. Malliaras, and H. J. Bolink, "Ion-Selective Organic Electrochemical Transistors," *Adv. Mater.*, vol. 26, pp. 4803–4807, 2014.
- [78] A. Pierre, S. E. Doris, R. Lujan, and R. A. Street, "Monolithic Integration of Ion-Selective Organic Electrochemical Transistors with Thin Film Transistors on Flexible Substrates," *Adv. Mater. Technol.*, vol. 4, no. 1800577, pp. 1–5, 2019.
- [79] H. Tang, F. Yan, P. Lin, J. Xu, and H. L. W. Chan, "Highly sensitive glucose biosensors based on organic electrochemical transistors using platinum gate electrodes modified with enzyme and nanomaterials," *Adv. Funct. Mater.*, vol. 21, no. 12, pp. 2264–2272, 2011.
- [80] C. Liao, M. Zhang, L. Niu, Z. Zheng, and F. Yan, "Highly selective and sensitive glucose sensors based on organic electrochemical transistors with graphene-modified gate electrodes," *J. Mater. Chem. B*, vol. 1, no. 31, pp. 3820–3829, 2013.
- [81] C. Liao, C. Mak, M. Zhang, H. L. W. Chan, and F. Yan, "Flexible organic electrochemical transistors for highly selective enzyme biosensors and used for saliva testing," *Adv. Mater.*, vol. 27, no. 4, pp. 676–681, 2015.
- [82] X. Ji *et al.*, "Highly Sensitive Metabolite Biosensor Based on Organic Electrochemical Transistor Integrated with Microfluidic Channel and Poly(N-vinyl-2-pyrrolidone)-Capped Platinum Nanoparticles," *Adv. Mater. Technol.*, vol. 1, no. 5, pp. 1–8, 2016.
- [83] A. M. Pappa *et al.*, "Organic Transistor Arrays Integrated with Finger-Powered Microfluidics for Multianalyte Saliva Testing," *Adv. Healthc. Mater.*, vol. 5, no. 17, pp. 2295–2302, 2016.
- [84] X. Strakosas *et al.*, "Catalytically enhanced organic transistors for in vitro toxicology monitoring

- through hydrogel entrapment of enzymes,” *J. Appl. Polym. Sci.*, vol. 134, pp. 1–7, 2017.
- [85] L. J. Currano, F. C. Sage, M. Hagedon, L. Hamilton, J. Patrone, and K. Gerasopoulos, “Wearable Sensor System for Detection of Lactate in Sweat,” *Sci. Rep.*, vol. 8, no. 15890, pp. 1–11, 2018.
- [86] J. M. Chem *et al.*, “Organic electrochemical transistor incorporating an ionogel as a solid state electrolyte for lactate sensing,” *J. Mater. Chem.*, vol. 22, pp. 4440–4443, 2012.
- [87] S. Y. Yang *et al.*, “Integration of a surface-directed microfluidic system with an organic electrochemical transistor array for multi-analyte biosensors,” *Lab Chip*, vol. 9, no. 5, pp. 704–708, 2009.
- [88] L. Kergoat, B. Piro, D. T. Simon, M. C. Pham, V. Noël, and M. Berggren, “Detection of glutamate and acetylcholine with organic electrochemical transistors based on conducting polymer/platinum nanoparticle composites,” *Adv. Mater.*, vol. 26, pp. 5658–5664, 2014.
- [89] S. Y. Yang *et al.*, “Electrochemical transistors with ionic liquids for enzymatic sensing,” *Chem. Commun.*, vol. 46, no. 42, pp. 7972–7974, 2010.
- [90] N. Y. Shim *et al.*, “All-plastic electrochemical transistor for glucose sensing using a ferrocene mediator,” *Sensors*, vol. 9, no. 12, pp. 9896–9902, 2009.
- [91] E. Bihar, Y. Deng, T. Miyake, M. Saadaoui, G. G. Malliaras, and M. Rolandi, “A Disposable paper breathalyzer with an alcohol sensing organic electrochemical transistor,” *Sci. Rep.*, vol. 6, no. 27582, pp. 2–7, 2016.
- [92] D. Gentili *et al.*, “Integration of organic electrochemical transistors and immuno-affinity membranes for label-free detection of interleukin-6 in the physiological concentration range through antibody-antigen recognition,” *J. Mater. Chem. B*, vol. 6, no. 33, pp. 5400–5406, 2018.
- [93] H. Liu *et al.*, “Ultrafast, sensitive, and portable detection of COVID-19 IgG using flexible organic electrochemical transistors,” *Sci. Adv.*, vol. 7, no. eabg8387, pp. 1–9, 2021.
- [94] N. M. Andoy, M. S. Filipiak, D. Vetter, Ó. Gutiérrez-Sanz, and A. Tarasov, “Graphene-Based Electronic Immunosensor with Femtomolar Detection Limit in Whole Serum,” *Adv. Mater. Technol.*, vol. 3, no. 1800186 1800186, pp. 1–12, 2018.
- [95] M. Ku *et al.*, “Smart, soft contact lens for wireless immunosensing of cortisol,” *Sci. Adv.*, vol. 6, no. 28, pp. 1–10, 2020.
- [96] X. Xu *et al.*, “Reconfigurable Carbon Nanotube Multiplexed Sensing Devices,” *Nano Lett.*, vol.

- 18, no. 7, pp. 4130–4135, 2018.
- [97] M. S. Chae, J. H. Park, H. W. Son, K. S. Hwang, and T. G. Kim, “IGZO-based electrolyte-gated field-effect transistor for in situ biological sensing platform,” *Sensors Actuators, B Chem.*, vol. 262, pp. 876–883, 2018.
  - [98] S. Casalini *et al.*, “Multiscale sensing of antibody-antigen interactions by organic transistors and single-molecule force spectroscopy,” *ACS Nano*, vol. 9, no. 5, pp. 5051–5062, 2015.
  - [99] M. Berto *et al.*, “Biorecognition in organic field effect transistors biosensors: The role of the density of states of the organic semiconductor,” *Anal. Chem.*, vol. 88, no. 24, pp. 12330–12338, 2016.
  - [100] M. Berto *et al.*, “EGOFET Peptide Aptasensor for Label-Free Detection of Inflammatory Cytokines in Complex Fluids,” *Adv. Biosyst.*, vol. 2, no. 2, pp. 1–8, 2018.
  - [101] E. Macchia *et al.*, “Single-molecule detection with a millimetre-sized transistor,” *Nat. Commun.*, vol. 9, no. 3223, pp. 1–10, 2018.
  - [102] N. Saraf, E. R. Woods, M. Peppler, and S. Seal, “Highly selective aptamer based organic electrochemical biosensor with pico-level detection,” *Biosens. Bioelectron.*, vol. 117, pp. 40–46, 2018.
  - [103] Y. Fu, N. Wang, A. Yang, H. K. wai Law, L. Li, and F. Yan, “Highly Sensitive Detection of Protein Biomarkers with Organic Electrochemical Transistors,” *Adv. Mater.*, vol. 29, no. 41, pp. 1–7, 2017.
  - [104] G. Scheiblin, R. Coppard, R. M. Owens, P. Mailley, and G. G. Malliaras, “Referenceless pH Sensor using Organic Electrochemical Transistors,” *Adv. Mater. Technol.*, vol. 2, no. 1600141, pp. 1–5, 2017.
  - [105] A. Tibaldi *et al.*, “Electrolyte-gated organic field-effect transistors (EGOFETs) as complementary tools to electrochemistry for the study of surface processes,” *Electrochem. commun.*, vol. 98, pp. 43–46, 2019.
  - [106] M. Yano *et al.*, “Zinc oxide ion-sensitive field-effect transistors and biosensors,” *Phys. Status Solidi Appl. Mater. Sci.*, vol. 211, no. 9, pp. 2098–2104, 2014.
  - [107] S. Han, S. Yamamoto, A. G. Polykravos, and G. G. Malliaras, “Microfabricated Ion-Selective Transistors with Fast and Super-Nernstian Response,” *Adv. Mater.*, vol. 32, no. 2004790, pp. 1–8, 2020.

- [108] D. J. Kim, N. E. Lee, J. S. Park, I. J. Park, J. G. Kim, and H. J. Cho, "Organic electrochemical transistor based immunosensor for prostate specific antigen (PSA) detection using gold nanoparticles for signal amplification," *Biosens. Bioelectron.*, vol. 25, no. 11, pp. 2477–2482, 2010.
- [109] R. Faddoul, R. Coppard, and T. Berthelot, "Inkjet printing of organic electrochemical immunosensors," *Proc. IEEE Sensors*, pp. 1088–1091, 2014.
- [110] J. M. Chem *et al.*, "Detection of bacteria with organic electrochemical transistors," *J. Mater. Chem.*, vol. 22, pp. 22072–22076, 2012.
- [111] K. Schmoltner, J. Kofler, A. Klug, and E. J. W. List-Kratochvil, "Electrolyte-gated organic field-effect transistor for selective reversible ion detection," *Adv. Mater.*, vol. 25, no. 47, pp. 6895–6899, 2013.
- [112] P. Seshadri *et al.*, "Low-picomolar, label-free procalcitonin analytical detection with an electrolyte-gated organic field-effect transistor based electronic immunosensor," *Biosens. Bioelectron.*, vol. 104, no. October 2017, pp. 113–119, 2018.
- [113] N. Aroonyadet, W. Jeamsaksiri, A. Wisitsoraat, and A. Tuantranont, "Top-down and sensitive indium oxide nanoribbon field effect transistor biosensor chips integrated with on-chip gate electrodes toward point of care applications," *Nanotechnology*, vol. 29, no. 405505, pp. 1–9, 2018.
- [114] M. S. Chae, Y. K. Yoo, J. Kim, T. G. Kim, and K. S. Hwang, "Graphene-based enzyme-modified field-effect transistor biosensor for monitoring drug effects in Alzheimer's disease treatment," *Sensors Actuators, B Chem.*, vol. 272, no. March, pp. 448–458, 2018.
- [115] Y. G. Kim, Y. J. Tak, H. J. Kim, W. G. Kim, H. Yoo, and H. J. Kim, "Facile fabrication of wire-type indium gallium zinc oxide thin-film transistors applicable to ultrasensitive flexible sensors," *Sci. Rep.*, vol. 8, no. 1, pp. 1–7, 2018.
- [116] K. M. Chang, C. T. Chang, and K. M. Chan, "Development of an ion sensitive field effect transistor based urea biosensor with solid state reference systems," *Sensors*, vol. 10, pp. 6115–6127, 2010.
- [117] W. Sant *et al.*, "Development of a creatinine-sensitive sensor for medical analysis," *Sensors Actuators, B Chem.*, vol. 103, no. 1–2, pp. 260–264, 2004.
- [118] M. Rovira, C. Fernández-Sánchez, S. Demuru, P. K. Brince, D. Briand, and C. Jimenez-Jorquera, "Multisensing Wearable Technology for Sweat Biomonitoring," *Eng. Proc.*, vol. 6, no. 1, p. 78, 2021.

- [119] S. Joshi, V. D. Bhatt, H. Wu, M. Becherer, and P. Lugli, “Flexible lactate and glucose sensors using electrolyte-gated carbon nanotube field effect transistor for non-invasive real-time monitoring,” *IEEE Sens. J.*, vol. 17, no. 14, pp. 4315–4321, 2017.
- [120] K. Maksymiuk, E. Stelmach, and A. Michalska, “Unintended changes of ion-selective membranes composition—origin and effect on analytical performance,” *Membranes (Basel)*, vol. 10, no. 266, pp. 1–14, 2020.
- [121] D. A. Bernardis, D. J. Macaya, M. Nikolou, J. A. Defranco, S. Takamatsu, and G. G. Malliaras, “Enzymatic sensing with organic electrochemical transistors,” *J. Mater. Chem.*, vol. 18, pp. 116–120, 2008.
- [122] S. Khan, S. Ali, A. Khan, B. Wang, and A. Bermak, “Printing Sensors on Biocompatible Substrates for Selective Detection of Glucose,” *IEEE Sens. J.*, vol. 21, no. 4, pp. 4167–4175, 2020.
- [123] V. Kesler, B. Murmann, and H. T. Soh, “Going beyond the Debye Length: Overcoming Charge Screening Limitations in Next-Generation Bioelectronic Sensors,” *ACS Nano*, vol. 14, no. 12, pp. 16194–16201, 2020.
- [124] J. Aleman, T. Kilic, and L. S. Mille, “Microfluidic integration of regeneratable electrochemical affinity-based biosensors for continual monitoring of organ-on-a-chip devices,” *Nat. Protoc.*
- [125] D. Gentili *et al.*, “Integration of organic electrochemical transistors and immuno-affinity membranes for label-free detection of interleukin-6 in the physiological concentration range through antibody–antigen recognition,” *J. Mater. Chem. B*, vol. 6, pp. 5400–5406, 2018.
- [126] P. Romele, M. Ghittorelli, Z. M. Kovács-Vajna, and F. Torricelli, “Ion buffering and interface charge enable high performance electronics with organic electrochemical transistors,” *Nat. Commun.*, vol. 10, no. 1, pp. 1–11, 2019.
- [127] P. Lin, F. Yan, and H. L. W. Chan, “Ion-sensitive properties of organic electrochemical transistors,” *ACS Appl. Mater. Interfaces*, vol. 2, no. 6, pp. 1637–1641, 2010.
- [128] D. A. Bernardis, D. J. Macaya, M. Nikolou, J. A. Defranco, S. Takamatsu, and G. G. Malliaras, “Enzymatic sensing with organic electrochemical transistors,” *J. Mater. Chem.*, vol. 18, pp. 116–120, 2008.
- [129] B. Weng *et al.*, “Wholly printed polypyrrole nanoparticle-based biosensors on flexible substrate,” *J. Mater. Chem. B*, vol. 2, pp. 793–799, 2014.

- [130] L. V Lingstedt *et al.*, “Effect of DMSO Solvent Treatments on the Performance of PEDOT : PSS Based Organic Electrochemical Transistors,” *Adv. Electron. Mater.*, vol. 5, pp. 1–8, 2019.
- [131] T. R. Chou, S. H. Chen, Y. Te Chiang, Y. T. Lin, and C. Y. Chao, “Highly conductive PEDOT: PSS films by post-treatment with dimethyl sulfoxide for ITO-free liquid crystal display,” *J. Mater. Chem. C*, vol. 3, no. 15, pp. 3760–3766, 2015.
- [132] S. Kim *et al.*, “Influence of PEDOT:PSS crystallinity and composition on electrochemical transistor performance and long-term stability,” *Nat. Commun.*, vol. 9, pp. 1–9, 2018.
- [133] Y. Liu *et al.*, “Epidermal mechano-acoustic sensing electronics for cardiovascular diagnostics and human-machine interfaces,” *Sci. Adv.*, vol. 2, pp. 1–12, 2016.
- [134] G. Tarabella *et al.*, “Effect of the gate electrode on the response of organic electrochemical transistors transistors,” *Appl. Phys. Lett.*, vol. 123304, pp. 1–3, 2010.
- [135] P. R. Paudel, V. Kaphle, D. Dahal, R. K. Radha Krishnan, and B. Lüssem, “Tuning the Transconductance of Organic Electrochemical Transistors,” *Adv. Funct. Mater.*, vol. 31, no. 2004939, pp. 1–12, 2020.
- [136] D. Gentili *et al.*, “Integration of organic electrochemical transistors and immuno-affinity membranes for label-free detection of interleukin-6 in the physiological concentration range through antibody–antigen recognition,” *J. Mater. Chem. B*, vol. 6, pp. 5400–5406, 2018.
- [137] A. J. Bandodkar and J. Wang, “Non-invasive wearable electrochemical sensors: A review,” *Trends Biotechnol.*, vol. 32, no. 7, pp. 363–371, 2014.
- [138] Y. Kim *et al.*, “Organic electrochemical transistor-based channel dimension-independent single-strand wearable sweat sensors,” *NPG Asia Mater.*, vol. 10, no. 11, pp. 1086–1095, 2018.
- [139] H. Y. Y. Nyein *et al.*, “Regional and correlative sweat analysis using high-throughput microfluidic sensing patches toward decoding sweat,” *Sci. Adv.*, vol. 5, no. 8, pp. 1–12, 2019.
- [140] L. B. Baker, K. A. Barnes, M. L. Anderson, D. H. Passe, and J. R. Stofan, “Normative data for regional sweat sodium concentration and whole-body sweating rate in athletes,” *J. Sports Sci.*, vol. 34, no. 4, pp. 358–368, 2016.
- [141] G. Palacios, R. Pedrero-Chamizo, N. Palacios, B. Maroto-Sanchez, S. Aznar, and M. Gonzalez-Gross, “Biomarkers of physical activity and exercise,” *Nutr. Hosp.*, vol. 31, no. 3, pp. 237–244, 2015.

- [142] R. A. Neal, H. C. Massey, M. J. Tipton, J. S. Young, and J. Corbett, “Effect of permissive dehydration on induction and decay of heat acclimation, and temperate exercise performance,” *Front. Physiol.*, vol. 7, no. 564, pp. 1–11, 2016.
- [143] N. L. Nelson and J. R. Churilla, “A narrative review of exercise-associated muscle cramps: Factors that contribute to neuromuscular fatigue and management implications,” *Muscle and Nerve*, vol. 54, pp. 177–185, 2016.
- [144] B. Lara *et al.*, “Sweat sodium loss influences serum sodium concentration in a marathon,” *Scand. J. Med. Sci. Sport.*, pp. 1–9, 2015.
- [145] D. A. Sakharov, M. U. Shkurnikov, M. Y. Vagin, E. I. Yashina, A. A. Karyakin, and A. G. Tonevitsky, “Relationship between lactate concentrations in active muscle sweat and whole blood,” *Bull. Exp. Biol. Med.*, vol. 150, no. 1, pp. 94–96, 2010.
- [146] L. Nela, J. Tang, Q. Cao, G. Tulevski, and S. J. Han, “Large-Area High-Performance Flexible Pressure Sensor with Carbon Nanotube Active Matrix for Electronic Skin,” *Nano Lett.*, vol. 18, no. 3, pp. 2054–2059, 2018.
- [147] C. Wu *et al.*, “A Microfluidic Ion Sensor Array,” *Small*, vol. 16, no. 1906436, pp. 1–6, 2020.
- [148] S. Zhang *et al.*, “Hydrogel-Enabled Transfer-Printing of Conducting Polymer Films for Soft Organic Bioelectronics,” *Adv. Funct. Mater.*, vol. 30, no. 1906016, pp. 1–8, 2020.
- [149] A. Tricoli, N. Nasiri, and S. De, “Wearable and Miniaturized Sensor Technologies for Personalized and Preventive Medicine,” *Adv. Funct. Mater.*, vol. 27, no. 1605271, pp. 1–19, 2017.
- [150] M. Cuartero, M. Parrilla, and G. A. Crespo, “Wearable potentiometric sensors for medical applications,” *Sensors*, vol. 19, no. 2, pp. 1–24, 2019.
- [151] E. Zdrachek and E. Bakker, “Potentiometric Sensing,” *Anal. Chem.*, vol. 91, no. 1, pp. 2–26, 2019.
- [152] T. Guinovart, G. A. Crespo, F. X. Rius, and F. J. Andrade, “A reference electrode based on polyvinyl butyral (PVB) polymer for decentralized chemical measurements,” *Anal. Chim. Acta*, vol. 821, pp. 72–80, 2014.
- [153] V. A. T. Dam, M. Goedbloed, and M. A. G. Zevenbergen, “Solid-Contact Reference Electrode for Ion-Selective Sensors,” *Eurosensors Conf. Paris, Fr.*, vol. 1, no. 4, p. 464, 2017.
- [154] I. Gualandi, M. Tessarolo, F. Mariani, D. Tonelli, B. Fraboni, and E. Scavetta, “Organic Electrochemical Transistors as Versatile Analytical Potentiometric Sensors,” *Front. Bioeng.*



- Biotechnol.*, vol. 7, no. 354, pp. 1–13, 2019.
- [155] K. Tybrandt, I. V Zozoulenko, and M. Berggren, “Chemical potential – electric double layer coupling in conjugated polymer – polyelectrolyte blends,” *Sci. Adv.*, vol. 3, pp. 1–7, 2018.
  - [156] S. Savagatrup *et al.*, “Plasticization of PEDOT:PSS by common additives for mechanically robust organic solar cells and wearable sensors,” *Adv. Funct. Mater.*, vol. 25, pp. 427–436, 2015.
  - [157] A. V. Volkov *et al.*, “Understanding the Capacitance of PEDOT:PSS,” *Adv. Funct. Mater.*, vol. 27, no. 1700329, pp. 1–10, 2017.
  - [158] N. Coppedè *et al.*, “Ion selective textile organic electrochemical transistor for wearable sweat monitoring,” *Org. Electron.*, vol. 78, no. 105579, pp. 1–6, 2020.
  - [159] S. Demuru, A. Marette, W. Kooli, P. Junier, and D. Briand, “Flexible Organic Electrochemical Transistor with Functionalized Inkjet-Printed Gold Gate for Bacteria Sensing,” *Proc. Eurosensors - Transducers*, vol. 1, pp. 2519–2522, 2019.
  - [160] T. Carey *et al.*, “Fully inkjet-printed two-dimensional material field-effect heterojunctions for wearable and textile electronics,” *Nat. Commun.*, vol. 8, no. 1202, pp. 1–11, 2017.
  - [161] T. Blaudeck *et al.*, “Simplified large-area manufacturing of organic electrochemical transistors combining printing and a self-aligning laser ablation step,” *Adv. Funct. Mater.*, vol. 22, no. 14, pp. 2939–2948, 2012.
  - [162] S. Inal, G. G. Malliaras, and J. Rivnay, “Benchmarking organic mixed conductors for transistors,” *Nat. Commun.*, vol. 8, no. 1, pp. 1–6, 2017.
  - [163] D. Khodagholy *et al.*, “High transconductance organic electrochemical transistors,” *Nat. Commun.*, vol. 4, pp. 1–6, 2013.
  - [164] Y. Liang *et al.*, “Tuning Channel Architecture of Interdigitated Organic Electrochemical Transistors for Recording the Action Potentials of Electrogenic Cells,” *Adv. Funct. Mater.*, vol. 29, no. 1902085, pp. 1–10, 2019.
  - [165] M. Braendlein *et al.*, “Lactate Detection in Tumor Cell Cultures Using Organic Transistor Circuits,” *Adv. Mater.*, vol. 29, no. 1605744, pp. 1–6, 2017.
  - [166] F. Mariani, I. Gualandi, M. Tessarolo, B. Fraboni, and E. Scavetta, “PEDOT: Dye-Based, Flexible Organic Electrochemical Transistor for Highly Sensitive pH Monitoring,” *ACS Appl. Mater. Interfaces*, vol. 10, no. 26, pp. 22474–22484, 2018.

- [167] O. Parlak, S. T. Keene, A. Marais, V. F. Curto, A. Salleo, and O. Parlak, “Molecularly selective nanoporous membrane-based wearable organic electrochemical device for noninvasive cortisol sensing,” *Sci. Adv.*, vol. 4, pp. 1–10, 2018.
- [168] Z. Mousavi, A. Ekholm, J. Bobacka, and A. Ivaska, “Ion-selective organic electrochemical junction transistors based on poly(3,4-ethylenedioxythiophene) doped with poly(styrene sulfonate),” *Electroanalysis*, vol. 21, no. 3–5, pp. 472–479, 2009.
- [169] S. T. Keene, D. Fogarty, R. Cooke, C. D. Casadevall, A. Salleo, and O. Parlak, “Wearable Organic Electrochemical Transistor Patch for Multiplexed Sensing of Calcium and Ammonium Ions from Human Perspiration,” *Adv. Healthc. Mater.*, vol. 8, no. 24, pp. 1–8, 2019.
- [170] T. R. Chou, S. H. Chen, Y. Te Chiang, Y. T. Lin, and C. Y. Chao, “Highly Conductive PEDOT:PSS Film by Post-Treatment with Dimethyl Sulfoxide for ITO-Free Liquid Crystal Display,” *Mol. Cryst. Liq. Cryst.*, vol. 612, no. 1, pp. 201–210, 2015.
- [171] S. Kim *et al.*, “Purification of PEDOT:PSS by Ultrafiltration for Highly Conductive Transparent Electrode of All-Printed Organic Devices,” *Adv. Mater.*, vol. 28, no. 46, pp. 10149–10154, 2016.
- [172] G. Tarabella, C. Santato, S. Y. Yang, S. Iannotta, G. G. Malliaras, and F. Cicoira, “Effect of the gate electrode on the response of organic electrochemical transistors,” *Appl. Phys. Lett.*, vol. 97, no. 123304, pp. 1–3, 2010.
- [173] K. Xu, M. Cuartero, and G. A. Crespo, “Lowering the limit of detection of ion-selective membranes backside contacted with a film of poly(3-octylthiophene),” *Sensors Actuators, B Chem.*, vol. 297, no. 126781, pp. 1–10, 2019.
- [174] J. T. Friedlein, M. J. Donahue, S. E. Shaheen, G. G. Malliaras, and R. R. McLeod, “Microsecond Response in Organic Electrochemical Transistors: Exceeding the Ionic Speed Limit,” *Adv. Mater.*, vol. 28, no. 38, pp. 8398–8404, 2016.
- [175] N. Di Rollo, D. Caesar, D. A. Ferenbach, and M. J. G. Dunn, “Survival from profound metabolic acidosis due to hypovolaemic shock. A world record?,” 2013.
- [176] A. Pachori, H. Kambalimath, S. Maran, B. Niranjana, G. Bhambhani, and G. Malhotra, “Evaluation of Changes in Salivary pH after Intake of Different Eatables and Beverages in Children at Different Time Intervals,” *Int. J. Clin. Pediatr. Dent.*, vol. 11, no. 3, pp. 177–182, 2018.
- [177] J. N. Hussain, N. Mantri, and M. M. Cohen, “Working up a good sweat - The challenges of standardising sweat collection for metabolomics analysis,” *Clin. Biochem. Rev.*, vol. 38, no. 1, pp.

13–34, 2017.

- [178] S. G. Higgins, A. Lo Fiego, I. Patrick, A. Creamer, and M. M. Stevens, “Organic Bioelectronics: Using Highly Conjugated Polymers to Interface with Biomolecules, Cells, and Tissues in the Human Body,” *Adv. Mater. Technol.*, vol. 2000384, pp. 1–35, 2020.
- [179] W. Lee *et al.*, “Transparent, conformable, active multielectrode array using organic electrochemical transistors,” *Proc. Natl. Acad. Sci. U. S. A.*, vol. 114, no. 40, pp. 10554–10559, 2017.
- [180] F. Hempel *et al.*, “PEDOT:PSS organic electrochemical transistor arrays for extracellular electrophysiological sensing of cardiac cells,” *Biosens. Bioelectron.*, vol. 93, pp. 132–138, 2017.
- [181] L. Zhang *et al.*, “Highly selective and sensitive sensor based on an organic electrochemical transistor for the detection of ascorbic acid,” *Biosens. Bioelectron.*, vol. 100, pp. 235–241, 2018.
- [182] A. Romeo *et al.*, “Drug-induced cellular death dynamics monitored by a highly sensitive organic electrochemical system,” *Biosens. Bioelectron.*, vol. 68, pp. 791–797, 2015.
- [183] D. Tu and S. Fabiano, “Mixed ion-electron transport in organic electrochemical transistors,” *Appl. Phys. Lett.*, vol. 117, no. 8, 2020.
- [184] N. Ruecha, R. Rangkupan, N. Rodthongkum, and O. Chailapakul, “Novel paper-based cholesterol biosensor using graphene/polyvinylpyrrolidone/polyaniline nanocomposite,” *Biosens. Bioelectron.*, vol. 52, pp. 13–19, 2014.
- [185] G. Mattana and D. Briand, “Recent advances in printed sensors on foil,” *Mater. Today*, vol. 19, no. 2, pp. 88–99, 2016.
- [186] S. Demuru, B. P. Kunnel, and D. Briand, “Real-Time Multi-Ion Detection in the Sweat Concentration Range Enabled by Flexible, Printed, and Microfluidics-Integrated Organic Transistor Arrays,” *Adv. Mater. Technol.*, vol. 2000328, pp. 1–9, 2020.
- [187] S. Y. Lee, G. R. Choi, H. Lim, K. M. Lee, and S. K. Lee, “Electronic transport characteristics of electrolyte-gated conducting polyaniline nanowire field-effect transistors,” *Appl. Phys. Lett.*, vol. 95, no. 013113, pp. 1–3, 2009.
- [188] L. Travaglini, A. P. Micolich, C. Cazorla, E. Zeglio, A. Lauto, and D. Mawad, “Advanced Functional Materials Single-material OECT-based flexible complementary circuits featuring polyaniline in both conducting channels,” *Adv. Funct. Mater.* 2020, vol. 2007205, pp. 1–10, 2020.

- [189] X. Ji *et al.*, “Highly Sensitive Metabolite Biosensor Based on Organic Electrochemical Transistor Integrated with Microfluidic Channel and Poly ( N-vinyl-2-pyrrolidone ) -Capped Platinum Nanoparticles,” *Adv. Mater. Technol.* 2016, vol. 1, no. 1600042, pp. 1–8, 2016.
- [190] Y. Li, Y. Mao, C. Xiao, X. Xu, and X. Li, “Flexible pH sensor based on a conductive PANI membrane for pH monitoring,” *RSC Adv.*, vol. 10, no. 1, pp. 21–28, 2019.
- [191] S. Y. Oh *et al.*, “Skin-Attachable, Stretchable Electrochemical Sweat Sensor for Glucose and pH Detection,” *ACS Appl. Mater. Interfaces*, vol. 10, p. 13729–13740, 2018.
- [192] A. Vacca *et al.*, “Preparation and characterisation of transparent and flexible PEDOT:PSS/PANI electrodes by ink-jet printing and electropolymerisation,” *RSC Adv.*, vol. 5, no. 97, pp. 79600–79606, 2015.
- [193] A. Kellenberger, N. Plesu, M. Tara-Lunga Mihali, and N. Vasilcsin, “Synthesis of polyaniline nanostructures by electrochemical deposition on niobium,” *Polymer (Guildf)*, vol. 54, no. 13, pp. 3166–3174, 2013.
- [194] Q. Jiang *et al.*, “Improved thermoelectric performance of PEDOT:PSS films prepared by polar-solvent vapor annealing method,” *J. Mater. Sci. Mater. Electron.*, vol. 24, no. 11, pp. 4240–4246, 2013.
- [195] W. Wang, F. Yang, C. Chen, L. Zhang, Y. Qin, and M. Knez, “Tuning the Conductivity of Polyaniline through Doping by Means of Single Precursor Vapor Phase Infiltration,” *Adv. Mater. Interfaces*, vol. 4, no. 1600806, pp. 1–8, 2017.
- [196] Y. Lee *et al.*, “Wireless, intraoral hybrid electronics for real-time quantification of sodium intake toward hypertension management,” *PNAS*, vol. 115, no. 21, pp. 5377–5382, 2018.
- [197] S. Nakata, M. Shiomi, Y. Fujita, T. Arie, S. Akita, and K. Takei, “A wearable pH sensor with high sensitivity based on a flexible charge-coupled device,” *Nat. Electron.*, vol. 1, no. 11, pp. 596–603, 2018.
- [198] M. Khademi and D. P. J. Barz, “Structure of the Electrical Double Layer Revisited: Electrode Capacitance in Aqueous Solutions,” *Langmuir*, vol. 36, no. 16, pp. 4250–4260, 2020.
- [199] R. D. Oliveira, C. S. Santos, J. R. Garcia, M. Vidotti, L. F. Marchesi, and C. A. Pessoa, “IR drop studies of poly(aniline)-based modified electrodes,” *J. Electroanal. Chem.*, vol. 878, p. 114662, 2020.

- [200] S. Ting *et al.*, “High-Gain Chemically Gated Organic Electrochemical Transistor,” *Adv. Funct. Mater.*, no. 2010868, pp. 1–9, 2021.
- [201] J. R. Sempionatto *et al.*, “An epidermal patch for the simultaneous monitoring of haemodynamic and metabolic biomarkers,” *Nat. Biomed. Eng.*, pp. 1–12, 2021.
- [202] J. Sabaté del Río, O. Y. F. Henry, P. Jolly, and D. E. Ingber, “An antifouling coating that enables affinity-based electrochemical biosensing in complex biological fluids,” *Nat. Nanotechnol.*, vol. 14, no. 12, pp. 1143–1149, 2019.
- [203] S. Imani *et al.*, “A wearable chemical-electrophysiological hybrid biosensing system for real-time health and fitness monitoring,” *Nat. Commun.*, vol. 7, no. 11650, pp. 1–7, 2016.
- [204] B. Paul, S. Demuru, C. Lafaye, M. Saubade, and D. Briand, “Printed Iontophoretic-Integrated Wearable Microfluidic Sweat-Sensing Patch for On-Demand Point-Of-Care Sweat Analysis,” vol. 2000910, pp. 1–11, 2021.
- [205] K. Parate *et al.*, “Aerosol-Jet-Printed Graphene Immunosensor for Label-Free Cytokine Monitoring in Serum,” *ACS Appl. Mater. Interfaces*, vol. 12, no. 7, pp. 8592–8603, 2020.
- [206] W. Gao *et al.*, “Fully integrated wearable sensor arrays for multiplexed in situ perspiration analysis,” *Nature*, vol. 529, pp. 509–514, 2016.
- [207] Q. Liu *et al.*, “Highly Sensitive and Wearable In<sub>2</sub>O<sub>3</sub>Nanoribbon Transistor Biosensors with Integrated On-Chip Gate for Glucose Monitoring in Body Fluids,” *ACS Nano*, vol. 12, p. 1170–1178, 2018.
- [208] Y. J. Hong *et al.*, “Multifunctional Wearable System that Integrates Sweat-Based Sensing and Vital-Sign Monitoring to Estimate Pre-/Post-Exercise Glucose Levels,” *Adv. Funct. Mater.*, vol. 28, no. 47, pp. 1–12, 2018.
- [209] J. Heikenfeld *et al.*, “Accessing analytes in biofluids for peripheral biochemical monitoring,” *Nat. Biotechnol.*, vol. 37, no. 4, pp. 407–419, 2019.
- [210] E. W. Nery, M. Kundys, P. S. Jeleń, and M. Jönsson-Niedziółka, “Electrochemical glucose sensing: Is there still room for improvement?,” *Anal. Chem.*, vol. 88, no. 23, pp. 11271–11282, 2016.
- [211] A. E. G. Cass *et al.*, “Ferrocene-Mediated Enzyme Electrode for Amperometric Determination of Glucose,” *Anal. Chem.*, vol. 56, no. 4, pp. 667–671, 1984.

- [212] X. Xuan, H. S. Yoon, and J. Y. Park, “A wearable electrochemical glucose sensor based on simple and low-cost fabrication supported micro-patterned reduced graphene oxide nanocomposite electrode on flexible substrate,” *Biosens. Bioelectron.*, vol. 109, pp. 75–82, 2018.
- [213] S. Demuru, R. Haque, M. O. Joho, A. Bionaz, P. Van Der Wal, and D. Briand, “3D-Integration of Printed Electrochemical Sensors in Pet Microfluidics for Biochemical Sensing,” *2019 20th Int. Conf. Solid-State Sensors, Actuators Microsystems Eurosensors XXXIII, TRANSDUCERS 2019 EUROSENSORS XXXIII*, no. August, pp. 2464–2467, 2019.
- [214] S. Demuru, B. P. Kunnel, and D. Briand, “Biosensors and Bioelectronics : X Thin film organic electrochemical transistors based on hybrid PANI / PEDOT : PSS active layers for enhanced pH sensing,” *Biosens. Bioelectron. X*, vol. 7, no. 100065, pp. 1–9, 2021.
- [215] D. McManus *et al.*, “Water-based and biocompatible 2D crystal inks for all-inkjet-printed heterostructures,” *Nat. Nanotechnol.*, vol. 12, no. 4, pp. 343–350, 2017.
- [216] K. Parvez, R. Worsley, A. Alieva, A. Felten, and C. Casiraghi, “Water-based and inkjet printable inks made by electrochemically exfoliated graphene,” *Carbon N. Y.*, vol. 149, pp. 213–221, 2019.
- [217] I. J. Fernandes *et al.*, “Silver nanoparticle conductive inks: synthesis, characterization, and fabrication of inkjet-printed flexible electrodes,” *Sci. Rep.*, vol. 10, no. 8878, pp. 1–11, 2020.
- [218] G. Bickerstaff, M. Koudelka-Hep, N. F. de Rooij, and D. J. Strike, “Immobilization of Enzymes on Microelectrodes Using Chemical Crosslinking,” in *Methods in biotechnology*, vol. 1, 1997, pp. 83–86.
- [219] P. A. Fiorito and S. I. Córdoba De Torresi, “Glucose Amperometric Biosensor Based on the Co-immobilization of Glucose Oxidase (GOx) and Ferrocene in Poly(pyrrole) Generated from Ethanol/Water Mixtures,” *J. Braz. Chem. Soc.*, vol. 12, no. 6, pp. 729–733, 2001.
- [220] X. V. Zhen, C. R. Rousseau, and P. Bühlmann, “Redox Buffer Capacity of Ion-Selective Electrode Solid Contacts Doped with Organometallic Complexes,” *Anal. Chem.*, vol. 90, no. 18, pp. 11000–11007, 2018.
- [221] E. MacChia *et al.*, “About the amplification factors in organic bioelectronic sensors,” *Mater. Horizons*, vol. 7, no. 4, pp. 999–1013, 2020.
- [222] M. Jia, W. M. Chew, Y. Feinstein, P. Skeath, and E. M. Sternberg, “Quantification of cortisol in human eccrine sweat by liquid chromatography – tandem mass spectrometry,” *Analyst*, vol. 141, pp. 2053–2060, 2016.

- [223] P. Boucher and P. Plusquellec, “Acute Stress Assessment From Excess Cortisol Secretion: Fundamentals and Perspectives,” *Front. Endocrinol. (Lausanne)*, vol. 10, pp. 1–12, 2019.
- [224] M. Qi, H. Gao, L. Guan, G. Liu, and J. Yang, “Subjective Stress, Salivary Cortisol, and Electrophysiological Responses to Psychological Stress,” *Front. Psychol.*, vol. 7, pp. 1–9, 2016.
- [225] E. E. Hill, E. Zack, C. Battaglini, M. Viru, A. Viru, and A. C. Hackney, “Exercise and circulating cortisol levels: The intensity threshold effect,” *J. Endocrinol. Invest.* 31, vol. 31, pp. 587–591, 2008.
- [226] W. Tang, L. Yin, J. R. Sempionatto, J. Moon, H. Teymourian, and J. Wang, “Touch-Based Stressless Cortisol Sensing,” *Adv. Mater.*, vol. 2008465, pp. 1–11, 2021.
- [227] S. Dalirirad and A. J. Steckl, “Aptamer-based lateral flow assay for point of care cortisol detection in sweat,” *Sensors Actuators, B Chem.*, vol. 283, pp. 79–86, 2019.
- [228] C. Cheng *et al.*, “Battery-free, wireless, and flexible electrochemical patch for in situ analysis of sweat cortisol via near field communication,” *Biosens. Bioelectron.*, vol. 172, p. 112782, 2020.
- [229] W. Limbut, P. Kanatharana, B. Mattiasson, P. Asawatreratanakul, and P. Thavarungkul, “A comparative study of capacitive immunosensors based on self-assembled monolayers formed from thiourea, thioctic acid, and 3-mercaptopropionic acid,” *Biosens. Bioelectron.*, vol. 22, no. 2, pp. 233–240, 2006.
- [230] D. Kinnamon, R. Ghanta, K. C. Lin, S. Muthukumar, and S. Prasad, “Portable biosensor for monitoring cortisol in low-volume perspired human sweat,” *Sci. Rep.*, vol. 7, no. 1, pp. 1–13, 2017.
- [231] F. Criscuolo, I. Taurino, T. Kilic, S. Carrara, and G. De Micheli, “An electrochemical sensor for quantitative analysis of Rhesus D antibodies in blood,” *Proc. - 2017 7th Int. Work. Adv. Sensors Interfaces, IWASI 2017*, pp. 236–240, 2017.
- [232] R. D. Munje, S. Muthukumar, A. P. Selvam, and S. Prasad, “Flexible nanoporous tunable electrical double layer biosensors for sweat diagnostics,” *Sci. Rep.*, vol. 5, pp. 1–11, 2015.
- [233] B. D. A. Bernards and G. G. Malliaras, “Steady-State and Transient Behavior of Organic Electrochemical Transistors,” *Adv. Funct. Mater.*, vol. 17, pp. 3538–3544, 2007.
- [234] D. A. Bernards and G. G. Malliaras, “Steady-state and transient behavior of organic electrochemical transistors,” *Adv. Funct. Mater.*, vol. 17, no. 17, pp. 3538–3544, 2007.
- [235] L. B. Baker and A. S. Wolfe, *Physiological mechanisms determining eccrine sweat composition*,

vol. 120. 2020.

- [236] S. Demuru *et al.*, “All-Inkjet-Printed Graphene-Gated Organic Electrochemical Transistors on Polymeric Foil as Highly Sensitive Enzymatic Biosensors,” *ACS Appl. Nano Mater.*, vol. 5, no. 1, pp. 1664–1673, 2022.
- [237] M. Figuera, P. D. Van Der Wal, and H. Shea, “Comparison of six different printed Ag inks for coulometric removal of chloride ions from seawater: Towards an integrated microfluidic platform for desalination,” *ECS Trans.*, vol. 75, no. 41, pp. 1–12, 2016.
- [238] S. Demuru, B. P. Kunnel, and D. Briand, “Real-Time Multi-Ion Detection in the Sweat Concentration Range Enabled by Flexible, Printed, and Microfluidics-Integrated Organic Transistor Arrays,” *Adv. Mater. Technol.*, vol. 5, no. 10, pp. 1–9, 2020.
- [239] S. H. Faulkner *et al.*, “The detection and measurement of interleukin-6 in venous and capillary blood samples, and in sweat collected at rest and during exercise,” *Eur. J. Appl. Physiol.*, vol. 114, pp. 1207–1216, 2014.
- [240] D. L. Glasco, N. H. B. Ho, A. M. Mamaril, and J. G. Bell, “3D Printed Ion-Selective Membranes and Their Translation into Point-of-Care Sensors,” *Anal. Chem.*, vol. 93, pp. 15826–15831, 2021.
- [241] C. J. Harvey, R. F. LeBouf, and A. B. Stefaniak, “Formulation and stability of a novel artificial human sweat under conditions of storage and use,” *Toxicol. Vit.*, vol. 24, no. 6, pp. 1790–1796, 2010.
- [242] A. Martín *et al.*, “Epidermal Microfluidic Electrochemical Detection System: Enhanced Sweat Sampling and Metabolite Detection,” *ACS Sensors*, vol. 2, pp. 1860–1868, 2017.
- [243] B. Paul, S. Demuru, C. Lafaye, M. Saubade, and D. Briand, “Printed Iontophoretic-Integrated Wearable Microfluidic Sweat-Sensing Patch for On-Demand Point-Of-Care Sweat Analysis,” *Adv. Mater. Technol.*, vol. 2000910, pp. 1–11, 2021.



# Curriculum Vitae

**Silvia Demuru**

📍 Pierre-à-Mazel 11, Neuchâtel, Switzerland

Born in Ozieri (SS), Italy, 21/06/1993

☎ +41779767179 / +393496883957 | ✉ [silviadem93@gmail.com](mailto:silviadem93@gmail.com)

🌐 [linkedin.com/in/silviademuru/](https://www.linkedin.com/in/silviademuru/)

## Education

### Ph.D. in Microsystems and Microelectronics

Neuchâtel, Switzerland

École Polytechnique Fédérale de Lausanne (EPFL), Microcity

06/2018 - Present

Section: Electrical and Micro Engineering

### Master degree in Micro and Nanotechnologies for Integrated Systems

Lausanne, Switzerland

EPFL/ Grenoble INP/ Politecnico di Torino

Grenoble, France

Section: Electrical and Electronics Engineering

Torino, Italy

**International** master program (20 students accepted/year in Italy)

09/2015 – 03/2018

### Bachelor degree in Biomedical Engineering

Torino, Italy

Politecnico di Torino

09/2012-07/2015

## Work experience

### Ph.D. Student at Soft Transducers Laboratory (LMTS - EPFL)

Neuchâtel, Switzerland

Development of novel wearable biosensors for sweat analysis.

06/2018 - Present

- Development of multi-sensing organic electrochemical transistors and potentiometric sensors on flexible polymeric substrates
- Improved sensing performances of ions, metabolites, and hormones
- Fabrication of the functional materials and development of the chemical bio-layers
- Electrochemical characterization of several types of sensors in physiological media
- Clinical testing at the Sports Medicine Center at CHUV (Lausanne) on healthy subjects

**Trainee at Microsystems Laboratory 4 (LMIS4 - EPFL)**

Lausanne, Switzerland

- Electrochemical analysis of nanoelectrodes in contact with living cells and cell culture

10/2017 – 02/2018

**Research Intern (Master thesis) at IBM TJ Watson Research Center**

Yorktown Heights,

- Electrochemical detection of neurotransmitters (dopamine, serotonin, adenosine) with improved sensitivity and selectivity by carbon microelectrodes
- Development of new processes for electropolymerizing thin-film coatings on microelectrodes

New York - USA

02/2017 – 08/2017

**Assistant Engineer (Summer Internship) at Institut Fresnel**

Marseille, France

- Optimization of the control of the scanning mirrors in a confocal microscope using MATLAB and LabVIEW resulting in less damaging of biological samples

06/2016 – 08/2016

**Laboratory Intern at Chilab Laboratory - Materials and Processes for Micro & Nano Technologies**

Chivasso, Italy

- Development of microfluidic platforms for cell culture studies by 3D printing and lithography processes

04/2015 – 06/2015

## Technical skills

---

- **Advanced fabrication:** Processing of flexible and organic sensors (polyimide and PET substrates), Laser cutting, Inkjet printing, 3D printing, Screen printing, Sputtering, Evaporation, Electrodeposition, Microfluidics (Soft-lithography and multi-layer laser cutting), Basic lithography processes, Imaging (SEM, AFM, Optical Microscopy).
- **Chemistry/Biology:** Preparation of ion-selective membranes, Membranes for Ag/AgCl pseudo-references, Enzymatic and antibody functionalization on different surfaces (organic materials, gold, graphene), Electrolyte solutions, Basics of cell culture.
- **Electrochemical characterization:** Potentiostat/Galvanostat (potentiometric, amperometric, cyclic voltammetry measurements), Electrochemical impedance spectroscopy, Semiconductor parameter analyzer.

## IT skills

---

- **Design and simulation:** CleWin, Inkscape, Solidworks, Spice, COMSOL Multiphysics.
- **Programming and data analysis:** Excel, OriginLab, MATLAB, LabVIEW, C.

## Soft skills

---

- Advanced project management skills (**Supervisor** of 5 semester projects and 2 technicians, managing project deadlines within an **SNF Sinergia project** with other 3 teams for 4 years)
- Excellent team-working skills (**Collaborations** with laboratory colleagues in an international environment and with several researchers in national/international institutions and industries: University of Zurich, CHUV Lausanne, SKAN Ag Allschwil, Université Paris Diderot, Barcelona Institute of Microelectronics IMB-CNM, University of Manchester, IBM Watson Research Center)
- Great communication skills (presentations at 5 technical **conferences**, power-point **presentations** to colleagues and collaborators, **teaching assistant** for 3 semesters in “Conception de mécanismes I”)

## Language

---

English (C1)

Italian (Native language)

French (B1)

## Hobbies

---

Passionate artist (oil and acrylic)

Playing chess

Hiking & Traveling

## Publications

---

1. S. Demuru, C.-H. Huang, K. Parvez, R. Worsley, G. Mattana, B. Piro, V. Noël, C. Casiraghi, and D. Briand, “*All-Inkjet-Printed Graphene-Gated Organic Electrochemical Transistors on Polymeric Foil as Highly-Sensitive Enzymatic Biosensors*”, 2022, **ACS Applied Nano Materials**, 5, 1, 1664–1673.
2. S. Demuru, B. P. Kunnel, D. Briand, “*Thin film organic electrochemical transistors based on hybrid PANI/PEDOT:PSS active layers for enhanced pH sensing*”, 2021, **Biosens. Bioelectron.** X 7, 1–9.
3. S. Demuru, B. P. Kunnel, D. Briand, “*Real-Time Multi-Ion Detection in the Sweat Concentration Range Enabled by Flexible, Printed, and Microfluidics-Integrated Organic Transistor Arrays*”, 2020, **Adv. Mater. Technol.**, 5, 2000328, 1–9.
4. B. P. Kunnel, S. Demuru, C. Lafaye, M. Saubade, D. Briand, “*Printed Ionophoretic-Integrated Wearable*

- Microfluidic Sweat-Sensing Patch for On-Demand Point-Of-Care Sweat Analysis*", 2021, **Adv. Mater. Technol.** 2000910, 1-11.
5. B. P. Kunnel, S. Demuru, "*An Epidermal Wearable Microfluidic Patch for Simultaneous Sampling, Storage, and Analysis biofluids with counterions monitoring*", 2022, **Lab on a chip**. Manuscript accepted for publication.
  6. M. Saubade, S. Norrenberg, C. Besson, S. Demuru, D. Briand, B. Paul, V. Gremeaux, C. Lafaye, "*Sweat as an indicator of health*", 2021, **Rev Med Suisse** 17, 1289–1293.
  7. S. Demuru, L. Nela, N. Marchack, S. J. Holmes, D. B. Farmer, G. S. Tulevski, Q. Lin, H. Deligianni, "*Scalable Nanostructured Carbon Electrode Arrays for Enhanced Dopamine Detection*", 2018, **ACS Sensors**, 3, 799.
  8. S. Demuru, H. Deligianni, "*Surface PEDOT:Nafion Coatings for Enhanced Dopamine, Serotonin and Adenosine Sensing*", **J. Electrochem. Soc.** 2017, 164, G129.

## Conferences

---

1. S. Demuru\*, B. P. Kunnel, and D. Briand, "*Wearable Electrochemical Sensing Transistors for Real-Time Sweat Analysis*", **BioNanoTech Montreux**, 2021 Nov 15-17, Montreux. **\*Oral presentation.**
2. S. Demuru\*, K. Chennit, V. Noël, B. Piro, G. Mattana, and D. Briand, "*An integrated flexible platform with printed organic electrochemical and field-effect transistors for biochemical sensing*", **MicroTAS**, 2020 October 4-9, Virtual. **\*Poster presentation.**
3. B. Paul\*, S. Demuru, R. I. Haque, P. van der Wal, C. Lafaye, M. Saubade, and D. Briand, "*Printed multisensing patch with integrated microfluidics for wearable sweat analysis applications*", **MicroTAS**, 2020 October 4-9, Virtual. **\*Poster presentation.**
4. M. Rovira\*, C. Fernández-Sánchez, S. Demuru, R. Haque, D. Briand, and C. Jimenez-Jorquera, "*Hybrid wearable technology for sweat biomonitoring*", **MicroTAS**, 2020 October 4-9, Virtual. **\*Poster presentation.**
5. S. Demuru\*, R. Haque, M. O. Joho, A. Bionaz, P. van der Wal, D. Briand, "*3D-Integration of Printed Electrochemical Sensors in PET Microfluidics for Biochemical Sensing*", **Transducers – Eurosenors XXXIII**, 2019 June 23-27, Berlin, Germany, 2464-2467, doi: 10.1109/TRANSDUCERS.2019.8808497. **\*Poster presentation.**
6. S. Demuru\*, A. Marette, W. Kooli, P. Junier, D. Briand, "*Flexible Organic Electrochemical Transistor with Functionalized Inkjet-Printed Gold Gate for Bacteria Sensing*", **Transducers – Eurosenors**

**XXXIII**, 2019 June 23-27, Berlin, Germany, 2519-2522, doi: 10.1109/TRANSDUCERS.2019.8808309.

**\*Poster presentation.**

7. S. Demuru\*, B. P. Kunnel, D. Briand, “*A Flexible Platform with Inkjet-Printed Organic Electrochemical Transistor Integrated in Microfluidics for Selective Ion Detection*”, **MicroTAS**, 2019 October 27-31, Basel, Switzerland. **\*Poster presentation.**
8. M. Rovira, C. Fernández-Sánchez, S. Demuru, P. K. Brince, D. Briand, C. Jimenez-Jorquera\*, “*Multisensing Wearable Technology for Sweat Biomonitoring*”, Eng. Proc. 2021, 6, 78, **8th International Symposium on Sensor Science**, 17–28 May 2021. **\*Oral presentation.**
9. B. P. K\*, S. Demuru, “*A Wearable Autonomous Colorimetric Sweat Induction System for Sweat Analysis*”, 2021, 6763, 2021, **43rd Annual International Conference of the IEEE Engineering in Medicine & Biology Society (EMBC)**, Oct 31 - Nov 4, 2021, Virtual. **\*Oral presentation.**
10. A. Marette, S. Demuru\*, D. Briand, “*Printed Organic Electrochemical Transistors on Flexible Bioresorbable Substrate for Biosensing*”, **Swiss Symposium in Point of Care Diagnostics**, 2018 October 18, Chur, Switzerland. **\*Poster presentation.**